THE DEVELOPMENT OF CREEP DAMAGE CONSTITUTIVE EQUATIONS FOR HIGH CHROMIUM STEEL BASED ON THE MECHANISM OF CAVITATION DAMAGE

XIN YANG, BACHELOR OF ENGINEERING (BENG)

A thesis submitted to the University of Huddersfield in partial fulfilment of the requirements for the degree of Doctor of Philosophy

The University of Huddersfield

September 2017

Copyright statement

i. The author of this thesis (including any appendices and/or schedules to this thesis) owns any copyright in it (the “Copyright”) and s/he has given The University of Huddersfield the right to use such copyright for any administrative, promotional, educational and/or teaching purposes.

ii. Copies of this thesis, either in full or in extracts, may be made only in accordance with the regulations of the University Library. Details of these regulations may be obtained from the Librarian. This page must form part of any such copies made.

iii. The ownership of any patents, designs, trademarks and any and all other intellectual property rights except for the Copyright (the “Intellectual Property Rights”) and any reproductions of copyright works, for example graphs and tables (“Reproductions”), which may be described in this thesis, may not be owned by the author and may be owned by third parties. Such Intellectual Property Rights and Reproductions cannot and must not be made available for use without the prior written permission of the owner(s) of the relevant Intellectual Property Rights and/or Reproductions.

Abstract

Due to increasing electrical energy power supply, thermal efficiency and the desire to reduce CO_2 emissions, creep-resistant high chromium steels are becoming widely developed and applied for components of electric power plants under high pressure at high temperature. The limited design factors such as strain histories, damage evolution and lifetime are important factors when creating the components of a power plant. Obtaining a long-term (100,000h, over 11 years) creep data is time consuming and costly, hence long-term creep data is very limited, and the extrapolation using the conventional empirical methods may not be reliable due to limited data (Chen et al., 2011; Shrestha et al., 2013; Ghosh et al., 2013). To design against failures, creep damage constitutive equations have the advantage of traceability from the physics based constitutive equation to the fundamental microstructural and damage behaviour. Thus, creep modelling constitutive equations for materials of the critical components of, for example, power plants and other safety critical systems, are a key issue in the research of materials.

In the past decade, a range of creep damage constitutive equations have been developed to describe creep damage behaviour for high chromium steel, however, some models are only based on creep deformation (creep microstructural degradation) and are not really concerned with cavitation damage, which is a dominant factor in creep rupture; most of them are proposed based on high stress levels of high chromium steel and extended to a low stress level, the modelling results fail to explore the phenomenon of stress breakdown. Besides, the cavitation damage equations were developed on experimental data of pure metal and super alloy, the fundamental nature of the evolution of creep cavitation damage is still unclear and necessary to solve for high chromium steel. Thus, the aim of this research project was to develop a novel creep damage constitutive equation for high chromium steel based on the mechanism of cavitation damage under a wide range of stress levels.

This research made contributions to the specialised knowledge on the following three aspects. Firstly, a modified hyperbolic sine law, which describes the relationship between minimum creep strain and applied stress, was applied to

high chromium steel. Through which we found that the modelling results fitted better with published experimental data by NIMS in comparison with conventional functions such as power law, hyperbolic sine law and linear power law. The other two aspects of innovation in the development of creep damage constitutive equation had been achieved. Secondly, using the quantitatively analysed results of the cavity size distribution along grain boundary by the superior 3D technology of X-ray micro-tomography, a novel creep cavitation damage equation was developed and applied to describe the evolution of cavity along grain boundary in the creep process for high chromium steel. Thirdly, the novel creep damage constitutive equations, that coupled appropriate creep deformation mechanisms with the new cavitation damage equation, were successfully applied to high chromium steel under a wide range of stress level according to comparisons made between the modelling results of novel creep damage constitutive equations, classic uniaxial KRH constitutive equations and experimental data for P91 steel at 600℃ and also applied to P91 steel at 625℃.

Acknowledgements

I would like to express my sincere gratitude to my supervisors, Dr. Qiang Xu and co-supervisors Prof. Joan Lu for opening this door of research to me. Their professional theoretical and practical knowledge in the field of Creep Damage Mechanics and Creep Damage Constitutive Equations Modelling has provided me with valuable guidance throughout the whole process of my PhD research project.

In particular, I would like to thank my supervisor Dr. Qiang Xu for educating and guiding me as a researcher with a rigorous academic attitude and invaluable academic experience in analytical problems and resolution problems; and also providing me with opportunities to take a part in interesting PhD research international academic exchanges and grant applications of research projects.

Aside from my supervisors, I would also like to thank my parents and wife for their financial support and encouragement. It would have be impossible to complete my Ph.D. degree without their generous support and help throughout the duration of my PhD.

Finally, I am also very grateful for being fortunate enough to be granted a partial fee waiver scholarship by the School of Computing and Engineering at the University of Huddersfield and being awarded the Santander Student Mobility Scholarship by Santander.

Contribution Statement

This research project involved Mr Xin Yang and Dr Qiang Xu. The contributions are stated bellow:

1. Qiang Xu conceived the idea of how to reveal the deficiency of existing models. Xin Yang produced the required Table 2.4. Qiang Xu produced the Figure 2.53.

2. Qiang Xu conceived the idea and the method to calibrate a set of cavity nucleation and cavity growth models. Xin Yang identified Sket and Renversade's experimental data that could be used for it. Xin Yang implemented the idea, developed the required theories and software and performed the actual numerical calculations.

3. Qiang Xu conceived the idea of how to determine the coefficients based on the void histogram, and outlined the mathematical relationship and the steps required to Xin Yang. Xin Yang collected the required theory related to the void number histogram and developed a programme based on the theory. Qiang Xu introduced the correct definition of f(R) of equation (5.19) in the debugging of the programme developed by Xin Yang's. Xin Yang performed the numerical calculations.

4. Qiang Xu conceived the idea of development of an applicable creep rupture criterion based on grain boundary cavitation: it is essentially to apply the developed cavity nucleation and cavity growth models to Reidel's generic theory to obtain a specific and practical solution. Xin Yang actually derived the specific equation (e.g. equation (5.11)).

5. Qiang Xu conceived the terminology and its use of U'. Xin Yang produced the relevant Tables and Figures.

List of Publications

Xu, Q., Yang, X., Lu, Z. (2017b). On the development of creep damage constitutive equations: minimum creep strain rate and stress function and cavity area fraction along grain boundary based creep fracture criterion. Material at High Temperature. Materials at High Temperatures, 34 (3), 229-237. doi: http://dx.doi.org/10.1080/09603409.2017.1289613.

Xu Q, Yang X, Lu, Z. (2017a). On the development of creep damage constitutive equations, keynote presentation, In HIDA-7: Life/Defect Assessment & Failures in High Temperature Industrial Structures, 15-17 May 2017, Portsmouth University, England.

Yang, X., Lu, Z. and Xu, Q. (2015). The Interpretation of Experimental Observation Data for the Development of Mechanisms based Creep Damage Constitutive Equations for High Chromium Steel. In: IEEE International Conference on Automation and Computing (ICAC 2015), 11th - 12th September 2015, Glasgow, Scotland.

Yang, X., Xu, Q., Lu, Z. and Barrans, S. (2014). Preliminary Review of the Influence of Cavitation Behavior in Creep Damage Constitutive Equations. In: Machinery, Materials Science and Engineering Applications 2014. Trans Tech Publications. pp. 46-51. ISBN 978-3-03835-113-9.

Yang, X., Xu, Q. and Lu, Z. (2013). The relative significance of internal damage mechanisms on the overall creep damage and ultimate failure of P91 steel. In: 6th International 'HIDA' Conference: Life/Defect Assessment & Failures in High Temperature Plant, 2nd – 4th December 2013, Nagasaki, Japan.

Attended Training courses and Conferences

2014.10 Attended training course on high chromium steels. For materials working in high temperature such as martensitic 9Cr steels P91/P92-Fabrication, Welding, Heat Treatment, Quality Check, Damage Mechanisms, Plant Experiment & Integrity/Life Assessment, 14th-15th October, 2014, ETD Training Centre, Fountain House, Surrey, UK.

2016.06 Visited the World's largest third-generation synchrotron radiation facility Japan synchrotron radiation research institute (Spring-8, JASRI). Santander PGR study Visits 2015/16:Dr Qiang Xu and Mr Xin Yang visited the world's largest third- generation synchrotron radiation facility, Japan synchrotron radiation research institute in Aioi, Japan, where they were able to work on collaborations with 3D/4D structural materials expert, distinguished professor and director Toda Hiroyuki, who works in Kyushu University (QS world ranking 142). Both the individuals were impressed by the advanced and extensive laboratories, and during the visit they discussed the possibility of future collaborations.

2016.09 Attended High Temperature Facility Alliance (HTF) international Seminar organised by High Temperature Facility Alliance. International Seminar on High Temperature Structural Performance in Power Generation: Current Knowledge and Future Challenges, 19-20, September, 2016, Museum of Science and Industry (MSI), Manchester, UK. Visited a new £2M High Temperature Facility lab based at Amec Foster Wheeler's Technology and Innovation Centre at Birchwood Park in Warrington.

2017.01 Attended Huddersfield University Event. Huddersfield Materials Forum, 12 January 2017, Bronte Lecture Theatres, University of Huddersfield.

2017.05 Attended the conference at Portsmouth University. International Conference: (HIDA-7) Life/Defect Assessment & Failure in High Temperature Industrial Structures, keynote presentation with supervisor Dr. Qiang Xu, 15-17 May, 2017, Portsmouth University, Portsmouth.

Involvement and contribution to grant applications

2015.10-Assisted with supervisor Dr. Qiang Xu in applying to a research project proposal. The Royal Society International Exchanges Scheme-2015 National Natural Science Foundation of China (NSFC) Cost share, the title of the collaborative research was the “Effect of stress states on the creep damage of FGHAZ in welds and its modelling” in partnership Wuhan University, China. Application Ref: IE150995.

2016.03-Application of Santander PGR study Visits 2015/16 with supervisor Dr. Qiang Xu. During the academic year of 2015/2016, Santander Student Mobility Scholarships (£1000) supported short study visits to other institutions, particularly those in the QS Top 500.

2016.12-Spring-8, 2017A, General Proposal for experiment: Study of characterization of creep cavitation of heat resistant 9% Chromium steel (P91) weld using synchrotron microtomography and serial sectioning techniques, Application No. 37778.

2017.06 Applied Spring-8, 2017B, Non-Proprietary Research Proposal for experiment. Title of Experiment: Study of the distribution of creep cavitation of heat resistant 9% Chromium steel (P91) weld: on grain boundary.

Contents

List of Tables

List of Figures

List of Abbreviations

2D	Two dimensional
3D	Three dimensional
ASME	American Society of Mechanical Engineers
ASTM	American Society for Testing and Materials
BM	Base Metal
BSE	Backscatter Electron
CDM	Continuum Damage Mechanics
DTI	Department of Trade and Industry
EBSD	Electron Backscatter Diffraction
ECCC	European Creep Collaborative Committee
ESRF	European Synchrotron Radiation Facility
FEA	Finite Element Numerical Analysis
FIB	Focused Ion Beam
HSE	Health and Safety Executive
IEA	International Energy Agency
IEO	International Energy Outlook
KRH	Kachanov-Rabotnov-Hayhurst
NEUP	Nuclear Energy University Programs
NIMS	National Institute for Materials Science
OP	Optical Microscopy
Q+T	Quenched and Tempered
RAFM	Reduced Activation Ferritic–Martensitic
SE	Secondary Electron
SEM	Scanning Electron Microscopy
SFR	Sodium Fast Reactor
SG	Steam Generator
SOP	Standard Operating Procedure
Spring-8	Japan Synchrotron Radiation Research Institute
TEM	Transmission Electron Microscopy

UKERC	UK Energy Research Centre
VHTR	Very High Temperature Reactor
WM	Weld Metal

Chapter 1 Introduction of research project

1.1 Background of research field

1.1.1 Increasing electric energy power supply and thermal efficiency and reducing of CO_2 emissions

The World Nuclear Organization reported that there will be a great increase of energy demand in the world in the future, especially in electricity. The world electricity consumption by region (Figure 1.1) indicates clearly that the electricity demand doubled between 1990 and 2011 and estimates an 81% growth between 2011 and 2035 (from 19,004 TWh to 34,454 TWh) in current policies scenario, and 69% (to 32,150 TWh) in the central new policies scenario (World Nuclear Organization, updated June 2017). The growth of electricity is over double in both cases.

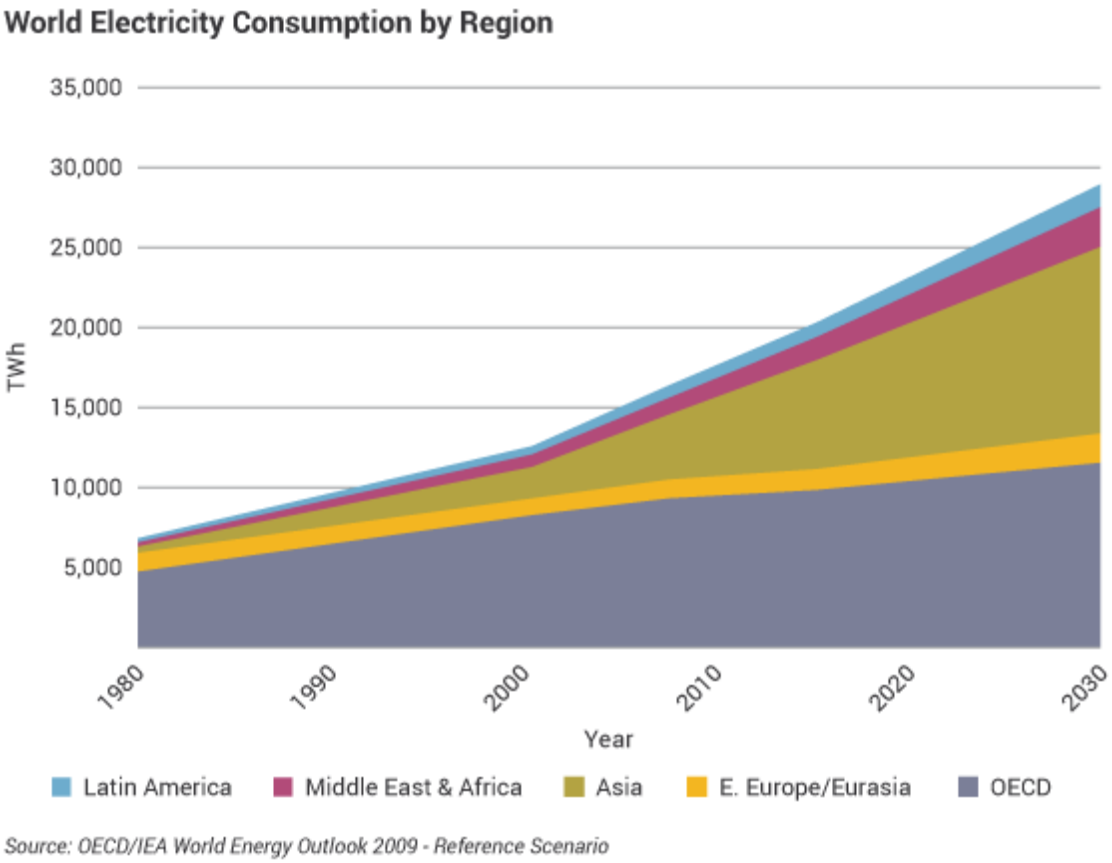

Figure 1.1 The world electricity computation by region from 1980-2030 (World Nuclear Organization, Updated June 2017).

In the case of International Energy Outlook 2016 (IEO2016), coal continues to be the single largest fuel used so far for the electricity generation. The coal-

fired electricity generation, which accounted for 40% of the total world electricity generation in 2012, is even predicted to decrease to 29% of its current total in 2040, but the coal-generation still remains the dominating type of energy as shown in Figure 1.2(U.S. Energy Information Administration, 2016).

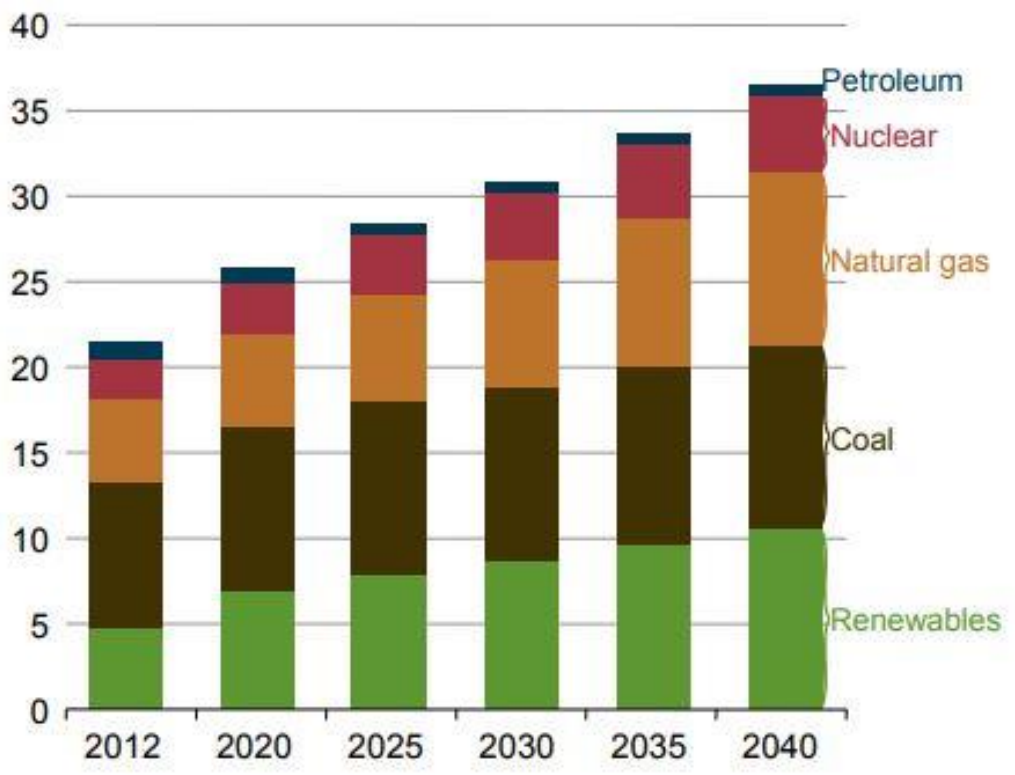

Figure 1.2 World net electricity generation by fuel, 2012-2014(trillion kilowatt-hours) (U.S. Energy Information Administration, 2016)

Burning fossil fuels, which produces CO_2 is one of most important factors contributing to humans influencing climate change and increasing the earth's temperature (European Commission, 2017). The International Energy Agency's (IEA) world energy outlook special report on 'Energy and Climate Change' was published in June 2015, it outlines a strategy to limit global warming to an average of no more than 2°C by Paris Climate Agreement (International Energy Agency, 2015). The report recommends a series of measures including increasing energy efficiency, reducing the use of inefficient coal-fired power plants and phasing out fossil fuels subsidies.

1.1.2 Creep resistant strength of high chromium steel

To increase the energy efficiency of coal-fired power plants and reduction of CO_2 emissions, it leads to the development and application of high chromium creep-resistant steels (contains 9-12wt% chromium element, chemical compositions and production details in appendix A (Strang, A.,2000; Ennis, P. J., Czyrska-Filemonowicz, A., 2003) for the components of electricity power plant as shown in Figure1.3 (Masuyama, 2006), according to Abson et al. (2007) and Figure1.4 (Masuyama, 2016).

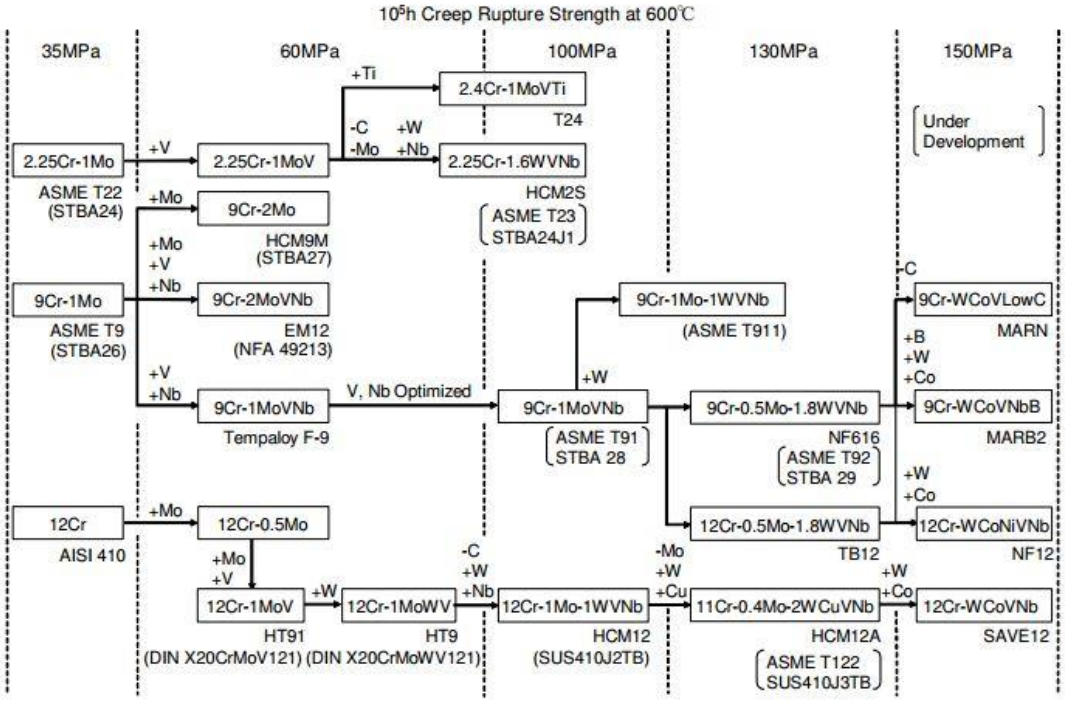

Figure 1.3 The development of 9-12%Cr steels (Masuyama, 2006) (Abson et al., 2007).

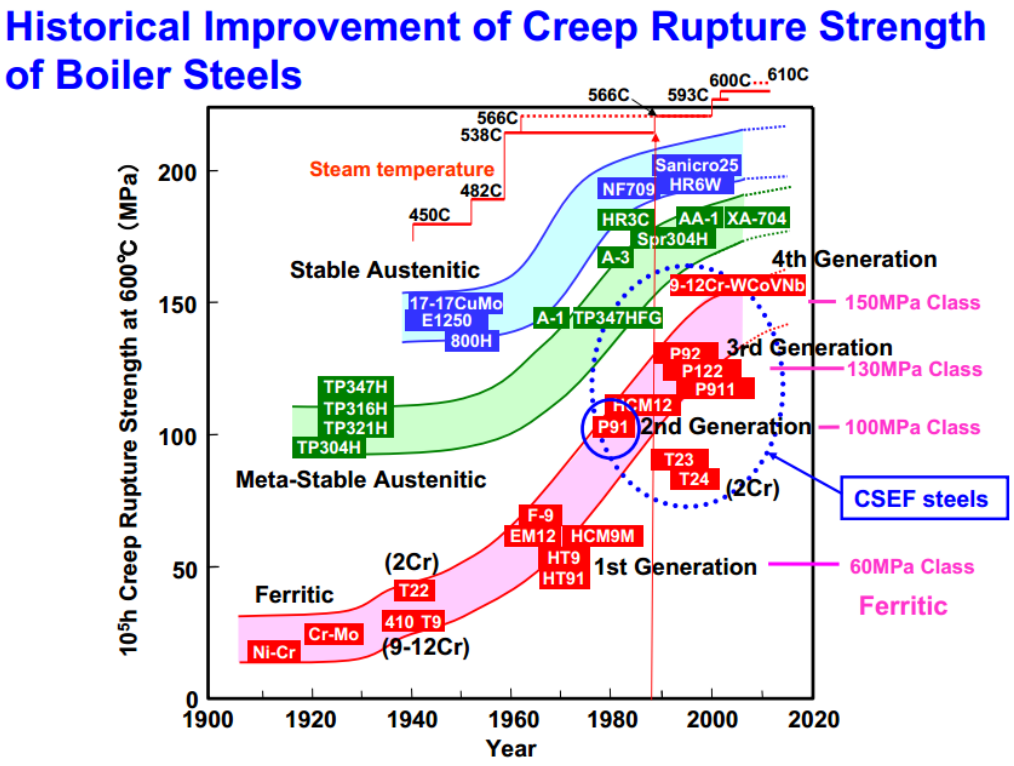

Figure 1.4 The development and application of the high chromium creep-resistant steels for the components of electricity power plant (Masuyama, 2016).

9-12% Cr steel are characterised by excellent mechanical properties and thermal properties such as being able to be subjected to high temperatures and stress conditions. Subsequently, these steels are extensively used in industrial power plants. The modified 9Cr1Mo steel exhibits better tensile and creep properties than the plain 9Cr1Mo steel through the addition of Vanadium and niobium. Furthermore, most of the Cr-Mo steels from low to high content of Chromium, and steadily improved creep rupture strength, have been used to construct new advanced fossil-fired steam power plants with higher efficiency and are a strong candidate structural material of 4th generation reactors as shown in Figure1.4, such as the primary circuit of the Very High Temperature Reactor (VHTR) and the Steam Generator of the Sodium Fast Reactor (SFR) (Kim et al., 2011) (Massé & Lejeail, 2012, 2013). It has been found that an increase in pressure and operating temperate from subcritical 180 bar(18MPa)/530–540°C to ultra-supercritical values of 300 bar(30MPa) and 600°C, has resulted in an increase of efficiency from 30–35% to 42–47%, which

is equivalent to a 30% reduction in specific CO_2 emissions (Hald, 2008). The creep rupture strength at 600℃ (lifetime around $10^6 h$) of P91 steel as shown in Figure1.4 is satisfied with expected service life (up to 60 years) (Kim et al., 2011; Shrestha et al., 2013) of a component in related industry such as power generation.

High chromium steel has been used successfully under super critical steam conditions at 600°C. Steam power stations are now in operation at pressures of 25-30MPa (Ennis and Czyrska-Filemonowicz, 2003), and lifetime specifications of 10^5h are the target for turbine components at pressures of 100MPa (Klueh, R.L. & Harries, D.R., 2001), and super critical steam of power plants in future generations are to be operated at 650°C (Maruyama et al., 2001).

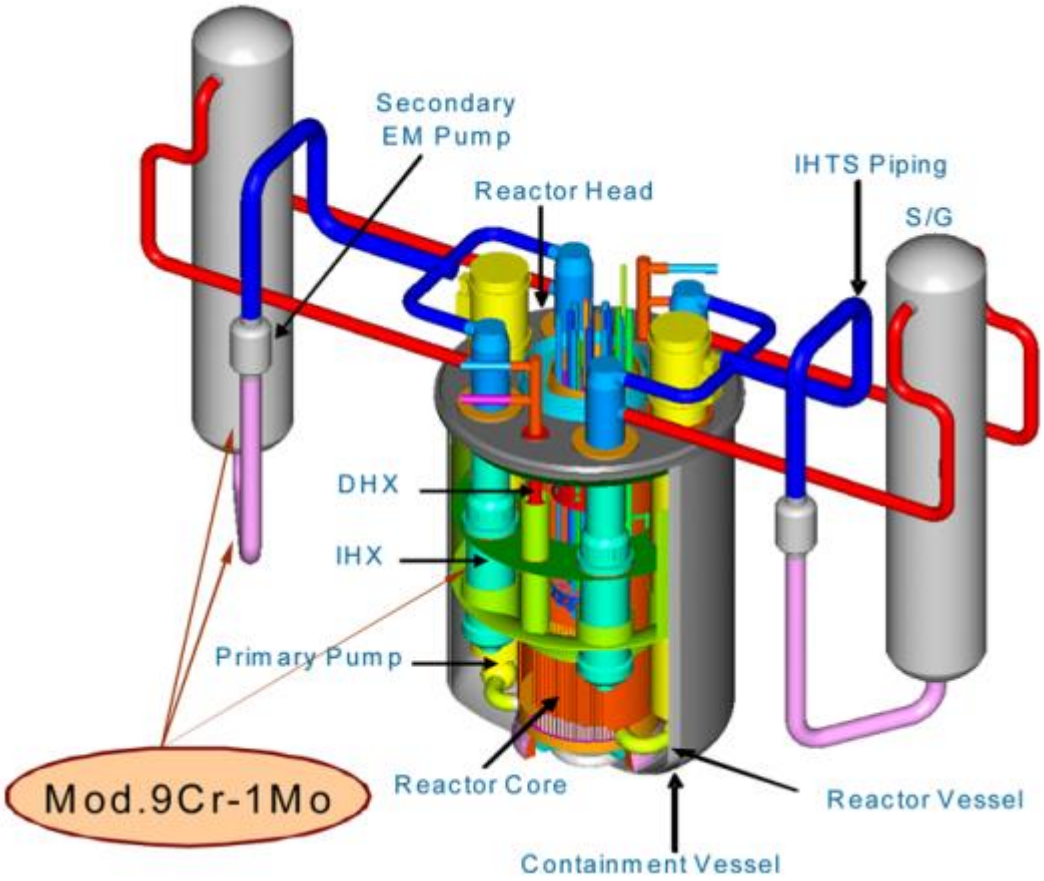

Figure 1.5 Structural material of 9Cr-1Mo steel in applications of power plant (Kim et al., 2011).

1.2 The importance of cavitation damage in engineering materials

Generally, creep cavitation is the most important factor of creep fracture, and is caused by the nucleation of cavities followed by growth and interlinkage, thus leading to failure (Gooch, 1982) (Eggeler, 1989) (Worswick, 2001) (Kassner & Hayes, 2003) (Sklenička, 2003) (Westwood et al., 2004) (Dobrzański, 2006) (Shrestha et al., 2013) (Gupta et al., 2013). The nucleation and growth of cavities usually account for 80% of the creep life time and governing the creep rupture can last up to 20% of its life time (Sklenička, 2003). Understanding the behaviour of cavitation is essential both scenically and technically, especially in regards to the residual lifetime of design components for a power plant.

In recent years, through experimental observation using traditional techniques, such as OP (optical microscopy), TEM (transmission electron microscopy), SEM (scanning electron microscopy) on pure metal(Cu)(Cane & Greenwood, 1975), super alloys (Ni-Cr alloy with Ti and Al) (Dyson, 1983), low chromium steel (1Cr-0.5Mo steels) (Needham, 1983), and high chromium steel (9-12% Cr steels) (Wu & Sandström, 1995) (Sklenička, 2003), it has been found that creep cavities are observed mostly on the grain boundaries, which are perpendicular to the direction of the applied stress. However, these investigations are limited by their resolution and the continuity of the cavitation process is not adequately captured. Hayhurst (D.R.), Lin and Hayhurst (R.J) (2008) claimed that creep deformation resistance and fracture mode of engineering materials was due to the kinetic phenomenon of grain boundary cavity formation under arbitrary stress state which depends critically on the cavity nucleation rate and growth rate. Thus, it is visible that creep cavitation takes a large role in the failure of components of engineering materials.

At present, there has been significant focus on the effects that alloy elements (W, Ta, Mo, N, B and Co) have on the creep resistance of high chromium steel for components of a power plant and elucidated the evolution of creep deformation (microstructure degradation), such as strain hardening, precipitation coarsening, and mobile dislocation (Ennis et al., 1997) (Czyrska-Filemonowicz et al., 2006) (Hald, 2008) (Panait et al., 2010) (Sawada et al.

2011). However, there is not a similar emphasis on the evolution process of cavitation and there is an absence of quantitative analysis into creep cavitation characterization.

In recent years, the advanced technology of synchrotron X-ray microtomography (e.g. ESRF, Spring-8) has overcome the problem of connectivity with high-resolution ($1\mu m$) and was applied to study the fracture behaviour of high chromium steel and characterized 3D visualization of the creep voids with increasing creep exposure times. The application of X-ray microtomography has provided better measures for us to explore the characterisation of nucleation, growth and the coalescence process of cavitation. Consequently, allowing the community as a whole to better understand the underlying cavitation characteristics as a function of applied stress and creep exposure time, and further develop a more accurate creep cavitation behaviour equation for the modelling the evolution of creep damage and predicting the lifetime of high chromium steel.

1.3 The importance of developing a constitutive equation

In high pressure and elevated temperature conditions, creep deformation and rupture are important factors in determining design factors such as strain histories, damage evolution and lifetimes for components of power plants (Mustata & Hayhurst, 2005). Obtaining long term creep data is time consuming and costly, hence creep data is very limited, and the extrapolation using the conventional empirical methods may not be reliable due to limited data, because of the method of extrapolation overestimated the lifetime of materials (Chen et al., 2011; Shrestha et al., 2013; Ghosh et al., 2013). To design against failures, creep damage constitutive equations require complex analyses such as the Continuum Damage Mechanics (CDM) method that has the advantage of providing traceability from the physics based constitutive equation to the fundamental microstructural behaviour (Hayhurst et al., 1984).

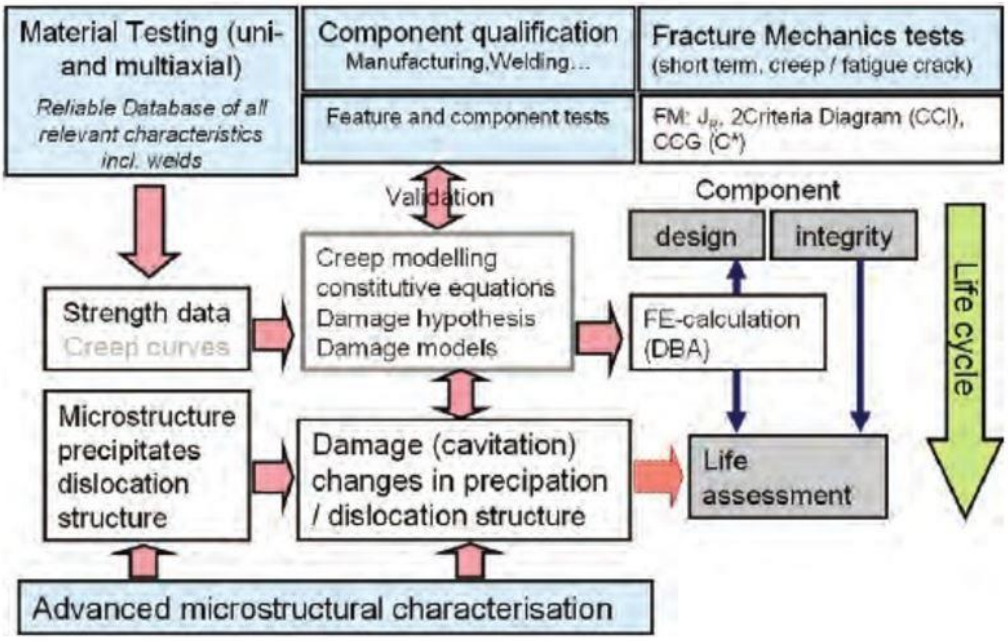

Figure 1.6 The assessment by a creep modelling constitutive equations for materials of the components of power plant (Feuillette et al., 2010).

Assessment by creep modelling constitutive equations for materials of the components of power plants is a key issue in the research of materials, as shown in Figure 1.6 (Feuillette et al., 2010). A wide range of creep model equations are used for the creep deformation behaviour of engineering materials. The development of more accurate models is an important research project for researchers in this field. Based on the range of creep deformation models that have employed within the power generation sector in Europe, as reviewed by the European Creep Collaborative Committee (Holdsworth & Merckling, 2003) (ECCC, 2005). Better alloy development and application through improved understanding and modelling of microstructural evolution and its relationship to mechanical properties is one of the major objectives of the project of improved materials for boilers and steam turbines as described by the UK Energy Research Centre (UKERC), and Department of Trade and Industry (DTI) (DTI, 2005). To develop and improve theories and practical methods for enhancing the process, and ensuring the safety of C&I systems, is the main goal of nuclear research for Health and Safety Executive (HSE), UK as of 2012 (ONR, HSE, 2012). In 2013, a report by the Nuclear Energy University Programs (NEUP) in the United States department of energy, a

constitutive model for creep damage in modified 9Cr-1Mo steels had been found and concluded (NEUP, 2013).

1.4 Existing creep damage constitutive equations for high chromium steel

In the past decade, a range of creep damage constitutive equations had been developed to describe creep damage behaviour for high chromium steel (Dyson, 2000; Gaffard et al., 2005; Yin and Faulkner, 2006; Semba, Dyson and Mclean, 2008; Pétry and Lindet, 2009; Basirat, 2012; Massé and Lejeail, 2012; Chen et al, 2011, Christopher et al., 2013), however, the main limitations of those equations can be summarized as below:

1) Some models (Pétry and Lindet, 2009; Oruganti et al., 2011; Ghosh et al., Christopher et al., 2013) are only based on creep deformation (creep microstructural degradation) and is not really concerned with the cavitation damage, which is dominant in creep rupture process;

2) Most of these constitutive equations (Yin and Faulkner, 2008; Chen et al., 2011; Basirat et al., 2012; Massé and Lejeail, 2012) proposed are based on high stress level of high chromium steel. Yang extended and modified equation which is based on classical constitutive equation that lower stress range, yet the modelling results could not explore the phenomenon of stress breakdown (Yang, Xu & Lu, 2013). The creep damage mechanisms change under different stress level, and the prior extension of application confirmed the necessity of developing a creep damage constitutive equation for a wide range of stress levels, it cannot be directly achieved by the simple extension from high stress level;

3) The traditional function (power law, hyperbolic sine law, even later modified linear power law) of minimum creep strain rate and stress did not fit well with the experimental data for high chromium steel in a wide range of stress, thus a modified function between minimum creep strain rates based on already published experimental data of high chromium steel, is needed.

4) The cavitation damage equation based on the Dyson's equation was developed on the experimental data of super alloy and only considered cavities nucleate continuous, however, the process of cavitation growth is still unclear, in terms of high chromium steel at a lower stress level. The fundamental nature of the evolution of creep cavitation is still necessary to explore, and the recent rapid development of synchrony X-ray microtomography technology provides some hope.

5) Development of a creep damage constitutive equation for P91 steel has been conducted by An (An, 2015), however, there is a big difference between the results of modelling and experimental data, the predicted lifetime is one time than experimental data for P91 steel under 70MPa under 600℃. The cavitation damage equation in An's model is same with the traditional one based on phenomenology to describing the evolution of cavities, it is short of the quantified cavitation characteristics. There is no new contributions to the description of cavitation damage, and selection of material parameters is ambiguous. Thus, the developed creep damage constitutive equation could not convince readers.

6) Another creep damage constitutive equation for low chromium steel was developed by Qihua Xu (Xu, 2016). Xu successfully applied the modified function between minimum creep strain rate and stress to low chromium steel, however, the creep cavitation damage was still using the typical equation that proposed high stress level due to limitations on the experimental data for low chromium steel under lower stress level (Xu, 2016).

A conference paper (Xu et al., 2013) and a modified version for an academic journal (Xu et al., 2017), published by the leader author Dr. Qiang Xu, summarized partially the main limitations of some existing equations and suggested further work based on preliminary introduction and literature review for the development of creep damage constitutive equations for high chromium

steel under a wide range of stress levels. This research includes development of constitutive equations for high chromium steel under a wide range of stresses.

1.5 Aims and objectives of this project

The aim of this research project was to develop a novel creep damage constitutive equation for high chromium steel under a wide range of stress levels. The constitutive equation should be coupled with the creep deformation mechanisms and cavitation damage which in turn will propose a new constitutive equation that more accurately describes the evolution of the cavitation process during creep exposer.

To achieve the aim of this project, the following objectives will be carried out:

1) To critically review the existing creep damage constitutive equations for high chromium steel and evaluate the advantages and limitations. The lead author's paper provides a preliminary review of some constitutive equations (Xu, Lu and Wang, 2013), this research will focus more on the derivations of the developed cavitation damage equation and analyse the advantage and limitations pertaining to the existing constitutive equations. Aside from the background and knowledge in the process, the author will highlight the expectations of novel creep damage constitutive equations for high chromium steel;

2) To develop or modify a novel function for minimum creep strain rate and stress based on the current published experimental data on high chromium steel;

3) To understand the creep damage (cavitation) mechanism for high chromium steel and develop a new creep damage equation for high chromium steel based on current experimental observation data;

4) To identity the appropriate creep deformation (microstructural degradation) for high chromium steel based on the mature theories of creep deformation equations and the experimental observation of microstructural degradation;

5) To couple the novel creep cavitation damage equation with the appropriate creep deformation to further develop a new creep damage constitutive equation;

6) To identify material parameters for high chromium steel at a constant temperature;

7) To validate the development of novel creep damage constitutive equations through comparing the modelling results with the experimental data of high chromium steel and the modelling results of classic models.

1.6 Structure of this dissertation

Chapter 1 introduces background information on the research field, and explains the importance of cavitation damage in engineering materials and developing a constitutive equation for creep deformation and rupture, and designing and predicting safety lifetime for components of a power plant. The aim and objectives of this research project have been presented above.

Chapter 2 makes contribution to build fundamental knowledge of the development of constitutive equations, introduces and summarises typical functions of minimum creep strain rate and stress, the stress breakdown phenomenon, creep fracture model, creep cavitation and deformation mechanisms. This is followed by exploring the expectations of developing a novel constitutive equations that are based on the current limited creep damage constitutive equations. Finally, the current state of experimental data on high chromium steel.

Chapter 3 collects creep test experimental data on: high chromium steel (NIMS): minimum creep strain rate under different stress levels for modified function of creep minimum strain rate and applied stress, creep curves and rupture lifetime, all of which shall be used to compare the modelling results of the novel constitutive equations with experimental creep curves and lifetime. The observation of experimental data evolution of cavitation characterization of high chromium steel for quantitative analysis of the evolution of cavitation with creep

exposure time collects for developing a novel cavitation damage equation to more accurately describe the evolution of cavitation in creep process for creep damage constitutive equations.

Chapter 4 introduces a novel modified hyperbolic sine law for the relationship between minimum creep strain rate and stress for low chromium steel; and applies the modified hyperbolic sine law for the relationship between minimum creep strain rate and stress to high chromium steel, and compares the modelling results of the modified function with the conventional functions.

Chapter 5: 1) provides a quantifiable analysis of experimental data; 2) understands the underlying mechanisms of cavitation damage; 3) develops architecture evolutions of cavitation damage characterisation as a function of applied stress and creep; 4) makes a fraction criterion of cavity area on grain boundary for the novel creep cavitation damage equation and compares the fraction criterion of novel creep damage equation with the conventional one.

Chapter 6: 1) couples the equations of creep deformation mechanisms with novel cavitation damage equations for novel developed creep damage constitutive equations; 2) identifies material parameters for the equation; 3) compares the modelling results with experimental data on high chromium steel; 4) compares the modelling results with classic uniaxial KRH constitutive equations and experimental data for P91 steel at 600℃.

Chapter 7 summarises the key significant contributions of this research:1) applies the modified hyperbolic sine law for high chromium steel; 2) develops a novel creep cavitation damage equation for high chromium steel based on the quantitative analysed results of the cavity size distribution along grain boundary using the superior 3D technology of X-ray micro-tomography; 3) validates the novel constitutive equations by comparing with classic ‘KRH’ equations and experimental data for high chromium.

Chapter 2 Literature on the development of constitutive equations

This chapter will collect literature related to this field and analyse the challenges involved in the development of creep damage constitutive equations based on phenomenological and physical observation:

Section 2.1: to understand the shapes of creep curves used in describing creep behaviour of engineering materials that change under different operating conditions, especially for high chromium steel;

Section 2.2: to introduce the typical function of minimum creep strain rate and applied stress for the creep damage constitutive equation;

Section 2.3: to understand stress breakdown phenomena existing in high chromium steel under different stress levels;

Section 2.4: to understand how creep fracture mechanisms change from ductile fracture to brittle fracture; and the creep fracture mechanisms for high chromium steel;

Section 2.5: to understand the dominant cavitation damage mechanism under different stress levels for high chromium steel;

Section 2.6: to introduce the traditional cavitation damage equation;

Section2.7: to consider suitable creep deformation (microstructural degradation) damage mechanisms for coupling into constitutive equation for high chromium steel based on the mature theories of creep deformation in engineering materials;

Section 2.8: to review current creep damage constitutive equations and analyse the advantages and disadvantages related to current creep damage constitutive equations and suggest the development of novel constitutive equations, especially for the cavitation damage equation in high chromium steel;

Section 2.9: to introduce typical creep facture criterions for current constitutive equations;

Section 2.10: to understand the current state of experimental data sets of high chromium steel for the development of constitutive equations.

2.1 The typical shapes of creep curves for describing the creep behaviour of a material

During the process of creep testing, creep (strain, elongation) is the time-dependent deformation defined as the observation of the strain at different time points under constant load at elevated temperatures in most application of engineering materials. The elevated temperature is usually defined as a value great than 0.4 times the absolute melting temperature of the material (Ashby & Jones, 1996). Typically, the creep curve for strain responds over time under constant stress and at a constant temperature, which reflects the creep behaviour of a material.

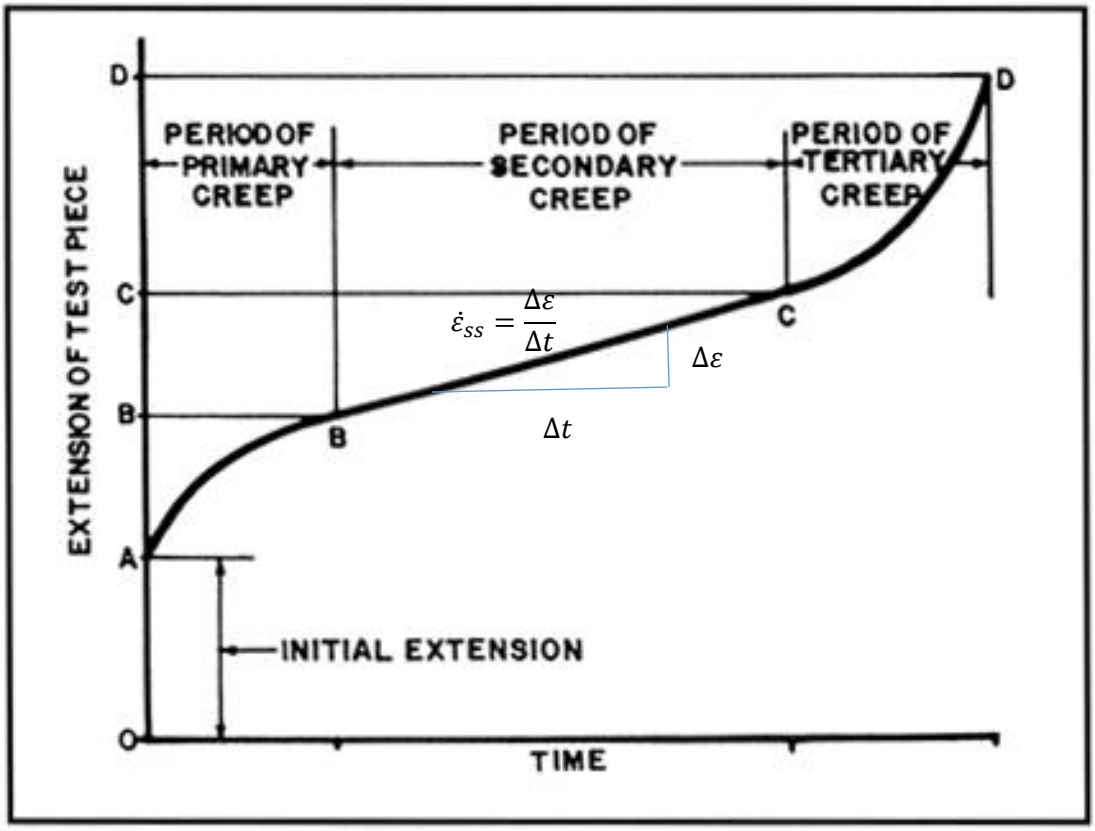

Figure 2.1 The typical creep curve for engineering materials under constant stress and temperature (French, 1993).

The characteristic of a creep curve consists of three regions in Figure 2.1(French, 1993): primary stage (AB), secondary stage (BC) and tertiary stage (CD):

(1) OA: initial strain, instantaneous response includes elastic and plastic, while a constant stress is applied to a specimen;

(2) AB: during the primary stage, the creep strain rate decreases with time from the beginning of creep until it reaches minimum creep strain rate as a result of strain hardening;

(3) BC: steady state stage, the minimum creep strain rate is maintained in steady state, and the strain rate begins to increase until a certain time. The strain hardening remains a constant. The slope of the steady state of the creep curve has the longest duration, thus creep rate in the steady state is very important for the creep behaviour. The next section (2.2) will further discuss the relationship between minimum creep strain rate and applied stress.

(4) CD: tertiary stage, a sharply increasing creep rate leads to final fracture or failure.

The creep curve shape of creep strain is high responsive to the changing of stress level and temperature as shown in Figure 2.2. It can be observed that the creep strains increase with higher stress at a constant temperature and creep strains increase in temperature under a constant stress, while the creep rupture time decreases. The period of steady state increases with decreasing stress and temperature. The steady state rate or minimum creep rate is influenced both by applying stress and increasing temperature. At a constant temperature, the function of minimum creep rate and applied stress is proposed (Norton, 1929; Bailey, 1930):

$$\dot{\varepsilon}_{ss} = A\sigma^{n} \quad (2.1)$$

where

$\dot{\varepsilon}_{ss}$ is the steady state creep rate,

A is creep constant,

n is creep stress exponent.

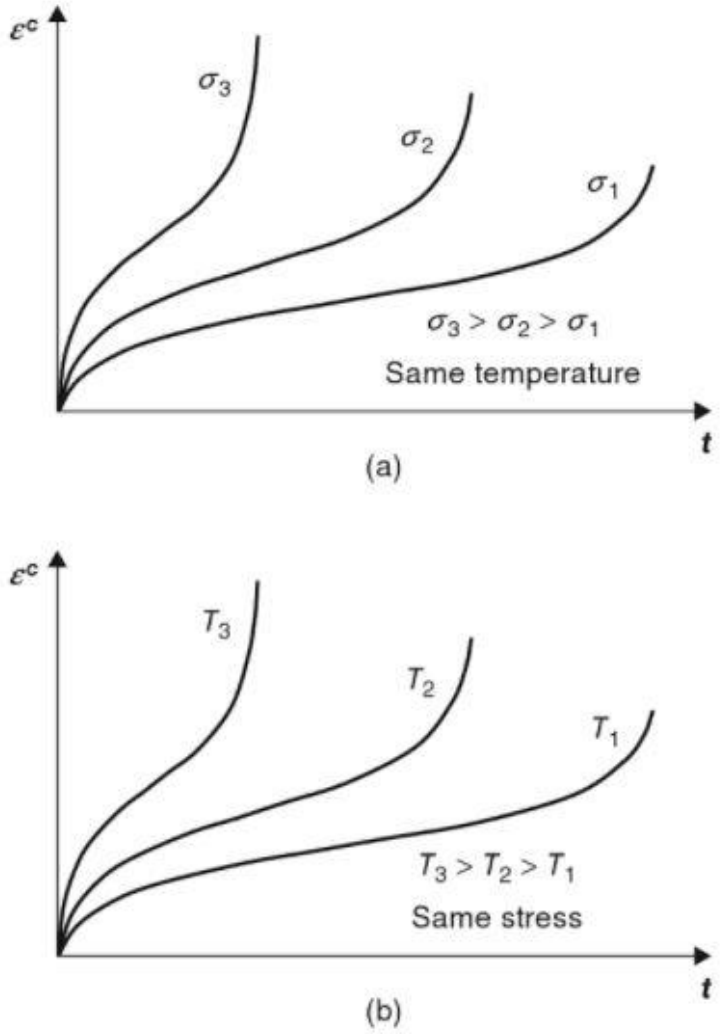

Figure 2.2 The effects of (a) stress and (b) temperature for creep behavior in general (Hyde et al., 2013).

The trends of typical creep curves of high chromium steel varies with different stress levels at a constant temperature as shown in Figure 2.3 (Samuel et al., 2013). With the decrease in stress level, the rupture lifetime of high chromium steel is obviously increasing. The shape of the creep curve at a lower stress level has a longer secondary stage (steady state stage, marked by blue circle) than those at a high stress level (marked by red circle). Thus, it displays that the relationship between applied stress and minimum creep strain rate (secondary stage) is an important factor in the development of creep damage constitutive equations. The next section 2.2 will further discuss the typical

relationship function between minimum creep strain rate and applied stress in detail.

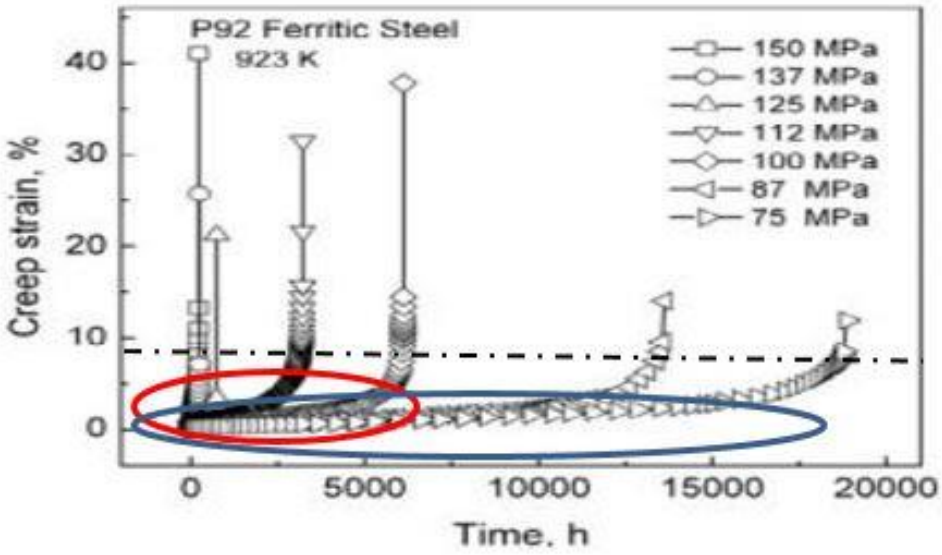

Figure 2. 3 Creep curves of P92 steels at 923K (650℃) under a range stress of 75-150MPa (Samuel et al., 2013).

2.2 Typical function of minimum creep strain rate and applied stress

This section will review and analyse the typical functions of minimum creep strain rate and applied stress. Based on the description of the creep curve during the investigation into creep behaviour of engineering materials and the effect of stress on creep curves in above section 2.1, many investigations have focused on the secondary stage of the creep process. Several typical functions between minimum creep strain rate and applied stress under constant temperature had been proposed and applied to the creep damage constitutive equations for modelling and predicting the lifetime of components for a power plant.

2.2.1 Power law

The typical (Norton) power law equation $\dot{\varepsilon} = A\sigma^n$ was introduced in the above section 2.1. The stress exponent n is not a constant and its value varies with temperature as shown in Figure 2.4. The stress levels have been classified as

high stress level (above 110MPa) with stress exponent above10; intermediate or transition stress level (70-110MPa) with values of stress exponent 4 or 5, and low stress level (under 70MPa) with values of stress exponent about 1 (Kloc and Sklenička, 2001, 2003, 2004; Chen et al., 2011) for high chromium steel.

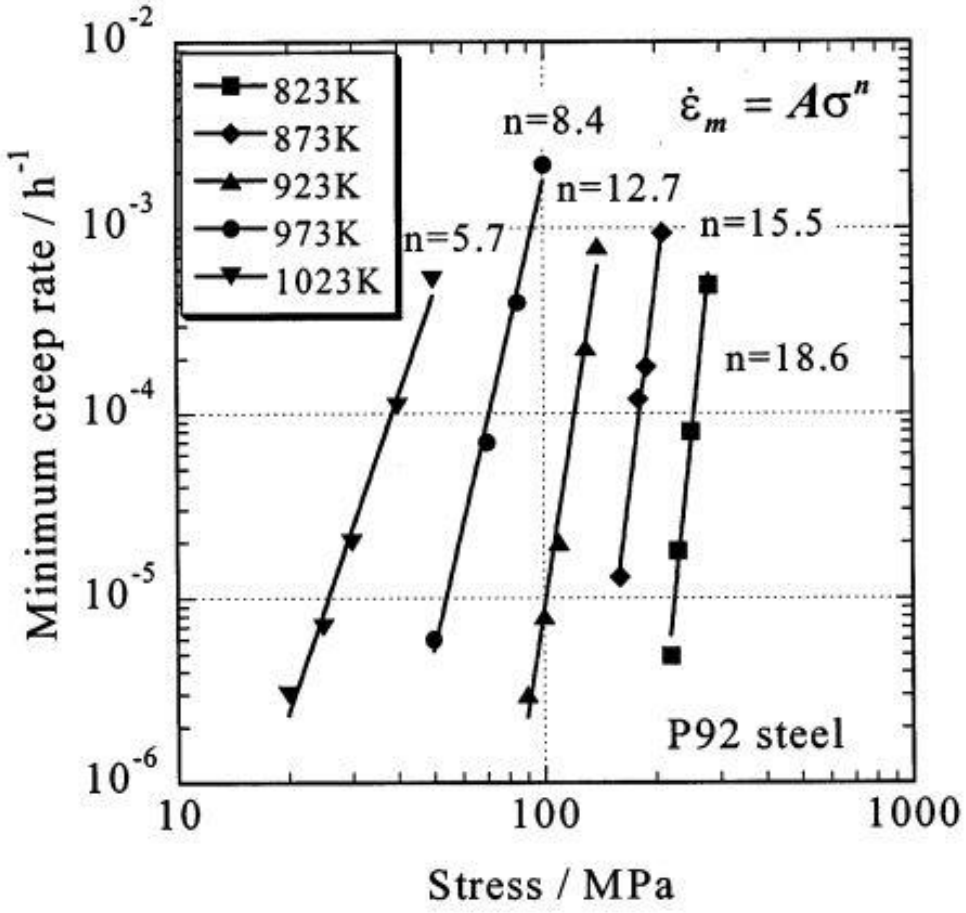

Figure 2.4 The relationship between minimum creep rate and stress of P92 steel (9Cr-0.5Mo) at various temperature (Sawada et al., 2001).

The power law relation reflects a more linear relationship of log minimum creep rate and log stress which is often found creep experimental data in a short range of stress. However, many steels and alloys typically exhibit varying stress exponent n under different stress levels. For example, Ennis (1997) reported that the stress exponent in the power law equation was found to be 16 at high stress and reducing to 6 at low stress for P92 steel in Figure 2.5, Kloc and

Sklenička (2001, 2003, 2004) reported the value of stress exponent was 12 at high stress level and the value of that 4.5 in the low stress regime, which is higher than the value of 1 derived from the constant stress at lower stress creep regime in Figure 2.6. The power law model could not quantify over large stress and temperature ranges for primary creep (Dyson, 2000). Kimiura et al. (2008, 2010) reported a more complex change in stress exponent n under different stress levels and temperature for P/T92 steel in Figure 2.7.

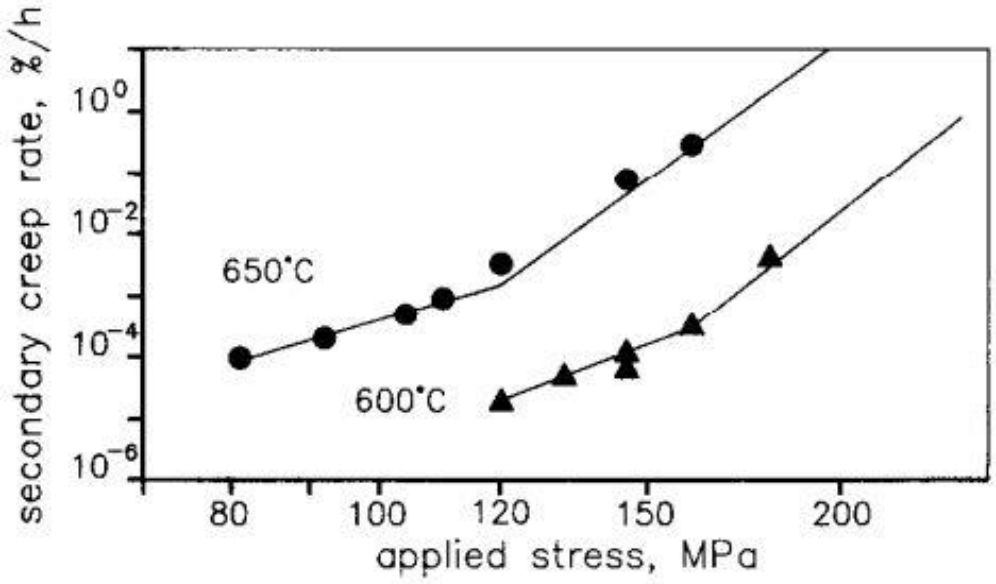

Figure 2.5 The function of minimum creep rate and applied stress for P92 steel (Ennis, 1997).

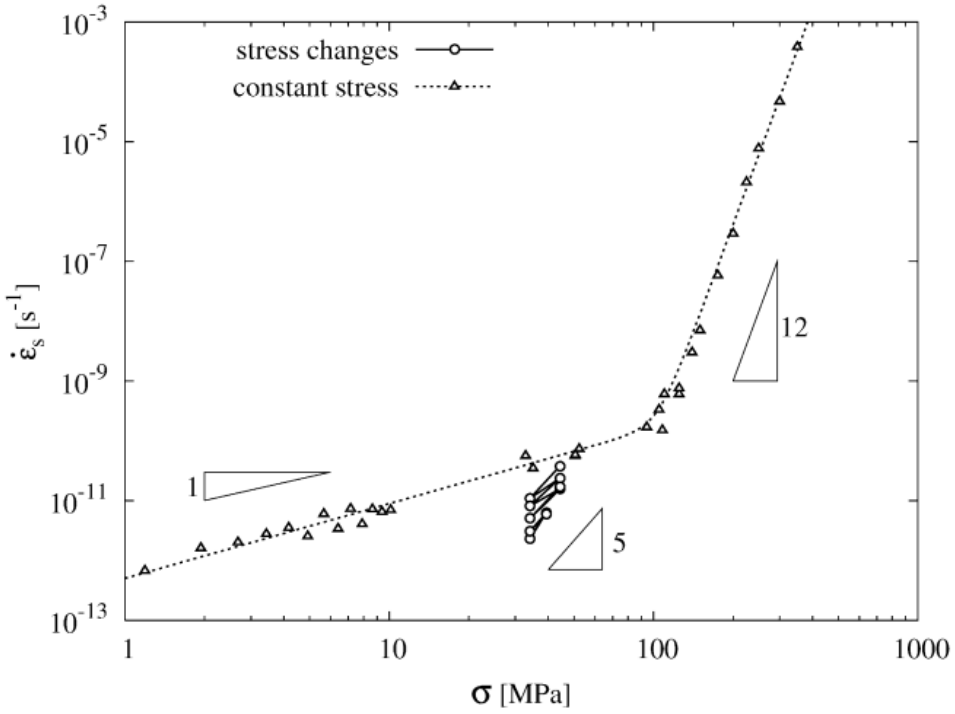

Figure 2.6 The relationship of minimum creep rate and applied stress in 9% chromium steel (Kloc, L., & Sklenička, 2004).

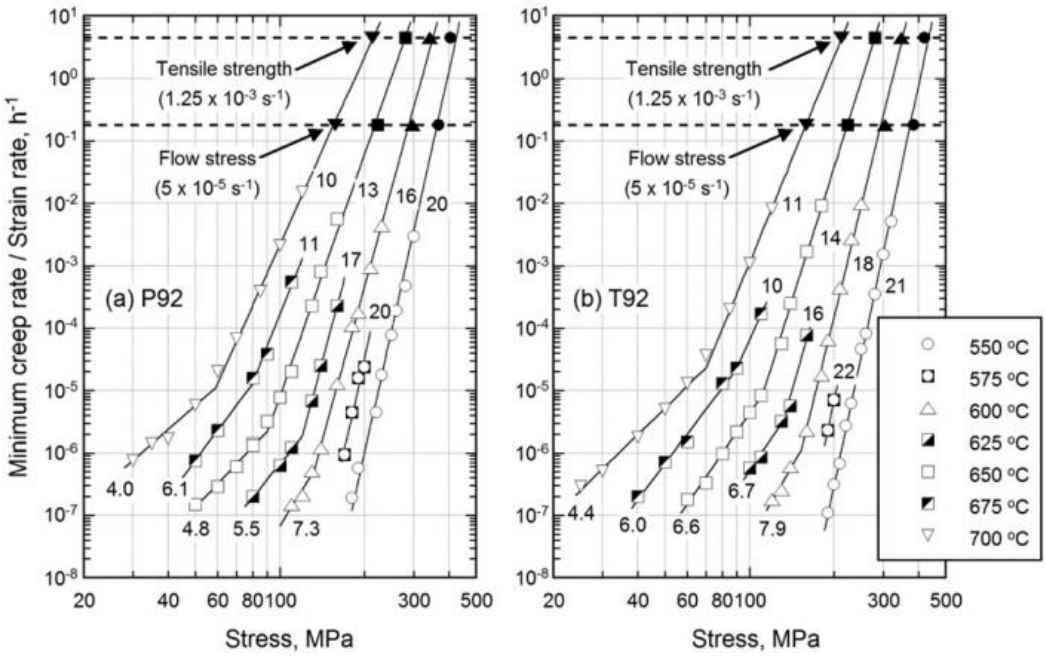

Figure 2.7 The relationship between minimum creep strain rate and applied stress for P/T92 steel (Kimura et al., 2008, 2010).

2.2.2 Hyperbolic sine law

Using the hyperbolic sine law equation on a continuous curve is believed to produce a minimum creep rate varying with the complete stress range according to Dyson (2000) (2001):

$$\dot{\varepsilon}_{min} = Asin\,\mathrm{h}(\mathrm{B}\sigma\,)\ (2.2)$$

where

$\dot{\varepsilon}_{ss}$ is the steady state creep rate;

A, B is the creep constant;

σ is the applied stress.

The hyperbolic sine law equation could provide a solution to the limitations of the power law function and can apply over larger stress and temperature ranges (Dyson, 2000, 2001).

2.2.3 The linear and power law

Altenbach, Gorash & Naumenko (2008, 2009), reported that the hyperbolic sine law is only capable of describing the linear creep range and has satisfactory fitting for high and low stress ranges, but is not suitable for transition stress range, therefore, they proposed a sum of the linear and power law stress functions:

$$\dot{\varepsilon} = \dot{\varepsilon}_0 \frac{\sigma}{\sigma_0} + \dot{\varepsilon}_0 (\frac{\sigma}{\sigma_0})^n = \dot{\varepsilon}_0 \frac{\sigma}{\sigma_0}\left[1 + \left(\frac{\sigma}{\sigma_0}\right)^{n-1}\right] = A\sigma[1 + (B\sigma)^n](2.3)$$

where

$\dot{\varepsilon}$ is strain rate;

$\dot{\varepsilon}_0$ is initial strain rate;

σ is applied stress;

σ_0 is the ‘transition stress’;

n is stress exponent.

2.2.4 Modified hyperbolic sine law for low chromium steel

A modified hyperbolic sine function was proposed by Qiang Xu and applied for a wide range of stress level in low chromium alloy by Qihua Xu (Xu, 2016):

$$\dot{\varepsilon}_{min} = Asinh(B\sigma^q) \quad (2.4)$$

where

$\dot{\varepsilon}_{ss}$ is steady state creep rate;

A, B is creep constant;

σ is applied stress;

q is material constant.

Four functions between minimum creep strain and applied stress were summarized in this section. The better quantitative description of the dependence of stress level in the minimum creep strain rate will be considered based on experimental data published by the National Institute for Materials Science (NIMS) regarding high chromium steel. And the modelling results of these four different function between minimum creep strain rate and applied stress will be compared with the experimental data of high chromium steel in Chapter 4. The best suitable equation, which is fitted well with the experimental data, shall be applied in the development of novel constitutive equations and Chapter 5.

2.3 Stress breakdown phenomenon

Creep rupture time of grade 92 steel under different stress levels were plotted in Figure 2.8. Arrhenius equation describes the creep rupture life t_r which is dependent on stress $\sigma$and temperature T as follow (Lee et al., 2006):

$$t_r = t_0\sigma^{-n}\exp\left(\frac{Q}{RT}\right) \quad (2.5)$$

where:

t_0 is a constant,

σ is applied stress

n is the stress exponent,

Q is the apparent activation energy,

R is the universal gas constant,

T is the absolute temperature.

Lee et al. pointed out how the stress exponent decreases from 17 in short-term creep to 8 in long term for ASTM Grade 92 steel at 550-650℃ (Lee et al., 2006). The dash-dot line divides two regions of high stress and low stress in Figure 2.8, confirming the breakdown phenomenon of creep strength in P92 steel. There is a transition from ductile to brittle with increasing rupture life, the brittle fracture causes the stress breakdown phenomenon. The observation's results of creep cavities nucleating at coarse precipitates of Laves phase along grain boundaries suggests that this is the reason of breakdown of creep strength (Lee et al., 2006).

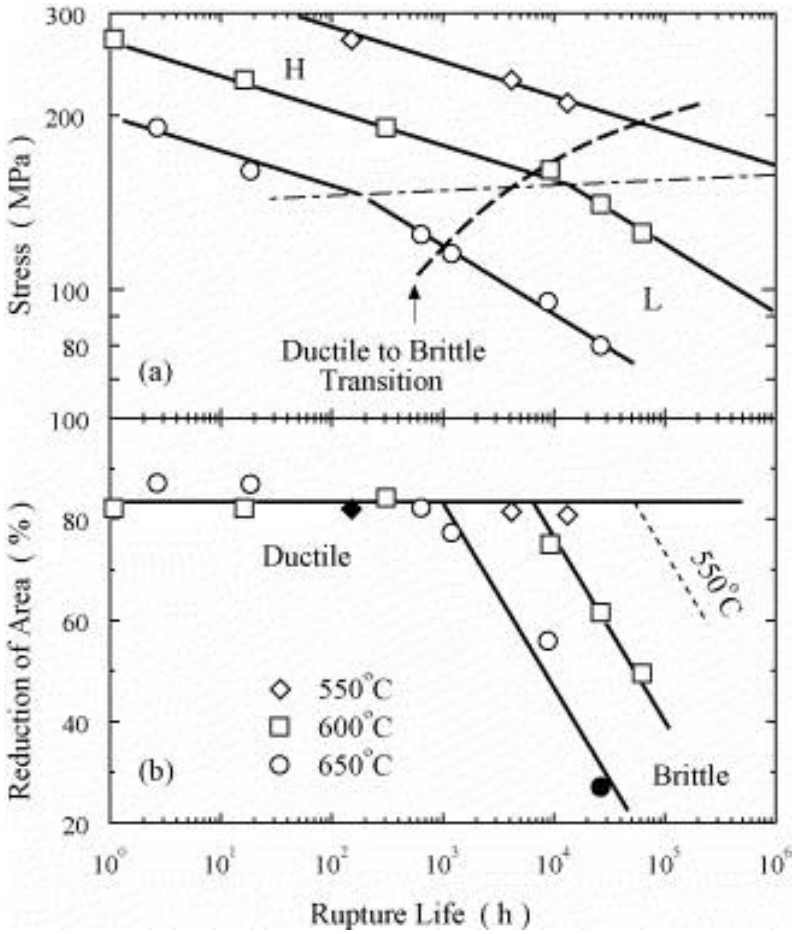

Figure 2.8 The rupture life time versus stress in P92 steels in high and low stress regions (Lee et al., 2006).

Increasingly more experimental data on the creep test of high chromium steel has been published, and the plots of stress and rupture life time indicates a common existing phenomenon of stress breakdown (dotted line) in Figure 2.9 (Pétry & Lindet, 2009) Figure 2.10 (Maruyama et al., 2010) and Figure 2.11 (Sawada et al., 2014). Thus, it is important to understand the fracture model and mechanisms of high chromium causing stress breakdown, only then shall it provide useful guidelines for the assessment of damage evaluation in predicting the lifetime of components, for example, a power plant by the creep damage constitutive equation modelling.

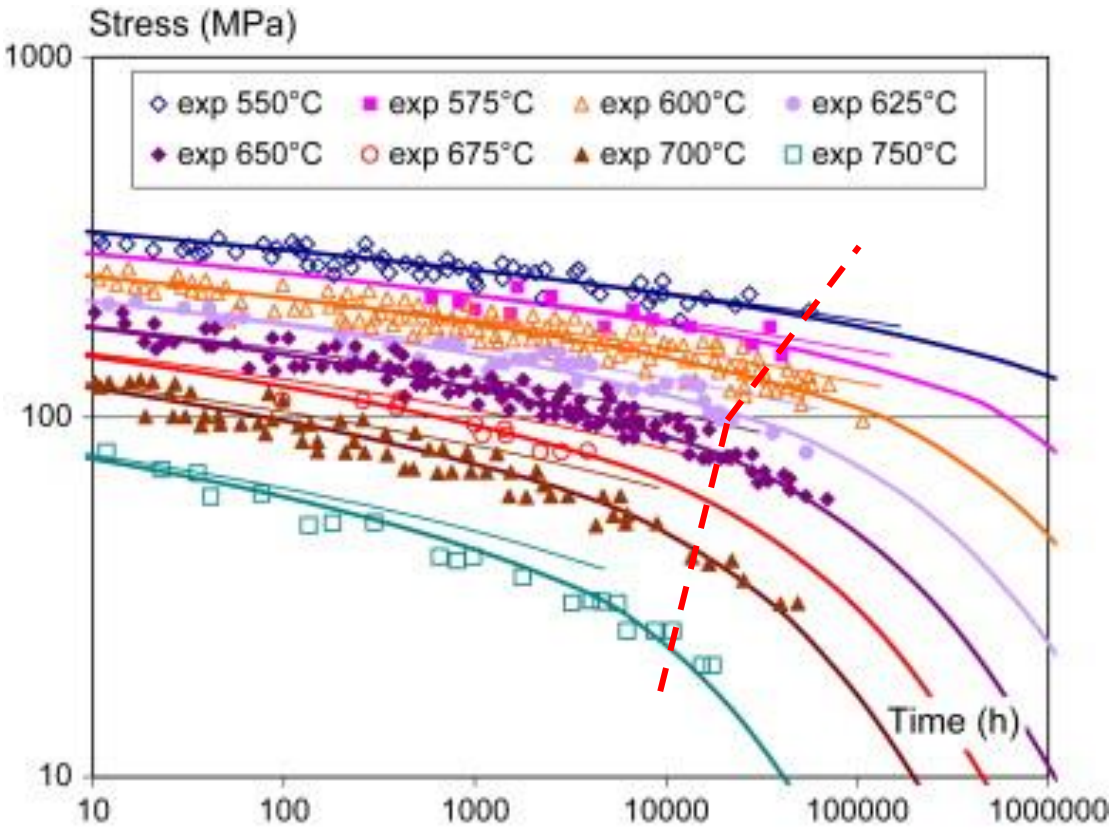

Figure 2.9 Rupture life time versus stress in P92 steel (Pétry & Lindet, 2009).

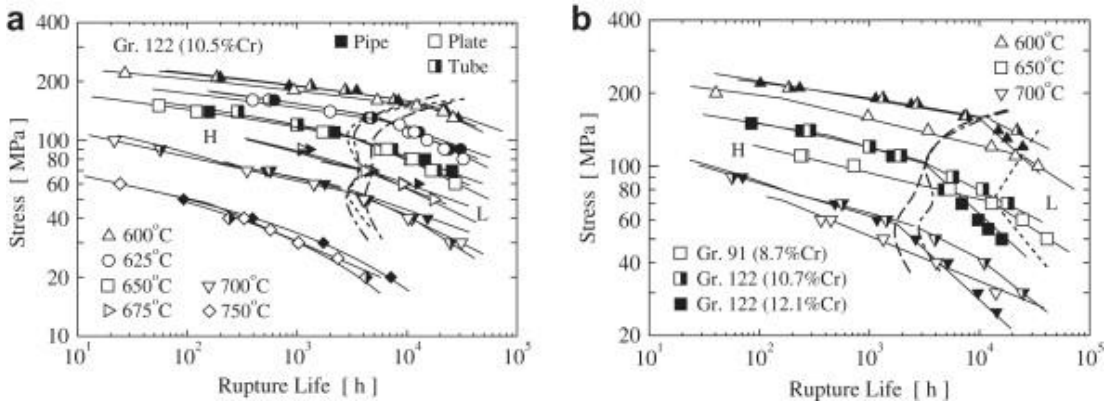

Figure 2.10 Stress and rupture life of high chromium steel of P91 and P122 (Maruyama et al., 2010).

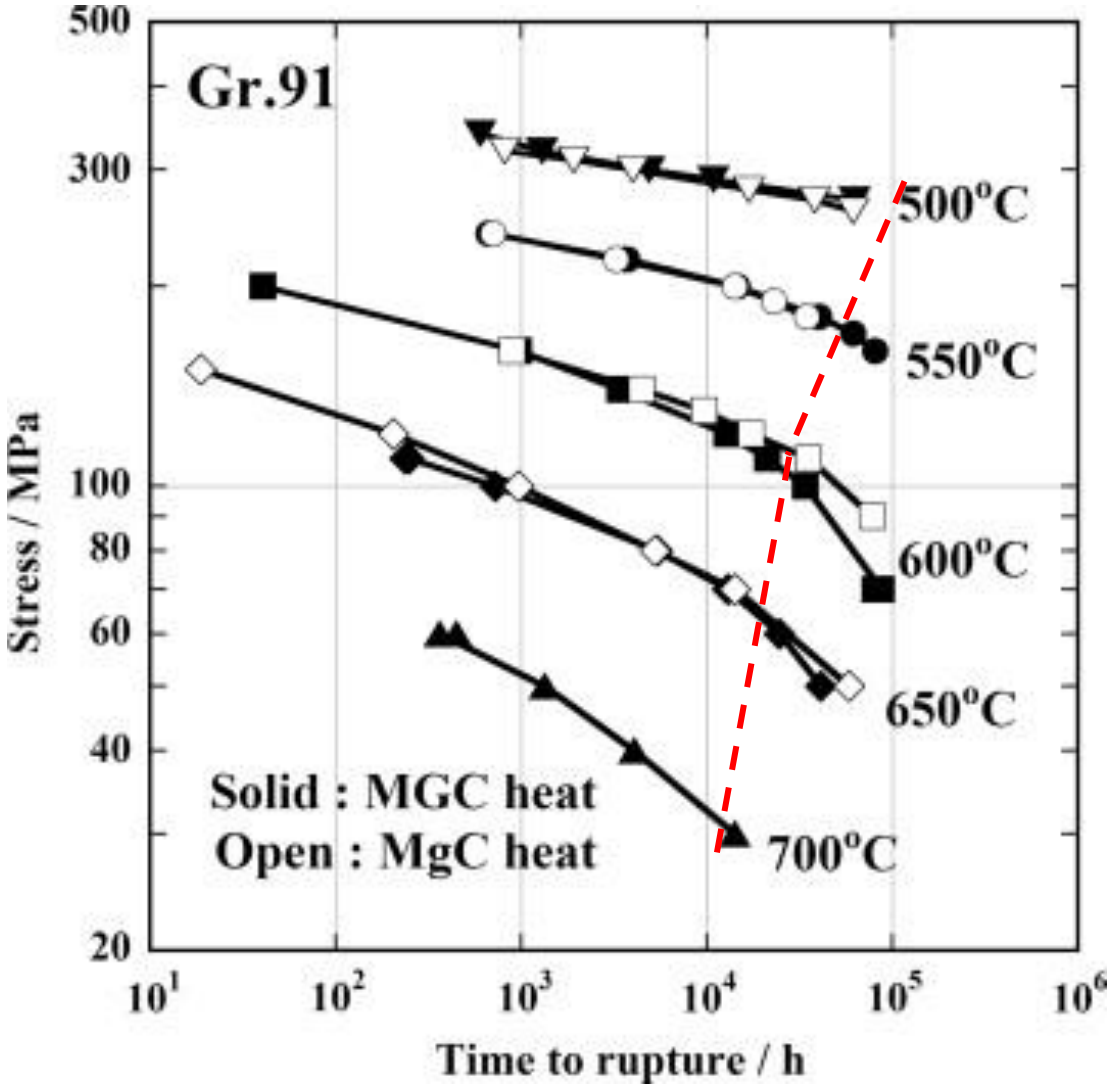

Figure 2.11 The experimental data of rupture time of P91 steel at a range of stress (Sawada et al., 2014).

2.4 Creep fracture

This section will introduce the main concepts of the fracture model and analyse the fracture mechanisms for high chromium steels under different stress levels and temperatures based on the literature covering the experimental observation in the past 20 years. It shall provide a better understanding regarding the evolution of creep damage behaviour for a better development of a new novel constitutive equation for high chromium steel.

2.4.1 Fracture mechanism map

There are three types of fracture models as shown in Figure 2.12 (Maruyama, 2008): a) brittle intergranular fracture; b) ductile intergranular or transgranular fracture with some ductility; c) rupture after 100% reduction in area.

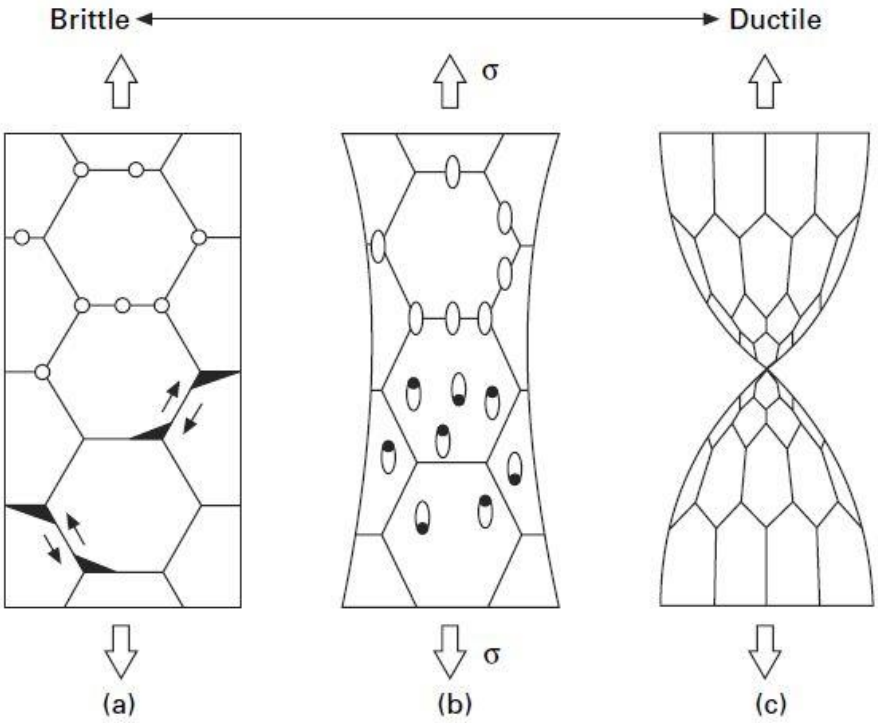

Figure 2.12 Fracture models at high temperature: (a) Brittle intergranular fracture (b) Ductile intergranular or transgranular and (c) rupture after 100% reduction of area (Maruyama, 2008).

The fracture model changes along with the fracture ductility ranging from ductile to brittle with decreasing strain at failure. At low stress levels, brittle fracture occurs in the other type of intergranular fracture along the grain boundaries as depicted in Figure 2.13 (a) (Jones, 2004). There are two types of brittle

intergranular fracture: one is the coalescence of cavities formed on grain boundaries aligned perpendicular to the applied stress; the other is wedge cracking formed at triple grain boundary junctions by stress concentration due to grain boundary sliding. At high stress level, most ductile fracture can be characterised as transgranular, which is through the grain rather than only along the grain boundaries as shown in Figure 2.13 (b) (Jones, 2004).

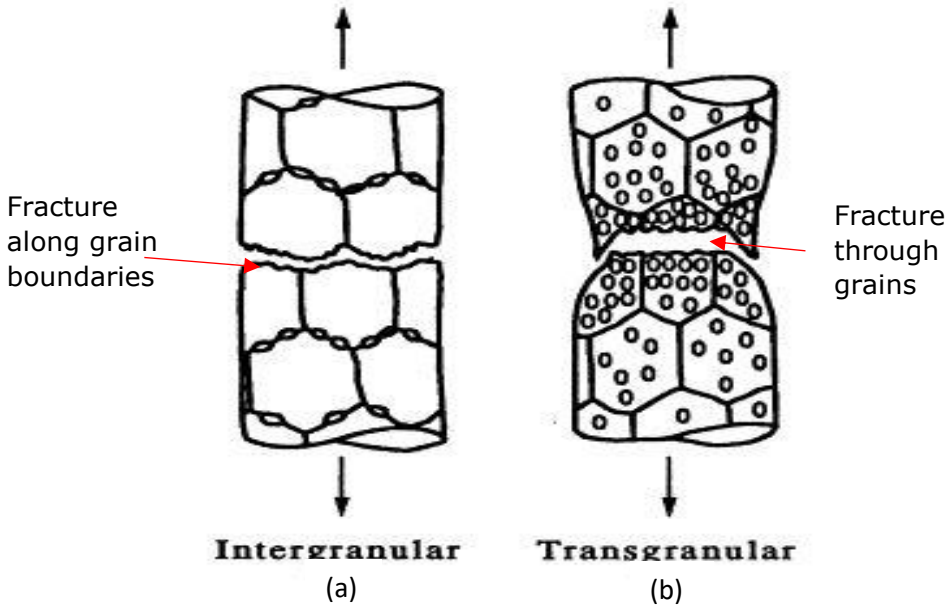

Figure 2.13 Microstructural features of creep fracture mechanisms (Jones, 2004).

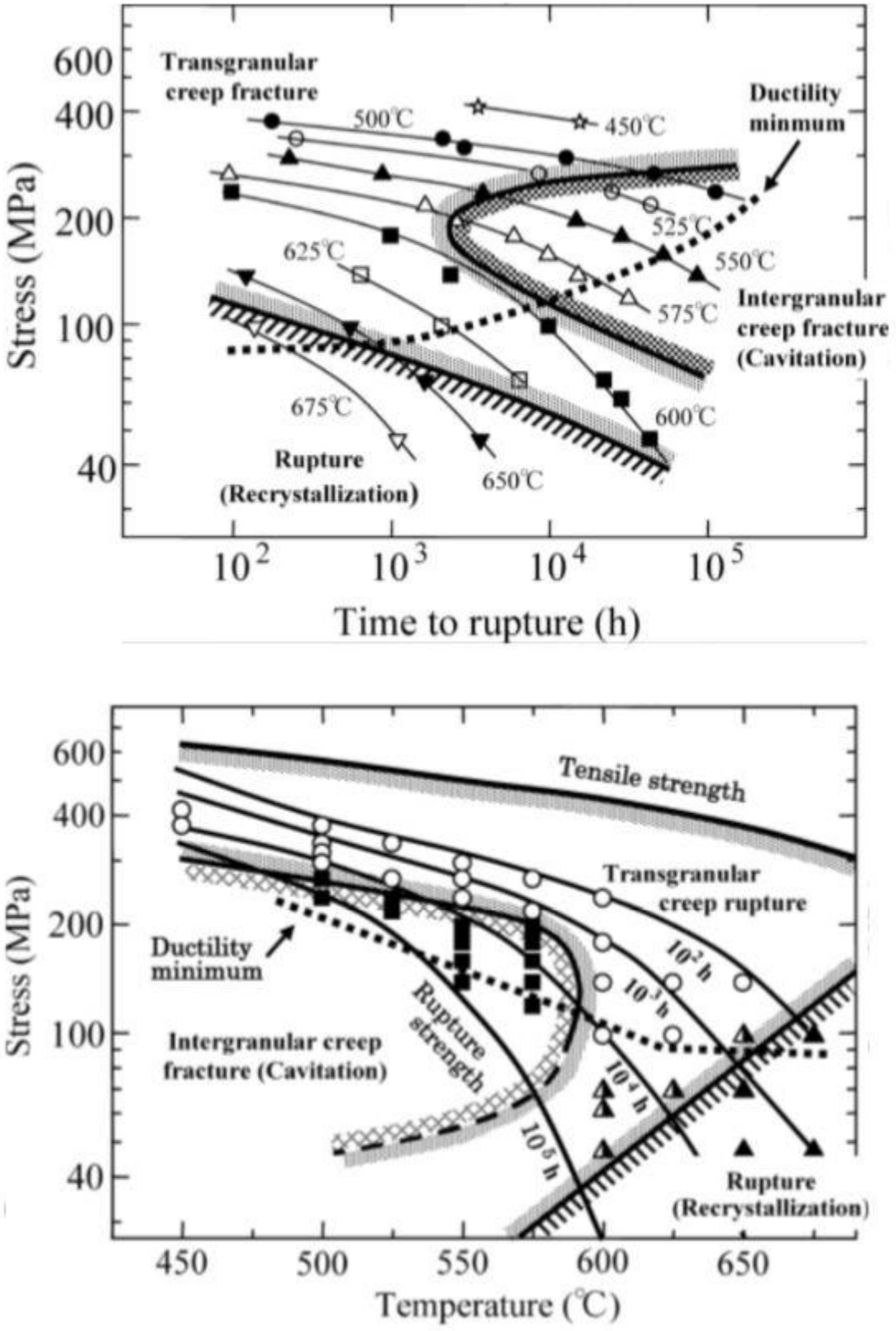

Figure 2.14 Creep Fracture Mechanism Map and Creep Damage of low chromium steel (1Cr-1Mo-0.27V) for Turbine Rotor (Shinya, 2006).

Based on the results of the SEM observation of creep ruptured specimens of low chromium steel, a creep fracture mechanisms map was constructed for low chromium steel as shown in Figure 2.14 (Shinya, 2006). The creep fracture mechanisms map plots the stress-time to rupture and stress-temperature, respectively. There are three kinds of creep fracture mechanism field for low chromium steel: (1) creep transgranular fracture appears in the field of high stress level region at temperature above 600℃; (2) creep intergranular fracture appears in the field of long-term time to rupture under low stress level region at 500-575℃; (3) a creep recrystallization rupture appears in short time-to-rupture under low stress level region at temperatures exceeding 600℃.

The transition from creep transgranular fracture to creep intergranular fracture for low chromium steel, according to Shinya et al. (2006) is believed to be due to the generation of long time-to-rupture region at temperature 500-575℃ and growth of creep cavities based on the observation of the specimens of low chromium steel specimens under 177MPa at 575℃. Abe (2008) suggests the evolution of creep voids at the grain boundary make a significant contribution to the creep fracture during creep process.

Creep fracture mechanisms are sensitive to change with operating conditions for low chromium steel, thus it is also necessary to collect and analyse more reliable data for the onset of rupture of high chromium steel. The next section will collect the experimental observation of fracture surfaces and analyse the creep fracture mechanism for high chromium steel, and attempt to understand the fundamentals of creep damage mechanism for the development of constitutive equations to predict more accurate lifetimes for power plant's components.

2.4.2 Creep fracture based on experimental observation of fracture surfaces for high chromium steel

This section will critically review the experimental observations of fracture surfaces on high chromium steel by the traditional technology in the past two decades, such as OP, TEM and SEM, and in turn shall provide analysis of the creep fracture mechanism for high chromium steel. The dominant damage of cavitation is the most important factor that needs to be taken into account for

the design and prediction of the lifetime of high chromium steel for components of power plants. The details of experimental observation of fracture surfaces for high chromium steel are in Appendix B (Figure 2.15-Figure 2.33).

Based on the collection and analysis of the above experimental observations on creep fracture surfaces by traditional 2D technology OP, TEM, SEM, there are four main kinds of results summarized below.

1) The fracture model is a ductile transgranular fracture for high chromium steels at high temperature under high stress level, reference (Eggeler et al., 1989), (Choudhary et al., 1999), (Gaffard et al., 2005), (Lee, et al., 2006), (Choudhary & Samuel, 2011), (Vanaja et al., 2012), (Choudhary, 2013), (Shrestha, 2013), (Palaparti et al., 2013), (Goyal et al., 2014), (Goyal & Laha, 2014), (Zhu et al., 2014), (Vanaja & Laha, 2015), (Ni et al., 2015), (Guguloth & Roy, 2017);
2) The fracture model is brittle intergranular fracture for high chromium steels at high temperature under low stress level, reference (Lee, et al., 2006) (Parker, 2013) (Nie et al., 2014), (Zhu et al., 2014);
3) Creep cavities mostly appeared or nucleated on/along the grain boundaries perpendicular to the direction of applied stress, reference (Choudhary et al., 1999), (Gaffard et al., 2005), (Aghajani et al., 2009), (Panait et al., 2010);
4) The Laves phase appeared mostly on subgrain boundaries and on grain boundaries, the cavities either at the nucleated boundaries next to the precipitation of Laves phase, attached with the Laves phase along grain boundaries, or Laves phase provides sites for cavity nucleation (Lee, et al., 2006) (Nie et al., 2014) (Zhu et al., 2014).

Based on the above experimental observations on fracture surfaces of high chromium steel, the dominant damage of cavitation on grain boundary is a kinetic phenomenon, and it influences the deformation. The fracture mode critically depends on the nucleation rate and growth rate of cavitation under different stress levels. The results of experimental observations suggests what is needed to be done in order to further develop a novel cavitation damage equation for creep damage constitutive equations for high chromium steel:

1) Identifying the evolution of cavitation damage mechanisms under different stress levels will be investigated in the next section 2.5;
2) Traditional theories of cavitation damage calculated equations will be introduced in the next section 2.6;
3) To review cavitation damage equation in current creep damage constitutive equations and analyse the advantages and limitations of current creep damage constitutive equations in section 2.8. The creep deformation (microstructure degradation) damage, which coupled with the dominant cavitation damage into constitutive equation, shall be explored in section 2.7.
4) To collect and summarize the critical experimental data of high chromium steel, with special attention payed to cavitation, and the quantitative relations between creep properties and cavitation that are caused by the application of different stress levels and creep exposure times all of which are fundamental in understanding the underlying creep damage mechanisms in section 5.

2.5 Creep cavitation damage mechanism

2.5.1 Dominant damage mechanism of cavitation in creep process

Generally, it is well accepted that cavity nucleation, growth and coalescence lead to the failure of this type of engineering material during creep (Gooch, 1982) (Eggeler, 1989) (Kassner & Hayes, 2003) (Westwood et al., 2004) (Sklenička, 2003) (Dobrzański, 2006) (Yao et al., 2007) (Shrestha et al., 2013) (Gupta et al., 2013). Based on the summarized and analysed experimental observation of fracture surface in high chromium steel in section 2.4, the observed images illustrate the importance of creep damage in the creep process, which is leading to final fracture.

Furthermore, Figure 2.34 illustrates that the nucleation and growth of cavity accounted for about 80% of life time while the coalescence of cavity and final rupture took about 20% of life time (Sklenička, 2003) (Yao et al., 2007). Furthermore, there is a similar description of the development of cavitation

during creep process in Figure 2.32 (Dobrzański, 2006). These findings indicate that cavitation is the most dominant factor in the creep damage process.

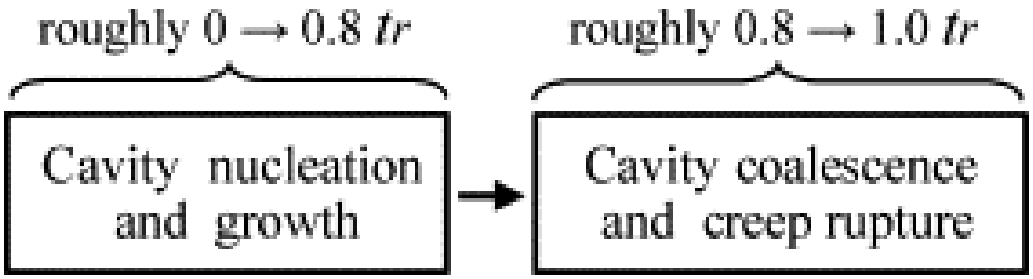

Figure 2.15 Scheme of cavitation damage development (Yao et al., 2007).

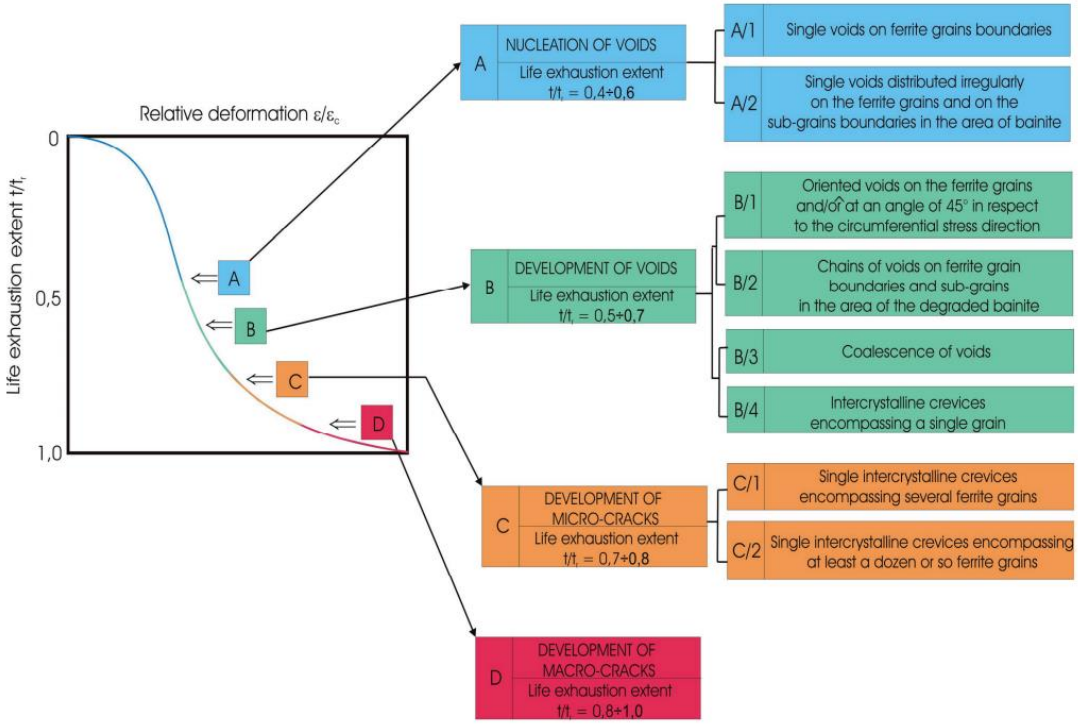

Figure 2.16 Development of the internal damage of cavitation during creep service for Cr-Mo steel (Dobrzański, 2006).

Based on the macroscopic simulation using creep damage constitutive equations including different creep deformation (microstructural degradation) damage and cavitation damage, model results also indicated that cavitation is the largest contributing factor to failure (Yin and Faulkner, 2006; Yang et al., 2013). Yin & Faulkner studied the severity of each different damage mechanism based on their developed constitutive equation. The modelling of creep damage constitutive equation was calculated with each individual creep damage

mechanism being considered whilst setting other damage mechanisms to zero. The modelling results shown in Figure 2.33 display that the strain curve b only considered cavitation damage, and it indicates the cavitation damage mechanism is the dominating factor in all creep damage mechanisms, which will result in a fracture of high chromium steel (P92) (Yin & Faulkner, 2006). The author conducted similar research based on a modified constitutive equation proposed by Yin, during which the modelling results also indicated that the cavitation damage mechanism is amongst the most significant internal damage mechanism contributing to the ultimate failure of the material for T/P91 steel as shown in Figure 2.37 (Yang et al., 2013).

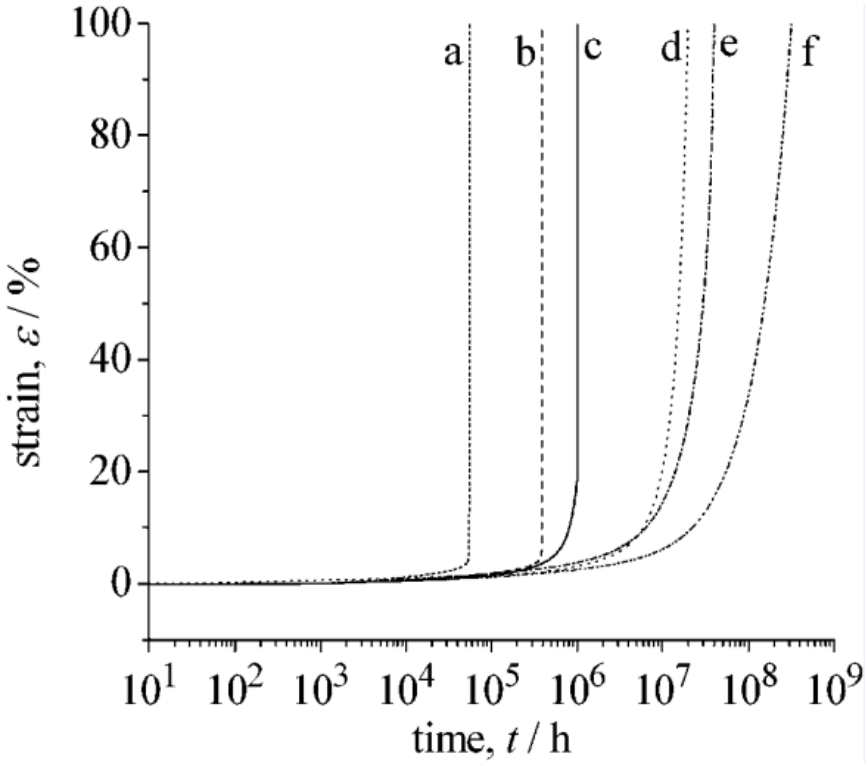

Figure 2.17 The modelling results of Yin's constitutive equation with different damage mechanisms (a) all damage; (b) only particle coarsening; (c) only dislocation multiplication; (e) only solute depletion; (f) no damage. (Yin & Faulkner, 2006).

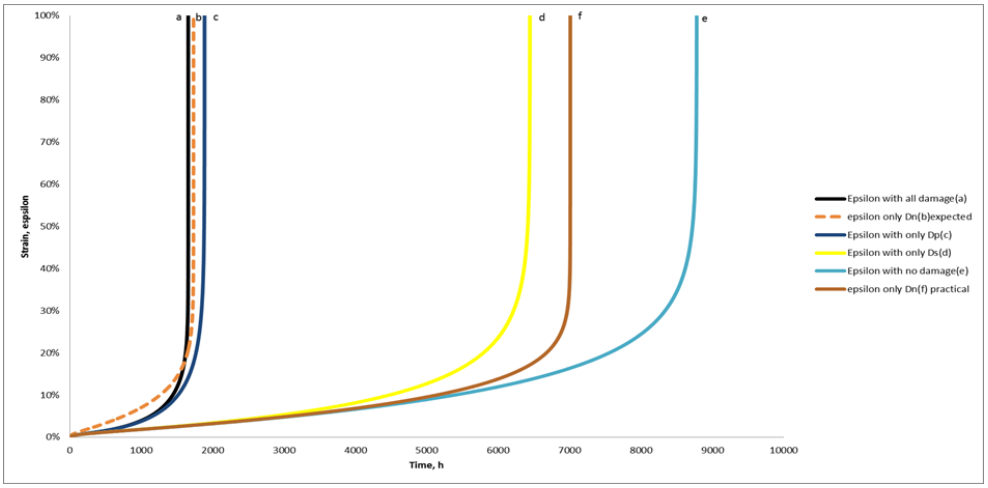

Figure 2.18 The comparison of creep rate by different internal creep damage mechanisms under 130MPa at 600℃ for T/P91 steel (Yang et al., 2013).

2.5.2 Creep damage mechanism at high temperature for high chromium steel

According to different applications of creep stress level at a constant temperature, there is a change in cavitation damage mechanism that will govern creep damage fracture for high chromium steels. This section will discuss the dominant cavity damage mechanism for high chromium steels under high and low stress levels. The author has already presented this summary and analysis in a published paper (Yang, Xu & Lu 2015).

2.5.2.1 Dominant cavity growth mechanism for high chromium steels under high stress levels

In earlier studies, Dyson pointed out that the cavity nucleation rate was proportional to strain rate, and fracture was controlled mainly by nucleation rate at high stress level (Dyson, 1983). Later, however, increasingly more research indicates that the principle rupture mechanism was the viscoplasticity-assisted ductile rupture at high stress level. The damage mechanism begins with void nucleation at the preferential stress concentration areas inside the grains; then void growth was assisted by grain deformation and followed by coalescence of the cavities. The evolution of cavity damage was controlled by cavity constrained growth dominantly (Dyson, 2000) (Massé & Lejeail, 2012).

Recently, the spatial distribution and 3D characteristics of the creep void with increasing creep exposure time for high chromium steel by three dimensional

techniques of X-ray micro-tomography have been provided under a stress range between 120MPa and 180MPa at 600℃ (Gupta et al., 2013). Based on the experimental data of cavitation volume fraction, the average diameter of voids and the number density of cavitation curves, void volume fraction and the number density both increase, and interestingly void volume fraction increases more rapidly. It reveals that void nucleation or growth and coalescence process dominate. Furthermore, these results mean that the void growth by coalescence is progressively strengthened over nucleation as the stress is reduced in the range of 120-180MPa (Gupta et al., 2013). Thus, the dominant cavity growth mechanism is controlled cavitation damage for high chromium steel under high stress level.

2.5.2.2 Dominant cavity nucleation mechanism for high chromium steels under low stress levels

Generally speaking, the creep deformation under low stress is diffusional and the void nucleation is controlled by the maximum shear stress, this idea is in good agreement with the general understanding reported by Miannay (2011), and according to Xu (Xu, Lu & Wang, 2013). Dyson pointed out the cavity nucleation rate was proportional to strain rate, and fracture was controlled mainly by nucleation rate at a low stress level (Dyson, 1983).

With finer resolution of cavity size, Gupta et al (2013) reported the number density and mean size of crept specimen under different stress levels. It reveals that though the number density under lower stress at failure is much higher than that of those under high stress, and the number density at lower stress is 2.5 than that in high stress; this strongly indicates the significant effect of time and the cavity nucleation is visco-type rather than stress controlled. As can be seen it is useful and important to obtain the nucleation rate with time under different stress level. The dominant cavity nucleation mechanism is for high chromium steel under low stress levels.

2.6 Traditional creep cavitation damage equations

The damage mechanism is due to creep (a) cavity nucleation and (b) cavity growth on grain boundary as shown in Figure 2.38 (Lin, Liu & Dean, 2005). This section will introduce the traditional creep cavitation damage equations.

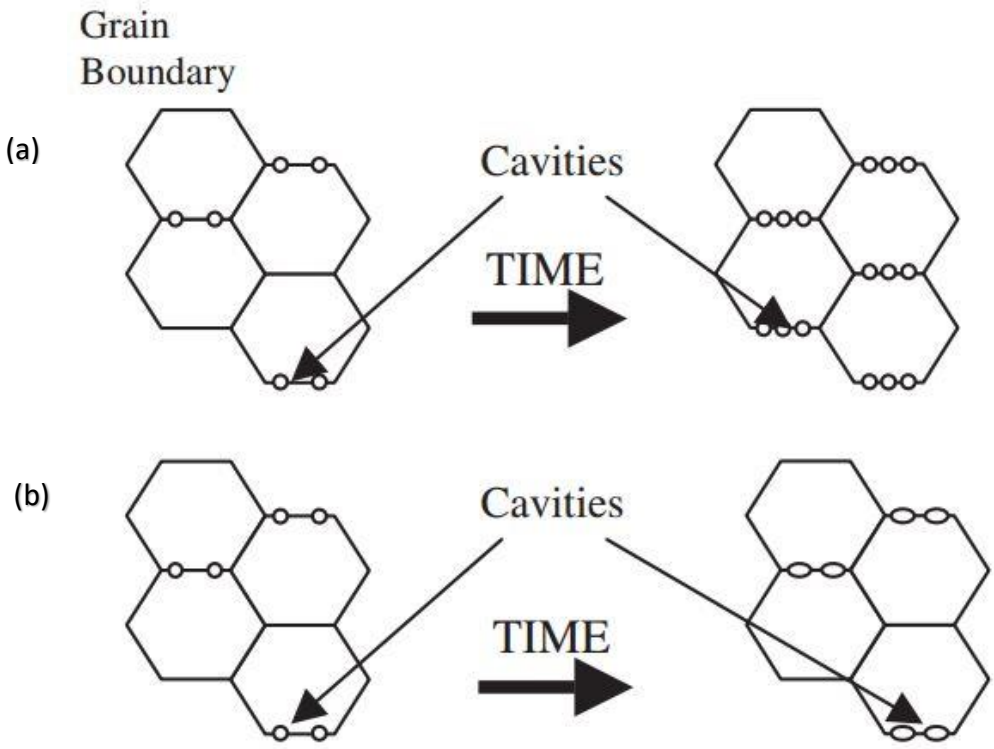

Figure 2.19 Schematics shows (a) cavity nucleation (b) cavity growth (Lin, Liu & Dean, 2005).

2.61 Cavity nucleation

Raj and Ashby (1975) proposed that the cavity nucleation rate (number of cavities generated per time and area), which is based on vacancy condensation, is given as below (Raj & Ashby, 1975), and according to Riedel (1987):

$$J^* = \beta^* N_o^* \quad (2.6)$$

Where:

J^* is the cavity nucleation rate,

N_o^* is the area density of critical clusters,

β^* is the rate (per unite time) at which single vacancies are absorbed by a critical cluster.

Needham and Gladman (1980) proposed that the cavity nucleation rate at small creep strain, $\dot{N}$, is in a linear relationship with the normal strain rate $\dot{\varepsilon}$ in

engineering steels and alloys, and according to Westwoood, Pan & Crocombe (2004):

$$\dot{N} = B\dot{\varepsilon} \ (2.7)$$

where

$\dot{N}$ is the cavity nucleation rate,

B is an empirical constant depending on temperature,

$\dot{\varepsilon}$ is creep strain rate.

Dyson (1983) noticed that the number of cavities (N) per unit grain boundary area is a linear relationship with the creep strain for 2.25Cr-1Mo, Type 347 steel, Nimonic 80A and iron. Thus, the number of cavities (N) per unit grain boundary is related to (according to Kassner & Hayes (2003)):

$$N = a'\varepsilon \ (2.8)$$

where:

N is the cavity nucleation rate per unite grain boundary area;

a' is an empirical factor of proportionality having the physical dimension (m^{-2});

ε is strain rate.

Riedel (1987) proposed the power law form for continuous nucleation based on the cavity size function:

$$J^* = A_2 t^{\gamma} \ (2.9)$$

Where

J^* is creep nucleation rate,

A_2 and γ may possible depend on stress and strain rate,

t is time.

2.62 Cavity growth

2.6.2.1 Unconstrained diffusion controlled cavity growth

Riedel (1987) suggested that unconstrained diffusion controlled cavity growth on grain boundary based on Hull and Rimmer (1959) and proposed a diffusion

growth mechanism of an isolated cavity in a material under an applied external stress:

$$\frac{da}{dt} = \frac{\Omega\delta D_{gb}[\sigma - \sigma_0]}{1.22kTIn(\lambda_s/4.24a)a^2} \quad (2.10)$$

where:

Ω is the atomic volume;

δ is the grain boundary width in Figure 2.39;

D_{gb} is the diffusion coefficient at the grain boundary;

σ is normal stress to the grain boundary;

σ_0 is the sintering stress;

k is Boltzmann constant;

T is temperature;

λ_s is the cavity separation as shown in Figure 2.39;

a is the cavity radius in Figure 2.39 .

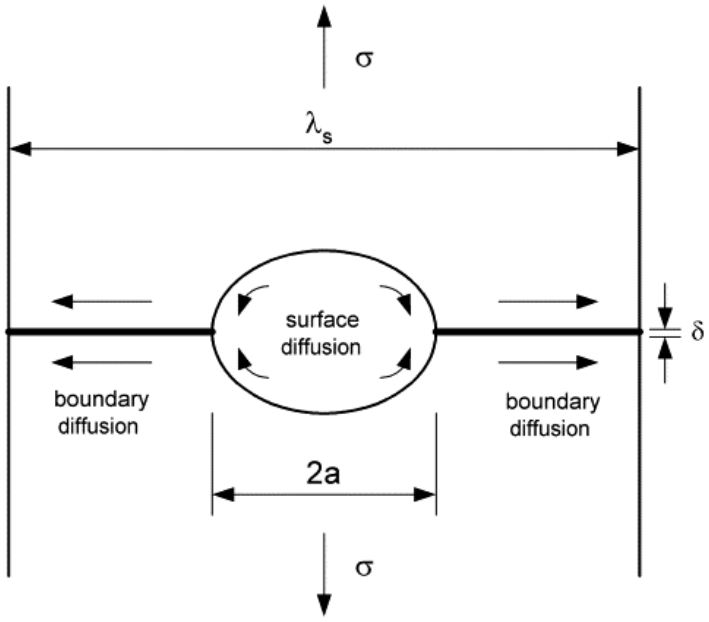

Figure 2.20 Cavity growth from diffusion across the cavity surface and through the grain boundaries due to a stress gradient (Kassner & Hayes, 2003).

2.6.2.2 Constrained diffusion controlled cavity growth

Dyson (1976, 1979) originally suggested constrained cavity growth. Riedel (1987) explained that constrained cavity growth meant the rate of cavity growth can be controlled by the deformation rate of the surrounding material, and proposed the constrained cavity growth rate based on the following equation by Rice (1981), Riedel (1983b), Tvergaard (1984a):

$$\dot{R} = \frac{\sigma_I^{\infty} - (1-\omega)\sigma_0}{h(\psi)R^2\{q(\omega)kT/(2\Omega\delta D_b) + \ q'\sigma_e^{\infty}/(\dot{\varepsilon}_e^{\infty}\lambda^2 d)\}} \quad (2.11)$$

Where:

σ_I^{∞} is normal stress;

ω is the area fraction of cavitated grain boundary;

the abbreviation $q(\omega)$ is equal to $q(\omega) = -2\ln\omega - (3-\omega)(1-\omega)$;

σ_0 is sintering stress;

$h(\psi)$ is the cavity volume divided by the volume of a sphere with radius R and equal to 0.61 with $q' = 12.5$;

R is initial void radius;

k is Boltzmann constant;

T is temperature;

Ω is atomic volume;

δD_b is the grain boundary width (δ) and the grain boundary diffusion coefficient (D_b);

σ_e^{∞} is the applied equivalent stress for axisymmetric loading;

$\dot{\varepsilon}_e^{\infty}$ is the equivalent strain rate;

λ is the mean grain size.

Riedel (1987) proposed the cavity size distribution function, and suggested the cavity growth rate in the power-law form:

$$\dot{R} = A_1 R^{-\beta} t^{-\alpha} \quad (2.12)$$

where A_1, α and β may possibly depend on stress and strain rate. Research has found the value of β is close to 2 with the cavity constrained diffusion mechanism (Riedel, 1987) (Dyson, 1983) (Kassner & Hayes, 2003) (Kassner, 2008).

2.7 Creep deformation (Microstructural degradation) mechanism in high chromium steel

Besides the dominant mechanism of cavitation damage, the microstructural degradation which affects the creep strength of steels is the other key factor for the development of constitutive equations and more accurately predicting the lifetime of components. Some mature microstructure-based models used for the assessment of creep strength have been proposed. In general, the effect of microstructural degradation changes based on creep strength in 9-12% of Cr steels as shown in Figure 2.40 (Sklenička, 2003). This section will review classic creep deformation mechanisms such as strain hardening, particle coalescing, mobile dislocation and solid solution of particles, and consider suitable creep deformation mechanisms for the development of constitutive equations based on the results of quantitative microstructural investigations of high chromium steel.

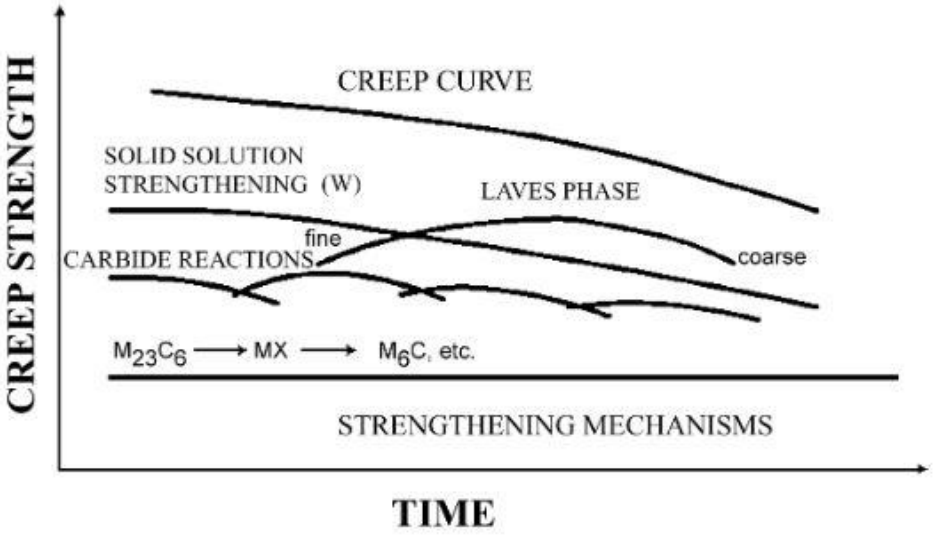

Figure 2.21 The effect of microstructural degradation changes on creep strength in 9-12% Cr steels (Sklenička, 2003).

2.7.1 Strain hardening

Ion proposed the dimensionless parameter H used for modelling primary creep. H is normally named as strain hardening and defined as (Dyson, 2000):

$$H = \frac{\sigma_i}{\sigma} \quad (2.13)$$

Where:

σ is the uniaxial stress;

σ_i is an internal back stress generated during stress redistribution with 'hard' regions on the microstructure (particles, subgrains, etc.) where inelastic strain accumulates.

The evolution of H is as follow:

$$\dot{H} = \frac{h'}{\sigma}\left(1 - \frac{H}{H^*}\right)\dot{\varepsilon} \quad (2.14)$$

The value of H ranged from zero to a microstructure-dependent maximum of H^* (< 1).The constant $h' = E\phi$, where E is the Young's modulus and ϕ is the volume fraction of all phases giving rise to the stress redistribution.

2.7.2 Particle coarsening

The particle coarsening is one of most important degradation processes for creep resistant steels. Based on Dyson's approach, particle coarsening is caused by the interparticle spacing of the hardening particles, and the dimensionless parameter of the particle coarsening equation is defined as (Dyson, 2000):

$$D_p = 1 - \frac{P_i}{P} \quad (2.15)$$

Where

P_i is the initial spacing;

P is the current particle spacing;

The particle coarsening rate is described by:

$$\dot{D}_p = \frac{K_p}{3}\left(1 - D_p\right)^4 \quad (2.16)$$

Table 2.1 Main precipitations in 9-12% Cr steels (Hald, 2008).

Steel	Precipitate	Formula	Remark
12CrMoV	$M_{23}C_6$	$(Cr,Fe,Mo)_{23}C_6$	Precipitate during tempering
P91	$M_{23}C_6$	$(Cr,Fe,Mo)_{23}C_6$	Precipitate during tempering
	MX	(Nb,V)(N,C)	Undissolved during austenitisation
	MX	(V,Nb)(N,C)	Precipitate during tempering
	Laves phase	$(Fe,Cr)_2Mo$	Precipitate during creep ($T<650\,°C$)
P92	$M_{23}C_6$	$(Cr,Fe,Mo,W)_{23}C_6$	Precipitate during tempering
	MX	(Nb,V)(N,C)	Undissolved during austenitisation
	MX	(V,Nb)(N,C)	Precipitate during tempering
	Laves phase	$(Fe,Cr)_2(Mo,W)$	Precipitate during creep ($T<720\,°C$)

9-12% of Cr steels contain several precipitate types during creep processes, as shown in Table2.1 (Hald, 2008). The effect of the evolution of the particle coarsening has been studied in high chromium steel. In 2003, Nakajima et al. conducted research into the coarsening of $M_{23}C_6$ and MX precipitates in T91 steel during creep processes (Nakajima et al., 2003). Czyrska-Filemonowicz et al. (2006) also studied the microstructure and properties of modified 9% Cr steels (P92), and the results of quantitative microstructural investigations show that precipitates were formed (MX and $M_{23}C_6$) as seen in Figure 2.41. A similar research of microstructure and long-term creep properties of 9-12% Cr steels was completed by Hald (2008). The evolution of particle sizes of precipitates in P91 and P92 steel at 600℃ have been measured and modelled in Figure 2.42. These research figures show that the Lave phases significantly nucleate and grow during creep exposure, the mean diameter of Lave phase increased several times; the particle of $M_{23}C_6$ slights increase with no obvious changes of MX. Thus, the creep deformation (microstructural degradation) mechanism of particle coarsening will be considered when forming a new creep damage constitutive equations for high chromium steel.

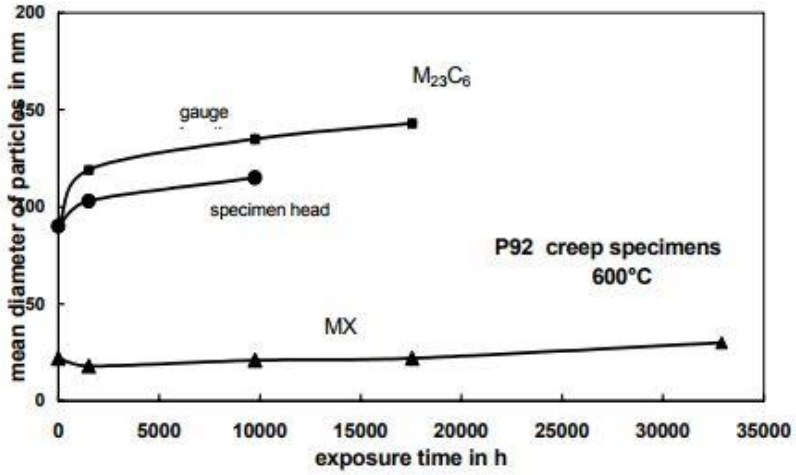

Figure 2.22 Size of precipitates formed during creep exposure of P92 steel under 145MPa at 600℃ (Czyrska-Filemonowicz et al., 2006).

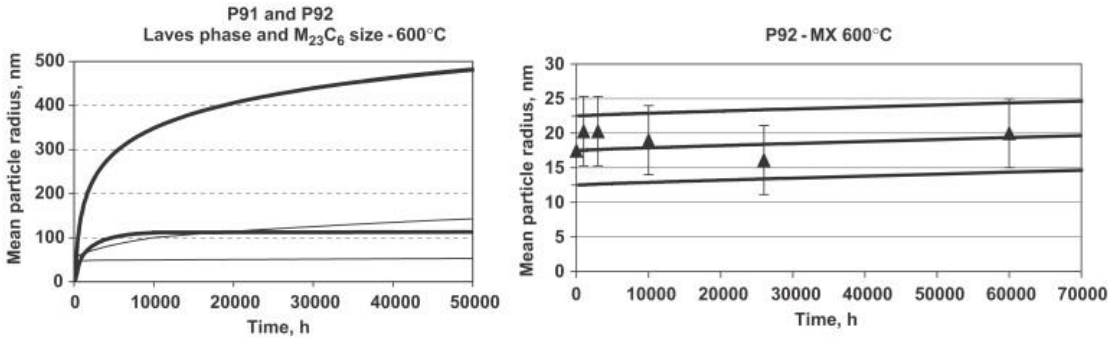

Figure 2.23 Left: the particle sizes of $M_{23}C_6$ (thin lines) and Laves phase (thick lines) in steels of P91 and P92 changes with creep time. Right: Size evolution of MX particle in P92 steel changes with creep time (Hald, 2008).

2.7.3 Mobile dislocation

The multiplication of mobile dislocation described by (Yin and Faulkner, 2006):

$$D_d = 1 - \frac{\rho_0}{\rho_t} \quad (2.17)$$

Where ρ_0 and ρ_t are dislocation density at $t = 0$ and at any time instant t.

The evolution of mobile dislocation rate is as follows:

$$\dot{D}_d = C(1 - D_d)^2 \dot{\varepsilon} \quad (2.18)$$

where C is a material constant.

In the study of the evolution of the microstructure of the specimens after creep testing under a stress range of 104-160MPa at 600℃ and 650℃ for P92 steel, the experimental observation shows the change in the dislocation density in the subgrains for the structural characteristics (Ennis et al., 1997). Czyrska-Filemonowicz, Zielińska-Lipiec and Ennis studied the microstructure and properties of modified 9% Cr steels, the results of quantitative measurements of dislocation density and sub-grain changes with creep exposure time under 145MPa at 600 and 650℃ (Czyrska-Filemonowicz, Zielińska-Lipiec & Ennis, 2006), the diagram in Figure 2.43 shows the dislocation density decreases quickly after about 5000h and the subgrain increases after about 1000h.

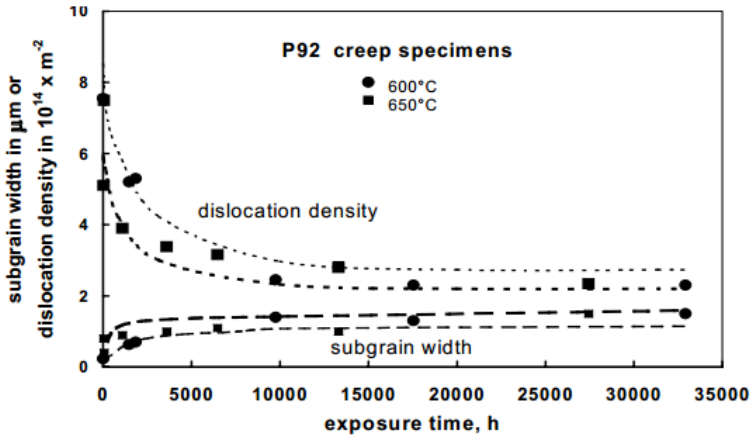

Figure 2.24 The diagram shows the results of quantitative measurements of dislocation density and sub-grain width with increasing creep time for P92 specimens exposed at 600 and 650°C (Czyrska-Filemonowicz, Zielińska-Lipiec & Ennis, 2006).

In the study of microstructural degradation of P91 steel during creep under low stress (Sawada et al., 2011), the mean subgrain size increased and the dislocation density decreased during creep exposure as shown in Figure 2.44. Based on the above microstructure degradation of the subgrain and dislocation density in high chromium steel under different stress level, the creep deformation (microstructural degradation) mechanism of mobile dislocation will be considered for the creep damage constitutive equations for high chromium steel.

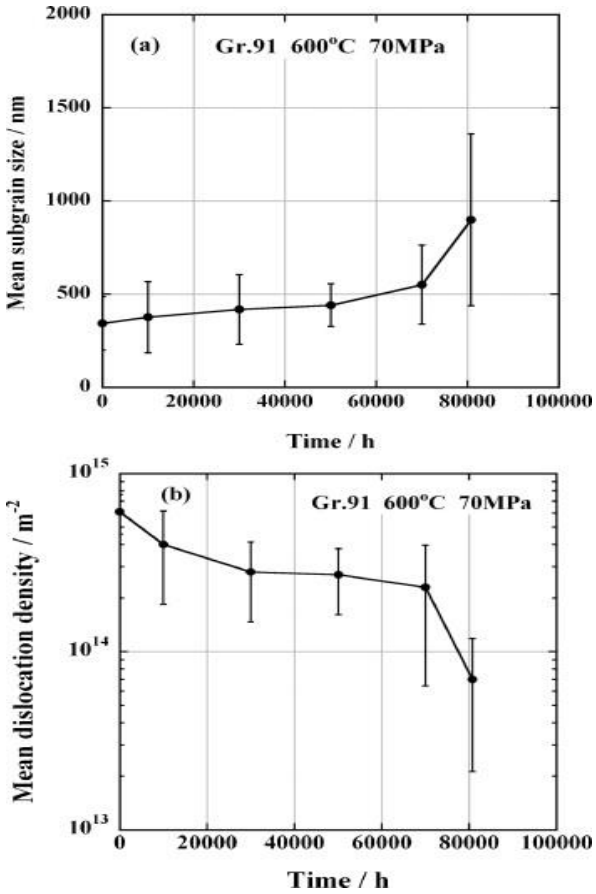

Figure 2.25 (a) The mean subgrain size and (b) the mean dislocation density change with time for Grade 91 steel under 70MPa at 600℃ (Sawada et al., 2011).

2.7.4 Solid solution

Dyson (2000) pointed that Wert and Zener's (1950) nucleation and growth kinetics equation had modelled the depletion of W/Mo from the matrix by nucleation and growth of Laves phase (Fe_2W/Mo) in 9-12% Cr steel. A damage parameter of solid solution is varying between zero and unity and measures from the matrix:

$$D_s = 1 - \frac{\bar{C}_t}{C_0} \quad (2.19)$$

where C_0 is the initial concertation of W/Mo, $\bar{C}_t$ is the average concentration in matrix at time t. The solute depletion damage evolution rate presented by Wert-Zener equation:

$$\dot{D}_s = K_s D_s^{\frac{1}{3}}(1 - D_s) \ (2.20)$$

where K_s is material parameter.

In the research of microstructure of the Grade 91 steel in the long term, i.e. more than 100,000h of creep exposure at 600℃, the size distribution of Laves phases after creep was displayed in Figure 2.45 (a) and Laves phases are easily observed by BSE images because of Laves phases are enriched in Mo in Figure 2.45(b) (Panait et al., 2010).

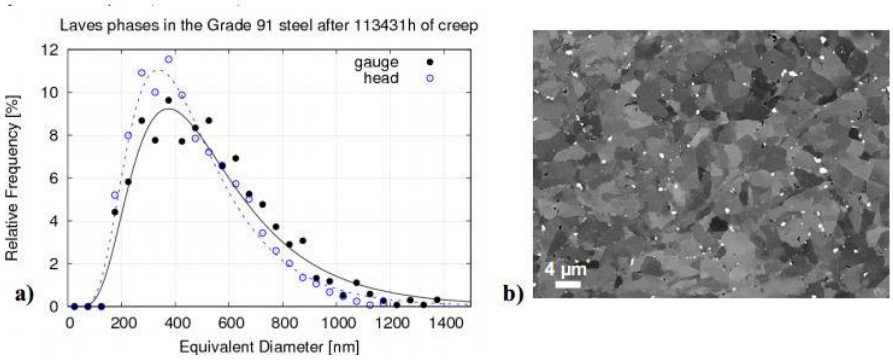

Figure 2.26 Size distribution of Laves phases in the P91 steel (b) BSE image of Laves phases (white) (Panait et al., 2010).

Before Laves phase particles nucleation, Si and Mo segregated to micrograin boundaries, where they alter the thermodynamic and kinetic conditions for Laves phase formation. When critical Si and Mo concentrations were established, Laves phase particles were able to nucleate as shown in Figure 2.46.

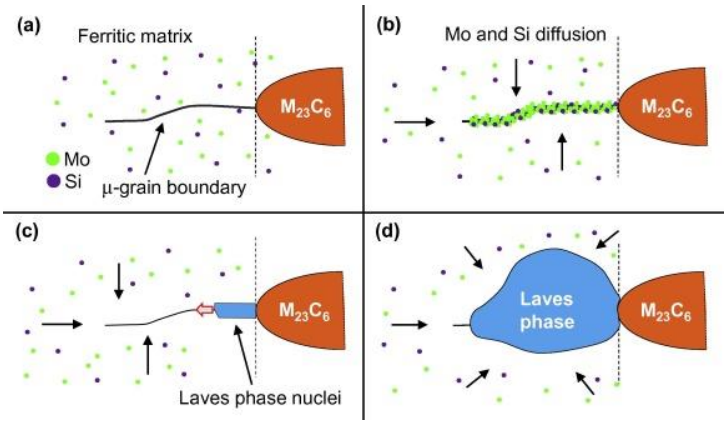

Figure 2.27 The evolution of Laves phase nucleation concentrated with Si and Mo (Isik et al., 2014).

In 2012, Kipelova et al. studied the evolution of Laves phase in a modified P911 heat resistant steel during creep at 923K (650℃). This research indicated that there is mostly no change in chemical elements of W and Mo at 1% strain and fracture of specimen (Kipelova et al., 2012). In other words, this means that there was not the depletion of W/Mo from the matrix by nucleation and growth of Laves phase in high chromium steel. Thus, the creep deformation (microstructural degradation) mechanism of solid solution will be not considered for the creep damage constitutive equations for high chromium steel.

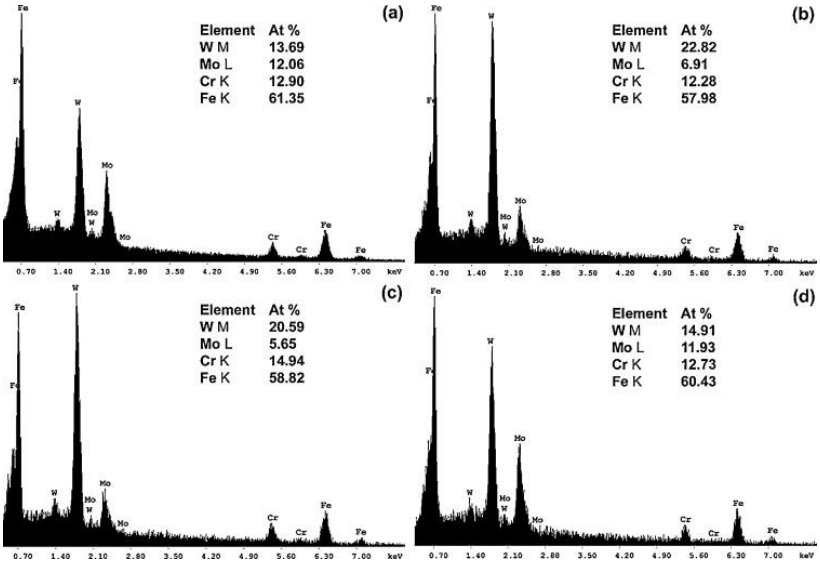

Figure 2.28 The chemical composition of Laves phase at creep strains of (a) 1%, (b) 4%, (c) 6% and (d) in the fractured specimen (Kipelova et al., 2012).

2.8 Current creep damage constitutive equations

This section will critically review the approaches of existing classic creep damage constitutive equations for predicting the lifetime of components of electric power plants, especially for high chromium steel, after which it shall analyse the advantage and limitations of current creep damage constitutive equations. The author will demonstrate the necessity of developing novel creep damage constitutive equations and the expectations surrounding novel creep damage constitutive equations for high chromium steel.

2.8.1 Kachanov and Robotnov equation (1969)

Kachanov (1958) first proposed the concept of continuum creep damage mechanics (CDM), after which Robotnov (1969) developed constitutive equations by describing creep behaviour attempts to using the concept of damage, which employs internal state variable to quantify the strain rate response to an applied stress. The Robotnov-Kachanove equation is expressed as:

$$\dot{\varepsilon} = \dot{\varepsilon}_0 [\frac{\sigma}{\sigma_0 (1-D)}]^n \quad (2.21)$$

$$\dot{D} = \dot{D}_0 \left(\frac{\sigma}{\sigma_0 (1-D)}\right)^v \quad (2.22)$$

Where:

$\dot{\varepsilon}$ is creep strain rate, σ is applied stress;

σ_0 , $\dot{\varepsilon}_0$, $\dot{D}_0$ presents initial state of stress, strain rate and damage rate, respectively;

n and v denote stress exponent;

the value of damage parameter D is varying between 0 and 1.

- **Advantages and limitations:**

It cannot be denied that their contribution has helped lay the foundations for continuum creep damage mechanics (CDM) and for creep damage constitutive

equations, however, the damage parameter is far too simple, especially if there is more than one physical damage mechanism for engineering alloys in a complex service condition. For example, the creep deformation (microstructural degradation) mechanisms in high chromium steel introduced in section 2.4 of chapter 2.

2.8.2 Kachanov-Robotnov-Hayhurst (KRH) equation (1996) and its modified version by Xu (2001)

Based on the Kachanov and Robotnov's equation, Hayhurst had developed the creep damage equations in both versions of uniaxial and multi-axial being named as the Kachanov-Robotnov-Hayhurst (KRH) equation for low chromium steels. The cavity nucleation is also dependent on the state of stress based on experiments by Cane (1979) (1981), Needham and Gladman (1980), according to Perrin and Hayhurst (1996). It reveals that the state of stress may be conveniently characterized by the ratio of the maximum principal stress, σ_1 and the effective stress, σ_e. More so, Cane (1979) (1981) proposed that the cavitated area fraction, A_f, is related to the accumulated effective creep strain, ε_e, the effective stress, σ_e, and the maximum principal stress, σ_1, as displayed in the equation below:

$$A_f = C_f \varepsilon_e \frac{f(\sigma_1)}{g(\sigma_e)} \quad (2.23)$$

where C_f is a proportional constant. The function $f(\sigma_1)/g(\sigma_e)$ may be approximated to $(\sigma_1/\sigma_e)^v$, where the value of constant v varies in a range of 0.5-3 based on the microstructure of material.

The cavitated area fraction could be considered to represent the effects of cavity nucleation and growth (Perrin and Hayhurst, 1996):

$$\dot{\omega} = C\dot{\varepsilon}_e(\frac{\sigma_1}{\sigma_e})^v \quad (2.24)$$

where C is a constant of proportionality,

$\dot{\varepsilon}_e$ is the effective creep strain rate,

v is a constant that defines the multi-axial stress rupture criterion of the material,

ω is the damage variable.

Thus, uni-axial KRH equations are proposed as:

$$\dot{\varepsilon} = Asinh\left(\frac{B\sigma(1-H)}{(1-\emptyset)(1-\omega)}\right) \quad (2.25)$$

$$\dot{H} = \frac{h'}{\sigma}\left(1-\frac{H}{H^*}\right)\dot{\varepsilon}$$

$$\dot{\emptyset} = \frac{K_c}{3}(1-\emptyset)^4$$

$$\dot{\omega} = C\dot{\varepsilon}$$

where:

A, B, C, h', H^* and K_c are material constants in uniaxial state;

H means the strain hardening at primary stage of creep;

$\emptyset$ is the coarsening of precipitates;

ω is the cavitation damage.

Multi-axial KRH equations proposed as:

$$\dot{\varepsilon}_{ij} = \frac{3S_{ij}}{2\sigma_e} A \sinh\left[\frac{B\sigma_e(1-H)}{(1-\emptyset)(1-\omega)}\right] \quad (2.26)$$

$$\dot{H} = \frac{h'}{\sigma_e}\left(1-\frac{H}{H^*}\right)\dot{\varepsilon}_e$$

$$\dot{\emptyset} = \frac{K_c}{3}(1-\emptyset)^4$$

$$\dot{\omega} = CN\dot{\varepsilon}_e\left(\frac{\sigma_1}{\sigma_e}\right)^v$$

where A, B, C, h', H^* and K_c are material constants in uniaxial state,

H means the strain hardening at primary stage of creep,

$\emptyset$ is the coarsening of precipitates,

ω is the cavitation damage,

σ_e is effective stress,

$\dot{\varepsilon}_e$ is effective creep strain rate,

σ_1 is maximum principal stress,

v is stress state index.

A modified model based on multi-axial KRH equations by Xu (Xu, 2001):

$$\dot{\varepsilon}_{ij} = \frac{3S_{ij}}{2\sigma_e} A \sinh\left[\frac{B\sigma_e(1-H)}{(1-\emptyset)(1-\omega_d)}\right] \quad (2.27)$$

$$\dot{H} = \frac{h'}{\sigma_e}\left(1 - \frac{H}{H^*}\right)\dot{\varepsilon}_e$$

$$\dot{\emptyset} = \frac{K_c}{3}(1-\emptyset)^4$$

$$\dot{\omega} = CN\dot{\varepsilon}_e \cdot f_2$$

$$\dot{\omega}_d = \dot{\omega} \cdot f_1$$

$$f_1 = (\frac{2\sigma_e}{3S_1})^{\alpha}\exp\{b[\frac{3\sigma_m}{S_s} - 1]\}$$

$$f_2 = (\exp\{p\left[1 - \frac{\sigma_1}{\sigma_e}\right] + q[\frac{1}{2} - \frac{3\sigma_m}{2\sigma_e}]\})^{-1};$$

where:

A, B, C, h', H^* and K_c are material constants;

H, $\emptyset$ and ω are same means with those in uniaxial version equations;

σ_1, σ_e, is maximum principal, equivalent stress, respectively;

N is equal to 1, while $\sigma_1 > 0$ (tensile) or N is equal to 0, while $\sigma_1 < 0$ (compressive);

v is the tri-axial stress-state sensitivity of the material;

f_1 and f_2 are functions of stress states.

- ***Advantages***

The KRH was successively applied to the description of the creep behaviour of low chromium steel. The models included different mechanisms of microstructure degradation evolutions and cavitation damage and were based on the simple phenomenological experimental observation. Furthermore, the modelling results fit well with the experimental data of low chromium steels. Dr. Qiang Xu's modified version based on KRH equations added function f_1 and f_2 to better phenomenologically unify tertiary deformation, creep damage and creep rupture (2001, 2003, and 2004), and more accurately model the results of creep deformation and rupture time have been improved.

- ***Limitations***

The limitations of KRH equations were also reported by Dr. Qiang Xu (2001, 2003, and 2004), the method only used lifetime and ignored creep deformation consistency. Firstly, KRH and Xu's equations lack of consideration into the stress breakdown phenomenon which was summarized in section 2.3 and needs clear description on the evolution of creep cavitation damage. The KRH constitutive equation model was applied to the specific cast of P91 steel (Bar257, A-369 FP91) at 650℃ and 625℃ in a stress range of 90-110MPa (Hyde et al., 2006), however, there is an absence of a detailed analysis of the features of the creep deformation and cavitation damage for high chromium steel and the estimated lifetime of material is not identified.

2.8.3 Dyson's framework (2000)

Dyson summarized different creep damage mechanisms in categories for engineering alloys in evolution for use in life prediction and is shown in Table 2.2.

Table 2.2 Creep damage categories, mechanisms, and incorporation into CDM (Dyson, 2000).

CREEP DAMAGE CATEGORY	DAMAGE MECHANISM	DAMAGE PARAMETER	DAMAGE RATE	STRAIN RATE
Strain-Induced	Creep-constrained Cavity Nucleation-Controlled	$D_n = \frac{\pi d^2 N}{4}$	$\dot{D}_n = \frac{k_N}{\varepsilon_{f,u}}$	$\dot{\varepsilon} = \dot{\varepsilon}_0 \sinh\left[\frac{\sigma(1-H)}{\sigma_0(1-D_N)}\right]$
	Creep-constrained Cavity Growth-Controlled	$D_n = \frac{\pi d^2 N}{4}$ $D_G = \left(\frac{r}{l}\right)^2$	$\dot{D}_n = 0$ $\dot{D}_n = \frac{d}{2lD_G}\dot{\varepsilon}$	$\dot{\varepsilon} = \dot{\varepsilon}_0 \sinh\left[\frac{\sigma(1-H)}{\sigma_0(1-D_N)}\right]$
	Multiplication of Mobile Dislocation	$D_d = 1 - \frac{\rho_i}{\rho}$	$\dot{D}_d = C(1 - D_d)^2\dot{\varepsilon}$	$\dot{\varepsilon} = \frac{\dot{\varepsilon}_0}{(1-D_d)}\sinh\left[\frac{\sigma(1-H)}{\sigma_0}\right]$
Thermally-Induced	Particle-Coarsening	$D_p = 1 - \frac{P_i}{P}$	$\dot{D}_p = \frac{K_p}{3}(1 - D_p)^4$	$\dot{\varepsilon} = \dot{\varepsilon}_0 \sinh\left[\frac{\sigma(1-H)}{\sigma_0(1-D_p)}\right]$
	Depletion of Solid-Solution	$D_s = 1 - \frac{\bar{c}_t}{c_0}$	$\dot{D}_s = K_s D_s^{1/3}(1 - D_s)$	$\dot{\varepsilon} = \frac{\dot{\varepsilon}_0}{(1-D_s)}\sinh\left[\frac{\sigma(1-H)}{\sigma_0}\right]$

Where

D is damage parameter, subscripts indicate specific mechanism defined in the text,

σ is uniaxial stress,

T is tempearuture,

R is Radius of test piece or component,

d is grain size,

N is number density of cavitated grain boundary facets,

r is cavity radius,

l is intracavity spacing,

$\varepsilon_{f,u}$ is uniaxial strain at fracture,

k_N is cavitation constant $\leq 1/3$,

ρ is dislocation density, subscript i denotes initial value,

C is material constant,

P is particle spacing, i denotes initial value,

K_p is rate constant for particle coarsening,

$\bar{C_t}$ is mean concentration of W/Mo in matrix at time t,

C_0 is concentration of W/Mo in matrix at time t.

Dyson pointed out that grain boundary creep cavitation can be the mechanistic cause of fracture. There are two extremes of behaviour of cavitation: (1) unconstrained cavitation due to a low density of cavity under high stress and/or low temperature; and (2) constrained cavitation because of a high density of cavity, low stress and/or high temperature (Dyson, 2000). The theories of constrained and unconstrained cavitation have been introduced in the above section 2.6, which states that the accuracy of cavitation equation modelling is limited by the uncertainty of the input data. When cavitation is constrained, the damage parameter D_N, which denotes the fraction of grain boundary facet cavitation, is effected by reducing the loading area $(1 - D_n)$. The evolution rate of the damage parameter D_N is zero, while cavity growth is a controlled mechanism. When cavities nucleate continuously, $\dot{D}_n$ could be used to describe the evolution of cavitation damage using a nucleation rate model which is in a linear relationship with strain rate (Dyson, 2000):

$$\dot{D}_n = \frac{k_N}{\varepsilon_{fu}}\dot{\varepsilon} \quad (2.28)$$

where the $\dot{D}_n$ denotes the continuously cavities nucleation damage, ε_{fu} is the uniaxial strain at fracture and k_N has an upper limit of 1/3, when all transverse grain boundaries are cavitated.

Dyson proposed a framework to incorporate the dominant creep damage mechanisms of primary strain hardening (H), multiplication of mobile dislocations (D_d), particle coarsening (D_p) and creep cavitation damage (D_n) all In order to aim to reflect the evolution of creep strain state using hyperbolic sine stress function.

$$\dot{\varepsilon} = \frac{\dot{\varepsilon}_0}{(1-D_d)}\sinh\left[\frac{\sigma(1-H)}{\sigma_0(1-D_p)(1-D_N)}\right] \quad (2.29)$$

$$\dot{H} = \frac{h'}{\sigma}\left(1-\frac{H}{H^*}\right)\dot{\varepsilon}$$

$$\dot{D}_d = C(1-D_d)^2\dot{\varepsilon}$$

$$\dot{D}_p = \frac{K_p}{3}(1-D_p)^4$$

$$\dot{D}_n = \frac{k_N}{\varepsilon_{fu}}\dot{\varepsilon}$$

Where:

$\dot{\varepsilon}$ is creep strain rate;

$\dot{\varepsilon}_0$ is initial strain rate;

σ is applied stress;

σ_0 is initial state of stress;

H is the strain hardening;

D_d is multiplication of mobile dislocation;

D_n is cavitation damage parameter that presents cavity nucleaton;

h', H^*, C, K_p are material constants;

k_N is cavitation constant and upper limit of 1/3;

ε_{fu} is uniaxial strain at fracture.

- ***Advantages***

The advantage of Dyson's constitutive equations provide a mathematical framwork and incorporate a physical based creep deformation (microstructial degredation) mechanisms of stress redistribution around hard regions(strain hardening), multiplication of moblie dislocation, particles coarsening and cavitation damage of nucleation controlled on all transverse grain boundaries. Compared with the damage parameter D in Kachanov and Robotnov equation, the dominant damage parameter of cavitation D_n is based on the quantified analysis results of traditional electron microscopy techniques. Integrating the equation of creep cavity nulceation rate, it means the damage parameter D_N $(D_n = A\varepsilon)$ of fraction area of cavitation is a linear relationship with creep strain. Experimental data of the linear relationship between creep strain and cavity density could provide evidence for the damage parameter D_N for superalloy (Nimonic 80A) as shown in Figure 2.48.

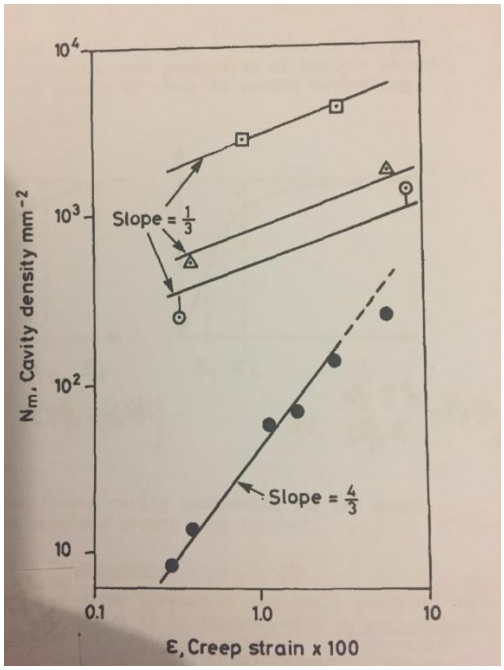

Figure 2.29 Variation of cavity density with creep strain in superalloy Nimonic 80A (Dyson, 1983).

On the other hand, the hyperbolic sine function for constitutive equations could be more adequate for a large range of stress and temperature than power-law

formulation.Thus, Dyson's equation should be more confident in dealing with creep life assessment than Kachanov and Robotnov's equation (Dyson, 2000), because it decribes in more detail about the evolution of creep cavitation damage in engineering materials.

- ***Limitations***

Based on the review of cavitation damage mechanisms in section 2.6, it indicates that the caviation would be continously nucleated under low stress levels and suffer constrained diffusion growth under high stress level at high temperature. However, the cavitation damge equation D_n in Dyson's equation presents only cavitation with continuous nucleation and specifically deals with the cavitation controlled growth rate for zero at the beginning of the creep process.

Moreover, the cavitation damage equation D_n is not suitable for all engineering materials. For example, the test was terminated after 1%, 5% and 12% strain for 12% Cr steel under 80MPa at 923K($650℃$), hence the relationship between cavity density and strain is linear at these three strain points as shown in Figure 2.49. (Eggeler et al., 1989), but there is no more experimental data to further prove the linear relationship between cavitation damage and strain for high chromium steel.

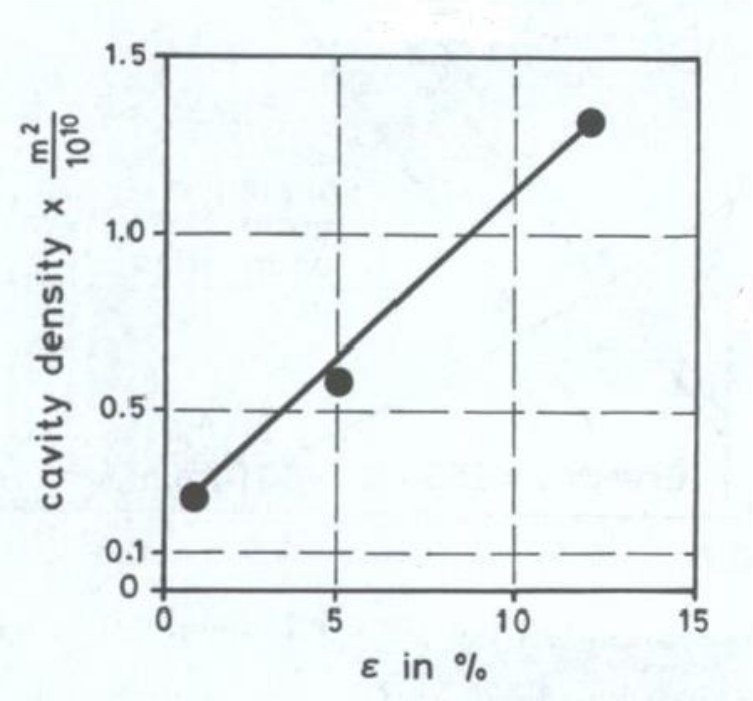

Figure 2.30 Cavity density as a function of strain at strain 1%, 5%, and 12% for 12% Cr-Mo-V steel 923K under 80MPa at 650℃ (Eggeler et al., 1989).

On the contrary, the experimental data of the void area fraction or void area number density with strain for different notch root radius dual phase steel (DP780) and a commercial free-cutting steel JIS SUM24L (1.1%Mn, 32% S, 0.28% Pb, 0.075 P and balance Fe) are not a linear realtionship in Figure 2.50 and Figure 2.51. Thus, there should be a more objective equation for describing both the evolution of cavity nucleation and growth damage mechanisms in engineering materials, especially for high chromium steel.

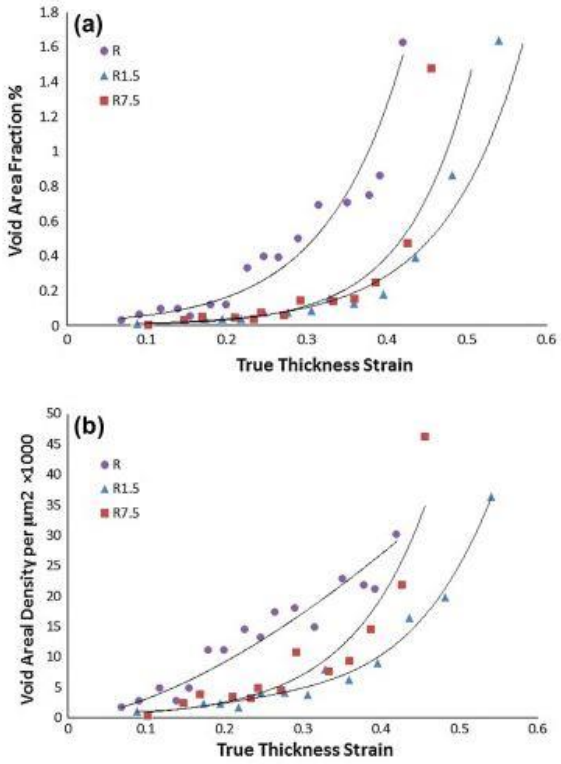

Figure 2.31 (a) Variation of void area fraction with strain, (b) void areal density with strain for dual phase steel (DP780) with smooth radius for 12mm and notch root radius of 1.5 and 7.5 mm (Saeidi et al., 2014).

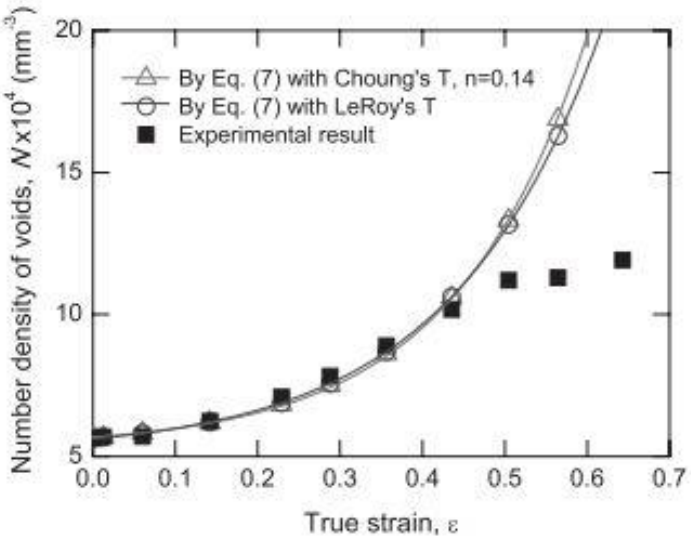

Figure 2.32 Experimental measurements of the evolution of number density of voids with the changing of creep strain (SEO et al., 2015).

2.8.4 Review of current creep damage constitutive equations based on Dyson framework for high chromium steel

2.8.4.1 Modified equations by Yin and Faulkner (2006)

Yin and Faulkner (2006) thought the cavitation damage equation D_n proposed by Dyson (2000) was too simple in some cases, and creep damage due to cavitation damage will increase with increasing temperature if vacancy condensation plays a role in grain boundary cavitation. Based on measuring the area fractions of grain boundary cavities in a modified Al alloy by Khaleel et al. (2001), the quantitatively analysed results indicate that the creep damage increases slowly at low strains and increases quickly at higher strains with increasing creep strain (Yin and Faulkner, 2006). There are similar results in the quantitative study of type 321 stainless steel by Chabaud-Reytier et al (2001), consequently, Yin and Faulkner (2006) proposed the creep cavitation damage by adding an exponent for creep rate:

$$D_N = A\varepsilon^B \quad (2.30)$$

Where A and B are related to temperature. Therefore, the cavitation damage rate is expressed as:

$$\dot{D}_n = A'\varepsilon^{B'}\dot{\varepsilon} \quad (2.31)$$

where $A' = AB$ and $B' = B - 1$. When $B = 1$ is a special case of this equation as same as Dyson's cavitation damage equation.

Based on Dyson's framework, Yin and Faulkner (2006) suggested creep damage constitutive equations for high chromium steel (9wt-% Cr steel):

$$\dot{\varepsilon} = \frac{\dot{\varepsilon}_0}{(1-D_d)(1-D_s)} sinh\left[\frac{\sigma(1-H)}{\sigma_0(1-D_p)(1-D_N)}\right] \quad (2.32)$$

$$\dot{H} = \frac{h'}{\sigma}\left(1 - \frac{H}{H^*}\right)\dot{\varepsilon}$$

$$\dot{D}_d = C(1-D_d)^2\dot{\varepsilon}$$

$$\dot{D}_p = \frac{K_p}{3}\left(1-D_p\right)^4$$

$$\dot{D}_s = K_s D_s^{1/3}(1-D_s)$$

$$\dot{D}_n = A'\varepsilon^{B'}\dot{\varepsilon}$$

where

A, B, C, h', H^*, K_s and K_p are material constants.

- **Advantages**

The different creep deformation mechanisms of high chromium steel had been taken into consideration by Yin and Faulkner's constitutive equations. The grain boundary cavitation damage had been considered according to experimental data of Al alloy and type 321 steel by vacancy condensation. It is different to say that the evolution of the characterisation of cavitation in Al alloy and type 321 steel is same with high chromium steel, but the novel modified equation of cavitation damage with adding exponent for creep strain expressed that quickly increasing of the creep cavitation damage at higher strains with increasing creep strain. It is acceptable at that stage.

- **Limitations**

This model of cavitation damage had no further validated by the experimental data of the evolution of cavity in high chromium steel. The material constant of A is dependence of temperature in the cavitation damage equation proposed by Yin and Faulkner (2006), however, Basirat et al. (2012) realized both temperature and stress level influence the value of material constant A. Thus, the value of material constant which is dependence of temperature and stress has a great impact of the cavitation damage mechanisms.

2.8.4.2 Modified equations by Chen et. Al. (2011)

Chen et al. (2011) had essentially adopted the approach of creep cavitation damage equation proposed by Yin and Faulkner (2006), then developed a creep constitutive equations for T/P91 steel. The power law function is coupled creep deformation mechanisms including strain hardening, solute depletion of precipitates, the coarsening of particles and cavitation damage mechanism under high stress level (130-200MPa) at 600℃. The developed constitutive equations express as:

$$\dot{\varepsilon} = \dot{\varepsilon}_0 \frac{1}{(1-D_s)} \left[\frac{\sigma(1-H)}{\sigma_0 (1-D_p)(1-D_N)} \right]^n \quad (2.33)$$

$$\dot{H} = \frac{h'}{\sigma}\left(1 - \frac{H}{H^*}\right)\dot{\varepsilon}$$

$$\dot{D}_s = K_s D_s^{1/3}(1 - D_s)$$

$$\dot{D}_p = \frac{K_p}{3}\left(1 - D_p\right)^4$$

$$\dot{D}_n = A'\varepsilon^{B'}\dot{\varepsilon}$$

$$\dot{\sigma} = \sigma\dot{\varepsilon}$$

where A, B, C, h', H^*, K_s and K_p are material constants,

σ is applied stress,

n is stress exponent.

In the author's earlier research, the modelling results of the modified equations had been validated by comparing with experimental data of high chromium steel under high stress level, however, it was unsuccessfully applied to lower stress level. The creep curve under low stress is not the right type in leading to rupture and not sharp enough to be observed as brittle intergranular fracture type with low ductility(Parker, 2013) as shown in Figure 2.52 (Yang, Xu & Lu, 2013).

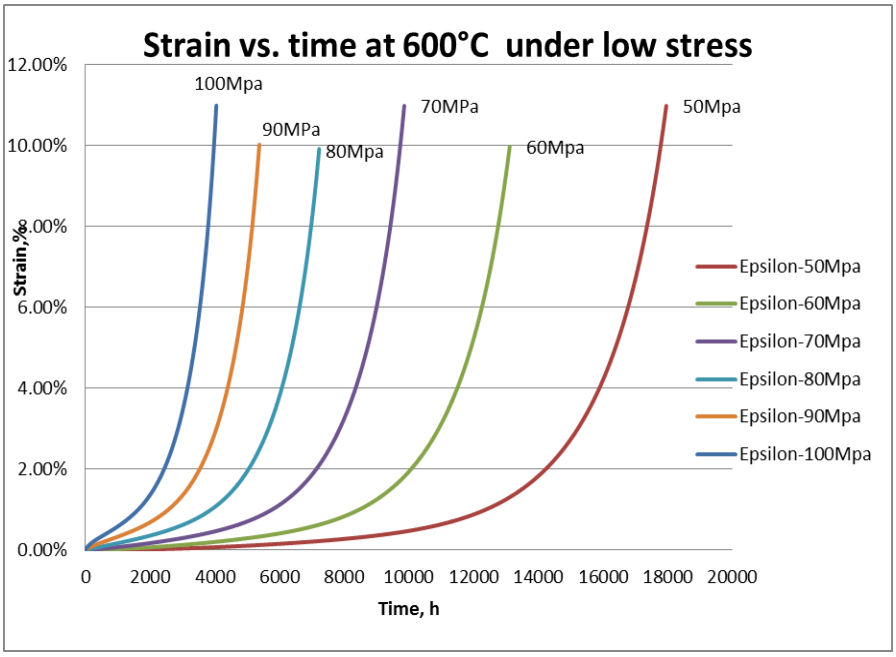

Figure 2.33 The graph of strain versus time under low stress by application of Yin's modified creep damage constitutive equations (Yang, Xu & Lu, 2013).

2.8.4.3 Basirat's equation (2012)

Basirat et al. (2012) inserted the creep deformation mechanisms and cavitation damage mechanism (adopted modified cavitation damage equation by Yin and Faulkner (2006)) into Orowan's equation, then the modified constitutive equations became:

$$\dot{\varepsilon} = \frac{b \cdot \rho_m \cdot v_g}{M\left(1 - D_s\left(1 - D_p\right)(1 - D_N)\right)} \quad (2.34)$$

$$\dot{D}_s = K_s D_s^{1/3}(1 - D_s)$$

$$\dot{D}_p = \frac{K_p}{3}\left(1 - D_p\right)^4$$

$$\dot{D}_n = A\dot{\varepsilon}\varepsilon^{0.9}$$

Basirat et al. (2012) suggested both temperature and stress level have great influence on the value of material constant A in the cavitation damage equation and the specific variation of cavitation damage coefficient A for P91 steel is shown in Table 2.4 and Figure 2.53 (Xu, Yang and Lu, 2017). It is hard to use them in constitutive equation modelling for the predication of lifetime with confidence due to the lack of a clearly trend in Figure 2.53.

Table 2.3 The variation of creep cavity damage coefficient A with different stress and temperature (Basirat et al., 2012).

Parameter	$\sigma = 80MPa$	$\sigma = 100MPa$	$\sigma = 150MPa$	$\sigma = 200MPa$	Temperatures(℃)
A	57	83	1	112	600
A	57	83	47	145	650
A	57	83	113	146	700

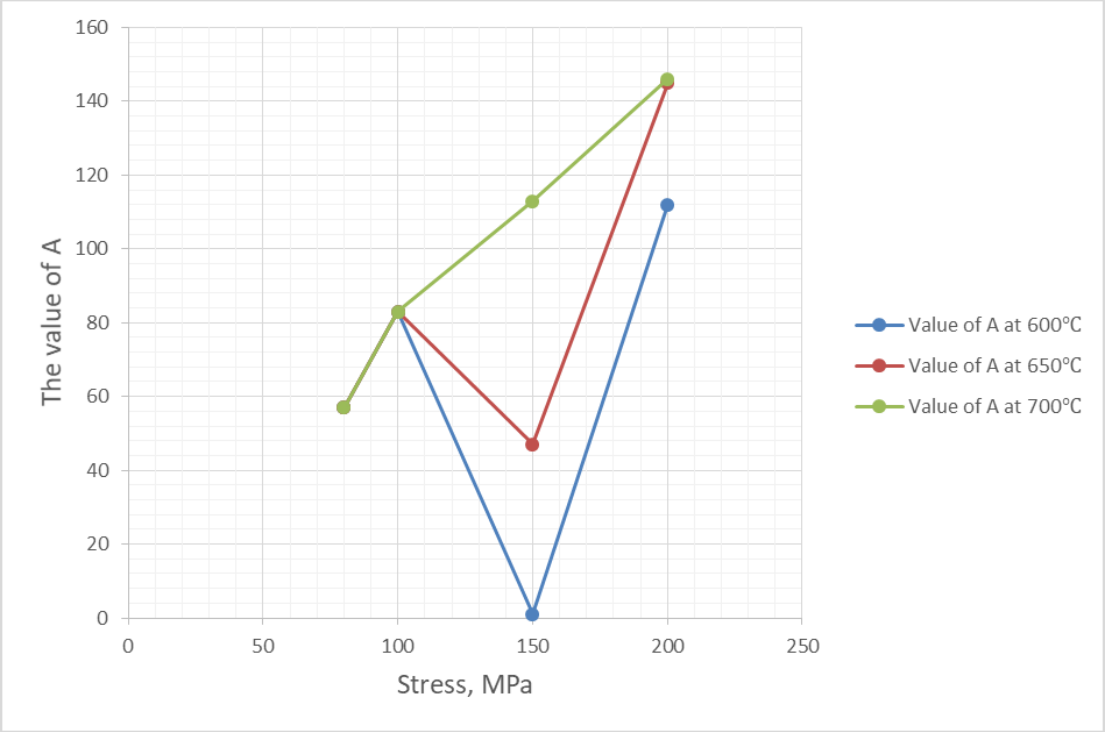

Figure 2.34 The variation of creep cavity damage coefficient A with different stress and temperature (Xu, Yang and Lu, 2017b).

2.8.5 Recently developed constitutive equations only with creep deformation mechanisms and without creep cavitation damage for high chromium steel (2011-2013)

Below are several of the most developed creep damage constitutive equation models that have been advanced to take better account of the evolution of creep deformation (microstructural degradation) for high chromium steel. However, these are not concerned with the dominant damage mechanism of cavitation which manifested in section 2.6 and the creep fracture has deviated to the physical based foundation towards more phenomenological.

- ***Pétry and Lindet (2009)***

$$\varepsilon = \varepsilon^{e} + \varepsilon^{vp} \quad (2.35)$$

$$\sigma = C \cdot \varepsilon^{e}$$

$$\dot{\varepsilon}^{vp} = \frac{3}{2}\dot{\varepsilon}_0 \sinh\left(\frac{\sigma_{eq}(1-H)}{K(1-D)}\right)\frac{\sigma^{D}}{\sigma_{eq}}$$

$$\begin{cases} H = H_1 + H_2 \\ \dot{H}_1 = \dfrac{h_1}{\sigma_{eq}}(H_1^* - H_1)\dot{p} \\ \dot{H}_2 = \dfrac{h_2}{\sigma_{eq}}\dot{p} \end{cases}$$

$$\dot{D} = A_0 \sinh\left(\frac{\alpha\sigma_1 + (1-\alpha)\sigma_{eq}}{\sigma_0}\right)$$

where:

$\varepsilon, \varepsilon^e, \varepsilon^{vp}$ is total strain, elastic strain and viscoplastic strain tensor, respectively;

$\mathbb{C}$ is Hooke's fourth rank elasticity tensor;

σ^D is deviatoric stress tensor;

σ_{eq} is Von Mises equivalent stress;

σ_1 is maximum principal stress;

$\dot{p}$ is plastic strain rate;

H is isotropic hardening;

D is cavitation damage;

$\dot{\varepsilon}_0, K, h_1, h_2, H_1^*, A_0, \sigma_0, \alpha$ are material parameters.

Pétry and Lindet's model was modified on Hayhurst's approach by subdividing the hardening variable H into a more complex variable involving the increase and decrease in the whole process of hardening variable. The model originally neglected the influence of thermal ageing and cavitation damage and is represented by the variable D which is dependent of stress state (Pétry and Lindet, 2009). The research paper of by Qiang Xu (2011) pointed out the compromise in determining the value of α due to the lack of experimental data for notched bar test (Xu, Lu and Wang, 2013). Thus, the model is not confident enough for predicting the lifetime of components.

- ***Oruganti's equation (2011)***

$$\dot{\varepsilon} = \dot{\varepsilon}_0 \exp\left(-\frac{Q_d}{RT}\right) \sinh\left[\frac{\sigma(1 - H^*(1 - D_s))}{\sigma_0(1 - D_p)}\right] \quad (2.36)$$

$$\dot{\sigma} = K_1\left(1 - \frac{\sigma_0}{K_2}\right)\dot{\varepsilon}$$

$$\dot{D}_s = \frac{\dot{\varepsilon}}{S_i}(K_{s1} + K_{s2}\exp(-\frac{Q_s}{RT}))(1 - D_s)^2$$

$$\dot{D}_p = \frac{K_p}{P_i^2}\exp(-\frac{Q_d}{RT})\left(1 - D_p\right)^4$$

where

K_1 , K_2 are constants for a given material,

σ_0 increases proportionately with strain and approach a steady value of K_1 at a rate determined by K_2,

K_{s1} and K_{s2} are the coefficients corresponding to the temperature independent and temperature-dependent parts of subgrain growth,

Q_s is the activation energy,

K_p, Q_s, Q_d, P_i, S_i, H^* are physically bounded by experimental data.

Oruganti et al. (2011) proposed this model based on Dyson's framework. The coarsening of carbon nitrides and subgrain structure resulting from martensitic transformation were incorporated in the creep damage constitutive equations, however, the modelling results shows a big gap in the tertiary stage of creep curve in Figure 2.54, which may be due to this model neglecting the cavitation damage mechanism which contributes most to final fracture in the tertiary stage.

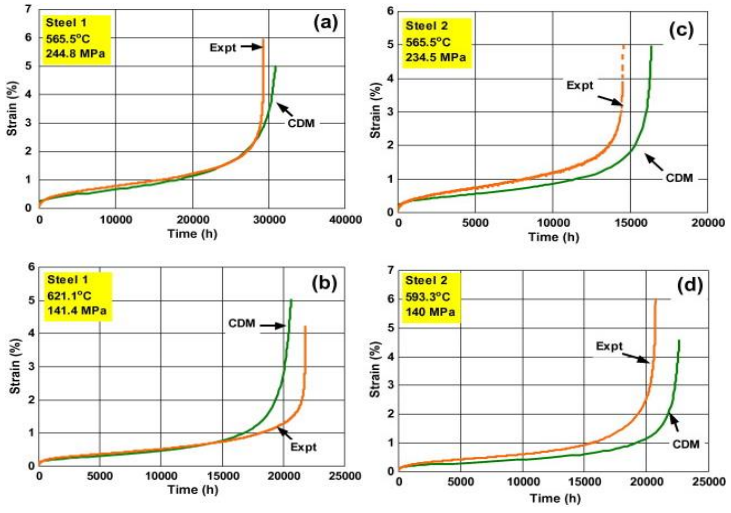

Figure 2.35 The modelling result of Oruganti's constitutive equation compared with experimental data for 9-10%Cr ferritic steels (Oruganti et al., 2011).

- ***Ghosh's equation (2013)***

$$\dot{\varepsilon} = \dot{\varepsilon}_0(1 + D_d)\exp[-\frac{Q_d}{RT}]\sinh\left[\frac{\sigma(1-H)}{\sigma_0(1-D_p)}\right] \quad (2.37)$$

$$\dot{H} = \frac{h'}{\sigma}\left(1 - \frac{H}{H^*}\right)\dot{\varepsilon}$$

$$\dot{D}_d = C\dot{\varepsilon}$$

$$\dot{D}_p = \frac{K_p}{3}(1 - D_p)^4$$

$$\dot{\sigma} = \sigma\dot{\varepsilon}$$

where

$\dot{\varepsilon}_0$ is strain rate and depends on precipitation volume fraction and mobile dislocation density,

Q_d is the activation energy,

C is material parameter of the evolution of dislocation density.

Ghosh applied the modified model to both low and high chromium steel. The modelling results shown in Figure 2.55 and Figure 2.56 fail to fit well with the experimental data. The creep deformation and damage mechanisms are different under different conditions, especially between high and low chromium steels. It is not scientific reasonable for application of a model that includes samples both high and low chromium steels.

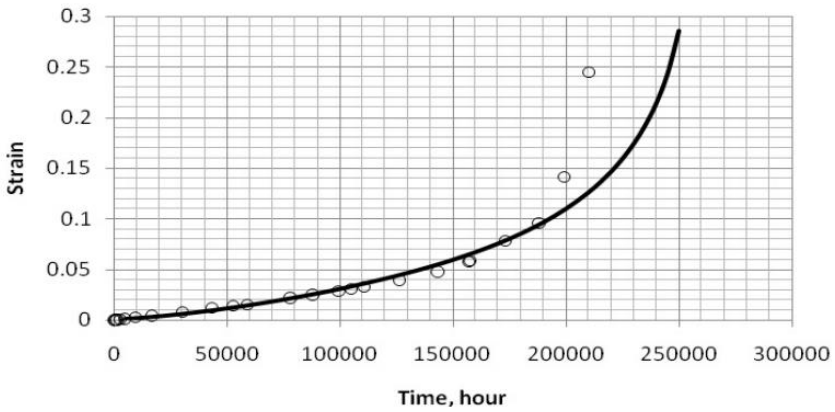

Figure 2.36 The modelling result of Ghosh's constitutive equation compared with experimental data for 2.25Cr1Mo steel under 98MPa at 500℃ (Ghosh et al., 2013).

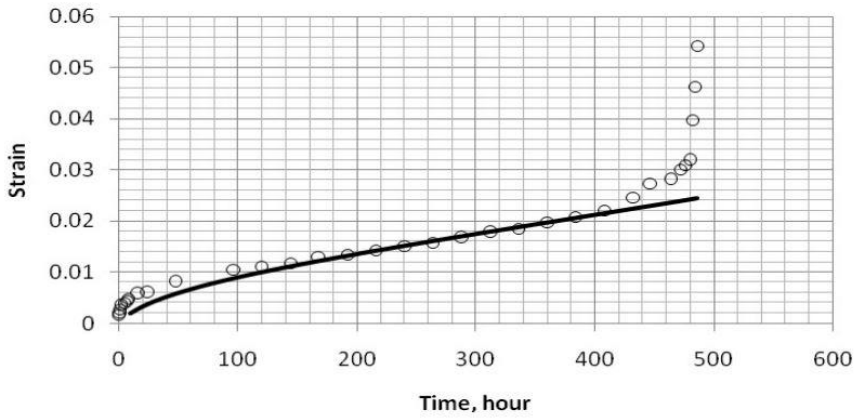

Figure 2.37 The modelling result of Ghosh's constitutive equation compared with experimental data for 9CrMoVNb steel under 260MPa at 540℃ (Ghosh et al., 2013).

- ***Constitutive equations modified by Christoper et al.(2013)***

$$\dot{\varepsilon} = \dot{\varepsilon}_0(1 + D_d)\sinh\left[\frac{\sigma(1-H)}{\sigma_0(1-D_p)}\right] \quad (2.38)$$

$$\dot{H} = \frac{h'}{\sigma}\left(1 - \frac{H}{H^*}\right)\dot{\varepsilon}$$

$$\dot{D}_d = k_2(\frac{\rho_{ss}}{\rho_{N,i}})^{0.5}(1 + D_d)^{0.5}(1 - (1 + D_d))^{-1}\left((\frac{\rho_{N,i}}{\rho_{ss}})^{0.5}\right)\dot{\varepsilon}$$

$$\dot{D}_p = \frac{K_p}{3}(1 - D_p)^4$$

$$\dot{\sigma} = \sigma\dot{\varepsilon}$$

Where $\dot{\varepsilon}_0$ is the characteristic strain rate,

D_d is a non-dimensional damage parameter for network dislocation coarsening,

$\rho_{N,i}$ and ρ_{ss} are the dislocation density at any strain and initial dislocation density, respectively,

k_2 is derived from Kocks–Mecking phenomenological approach.

Christopher's equation had considered of the evolution of creep deformation (microstructural degradation) did not consider the cavitation damage. The modelling results as shown in Figure 2.57 and Figure 2.58 indicate that a great

gap of creep lifetime and rupture strain between the predicted modelling and experimental data.

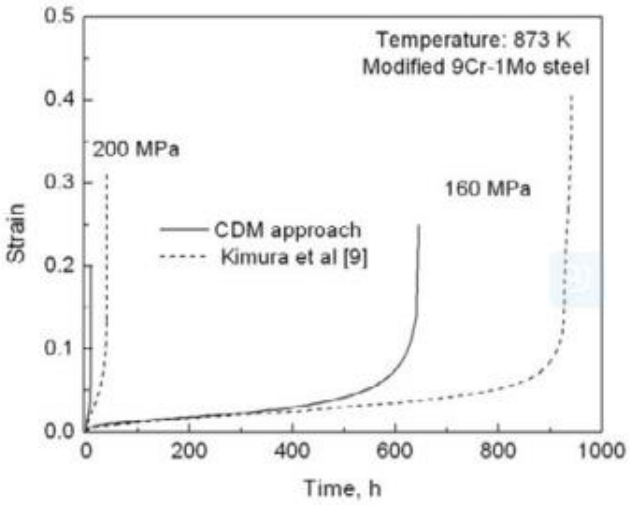

Figure 2.38 The modelling results of Christopher's constitutive equation compared with experimental data for modified 9Cr-1Mo steel under 160MPa and 200MPa at 873K (Christopher et al., 2013).

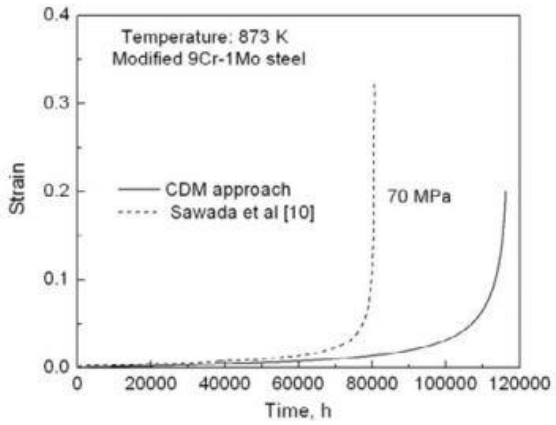

Figure 2.39 The modelling results of Christopher's constitutive equation compared with experimental data for modified 9Cr-1Mo steel under 70MPa at 873K (Christopher et al., 2013).

The above developed constitutive equations are only based on the evolution of creep deformation (microstructural degradation). Without the cavitation damage they do not reflect the real process of creep damage and the modelling results of those equations indicates a significant divergence in creep lifetime and rupture strain compared with experimental data.

2.8.6 The expectation of novel creep damage constitutive equations for high chromium steel

Based on the limitations of the existing creep damage constitutive equations, particularly for high chromium steel, the two main problems presented below will be taken into account in order to better fulfil the expectations of new equations:

1. The existing creep damage constitutive equations, used in a limited stress range, were mostly developed for high chromium steel under high stress level thus was not extended to low stress level. On the other hand, the function of the relationship between minimum creep strain rate and applied stress in range of levels will be invested and will be followed by suggestions to help formulate more accurate and functional constitutive equations. The review paper (Xu et al., 2013, 2017) has similar comments for existing creep damage constitutive equations, the author agreed with Xu after the investigation.

2. The precise measurements of the evolution of creep voids at grain boundaries during creep though advanced technology of X-ray microtomography could contribute to the improvement in the reliability of the novel creep cavitation damage equation and contribute to providing a more accurate estimate of the life time of high chromium steel.

2.9 Typical creep fracture criterion

The creep fracture criterion is a key factor for creep damage constitutive equations, this section will introduce the relationship between creep cavitation damage parameters and distribution of creep cavities on grain boundaries and typical creep fracture criterion for exciting creep damage constitutive equations, which had been summarized in the author's research published paper (Yang, Xu and Lu, 2015). This section provides suggestions for the fracture criterion in the development of novel constitutive equations.

There are three main relationships between creep cavitation damage parameters and distribution of creep cavities on grain boundaries used to

evaluate the creep damage as shown below and their definition is shown in Figure 2.59 (Toda, et al., 1996):

1. Area fraction of cavities, p: the total volume of cavities;
2. Fraction of cavities on grain boundary lines, L: the fraction of cavities on grain boundary lines, $\sum 2c_i$: fraction of the total length of cavities, $2l$: the length of each grain boundary line;
3. Areal cavity density, M: the number of cavities in a unit area;
4. A-parameter, A: a number fraction of cavitated grain boundary lines to the total number of grain boundary lines.

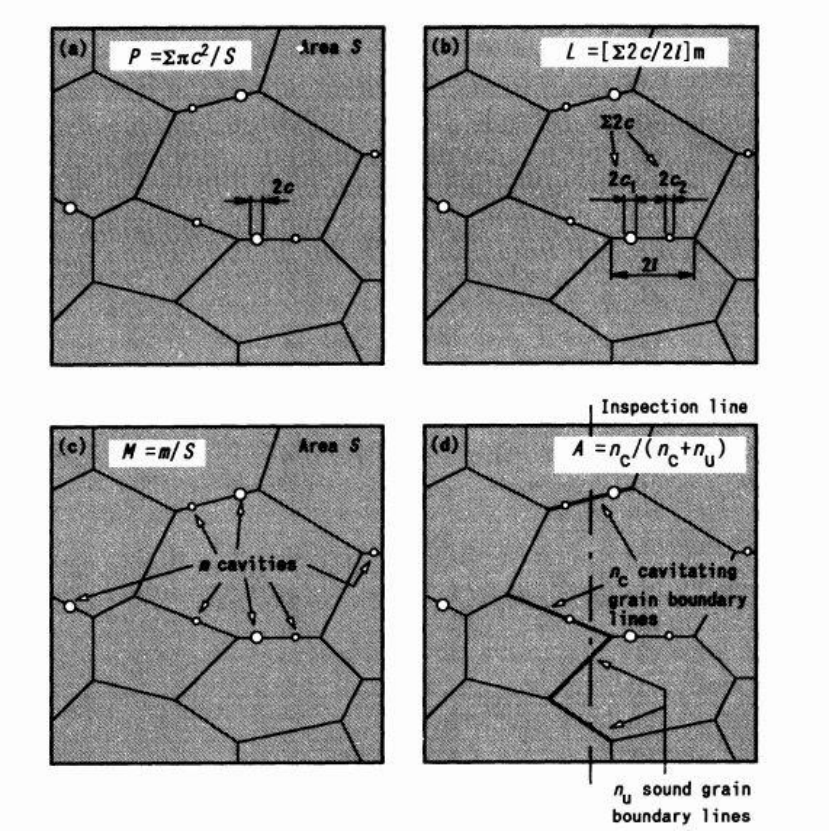

Figure 2.40 Creep damage parameter: (a) Area fraction of cavities, (b) Fraction of cavities on grain boundary lines, (c) Areal cavity density, (d) A-parameter (Toda, et al., 1996).

2.9.1 Dyson and KRH （ω=1/3）

Section 2.8 has already introduced Dyson and the KRH model. The variable parameter ω presents cavitation damage and varies from zero. The maximum value of ω at failures, which is the area fraction of cavitation damage for all

grain boundary, is approximately 1/3. Creep cavitation can either be nucleation or growth controlled, which is linear to strain rate.

2.9.2 Pétry and Lindet ($t_R min = \{t(\varepsilon = \varepsilon_c = 10\%), t(D = D_c)\}$)

Pétry and Lindet's modified creep damage constitutive equations, introduced and discussed in section 2.8, suggested that the modelling computations were stopped when the macroscopic strain reached the value of 10% ($\boldsymbol{\varepsilon_c}$) because of numerical convergence reasons. The damages varied between zero at initial state and threshold value $\mathrm{D_c}$ which varies between 0.1 and 0.3. Pétry and Lindet applied the weakest link approach and proposed the fracture criterion:

$$\mathrm{t_R min} = \{\mathrm{t}(\varepsilon = \varepsilon_c = 10\%), \mathrm{t}(\mathrm{D} = \mathrm{D_c}).$$

2.10 Current state of experimental data of high chromium steel

There are four main aspects in current state of experimental data of high chromium steel summarized below:

1) Generally, creep data contain a full set of data, such as the chemical compositions of materials, material production procedures (heat treatment), and creep specimens for optical micrographs or SEM. Creep date sheet of high chromium steel are mainly published by ECCC and NIMS. ECCC (2005, 2014) had been collated and formally assessed the high chromium steel of Steel 91 (T/P91), ASTM Grade 92 (T/P92), Cast Steel 91, E911 steel, most of them were focused on short-term (10,000h) creep under high stress level. NIMS (2007) had published long-term (exceeding 100,000h) creep deformation properties for ASME Grade 91 steel (9Cr-1Mo-V-Nb) in a higher range of stress level, but some creep tests of those materials were processed under the stress condition of 50MPa, 60MPa, 70MPa at different temperature.

2) The evolution of microstructural degradation of high chromium steel had for the majority been studied by OP, TEM, and SEM during creep process. The observation mostly focused on the influence of creep resistance by metallic element process and the evolution of precipitates.

In the section 2.7, the author reviewed classic creep deformation mechanisms and analysed the creep deformation mechanisms in high chromium steel based on experiential data.

3) The traditional technology of OP, TEM, and SEM had widely been used for observing the fracture surface of high chromium steel, some of experimental observations indicated that cavitation was the dominant damage mechanism leading to final fracture. The author has already summarized and analysed this experimental data in section 2.4 and has clearly understood the creep fracture mechanisms for high chromium steel.

4) In chapter 4, this research will collect and analyse the critical experimental data of high chromium steel by the advanced 3D technology of microtomography X-ray. The whole evolution process of cavitation characterisation with increasing creep exposure provide a better understanding of the cavitation damage mechanisms and provide hope in developing novel constitutive equations for high chromium steel.

Chapter 3 Collection and analysis of the critical experimental data of high chromium steel for the development of novel creep damage equations

This section collects and analyses critical experimental data needed to solve problems involved with the development of novel creep damage constitutive equations for high chromium steel. Based on the previous chapters, there are three main aspects of experimental data to collect and analyse in order to formulate a novel creep damage constitutive equations for high chromium steel:

1) A set of based creep test data sheet (section 3.1):
   Creep rupture time under different stress levels are needed for comparison with the modelling of predicting lifetime of high chromium steel; creep curve of creep strain against time is needed for comparison of modelling results; minimum creep strain rate under different stress levels is needed to describe the relationship between minimum creep strain rate and applied stress;
2) The experimental observation of the evolution of microstructural degradation (such as precipitates, alloying element) in high chromium steel for identifying the creep deformation mechanism and equations for creep damage constitutive equations. This aspect was completed in section 2.7 (chapter 2) in the introduction of creep deformation mechanisms;
3) The experimental observation and quantitative analysis of the evolution of cavitation characterization for the development of a novel creep cavitation damage equation (section 3.2).

3.1 The experimental data of creep test for high chromium steel based on NIMS publication

3.1.1 Creep rupture times of P91 steel under different steel at 600℃ and 625℃

The data of creep rupture times of P91 steel under different steel at 600℃ and 625℃ was extracting from the NIMS creep data sheet published by NIMS (2014)

and is shown in Table 3.1 and Table 3.2. This set of data regarding creep rupture times can be used to model the development of constitutive equations in chapter 6 because of available data and simplification.

Table 3.1 Experimental data of P91 steel rupture time under different stress levels at 600℃

Stress (MPa)	Rupture time (h)
70	80736.8
100	34141
110	21206.3
120	12858.6
140	3414.7
160	971.2

Table 3.2 Experimental data of P91 steel rupture time under different stress levels at 625℃

Stress (MPa)	Rupture time (h)
90	21372.4
100	9895.4
120	1657.9
140	399

3.1.2 Creep curve of P91 steel under different stress at 600℃

The creep curve of creep strain against time of Grade 91 (9Cr–1Mo–V–Nb–N) steel under different stress levels at 600℃ was published by researchers of NIMS (2014) as shown in Figure 3.1 and Figure 3.2. And these creep curves had been used for validation by Christopher (2013). The computational modelling of the development creep damage constitutive equations will be

validated against the creep curve of creep strain rate versus time under different stress levels at 600℃ in chapter 6.

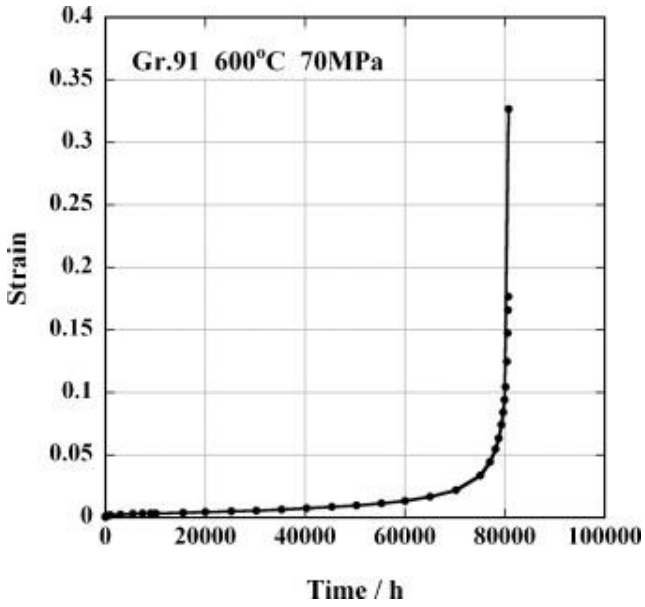

Figure 3.1 The creep curve of creep strain versus time for grade 91 at 600℃ (Sawada et al., 2011).

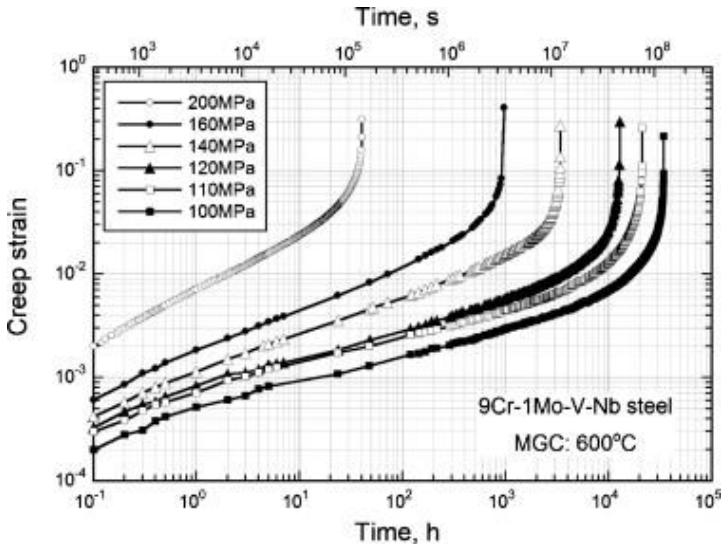

Figure 3.2 Creep curves of creep strain and versus time for 9Cr-1Mo-V-Nb steel at 600℃ (Kimira et al., 2009).

3.1.3 Minimum creep strain rate under different stress at 600℃

The experimental data of the minimum creep strain rate under different stress levels at 600℃ and 625℃ will be selected from Table 3.3 and Table 3.4 and shall be analysed to provide insight into the relationship between minimum creep strain rate and applied stress. The modelling results of the conventional power law, hyperbolic and linear power law, along with modified hyperbolic sine law will be compared with experimental data of minimum creep strain rate and stress, in order to identify which fitted well with the experimental data and which will be implemented in the development of new damage constitutive equations in the following chapter.

Table 3.3 Experimental data of minimum creep rate at 600℃ for P91 (9Cr-1Mo-V-Nb) extracting from NIMS creep data sheet (NIMS, 2014).

Tempature (℃)	Stress (MPa)	Minimum creep rate
600	200	1.4×10^{-3}
	160	4.2×10^{-5}
	140	7.7×10^{-6}
	120	1.5×10^{-6}
	110	8.1×10^{-7}
	100	4.0×10^{-7}
	80	1.3×10^{-7}
	70	9.6×10^{-8}

Table 3.4 Experimental data of minimum creep rate at 625℃ for P91 (9Cr-1Mo-V-Nb) extracting from NIMS creep data sheet (NIMS, 2014).

Tempature (℃)	Stress (MPa)	Minimum creep rate

625	140	1.5×10^{-4}
	120	3.5×10^{-5}
	100	4.5×10^{-6}
	90	1.7×10^{-6}
	80	6.4×10^{-7}
	70	4.4×10^{-7}
	60	2.8×10^{-7}
	50	1.1×10^{-7}

3.2 The experimental observation of cavitation damage in high chromium steel

This section will collect the critical experimental observation of the evolution of the cavitation characterization for the development of novel cavitation damage equations. In recent years, 3D dimensional techniques, namely X-ray micro-tomography, have been applied for the characterization of creep cavitation damage behaviour in copper (Dzięcioł, 2010), ferritic and martensitic steels (DP steels) (Landron et al., 2011) and high chromium steel (Sket et al., 2010) (Gupta, 2013) (Renversade et al., 2014) (Yadav et al., 2014) (Yadav et al., 2015). 3D images of conventional structural materials with high absorption X-ray has been realised by synchrotron micro-tomography, providing new insights into creep cavitation damage (Gupta, 2013) (Gupta, 2015). The 3D images of cavities reveal the nature of the spatial distribution and 3D cavitation characteristics of the creep voids. Quantitative analyses of the cavitation characteristics revealed by 3D datasets, when scaled with respect to time, stress and temperature, provide suitable quantitative functional relations between internal cavitation characteristics and macroscopic creep properties for developing novel creep damage constitutive equations to predict residual life of creep failure.

3.2.1 The experimental observation of the evolution of cavity in P91 steel (2013)

Chiantoni et al. assessed the ductile damage in P91 steel at high temperature by using advanced X-ray micro-tomography, which was used to measure the void. The equivalent diameter of the micro-voids over 15μm are represented in blue colour on 3D reconstruction of the sample of P91 steel at high temperature as shown in Figure 3.3 (Chiantoni et al., 2013).

According to cavitation damage mechanics, the damage parameter represents the ratio between the area of voids and the total cross-sectional area,

$$D = \frac{A_{void}}{A} \quad (3.1)$$

Where:

A_{void} is the area of the voids;

A is the total cross-sectional area;

D is the mean value of cavitation damage.

The mean cavity damage profiles along the axes of specimens is shown in Figure 3.4. It indicates the peak value of the mean damage is close to the centre of the creep test P91 steel samples. The relationship between the mean cavity damage and applied stress or creep expose time should be further researched.

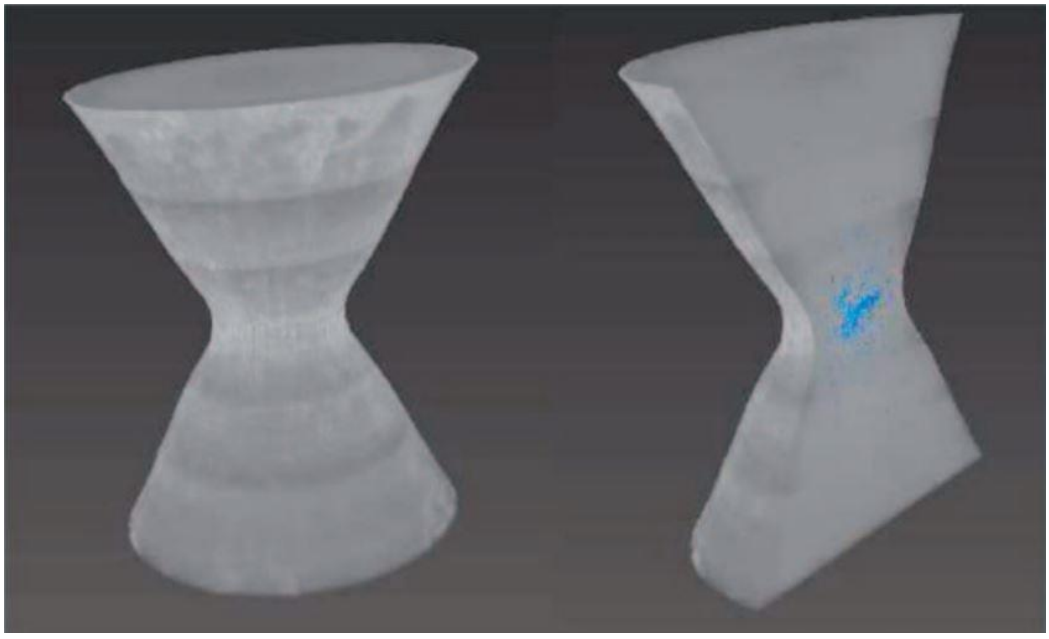

Figure 3.3 3D reconstruction of P91 steel sample tested at 1100℃, microvoids represented in light blue (Chiantoni et al., 2013).

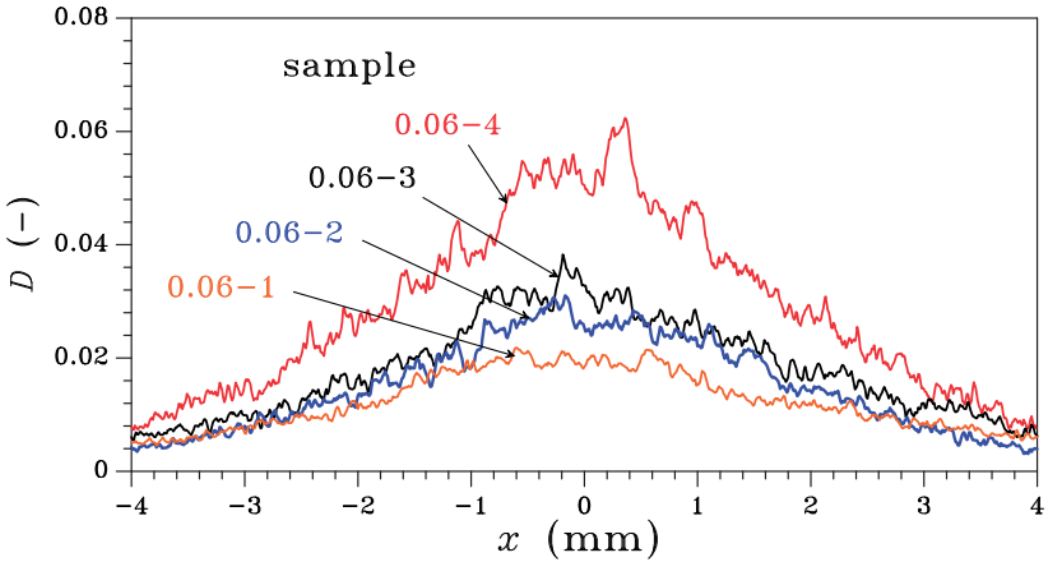

Figure 3.4 the mean damage profiles along the axes of P91 steel specimens (Chiantoni et al., 2013).

3.2.2 The observation of the evolution of cavity in CB8 steel (10.8%Cr) (2013)

The cavitation characterizing behaviour of a tempered martensitic steel CB8 (10.8%Cr) has been found to occur in the stress range of 120-150MPa at 600℃ by using 3D technology of X-ray micro-tomography (Gupta et al., 2013). The 3D reconstruction images obtained from SR-μCT scans on the CB8 samples tested on the stress range of 120-180MPa is shown in Figure 3.5.

Based on the quantitative analysis of creep void datasets obtained from the X-ray micro-tomography as shown in Figure 3.5, the variation of number density, void volume fraction and void size with initial applied stress is shown in Figure 3.6. As can be observed, cavitation characteristics undergo a transition as the number density of cavitation is reduced in the stress range 120-180MPa.

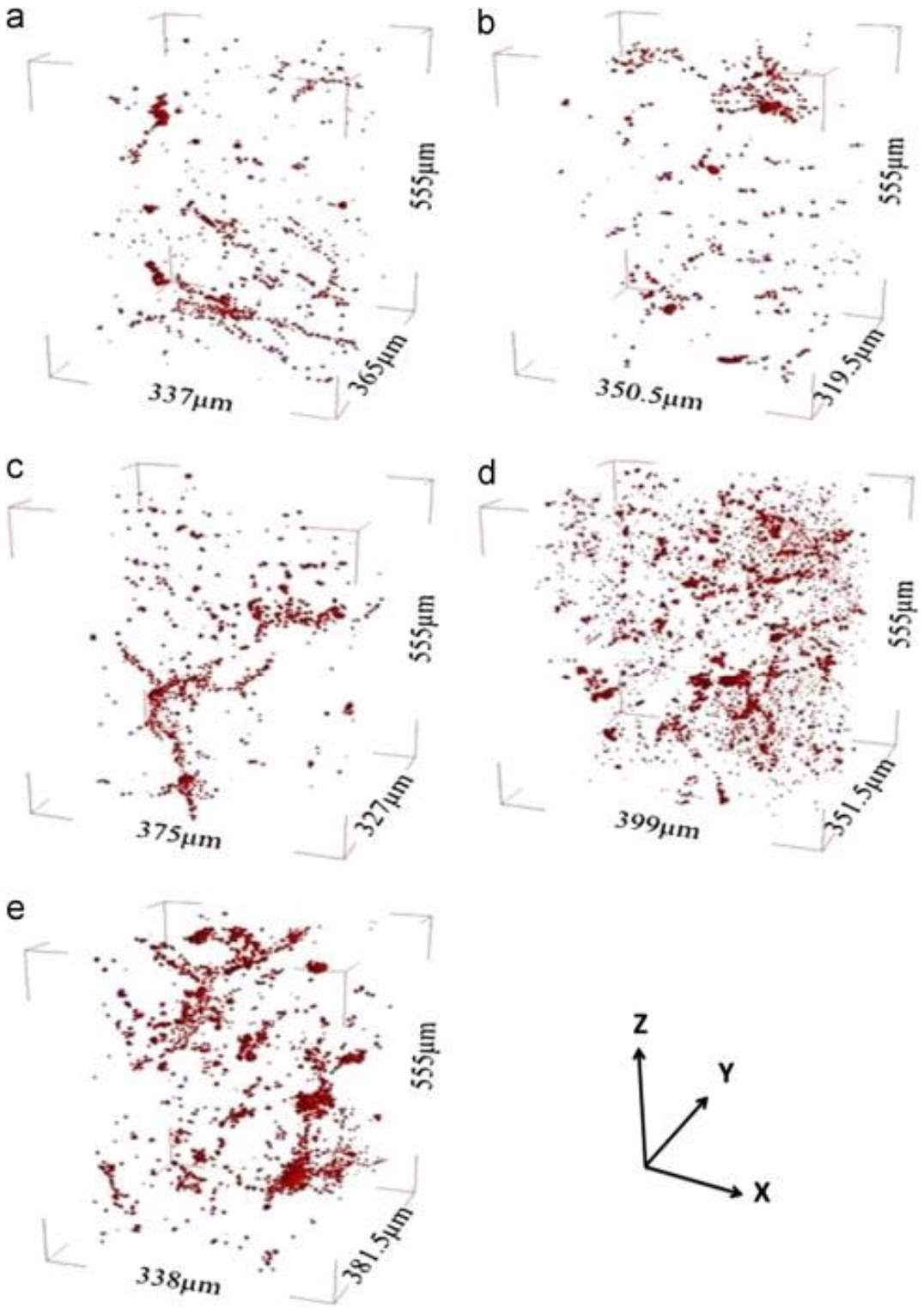

Figure 3.5 The 3D version of samples extracted from creep specimens by X-ray microtomography in different the stress ranges 120–180 MPa at 600 °C for CB8 steel (Gupta et al., 2013): (a) 180 MPa/2825 h, (b) 165 MPa/6779 h, (c) 150 MPa/15316 h, (d) 135 MPa/29466 h and (e) 120 MPa/51406 h.

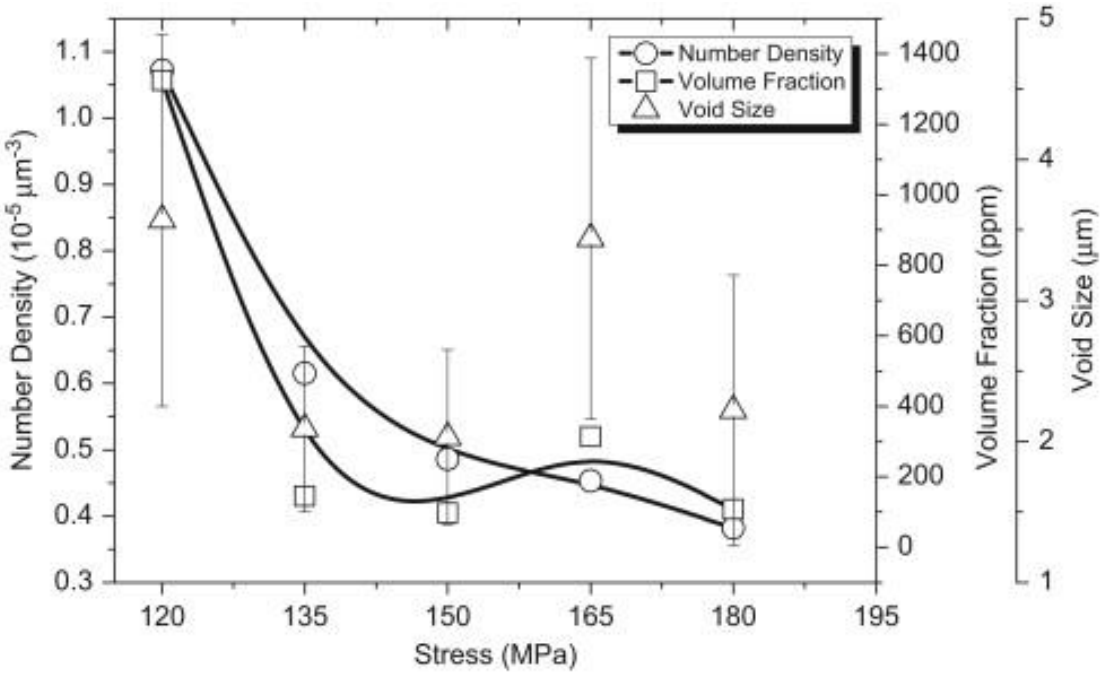

Figure 3.6 The variation of number density, void volume fraction and void size with different stress ranges 120–180 MPa at 600 °C for CB8 steel (Gupta et al., 2013).

The cavitation parameters (void volume fraction, v and number density, η) is dependent of rupture ductility, and the relationship between void volume fraction and number density with rupture ductility given below is based on a set data of experimental observations of cavities.

Void volume fraction of cavitation:

$$v = 165.76 + 6.7 \times 10^{8} \exp(-1.91\Lambda) \quad (3.2)$$

Number density of cavitation:

$$\eta = 0.399 + 7.0 \exp(-0.33\Lambda) \quad (3.3)$$

Where v=void volume fraction in ppm; η=number density in $10^{-5}\mu m^{-3}$; Λ=rupture ductility in %.

The evolution of the characterisation of cavitation has been explored by the 3D techniques of X-ray micro tomography and serial sectioning which has provided a new possible way to develop new models based on the quantified cavitation characteristics producing more accurate predictions of the creep life in the long-term and analysis of creep exposed high chromium steel.

3.2.3 Observation of the evolution of cavity in P91 steel (2014, 2015)

The creep tests of P91 steel under 60MPa at 650℃ were interrupted after 7000h and 9000h of testing. The characterisation of cavities has been studied and the spatial distribution of creep cavity is visualised in 3D reconstructed images as shown in Figure 3.7. These images were obtained from a field emission gun scanning electron microscope (FEG-SEM) equipped with focused ion beam (FIB) gun (Yadav et al., 2014).

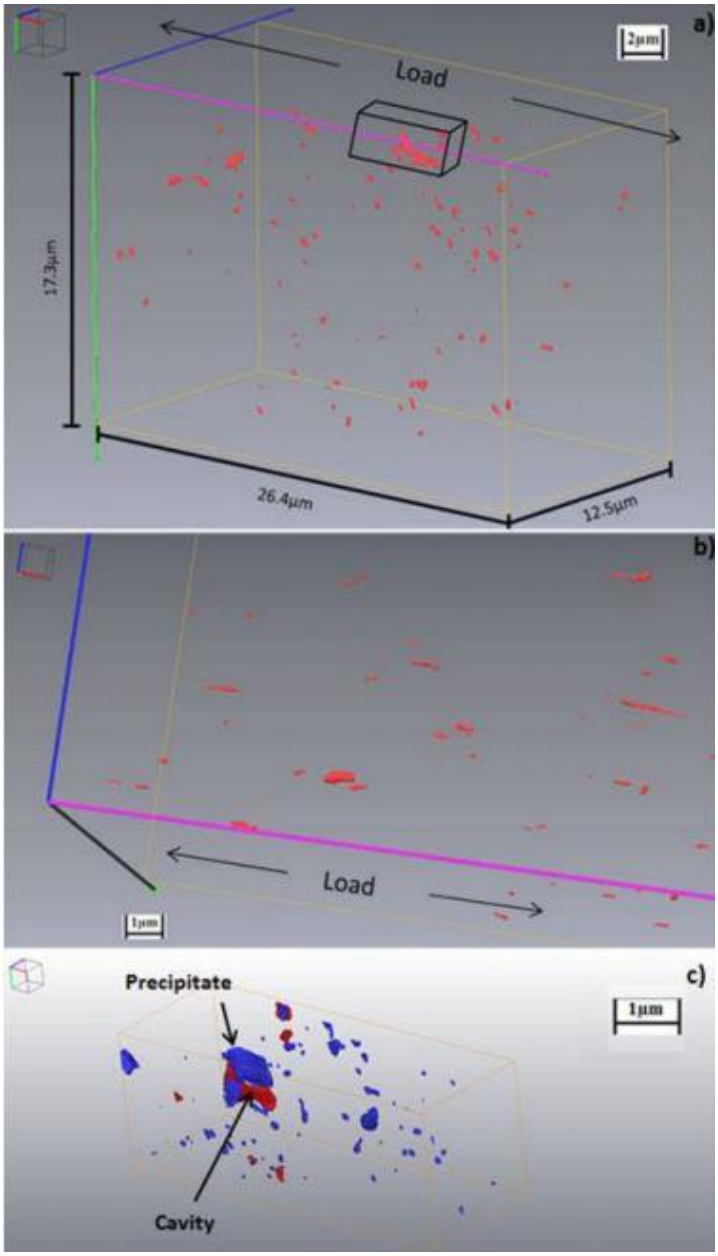

Figure 3.7 The 3D reconstruction of a specimen of 9%Cr steel crept for 9000h (Yadav et al., 2015).

The stereological quantitative methods for cavities of 9%Cr steel are presented below.

The number of cavities per unit volume:

$$(N_V)_j = \sum_i (N_A)_{i,j} / D_j \quad (3.4)$$

Where $\sum_i (N_A)_{i,j}$ is the number of sections of size i from cavities of all possible sizes per unit area, D_j is different size classes of cavity.

The total volume fraction of cavities

$$V = \sum_j V_j (N_V)_j \quad (3.5)$$

Where V_j is equal to $[\pi(D_j)^3/6]$, $(N_V)_j$ is the number of cavities per unit volume.

The number of big cavities per volume in different size classes of crept samples of P91 steel as received 7000h and 9000h under 60 MPa at 600℃ plots in Figure 3.8. According to the above stereological quantitative method, the volume fraction of cavities before (uncrept) and after (7000h, 9000h) creep test was calculated and is as shown in Table 3.5. It clearly indicates that the mean diameter and volume fraction of cavities was noticeably increasing along with the creep exposure time, during which the number of cavities per unit volume decreased. Therefore, the authors concluded that the growth and coalescence of pre-existing cavities was in need of further study (Yadav et al., 2015).

Table 3.5 The mean diameter, volume fraction and total number of cavities before and after creep (Yadav et al., 2015).

Specimen	Mean diameter(μm)	Volume fraction (%)	Total no.(mm^3)
Uncrept	2.56	0.11	4.95×10^4
7000h	3.99	0.27	3.95×10^4
9000h	5.42	0.47	2.77×10^4

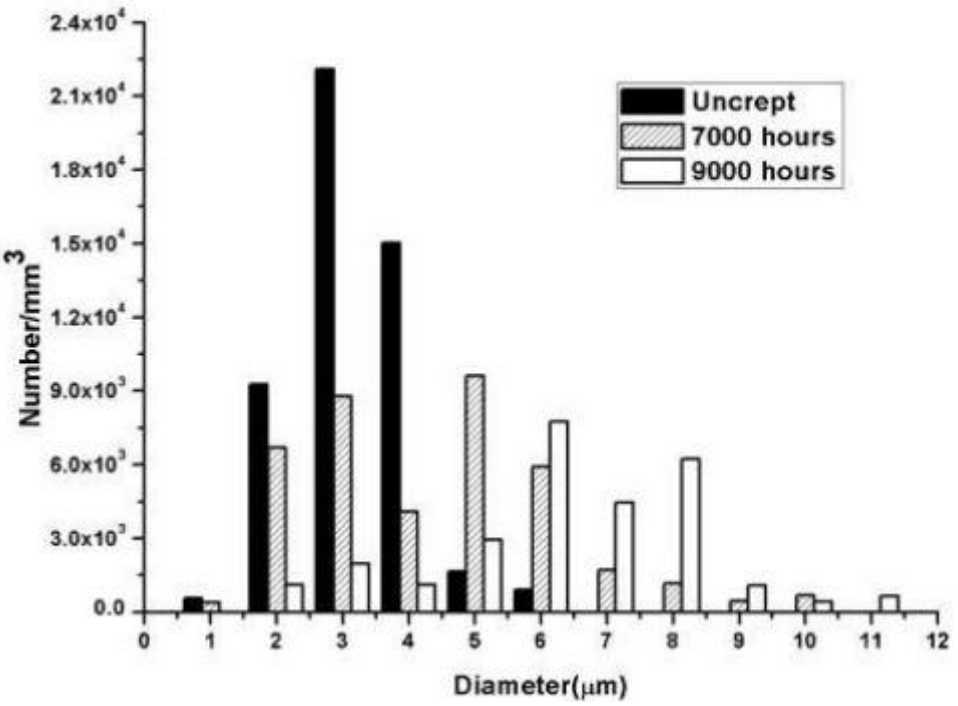

Figure 3.8 Number of big cavities per unit volume in (a) uncrept (b) 7000h (c) 9000h (Yadav et al., 2015).

3.2.4 The observation of the evolution of cavities in P92 steel (2014)

Using the electron backscatter diffraction (EBSD) method, creep cavitation damage formation for P92 under multiaxial stress was studied by Shigeyama et al. (2014). The laser microscopic images around notch tips showed creep voids are formed at the early stage and then increased leading up to the final fracture as shown in Figure 3.9. Void area fraction was measured with OLYMPUS OLS1100 (objective lens magnification: 650) at intervals of 500 mm as shown in Figure 3.10. After which, void area fraction was calculated using the equation

$$Void\ area\ fraction = \frac{Number\ of\ black\ pixels}{Total\ pixels} \quad (3.6).$$

Thus, the void area fraction changed with the creep life fraction around notched tip is shown in Figure 3.11.

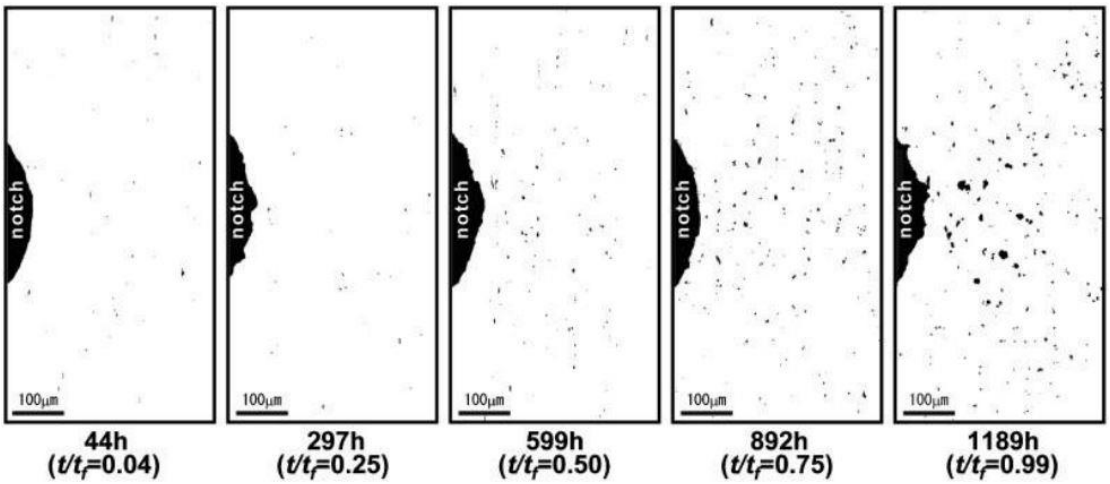

Figure 3.9 Laser microscopic images around notch tip for P92 steel at 600℃ under 14MPa (Shigeyama et al., 2014).

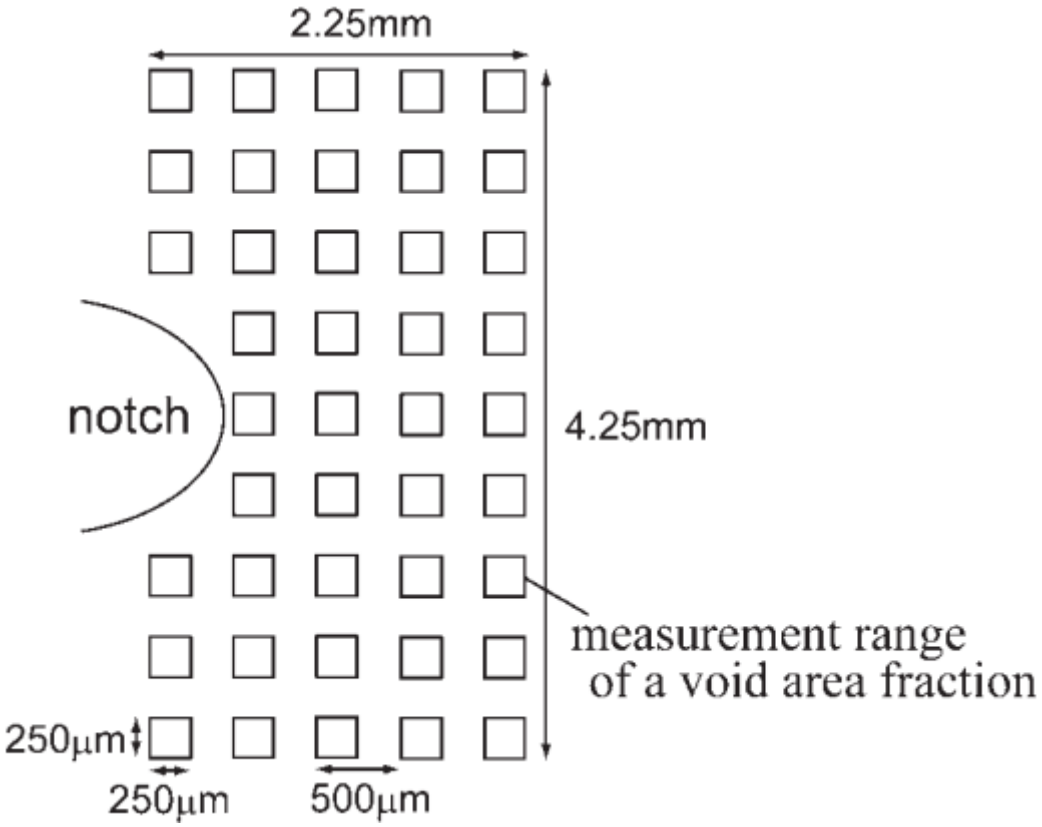

Figure 3.10 Measurement range of void area fraction (Shigeyama et al., 2014).

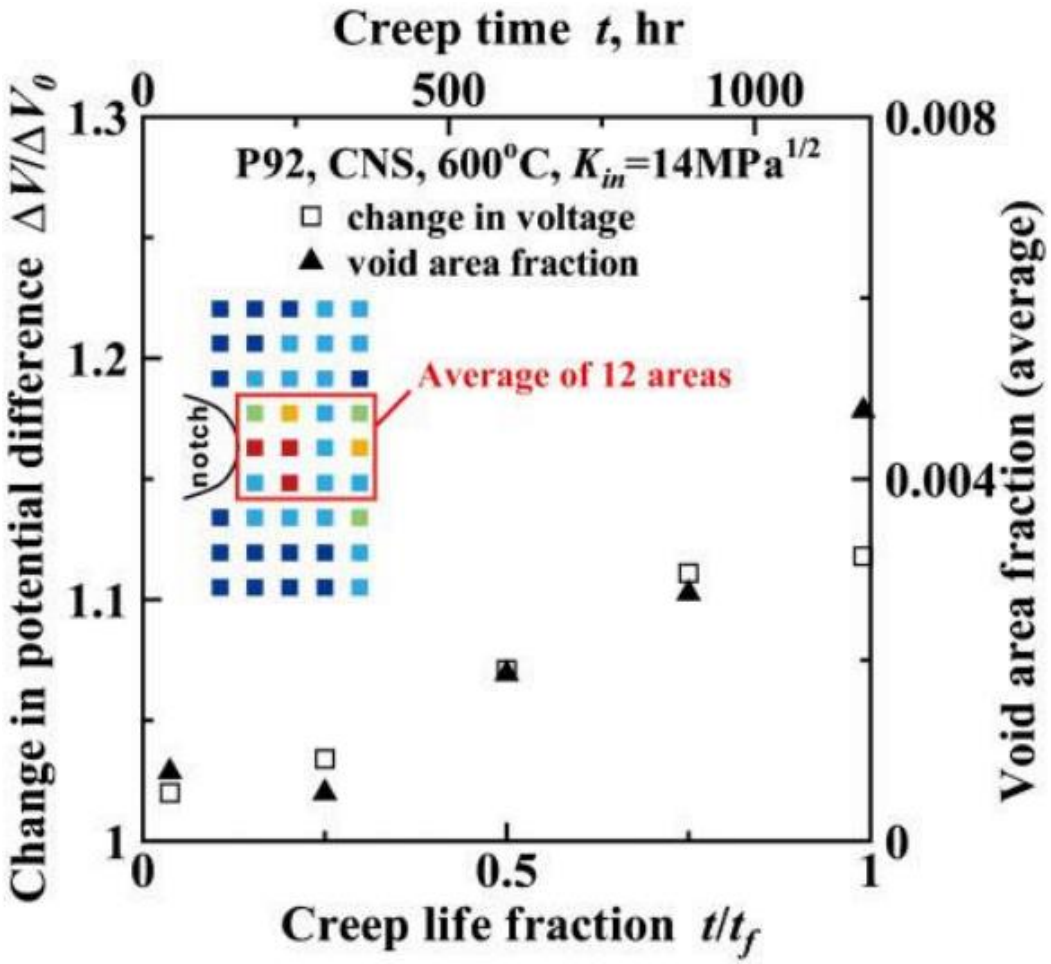

Figure 3.11 The change of potential difference and void area fraction under different creep life time (Shigeyama et al., 2014).

This research provides a reliable method to measure and calculate the evolution of creep damage and void fraction during creep expose. Creep voids were initiated at the early stage and continued forming up to the final fracture. The distribution of high void area fraction is in good agreement with that of high multiaxial stress and indicates that multiaxial stress affects the void formation (Shigeyama et al., 2014). However, there is still no function to describe the process of cavitation damage with exposure time for the modelling of constitutive equations.

3.2.5 The observation of the evolution of cavity in P91 and E911 steel (9wt. % Cr steel) (2010, 2014)

Two flat hollow cylinders made of martensitic 9wt.% Cr steel, ASTM steel Grades P91 and E911 were creep deformed under in-service conditions typical steam pipes at fossil-fuel fired power plants given in below Table 3.6 (Sket et al., 2010) (Renversade et al., 2014).

Table 3.6 Creep testing conditions: temperature (T), axial stress $(\sigma_{a)}$, internal pressure (P), creep time (t) and minimum strain-rate $(\dot{\varepsilon}_{min})$ (Sket et al., 2010) (Renversade et al., 2014).

$Material$	T(℃)	$\sigma_a(MPa)$	$P(MPa)$	$t(h)$	Specimen for tomographic measurements (Figure 3.12, 3.13)
$P91$	575	52.6	23.6	10,200(tertiary creep regime)	0.6mm in diameter, 2mm in length
E911	600	48.9	17.7	37,800(tertiary creep regime)	0.6mm in diameter, 2mm in length
E911	575	61.8	17.5	26,000(~80% lifetime)	0.6mm in diameter, 2mm in length

Based on the X-ray tomographic of the spatial distribution of voids in P91 and E911 reconstructions (Renversade et al., 2014) (Sket et al., 2010) as shown in Figure 3.12 and Figure 3.13, respectively, and the qualitative analysis results of void density indicated along the notch wall surface showing in Figure 3.14 and Figure 3.15, respectively. Thus, the high resolution of micro-tomographic reconstructions of characteristic cavities could provide quantitative analysis of the void spatial distribution as well as void shape, the equivalent diameter, number density and area fraction of voids, and then, a scientific and convincing

function describing the cavitation damage of nucleation and growth may be developed.

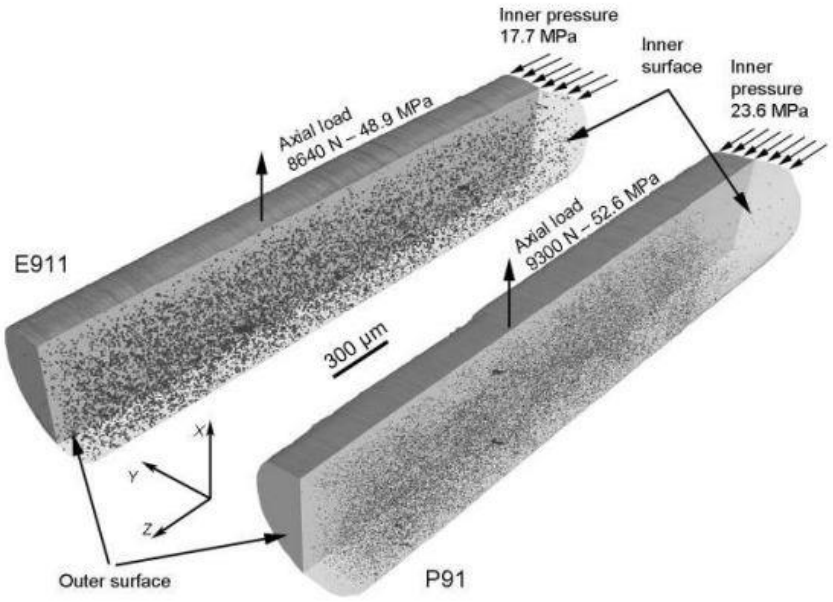

Figure 3.12 The X-ray tomographic reconstruction of void spatial distribution for E911 and P91 steels at 37800h and 10200h (Renversade et al., 2014).

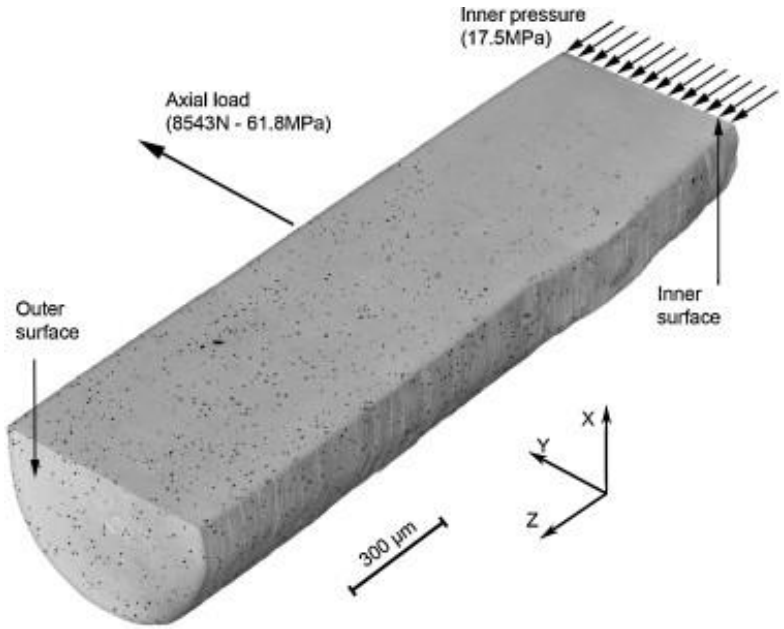

Figure 3.13 The X-ray tomographic reconstruction of void spatial distribution for E911 steel at 26000h (Sket et al., 2010).

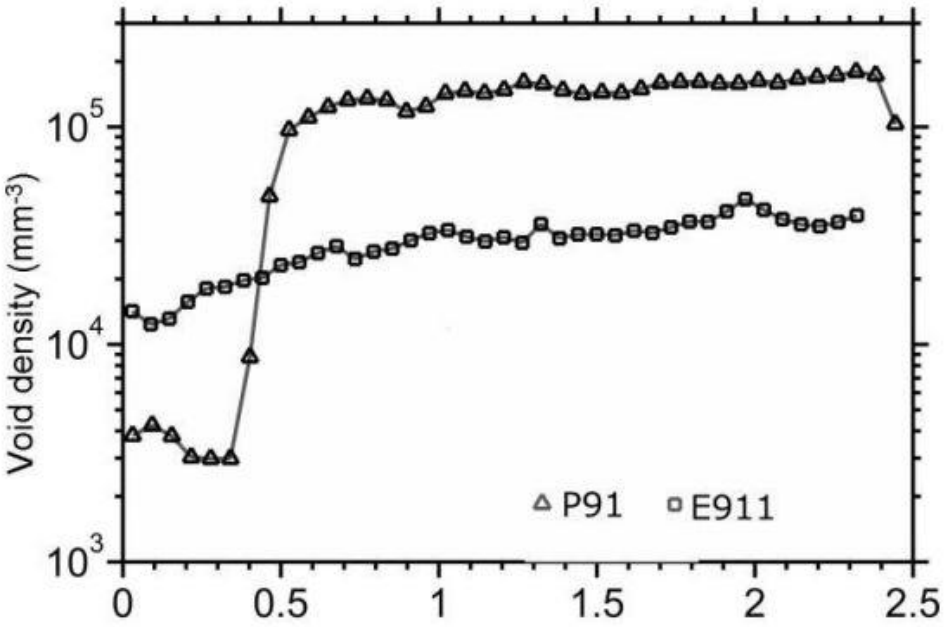

Figure 3.14 The qualitative analysis results of void density indicated along the notch wall surface for both P91 and E911 (Renversade et al., 2014).

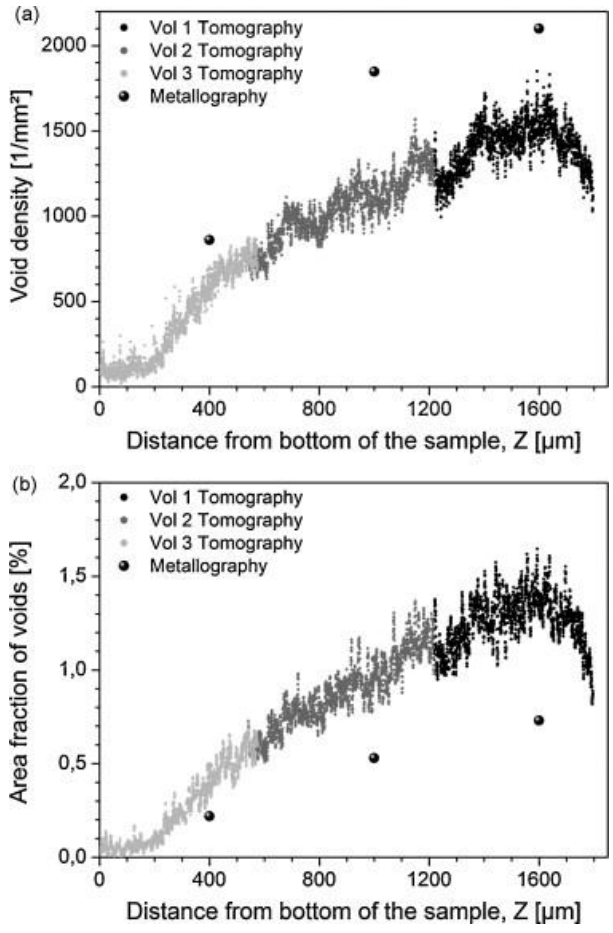

Figure 3.15 The qualitative analysis results of void density indicated along the notch wall surface for both P91 and E911 (Sket et al., 2010).

Chapter 4 Modified function of minimum creep rate and applied stress for creep damage constitutive equations for high chromium steel

The function of minimum creep rate and stress is one of the many features belonging to the creep damage constitutive equations, thus its accuracy is an important factor for the development of the creep damage constitutive equations. This section will introduce the development process of the modified hyperbolic sine law for describing the relationship of minimum creep rate and applied stress for low chromium steel. Based on successful application of the modified hyperbolic sine law for low chromium steel, this research will try to apply the modified function for long-term creep service of high chromium steel under a wide range of stress levels and compare the modelling results of the modified hyperbolic law with conventional functions and experimental data in order to check its feasibility for high chromium steel.

4.1 The application of the modified hyperbolic sine function of the relationship between minimum creep rate and applied stress for low chromium steel

The conventional hyperbolic sine function of minimum creep rate and stress (Kowalewski et al., 1994) (Perrin & Hayhurst, 1996) (Dyson & Mclean, 1998, 2001) (Dyson, 2000), as shown in equation (2.2), was applied to low chromium steel (2.25Cr-1Mo alloy); the modelling result of conventional hyperbolic sine law was demonstrated in Figure 4.1 (Xu, 2016) and mostly agreed with experimental data. However, its application to 0.5Cr-0.5Mo-0.25V alloy steel was not very satisfactory, and did not fit with experiment as shown in Figure 4.2 (Xu, 2016).

$$\dot{\varepsilon}_{min} = Asinh(\mathrm{B}\sigma) \quad (2.2)$$

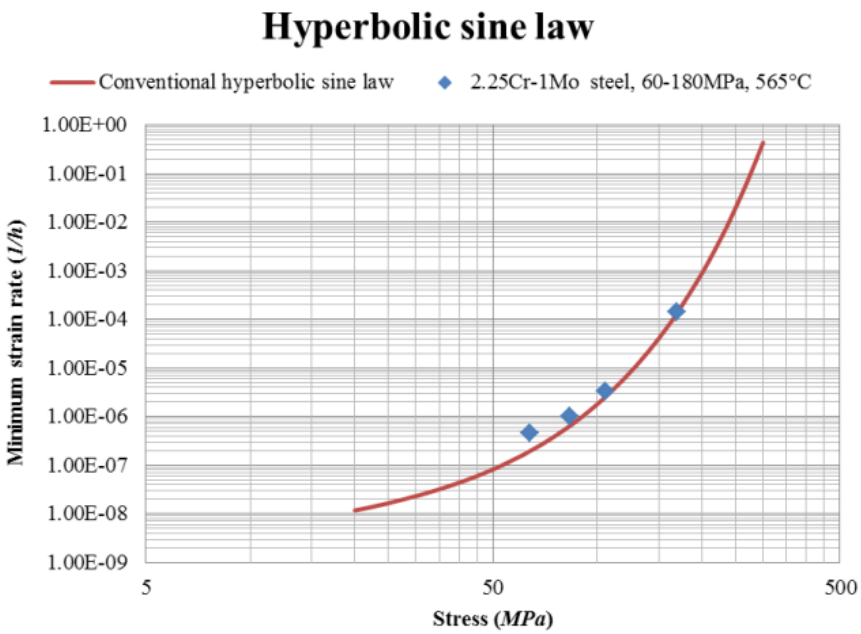

Figure 4.1 Comparison of conventional hyperbolic sine law with experimental data of 2.25Cr-1Mo steel (Xu, 2016).

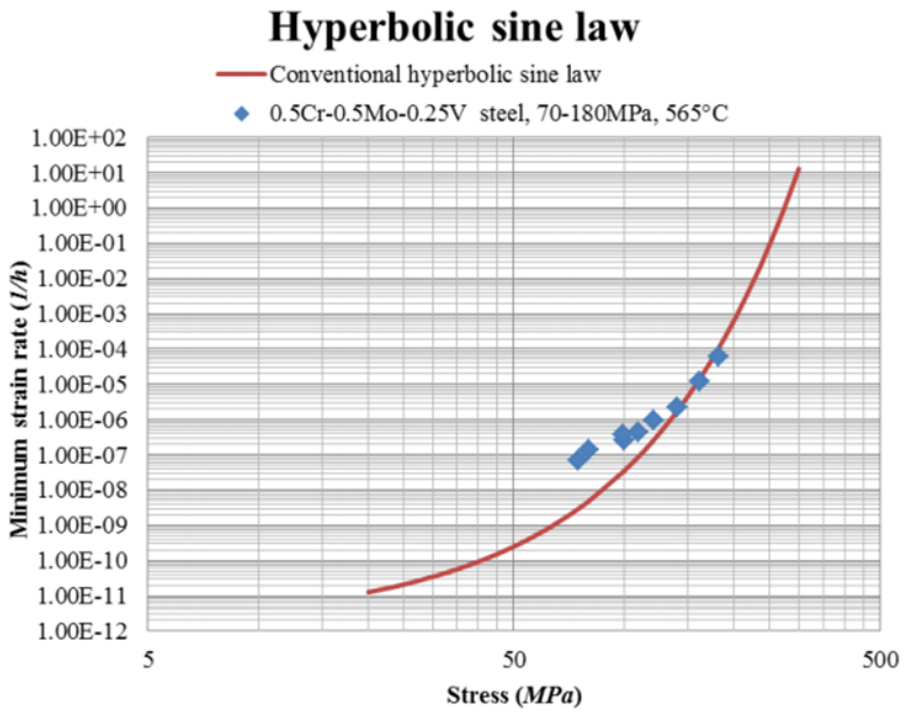

Figure 4.2 Comparison of conventional hyperbolic sine law with experimental data of 0.5Cr-0.5Mo-0.25V steel (Xu, 2016).

As the hyperbolic sine function was the most promising one among all the existing functions, and its application did not produce satisfactory fitting. The above exercise and other fittings with all the main existing functions attempted by Qihua Xu (Xu, 2016) did demonstrate again the incapability of all the existing functions, which has been well known for, at least more than 15 years for the research community. This has been a worldwide need for the development of better function to do so.

In order to resolve this problem, the idea of modified hyperbolic sine function (equation 2.4) was proposed by Qiang Xu (Xu, 2016), and it was successfully applied by Xu (Xu, 2016) to low chromium steel, which can be seen from Figure 4.3 and Figure 4.4.

$$\dot{\varepsilon}_{min} = Asinh(B\sigma^{q}) \ (2.4)$$

The modified hyperbolic sine law had been successfully applied to both 0.5Cr-0.5Mo-0.25V alloy steel and 2.25Cr-1Mo alloy steel with material parameters in Table 4.1, of which the modelling results are displayed in Figure 4.3 and Figure 4.4, respectively (Xu, 2016), both of which indicated that the modified version of the hyperbolic sine function was much more superior than the conventional hyperbolic sine function used in experiment of low chromium alloy steel. Thus, this research will try to apply the modified function of minimum creep strain rate and applied stress for a long-term service of high chromium steel in a wide range of stress levels in the next section 4.2.

Table 4.1 Material parameter of modified hyperbolic sine function for low chromium steel (Xu, 2016).

$Material$	A (MPa/h)	$B(\mathrm{MPa}^{-1})$	q
0.5Cr−0.5Mo−0.25V steel	4.12×10^{-8}	2.51×10^{-4}	2
$2.25Cr-1Mo\ steel$	5.57×10^{-7}	2.4×10^{-4}	2

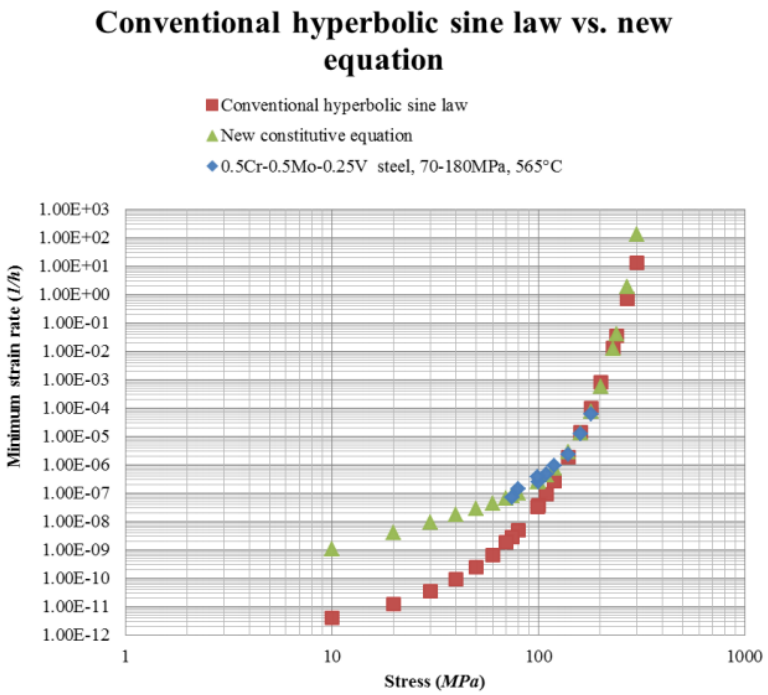

Figure 4.3 Comparison of modified hyperbolic sine law with conventional one and experimental data for 0.5Cr-0.5Mo-0.25V steel (Xu, 2016).

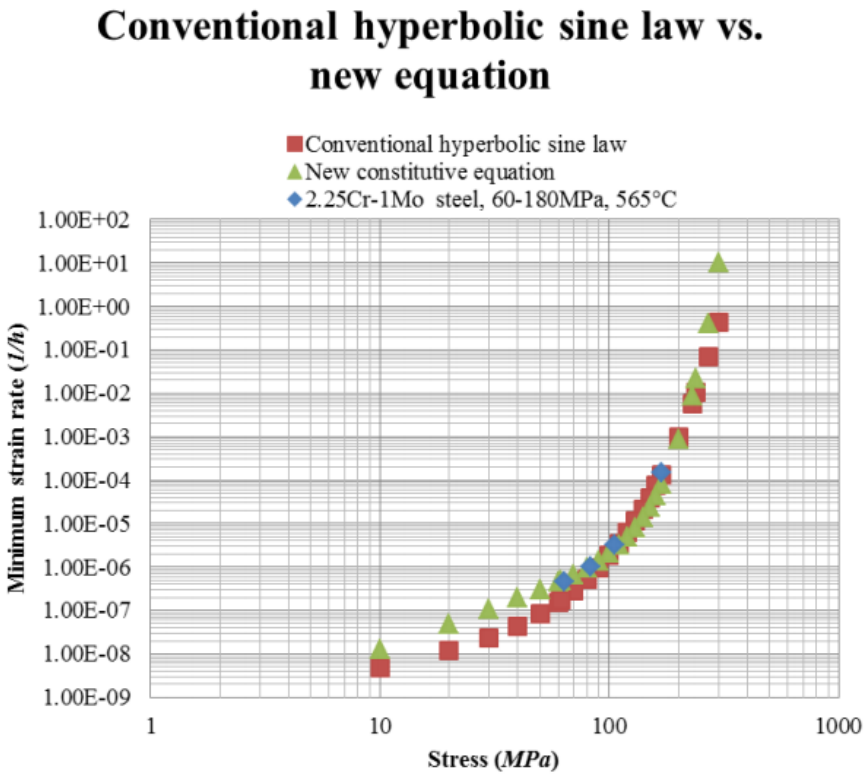

Figure 4.4 Comparison of modified hyperbolic sine law with conventional one and experimental data for 2.25Cr-1Mo steel (Xu, 2016).

4.2 The application of the modified hyperbolic sine law for describing the relationship of minimum creep rate and applied stress for high chromium steel

Several typical functions of creep minimum stain rate and stress were simply introduced in section 2.2 and summarized below in Table 4.2. This section will try to apply the modified function for long-term creep service of high chromium steel under a wide range of stress levels and compare the modelling results of the modified hyperbolic law with conventional functions and experimental data in order to check the feasibility for high chromium steel.

Table 4.2 The typical functions of minimum creep strain rate and stress (Altenbach, 1999) (Gorsah, 2008) (Holdsworth, 2008).

Power law creep (Norton, 1929) (Bailey, 1930)	$\dot{\varepsilon}_{min} = A\sigma^n$ (2.1)
Linear +power law (Altenbach et al., 2008) (Naumenko et al., 2009)	$\dot{\varepsilon}_{min} = A\sigma[1 + (B\sigma)^n]$ (2.3)
Hyperbolic sine law (Dyson & Mclean, 1997, 2001) (Dyson, 2000)	$\dot{\varepsilon}_{min} = Asin\,\mathrm{h}(\mathrm{B}\sigma)$ (2.2)

The specific data of creep test for P91 (9Cr-1Mo-V-Nb) steel for this research was taken from already published creep data sheets (NIMS, 2014) as shown in Table 3.3 and Table 3.4 that had been collected in chapter 3 and the relationship of stress and minimum creep rate is plotted in Figure 4.5 and Figure 4.6.

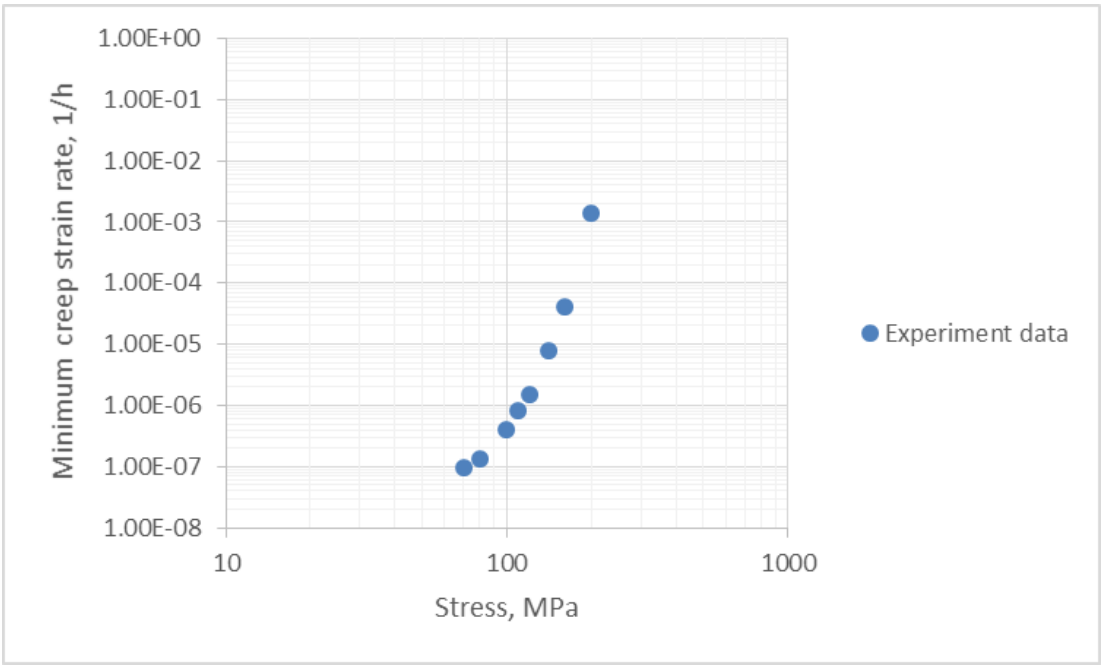

Figure 4.5 Experimental data of minimum creep strain rate and stress for P91 steel at 600℃ under 70-200MPa (NIMS, 2014).

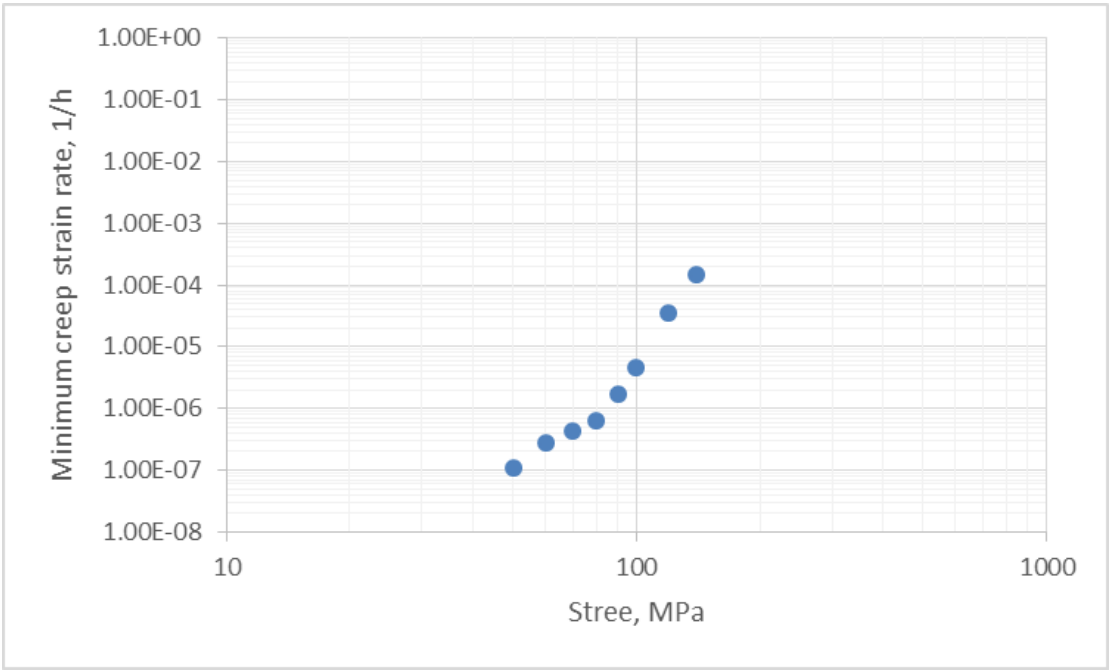

Figure 4.6 Experimental data of minimum creep strain rate and stress at 625℃ under 50-140MPa (NIMS, 2014).

The values of stress exponent n in equation (2.1) are changing under different temperatures as shown in Figure 4.7 (Kimura et al., 2009) and Figure 4.8 (Swada et al., 2001) and decreasing with the decrease of stress σ from 12 to 1 at different stress levels for P91 steel as shown in Figure 4.9 (Sklenička et al., 2003). Figure 4.7 and Figure 4.8 clearly indicated that the stress exponent n as constantly reduces when temperature increases, and it would be possible to get a function $n\ (\sigma, T)$ with interpolating more data, Dyson and Mclean (2001) thought it would be unwise to use the function $n\ (\sigma, T)$ for extrapolation.

As a known stress exponent $n = (\partial \ln \dot{\varepsilon} / \partial \ln \sigma)$, the stress exponents are a function of creep strain under constant stress (σ) and temperature (A) in Figure 4.8. Thus, it is necessary to develop a power-law function that as a variety of stress levels, temperature and minimum creep strain. The similar description of the disadvantage of power law creep equation was summarized by Dyson and Mclean for super alloy:1) it was limited to a range of stress levels and temperatures in ferritic steels and nickel-based super alloys using power-law formulation for describing creep rates; 2) the effects of materials ageing on creep resistance could not be modelled by a certain mechanism; 3)the simple model could not be adequately quantified over large stress levels and temperature ranges(Dyson, 2000) (Dyson & Mclean, 2001).

The other disadvantage in existing creep damage power law is that it is limited for finite element calculation. Currently, application of Finite Element Numerical Analysis (FEA) calculated software calculation with mostly hyperbolic sine law equation for low chromium steel (Qiang Xu, 2001, 2004) (Xu & Barrans, 2003) and high chromium steel (Hyde et al., 2006) (Pétry & Lindet, 2009).

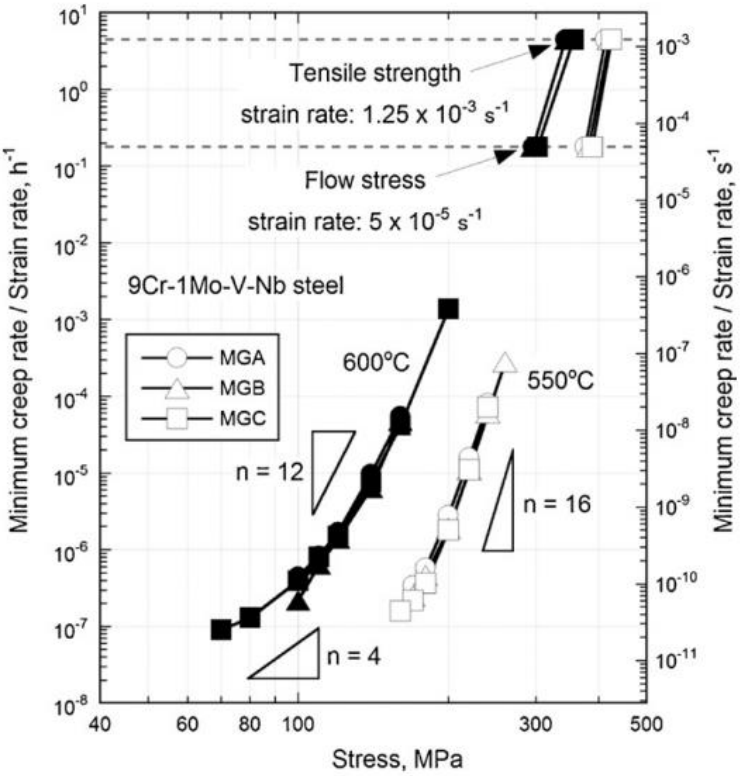

Figure 4.7 The relationship function between minimum creep strain rate and stress of P91 steel at various temperatures (Kimura et al, 2009).

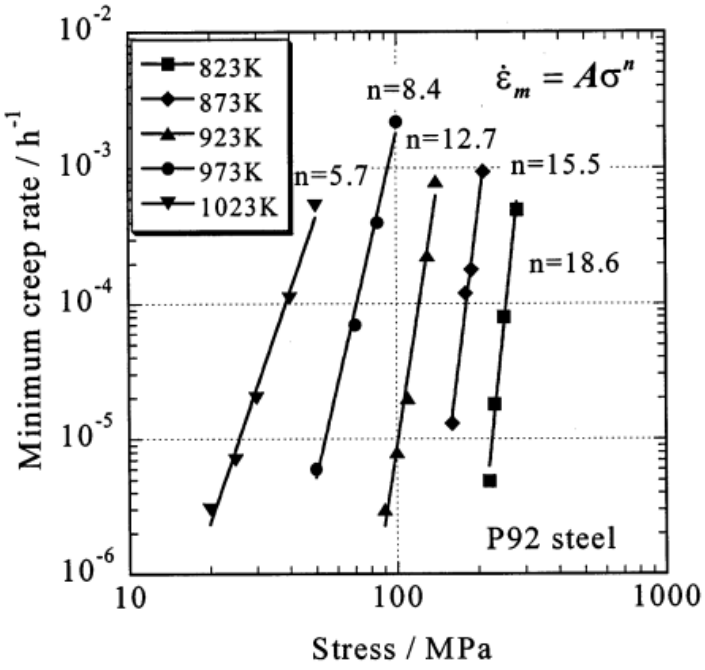

Figure 4.8 The relationship function between minimum creep strain rate and stress of P92 steel at various temperatures (Sawada et al., 2001).

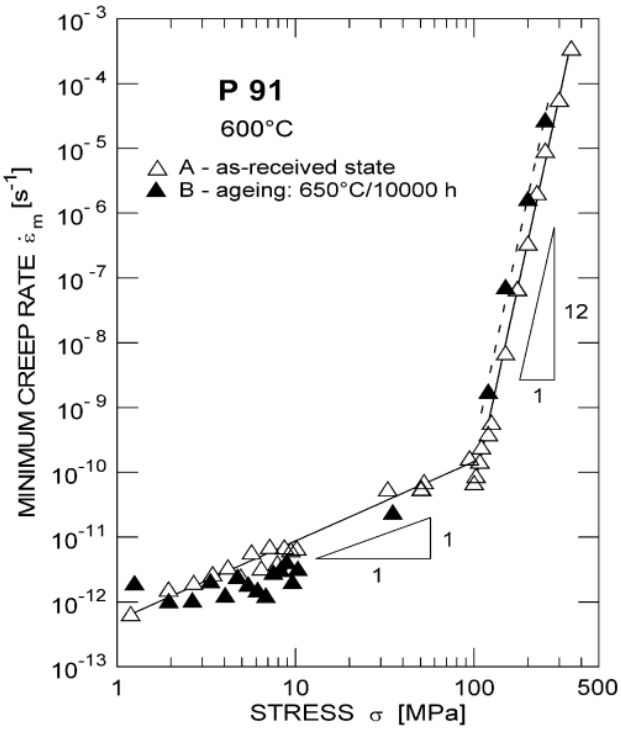

Figure 4.9 Steady state creep rate versus applied stress for P91 (Sklenička et al., 2003).

The modelling results of conventional hyperbolic sine law and 'linear power law' with the calibrated material parameters presented in Table 4.3 are re-produced as shown in Figure 4.10 and Figure 4.11 (Gorash, 2008). It reveals that the modelling results do not fit well with the experiment data on P91 steel.

Table 4.3 Material parameter A and B for conventional hyperbolic sine law and 'linear power law' using applied to P91 steel.

$Functions$	A	B	n
Conventional sine law	$4.5 \times 10^{-8}(1/h)$	$5 \times 10^{-2}(MPa^{-1})$	$-$
Linear power law	$2.5 \times 10^{-9}(MPa^{-1}/h)$	$-$	12

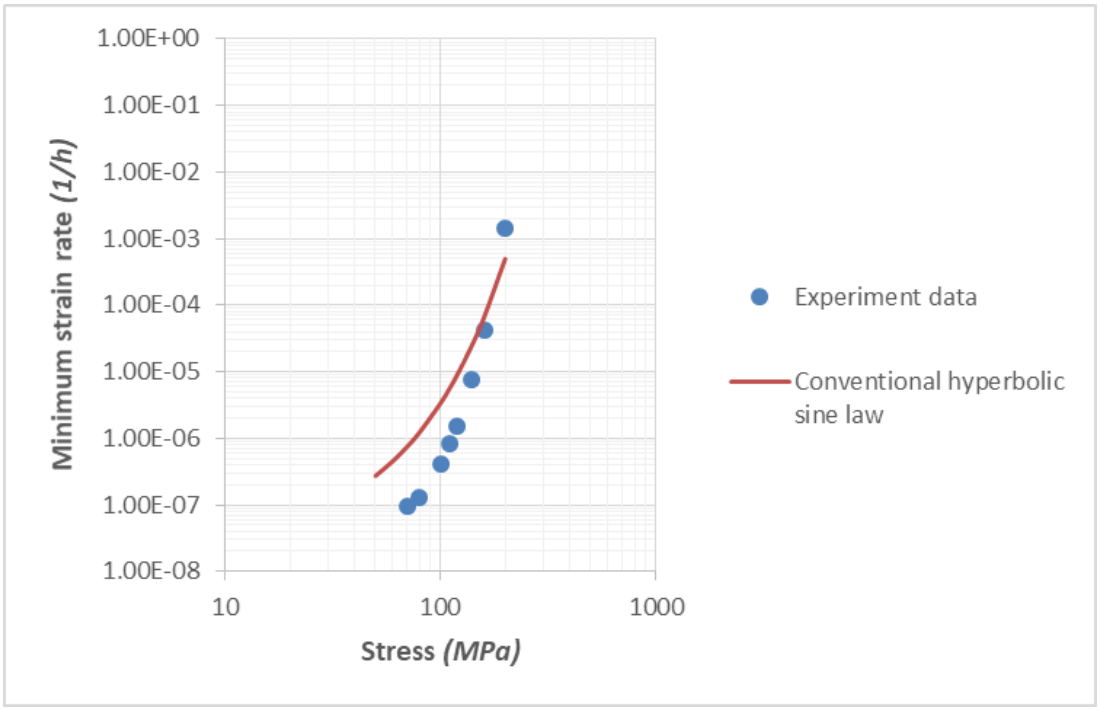

Figure 4.10 The modelling result of conventional hyperbolic sine law compares with experimental data of P91 steel 600℃.

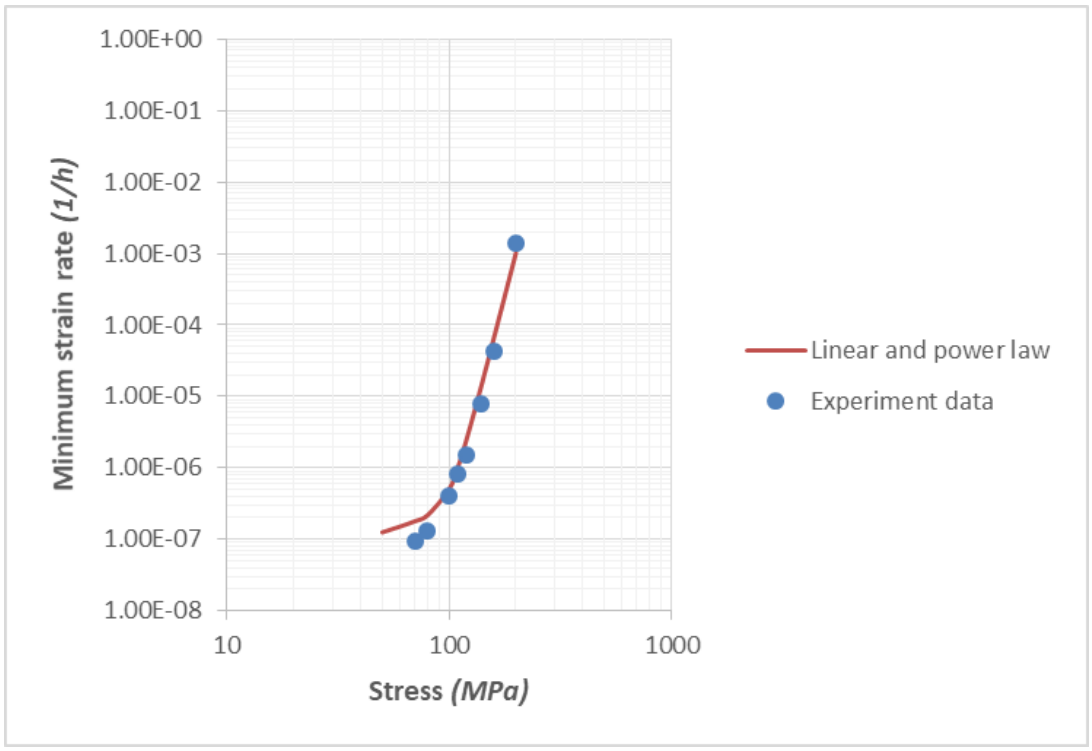

Figure 4.11 The modelling result of linear and power law compares with experimental data of P91 steel at 600℃.

The modified hyperbolic sine law, $\dot{\varepsilon}_{min} = Asinh(B\sigma^q)$, was applied to low chromium steel by Xu (2016), and in this research the law has been applied to P91 steel. The modelling result of the modfied hyperbolic sine law is plotted in Figure 4.12 for P91 at 600℃ with the calibrated material parameters as shown in Table 4.4. A good agreement for both the modelling results of modifed hyperbolic sine law and experimental data was achieved for long-term service of P91 steel. It is clearly indicated that the modified hyperbolic sine law fitted better with experimental data than the conventional sine law and 'linear + power' law for high chromium steel as shown in Figure 4.13. The modifed model had also been applied to P91 at 625℃ with the calibrated material parameters as shown in Table 4.5. The modelling result is in agreement with experimental data of P91 at 625℃ as shown in Figure 4.14. Thus, the modified hyperbolic sine law of minimum creep rate and applied stress will be taken into account when forming a new creep damage constitutive equations for high chromium steel.

Table 4.4 The calibrated material parameters for the modified hyperbolic sine law for P91 steel at 600℃.

$Material\ parameter$	A	B	q
$Unit$	MPa/h	MPa^{-1}	$-$
$Value$	5.46×10^{-8}	2.712×10^{-4}	2

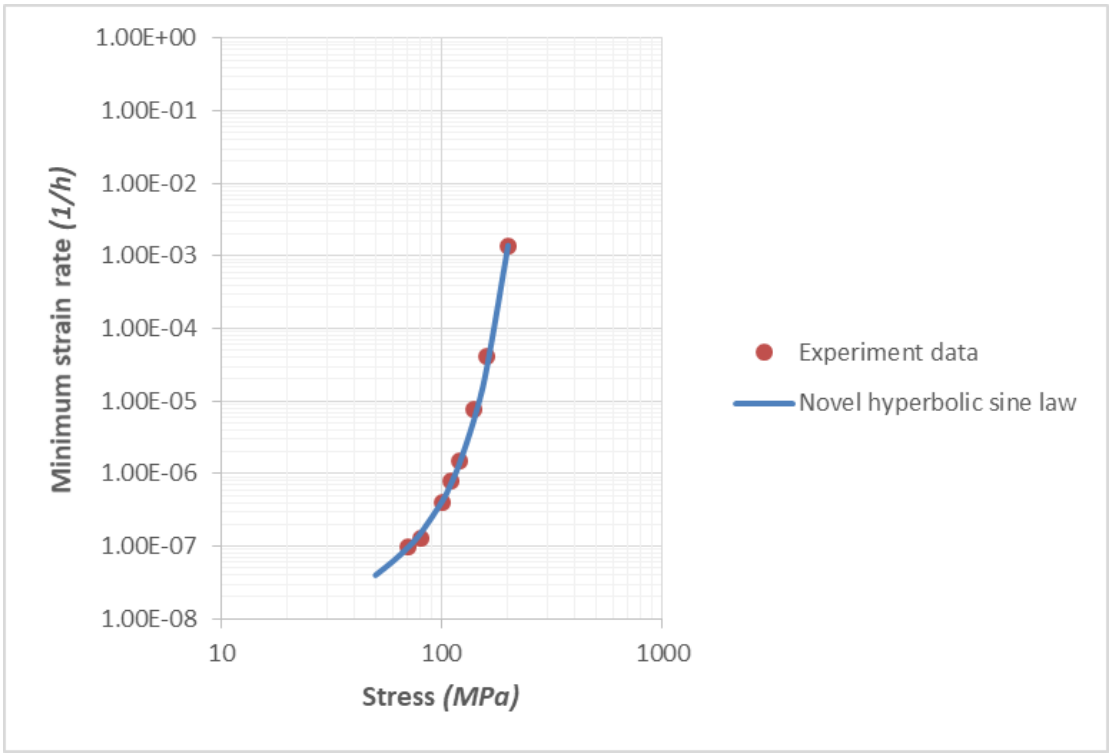

Figure 4.12 The modelling result of modified hyperbolic sine law compared with experimental data of long-term serviced P91 steel at 600℃.

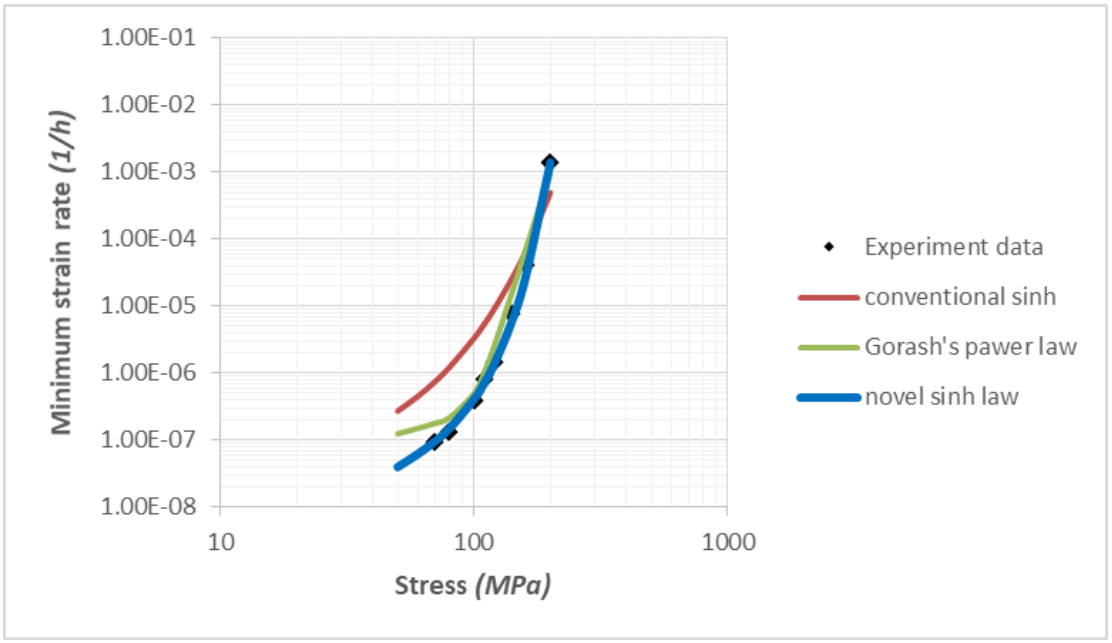

Figure 4.13 The comparison of different functions of minimum creep strain rate and applied stress.

Table 4.5 The calibrated material parameters for the modified hyperbolic sine law for P91 steel at 625℃.

$Material\ parameter$	A	B	q
$Unit$	MPa/h	MPa^{-1}	$-$
$Value$	7.89×10^{-8}	4.68×10^{-4}	2

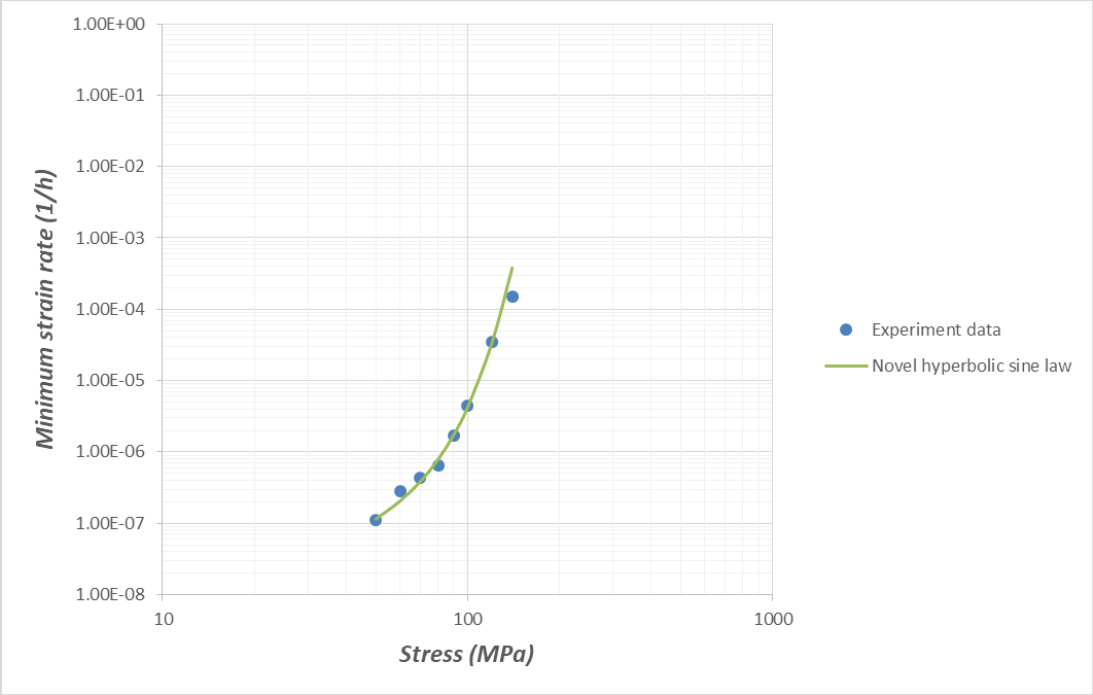

Figure 4.14 The modelling result of modified hyperbolic sine law compared with experimental data of long-term serviced P91 steel at 625℃.

Chapter 5 Development of a novel creep cavitation damage equation based on cavity area fraction along grain boundary for high chromium steel

There are a few well-known and unresolved problems in creep damage mechanics research community (Xu, Lu and Wang, 2017), and this research made one significant progress and one breakthrough:

1) Better creep strain rate and stress level function: modified hyperbolic sine law was conceived by Qiang Xu (Xu, 2016). It was applied to low chromium steel by Qihua Xu (Xu, 2016) and high chromium steel by Xin Yang in section 4.2. The work has contributed to a keynote presentation of an international conference (Xu, Yang and Lu, 2017a) and an academic journal publication (Xu, Yang and Lu, 2017b);

2) Grain boundary cavity based creep rupture criterion and its application: this is the first, in the world, to develop a scientific sound for creep rupture criterion using the advanced X-ray synchrotron cavitation data. It is expected that this approach will be adopted by the research community in time. The work has contributed to key note presentation (Xu, Yang and Lu, 2017a) and an academic journal publication (Xu, Yang and Lu, 2017b).

This chapter will develop a novel cavitation damage constitutive equation for describing the evolution of cavitation in creep process of high chromium steel for constitutive equation modelling based on the creep test experimental data of cavitation damage observation for high chromium steel in chapter 3. Thus, the four targets below shall be covered in this chapter:

1. To introduce Riedel's theory of cavity size distribution function for cavity nucleation and growth on grain boundary area, which is the theoretical foundation for the analysis of experimental data;

2. Based on the collection and analysis of experimental data of the cavitation characterization of high chromium steel in section 3.2 of chapter 3, we found that a novel creep cavitation damage equation needs to describe the evolution of cavitation along grain boundary in the creep process for high chromium steel based on the Riedel's theory of the cavity size distribution;
3. The fracture criterion for the novel creep damage constitutive equation and compare it with traditional ones;
4. Identify the material parameters for the novel creep cavitation equation for high chromium steel;
5. To provide supporting evidence for the novel cavitation damage equation for high chromium steel.

5.1 Basic theory of Riedel's cavity size function for cavity nucleation and growth on grain boundary area

There is a link between experimental data and theories on cavity nucleation and growth with the cavity size distribution function is denoted by $N(R,t)$, where NdR is the number of cavities per unit grain boundary area in the changing of radii between R and $R+dR$ (Riedel, 1987).

As proposed by Riedel (1985), if the late stages of the creep rupture process ignored the cavity coalescence and cavities growth from one size, R, to the next size, $R+dR$, the distribution function must continue in size space

$$\dot{N}+\frac{\partial(N\dot{R})}{\partial R}=0 \quad (5.1)$$

where the superposed dot indicated the time derivative and $\dot{R}(R,t)$ is the growth rate of cavities with a radius R at time t. The growth of cavity which is time dependent, stems from its dependence on the cavity spacing, which decreases continuously with more cavities nucleated. Cavity nucleation takes into the form of a boundary condition to equation (5.1): the flux size space, $N\dot{R}$, will be set equal to zero at some small radius, and must be equal to a prescribed cavity nucleation rate (Riedel, 1987):

$$N\dot{R}=J^{*}\ at\ R=0 \quad (5.2)$$

Equation (5.1) and (5.2) have a more general class solutions while the cavity growth rate and the nucleation rate have been formed by the power-low formulation (Riedel, 1987):

$$\dot{R} = A_1 R^{-\beta} t^{-\alpha} \quad (5.3)$$

$$J^* = A_2 t^{\gamma} \quad (5.4)$$

where A_1, A_2, α, β and γ are material constants and may possibly depend on stress and strain rate, they, however, do not depend upon time or the cavity size. Because the equations (5.1) and (5.2) in the power law functions have same similar solutions in the form $N(R,t) = t^P f(R/t^Q)$. If $Q = (\alpha - 1)/(\beta + 1)$ and $P = \beta Q + \alpha + \gamma$, the equation f is dependent on the co-ordinary R/t^Q. The ordinary differential equation for $f(R/t^Q)$ can be solved by separating of the variables. The final function of the cavity size distribution:

$$N(R,t) = \frac{A_2}{A_1} R^{\beta} t^{\alpha+\gamma} \left(1 - \frac{1-\alpha}{1+\beta} \frac{R^{\beta+1}}{A_1 t^{1-\alpha}}\right)^{\frac{(\alpha+\gamma)}{(1-\alpha)}} \quad (5.5)$$

The cavitated area fraction on grain boundaries, *w,* is obtained by integrating the areas which have orientations between $60°$ and $90°$ to the tensile axis, πR^2, occupied by the individual cavities times their density, NdR(Riedel, 1987):

$$w = \int \pi R^2 N(R,t) dR$$

$$= I(\alpha,\beta,\gamma) A_2 A_1^{\frac{2}{\beta+1}} t^{\alpha+\gamma+\frac{(1-\alpha)(\beta+3)}{\beta+1}} \quad (5.6)$$

where $N(R,t)$ calculated from equation (6.5), and the dimensionless factor $I(\alpha,\beta,\gamma)$ is the definite integral

$$I = \pi(1+\beta)^{(\beta+3)/(\beta+1)} \int_0^U x^{\beta+2} [1-(1-\alpha)x^{\beta+1}]^{(\alpha+\beta)/(1-\alpha)} dx \quad (5.7)$$

where I is independent of A_1, A_2, and t.

5.2 Experimental foundation of cavity size distribution along grain boundary in high chromium steel for novel cavitation damage equations

Based on the experimental observation of characteristic cavitation in high chromium steel in chapter 4, the distribution of void sizes function equation (5.5) proposed by Riedel fitted well with the experimental data of the histogram density functions of void equivalent R of E911 and P91 steels showing in Figure 5.1 and Figure 5.2 (Sket et al., 2010) (Renversade et al., 2014), while the identical value of $\beta = 1.95 \pm 0.05$ (closely to 2) and $\alpha = 1$. It is known that $\beta = 2$ is characteristic for the constrained diffusional mechanism of void growth (Riedel, 1987) (Kassner & Hayes, 2003) (Dyson, 1983). The void sizes function equation (5.5) with the material parameters $(\alpha = 1, \beta = 2)$ will simulate the distribution of void sizes along grain boundary and compare with experimental data in section 5.4.

In the case of $\alpha = 1$, the function of the cavity size distribution (5.5) could be given by recalling the formula of $(1 + 1/x)^x = \mathrm{e}$ for $x \to \infty$:

$$N(R,t) = \frac{A_2}{A_1} R^{\beta} t^{1+\gamma} exp\left(-\frac{1+\gamma}{1+\beta}\frac{R^{\beta+1}}{A_1}\right) \quad (5.8)$$

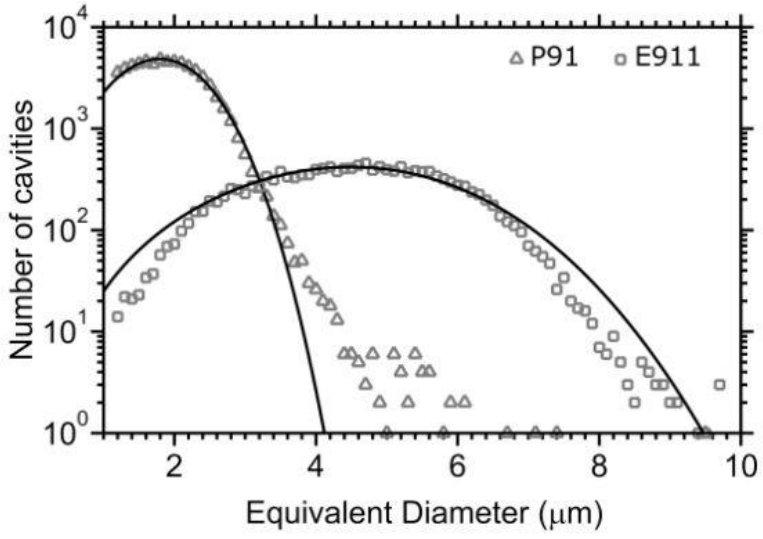

Figure 5.1 The equivalent diameter of voids versus the number of cavities in P91 and E911 steel. The continuous line represents the fit of the cavity size distribution function (Renversade et al., 2014).

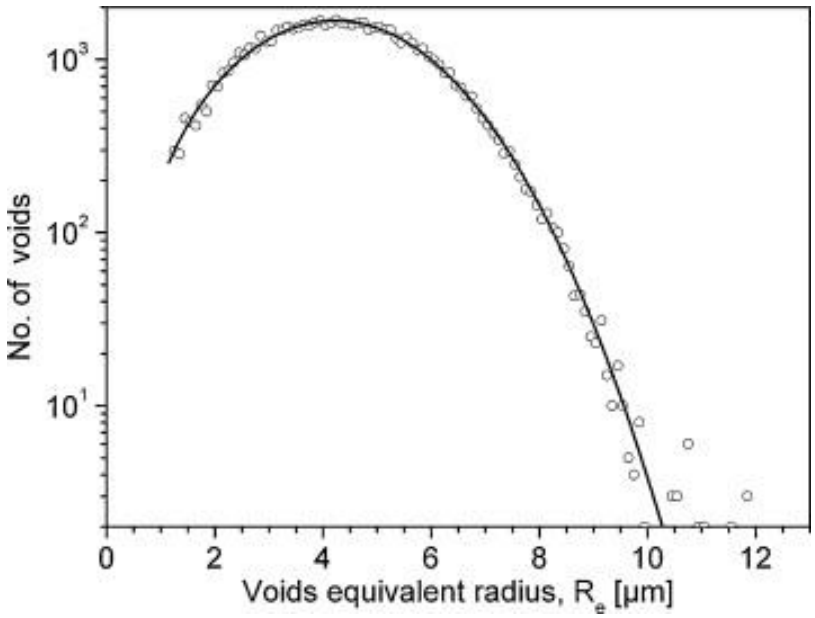

Figure 5.2 The equivalent diameter of voids versus the number of cavities in E911 steel. The continuous line represents the fit of the cavity size distribution function (Sket et al., 2010).

Based on equations (5.6) and (5.7), the cavitated area fraction, w, of the grain boundaries which have orientations between $60°$ and $90°$ to the tensile axis, could be determined quantitatively with the value of α, β and γ. Inputting the values of $\alpha = 1$ and $\beta = 2$ in to equations (5.7), the dimensionless factor $I(\alpha, \beta, \gamma)$ will be:

$$I = \pi(1+\beta)^{(\beta+3)/(\beta+1)} \int_0^U x^{\beta+2} [1-(1-\alpha)x^{\beta+1}]^{(\alpha+\gamma)/(1-\alpha)} dx$$

$$I = \pi \times 3^{\frac{5}{3}} \int_0^U x^4 dx \quad (5.9)$$

The steps of calculated above are the dimensionless factor equation (5.9). Using the power law of $\int x^a dx = \frac{x^{a+1}}{a+1}, a \neq -1$, indefinite integral can be calculated as:

$$\int_0^U x^4 dx = \frac{x^{4+1}}{4+1}$$

$$\int_0^U x^4 dx = \frac{x^5}{5} + \mathrm{C};$$

Based on upper and lower bounds calculation formula of

$$\int_a^b f(x)dx = F(b) - F(a)$$

$$\int_a^b f(x)dx \ = \lim_{x\to a+}(F(x)) - \lim_{x\to b-}(F(x)),$$

lower bounds:

$$\lim_{x\to 0+}\left(\frac{x^5}{5}\right) = \frac{0^5}{5} = 0;$$

upper bounds:

$$\lim_{x\to U-}\left(\frac{x^5}{5}\right) = \frac{U^5}{5}.$$

Thus,

$$\int_0^U x^4 dx = \frac{U^5}{5} - 0$$

$$\int_0^U x^4 dx = \frac{U^5}{5}$$

Instead of $\int_0^U x^4 dx$ for $\frac{U^5}{5}$, the solution of the dimensionless factor $I(\alpha, \beta, \gamma)$ equation (5.9) will be:

$$I = \pi \times 3^{\frac{5}{3}} \times \frac{U^5}{5} \quad (5.10)$$

Inputting equation (5.10) into equation (5.6), the cavity area fraction along the grain boundaries which have orientations between $60°$ and $90°$ to the tensile axis could be:

$$w = \pi \times 3^{\frac{5}{3}} \times \frac{U^5}{5} \times {A_1}^{2/3} A_2 \times t^{1+\gamma}$$

$$w = \pi \times \frac{3}{5} \times 3^{\frac{2}{3}} \times U^5 \times {A_1}^{2/3} A_2 \times t^{1+\gamma}$$

$$w = U' \times t^{1+\gamma} \quad (5.11)$$

where $U' = \pi \times \frac{3}{5} \times 3^{\frac{2}{3}} \times U^5 \times {A_1}^{2/3} A_2$.

The value of γ and U' will be determined and validated in section 5.4.

5.3 Fracture criterion for novel creep cavitation damage equation based on the cavity fraction on grain boundary of high chromium

Rupture is assumed to occur when the area coverage attains a critical value, denoted by w_f. The number value of w_f will be choose as $w_f = {\pi}/{4}$ for the equation (5.11) (Riedel, 1989), since regularly spaced cavities touch each other if $w_f = {\pi}/{4}$.

In the section 2.9 of Chapter 2 literature, the typical creep rupture criterion was summarized, and found that the critical value of damage is 1/3, it is important that we point out that the different creep rupture criterion between novel creep cavitation damage equation and typical one. The reason that the critical value of novel cavitation damage in new creep rupture criterion is higher than the typical one is due to the cavity area fraction caused just by integrating cavitation along grain boundary which have orientations between 60° and 90° (Riedel, 1989) to the tensile axis, comparatively, the critical value damage of 1/3 of the cavitation area fraction is for all of the grain boundaries that have applied stress to have completely cavitated, a suggestion made by Dyson and Gibbons (1987) (Perrin & Hayhurst, 1996) (Hayhurst et al., 2005).

5.4 Identifying material parameters for the novel creep cavitation damage constitutive equation for high chromium steel

5.4.1 The specific application with the value of γ = 1

Firstly, Riedel discussed the solution under special condition of $A_1 = A_2 = 1$ for the function of the cavity size distribution with different values of γ, it presented that the trending of the modelling curve shape with γ = 1 in Figure 5.3 is similar to that from experiment for P91 and E911 in Figure 5.1 and Figure 5.2.

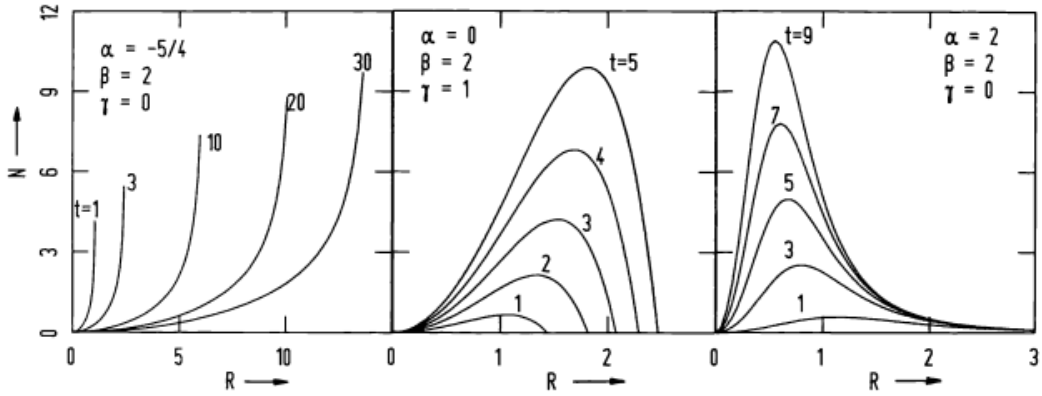

Figure 5.3 Evolution of the function of the cavity size distribution with special condition $A_1 = A_2 = 1$ (Riedel, 1989).

Secondly, in some cases, the cavity spacing is found to be decreasing inverse to the proportion of the creep strain, $\lambda = 1/(\sqrt{\alpha''})$, where α'' is an empirical factor with unit of $1/m^2$, the nucleation could be formed (Riedel, 1989):

$$J^* = 2\alpha''\dot{\varepsilon}^2 t \quad (5.12)$$

which is in time compatible with the power-low equation (5.4) of the cavity nucleation rate with $\gamma = 1$.

Based on the damage mechanism of cavity continuous nucleation rate as in equation (5.12) with $\gamma = 1$ and constrained diffusive growth, the time to cavity coalescence equation was proposed by Riedel (Riedel, 1989):

$$t_c = 0.90\left[\frac{h(\psi)}{d}\right]^{\frac{1}{2}}\left[\frac{1+\frac{3}{n}}{\alpha''}\right]^{\frac{1}{4}} w_f{}^{\frac{3}{4}}/\dot{\varepsilon} \quad (5.13)$$

Thus, the cavity continuous nucleation and constrained diffusive growth in some cases is with the value of $\gamma = 1$.

In some cases (Riedel, 1989), the sintering stress is neglected, the growth rate has the power-law form, $\dot{R} = (\lambda/R)^2$, the cavity spacing, λ, is determined by the number of cavities already nucleated,

$$1/\lambda^2 = \int J^* dt = \frac{A_2 t^{\gamma+1}}{\gamma+1} \text{ (5.14)},$$

so that $\beta = 2$ and $\alpha = \gamma + 1$. For time-independent nucleation, $\gamma = 0$, equation (5.14) gives the time to cavity coalescence on isolated boundary facets, t_c(Riedel, 1989):

$$t_c = \left(\frac{3\pi(1+3/n)}{J^*}\right)^{1/3}\left(\frac{\sigma_e^\infty}{\sigma_l^\infty}\frac{h(\varphi)}{\dot{\varepsilon}_e^\infty d}\right)^{2/3}\frac{w_f}{2r(2/3)}, \qquad (5.15)$$

where $r\left(\frac{2}{3}\right) = 1.354$.

A first example of low chromium steel ($2^1/_4\,Cr1Mo\ steel$) at 550℃ had been investigated by Needham (1983), according to Riedel (1985, 1989). The solid line in Figure 5.4 represents the time to cavity coalescence, t_c, calculated by equation (5.15) with $\alpha = 1$, $\beta = 2$, $\gamma = 0$ for constrained growth.

The rupture lifetime for unconstrained diffusive cavity growth rates with $\alpha = 0$, $\beta = 2$, $\gamma = 0$, t_f, follows to be (Riedel, 1989):

$$t_f = 0.33\left(\frac{h(\psi)kT}{\Omega\delta D_b\sigma}\right)^{2/5}\left(\frac{w_f}{J^*}\right)^{3/5} \text{ (5.16)}.$$

The equation 5.15 calculated for unconstrained cavity growth, the result is shown as a dash line in Figure 5.4

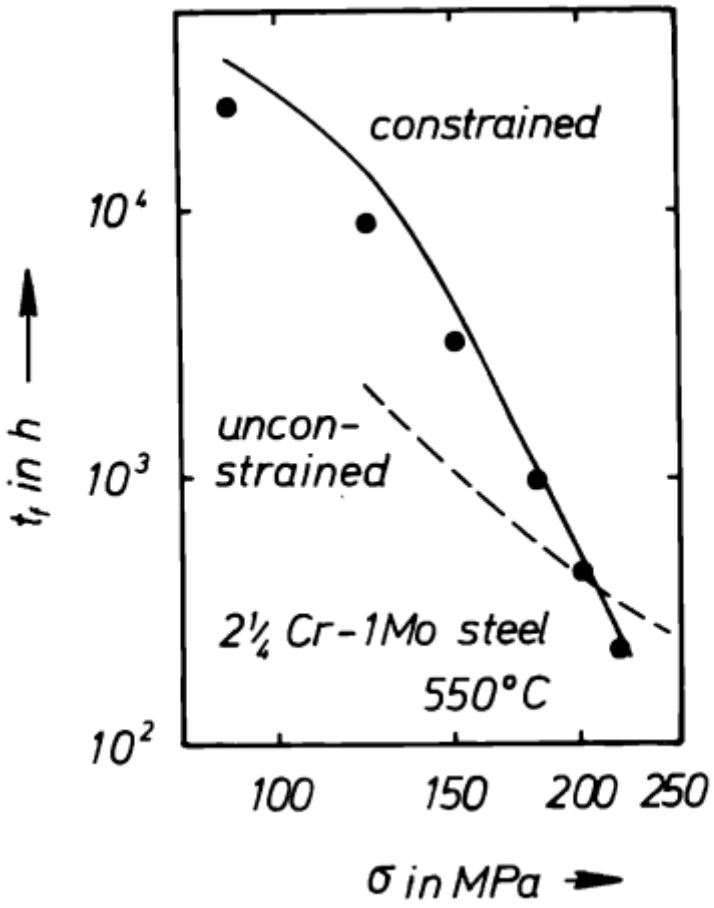

Figure 5.4 Rupture lifetime of low chromium steel (2 1/4Cr-1Mo). Solid line calculated by equation (5.15) with α=1, β=2, γ=0; Dashed line calculated by equation (5.16) with α=0, β=2, γ=0 (Riedel, 1985).

5.4.2 Determination of model constants

The information and the significance of the cavity size distribution curve, has not been fully digested and appreciated. Based on the dense information contained in these curves, it was determined that it would be appropriate to calibrate the cavity nucleation and growth models, initially described by equations (5.3 and 5.4). In doing so, extra mathematic/equation manipulation was needed and performed, then implemented, and the values of model constants were calibrated via trial and error method.

This section confirms simulation of the values of $\gamma = 1$. The equation (5.8) with the values of material parameter ($\alpha = 1, \beta = 2, \gamma = 1$) could model the cavity size distribution, the value of $\gamma = 1$ could be confirmed if the modelling results agree with the experimental data of the distribution of cavity size in high chromium steel.

The cavity constrained growth equation (5.3) could be transformed step by step:

$$\dot{R} = A_1 R^{-2} t^{-1}$$

$$\dot{R} = A_1 \frac{1}{R^2} \frac{1}{t}$$

$$R^2 \dot{R} = A_1 \frac{1}{t}$$

$$R^2 \frac{dR}{dt} = A_1 \frac{1}{t}$$

$$R^2 dR = A_1 \frac{1}{t} dt$$

$$\frac{1}{3} R^3 = A_1 \ln t + C \quad (5.17)$$

For one condition, the diameter of cavity size could reach1.2μm using time t_n or the diameter of cavity size reaching in any range of cavity diameter changing, for example, 2μm or 3 μm at time t_n.

For the other condition, the mean values of void at the end of the tests is about 5.7μm for P91 at 10200h (Remversade, 2014).

If there are known above two conditions of the diameter of cavity size at time t_n and 10200h, the value of A_1 and C in equation (5.17) could be solved.

With the values of with $\alpha = 1$, $\beta = 2$ and $\gamma = 1$, the distribution equation (5.8) of void on grain boundary could be written as:

$$N(R,t) = \frac{A_2}{A_1} R^2 t^2 exp\left(-\frac{2}{3}\frac{R^3}{A_1}\right) \quad (5.18).$$

And the continuous line represents the fit of equation (5.18) which can be rewritten by Sket et al. (Sket et al., 2010) in the following form:

$$f(R) = C_1 R^2 \exp\left(-\frac{C_2 R^3}{3}\right) \quad (5.19)$$

Then,

$$C_1 = \frac{A_2}{A_1}$$

$$C_2 = \frac{2}{A_1}.$$

So the value of A_2 could be:

$$A_2 = \frac{f(R)A_1}{R^2 \exp(-\frac{2}{3A_1}R^3)} (5.20)$$

Based on the experimental data of the distribution of non-coalesced void number and void equivalent radius for P91 steel in Figure 5.1, the value of A_2 could be solved with the values of $\alpha = 1$, $\beta = 2$ and $\gamma = 1$. For example, the number of the void equivalent radius 1.2μm is 3500 at the time of 10200h, or the number of the void equivalent radius 1.6μm is 4500 at the time of 10200h, or any point of the experiment in Figure 5.1.

Thus, the number of cavities could be modelled for the diameter of void size in the range 1.2 - 5.7μm. When the calibrated value of the time t_n is 1.07h with $\alpha = 1$, $\beta = 2$ and $\gamma = 1$, the theoretical modelling results fitted well with experimental data as shown in Figure 5.5. Figure 5.6 shows the calibrated process of the value of time t_n. Another possible method would be to develop an optimization software of three variable function for the cavity size distribution equation (5.8) with calibrated material parameters of A_1 and A_2 to fit well the experimental data. The percentage error between the modelling results and the experimental data is around 0.2%.

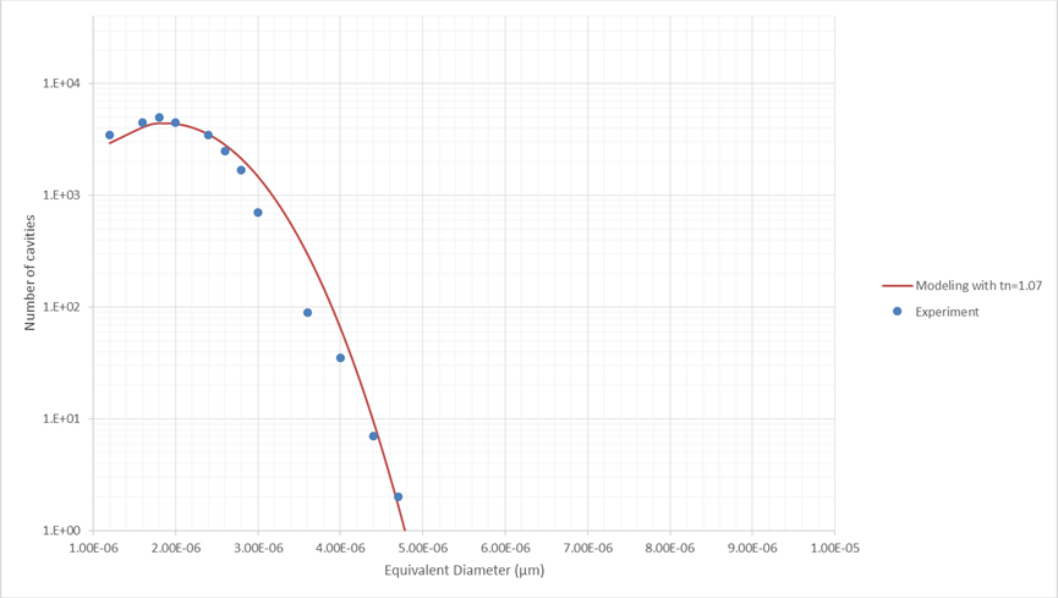

Figure 5.5 The modelling results of the cavity size distribution function with the value of α=1, β=2 and γ=1 compared with experimental data.

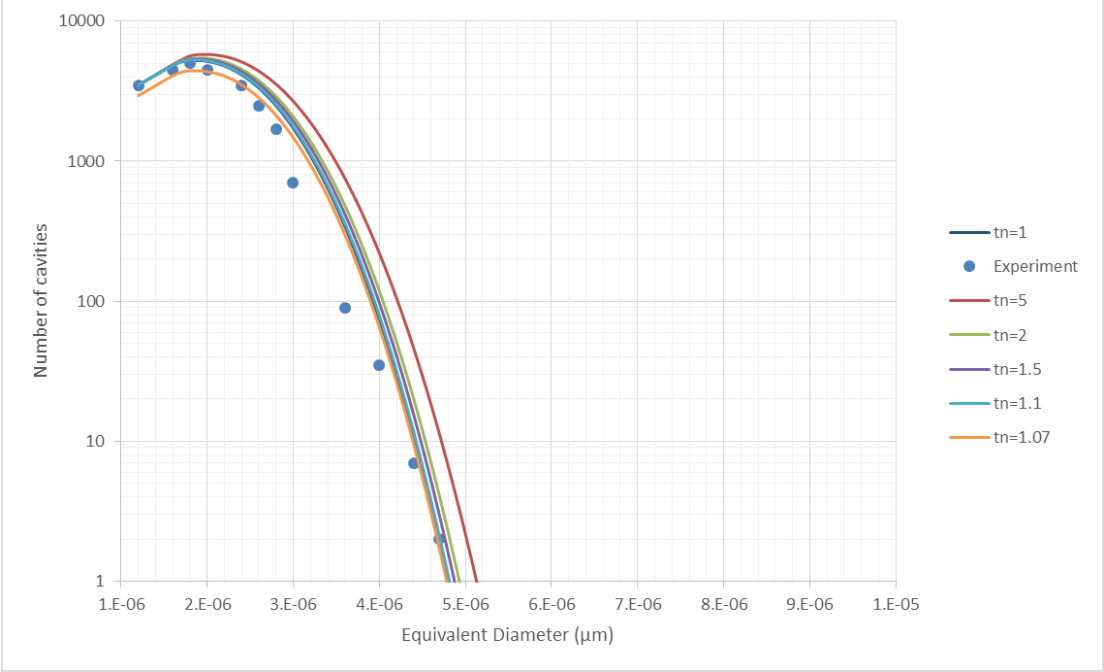

Figure 5.6 The calibrated process of the time t_n. The modelling results fitted well with experimental data with the value of $t_n = 1.07h$.

5.4.3 The value of U' material constant

Rupture is assumed to occur when the area coverage reaches a critical value, denoted by w_f. The number value of w_f will be shown as $w_f = {}^{\pi}/_{4}$, since regularly spaced round cavities touch each other if $w_f = {}^{\pi}/_{4}$ (Riedel, 1989).

Based on the above section about the confirmation simulation of the value of γ=1, the critical value is:

$$w_f = U' \times t^2 \ (5.21)$$

Based on the creep data sheet from NIMS of creep rupture time under different stress and temperature for P91 steel (NIMS, 2014) in Chapter 3, the value of U' was calculated out in Table 5.1 and Table 5.2 and showed a clear trend in Figure 5.7 and Figure 5.8.

Table 5.1 The calculated value of U' for P91 steel at 600℃ based on experimental data of P91 steel.

Stress (MPa)	Rupture time (h)	$U'(h^{-2})$
70	80736.8	1.2×10^{-10}
100	34141	6.738×10^{-10}
110	21206.3	1.746×10^{-9}
120	12858.6	4.75×10^{-9}
140	3414.7	6.736×10^{-8}
160	971.2	8327×10^{-7}

Table 5.2 The calculated value of U' for P91 steel at 625℃ based on experimental data of P91 steel.

Stress (MPa)	Rupture time (h)	$U'(h^{-2})$
90	21372.4	1.72×10^{-9}
100	9895.4	8.02×10^{-9}
120	1657.9	2.857×10^{-7}
140	399	4.933×10^{-6}

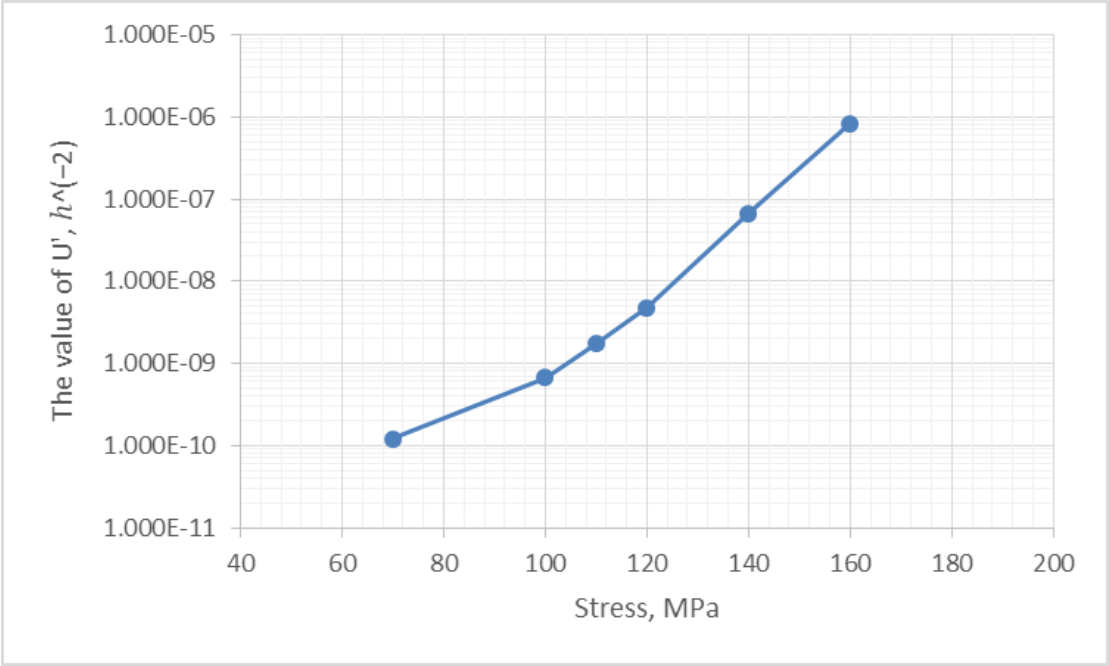

Figure 5.7 The trend of the values of U' under different stress at 600℃ for P91 steel.

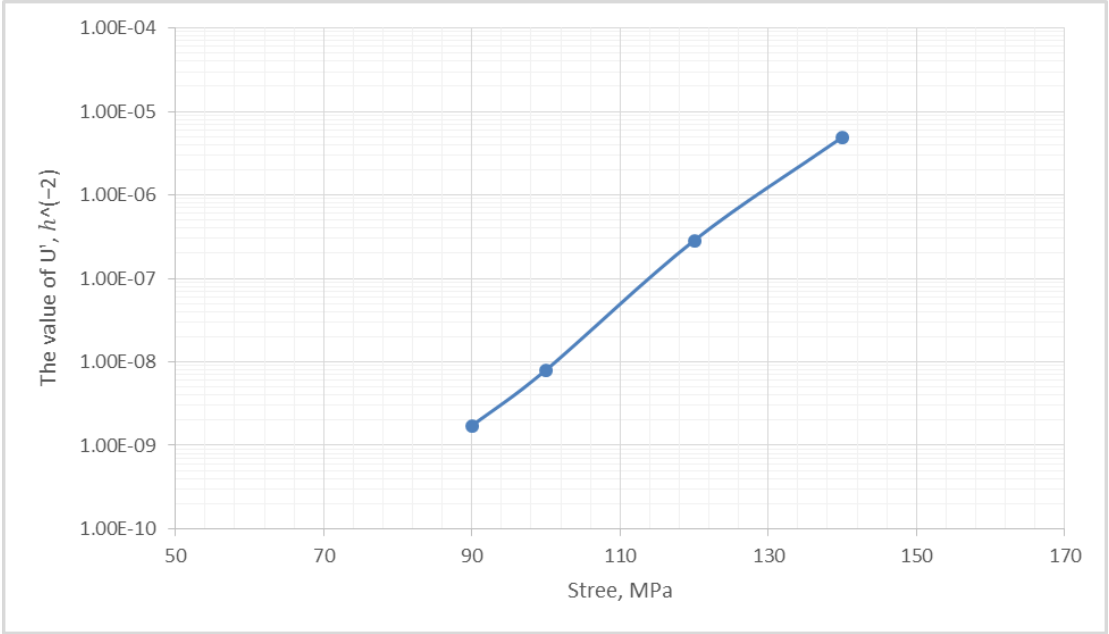

Figure 5.8 The trend of the values of U' under different stress at 625℃ for P91 steel.

5.5 Supporting evidence for novel creep cavitation damage

This section will investigate the coefficient A_2 dependence on stress. In order to establish the relationship of the coefficient A_2 dependence on stress, Xu has conceived the method (Xu, 2017), this section reports that method and the practical application of such method and attempts to validate the reliability of a novel creep cavitation damage equation (5.21) related to the cavity nucleation (5.4) and growth equation (5.3) by using limited experimental observation of cavity in high chromium steel.

In the above development of cavity area fraction along grain boundary w, the cavity nucleation rate is governed by equation (5.4) with the coefficient A_2 that is not changing with time, however, it might be dependent on stress, temperature or strain. The equation (5.4) with the confirmation validation value of $\gamma = 1$ can be converted as:

$$J = A_2 t dt$$

$$\mathrm{J} = \frac{1}{2} A_2 t^2 \quad (5.22)$$

where J is total number of cavities.

The quantitatively analysed results in accordance with cavity nucleation equation (5.22). The smaller the stress and the longer creep time, the higher the cavity number will be. The number density data was extracted by reading the graph from Figure 3.6 which was found in chapter 3.2 during the observation of the evolution of cavity in CB8 steel (10.8%Cr) and is also shown below in Table 5.3:

Table 5.3 The number density of cavity at failure under a range of stress.

$Stress\ (MPa)$	$Lifetime\ (h)$	$Number\ density\ of\ cavity\ (10^{-5}\mu m^{-3})$
120	51406	1.0625
135	29466	0.6376
150	15316	0.475
165	6779	0.45

180	2825	0.375

Using the above quantitatively analysed results, the dependence of the proportional coefficient A_2 on stress is obtained in Table 5.4 and shown in Figure 5.9. Figure 5.9 indicates clearly that the proportional coefficient A_2 is reduced slightly when stress is below 150MPa. The significant trending of the coefficient A_2 could be used for extrapolation to lower stress. Furthermore, the discovered results the agreement of the coefficient A_2 of cavity nucleation rate equation may depend upon stress or strain rate, not time nor cavity size, which was described in section 5.1 of chapter 5. In the previous chapter 2.8, it was noted that the deficiently of the value of material constant A in Yin's cavity nucleation equation which modified based on Dyson (2000) is the lack of a clear trend, however, the proportional coefficient A_2 of cavity nucleation related to the new creep cavitation damage equation is significantly logic trend in comparison with material constant A in Yin's nucleation equation as shown in Figure 2.53.

Table 5.4 the relationship between the values of the coefficient A_2 with stress.

Stress(MPa)	The proportional value of A_2
120	8.04139E-10
135	1.46871E-09
150	4.04979E-09
165	1.95844E-08
180	9.39776E-08

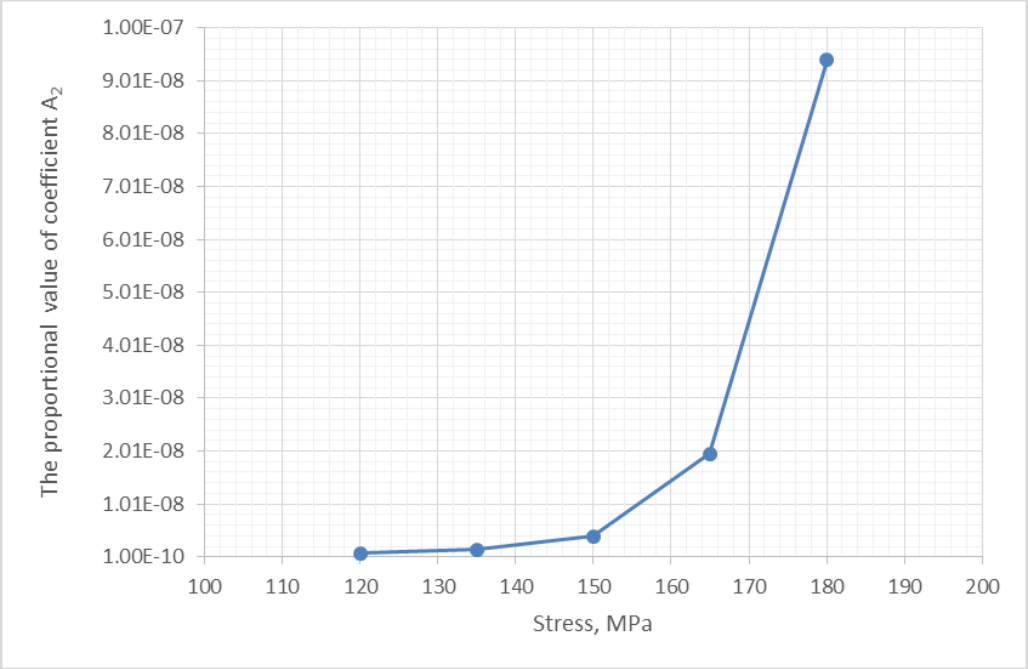

Figure 5.9 The relationship between the proportional value of the coefficient A_2 and stress.

In addition, the increasing trend of quadratic function curve of the number of total cavity equation (5.22) agrees well with the experimental data as shown in Figure 5.10 of relationship between cavity density and time for high chromium steel, the cavity density increases with exposure time.

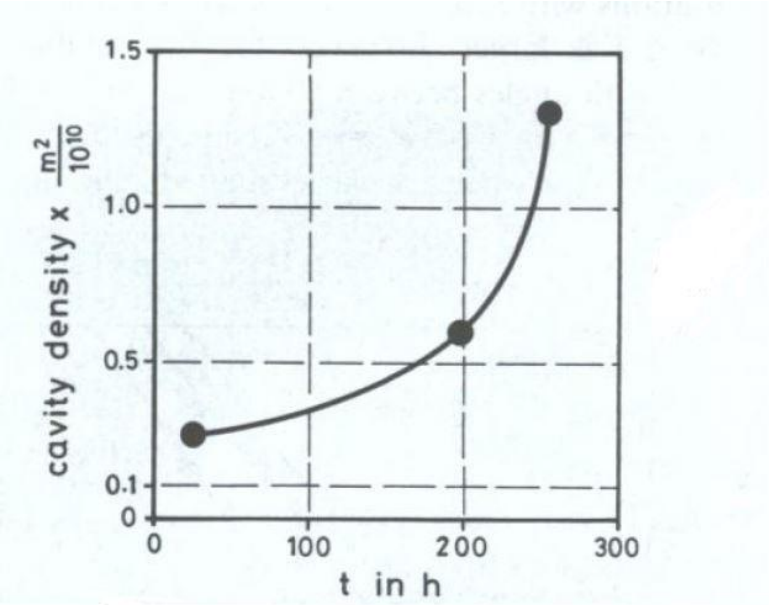

Figure 5.10 Cavity density as a function of time for 12% chromium ferritic steel (Eggeler et al., 1989).

Chapter 6 Novel creep damage constitutive equation

6.1 Coupling the creep deformation (microstructural degradation) with creep damage (creep cavitation) for novel creep damage constitutive equation

The development of novel creep damage constitutive equations should consider these four main aspects:

(1) Creep deformation (microstructure degradation) including strain hardening, particle coarsening, mobile dislocation, have been vastly developed in recent decades, the detail of which is provided in section 2.7 of Chapter 2. Mature creep deformation (microstructure degradation) shall be applied directly into the development of novel creep damage constitutive equations for high chromium steel.

- Strain hardening

$$\dot{H} = \frac{h'}{\sigma}\left(1 - \frac{H}{H^*}\right)\dot{\varepsilon} \quad (2.14)$$

- Particle coarsening

$$\dot{D}_p = \frac{Kp}{3}(1 - D_p)^4 \quad (2.16)$$

- Mobile dislocation

$$\dot{D}_d = C(1 - D_d)^2\dot{\varepsilon} \quad (2.18)$$

(2) The modified function of minimum creep strain rate and stress for creep damage constitutive equations for high chromium steel were proposed and applied better than conventional power law, linear power law and hyperbolic sine law in Chapter 4. The modified hyperbolic sine law for minimum creep strain rate versus stress would be taken into the novel creep damage constitutive equation:

$$\dot{\varepsilon}_{min} = Asinh(B\sigma^q)\ (2.4);$$

(3) Based on experiment foundation discussed in chapter 6, the novel creep cavitation damage equation presents the cavitated area fraction of grain boundaries which have orientations between $60°$ and $90°$ to the tensile axis for high chromium steel:

$$w = U't^2\ (5.21);$$

(4) The conventional creep damage constitutive equation in hyperbolic sine law with only cavity damage $'w'$ and without creep deformation is expressed by:

$$\dot{\varepsilon} = Asin\,\mathrm{h}\left(\frac{B\sigma}{(1-w)}\right)\ (6.1).$$

The modified function (equation (2.4)) of minimum strain and stress for high chromium steel was imported with the exponent $'\mathrm{q}'$ for stress $'\sigma'$ in chapter 4; correspondingly, the exponent $'p'$ would be imported for the novel creep damage constitutive equation and be written as:

$$\dot{\varepsilon} = Asin\,\mathrm{h}\left(\frac{B\sigma^q}{(1-w)^p}\right)\ (6.2)$$

Thus, the novel creep damage constitutive equation shall couple the creep deformation (microstructural degradation) with creep damage (creep cavitation) and become:

$$\dot{\varepsilon} = \frac{A}{(1-D_d)}\sinh\left[\frac{B\sigma^q(1-H)}{(1-D_p)(1-w)^p}\right]\quad (6.3)$$

$$\dot{H} = \frac{h'}{\sigma}(1-\frac{H}{H^*})\dot{\varepsilon}$$

$$\dot{D}_p = \frac{Kp}{3}\left(1-D_p\right)^4$$

$$\dot{D}_d = C(1-D_d)^2\dot{\varepsilon}$$

$$w = U't^2$$

where A, B, h', H^*, K_p, C and U are material parameters. All the material parameters are identified and applied to the novel creep damage constitutive equations for high chromium steel in next sections.

6.2 Identifying materials parameters for novel creep damage constitutive equations

For the classical uni-axial KRH creep damage constitutive equation (Perrin & Hayhurst, 1996), the dependence of creep rate is incorporated through the constant A which is related to the activation energy for volume diffusion Q_A

$$A = A_0 B exp\left(-\frac{Q_A}{RT}\right) \quad (6.4)$$

where A_0 is the constant of proportionality, R is the universal gas constant and T is the absolute temperature. B is the dependence of temperature and expressed as:

$$B = B_0 \exp\left(\frac{Q_B}{RT}\right) \quad (6.5)$$

where B_0 is a constant of proportionality and Q_B is an activation energy related to the kinetics of dislocation motion.

The material parameter of A and B for the novel creep damage constitutive equations (6.3) have some physical significance with typical one, but their values would be calculated in the other way.

In the section 4.2 of Chapter 4, the value of material parameters A ,B and q have been discussed in regards to the influence for the curve of creep strain modelling and calibrated in Table 4.4 and 4.5 based on referenced experimental data of minimum creep strain rate and different stress for P91 steel at constant temperature.

The material parameters H^*, h', K_p and C, are required for the novel creep damage constitutive equation. The material parameters have been obtained from the quantitative microstructural degradation data and used for high chromium steel in Appendix C.

The initial value of different material parameters obtained from literature and optimised parameters using in creep constructive equation for 9%Cr steel.

The optimisation algorithm equation provided minimum least square error function and could be expressed as (Christopher et al., 2013):

$$LS = \sum_{i=1}^{m}(\sum_{j=1}^{n}(\frac{\varepsilon_j{}^{pred} - \varepsilon_j{}^{exp}}{\varepsilon_j{}^{exp}})^2) \quad (6.6)$$

where m and n means the number of creep curves and number of creep strain versus time data point, respectively. The $\varepsilon_j{}^{pred}$ and $\varepsilon_j{}^{exp}$ denote the numerically predicted and experimental strain values, respectively. The best set of materials parameters should be adjusted to reach a minimum of the optimisation algorithm equation for P91 steel at $600℃$ in Table 6.1 (Christopher et al., 2013).

Table 6.1 The optimised material parameter for P91 steel at 600℃ (Christopher et al., 2013)

$Material\ paremeter$	$Optimised\ material\ parameter$
H^*	0.35
$h'(MPa)$	10300
$K_p(h^{-1})$	4.379×10^{-5}

And the material constant $'c'$ of mobile dislocation damage equation is taken from the summarized material parameters with the same conditions of 9%Cr steel at $600℃$. The value of exponent p calibrated while the modelling value of strain rate at fracture is the same or close to the experiment creep data for P91 at $600℃$. Thus, between any two values of P under high stress level or low stress level, there will be a linear function relationship between the value of P and stress: $P = -0.0087\sigma + 1.5613$ under 100MPa and $P = -0.0018\sigma + 0.8751$ above 100MPa as shown in Figure 6.1. Based on the trending equation of value of p equation, the value of p under different stress levels could be calculated and shown in Table 6.2.

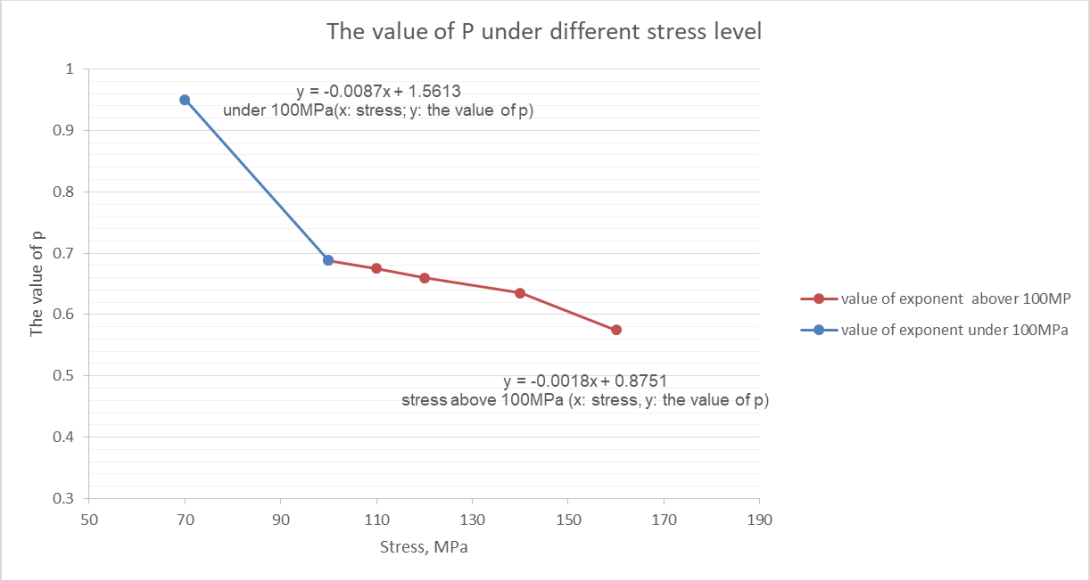

Figure 6.1 The value of exponent 'p' under different stress, which fitted to the experiment creep data for P91 at 600℃.

Table 6.2 The calculated value of p under different stress levels.

Stress(MPa)	The value of p
160	0.575
140	0.635
120	0.66
110	0.675
100	0.688
70	0.95

6.3 Comparing the modelling results to previous experimental data for high chromium steel

The novel constitutive equation (6.3) will be using the identifying material parameters for P91 steel at 600℃ as listed in Table 4.4 and Table 6.1 and calculated by the Euler's method. The modelling results of the development of novel creep damage constitutive equations are presented below in figures, and

as can be observed remarkably fit well with experimental data from NIMS (2014).

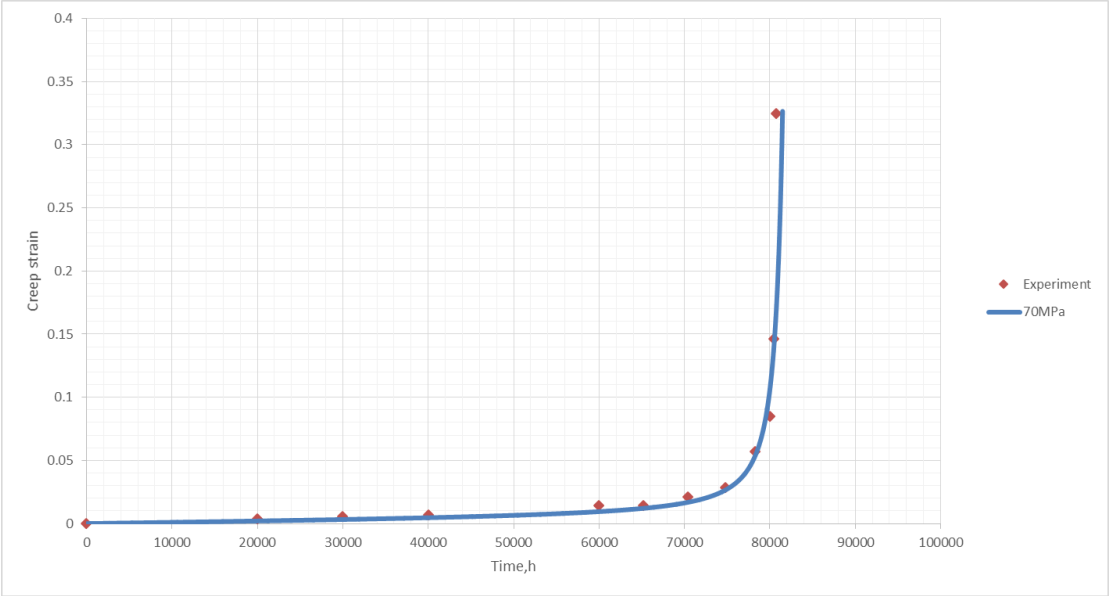

Figure 6.2 The modelling result compared with the experiment under 70MPa at 600℃.

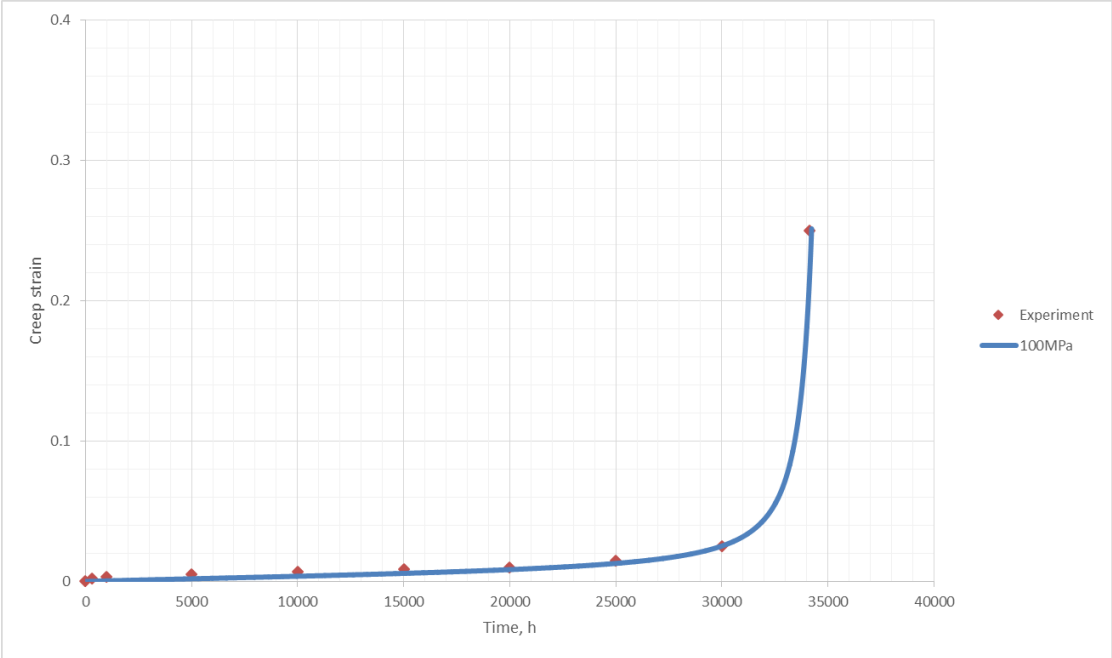

Figure 6.3 the modelling result compared with the experiment under 100MPa at 600℃.

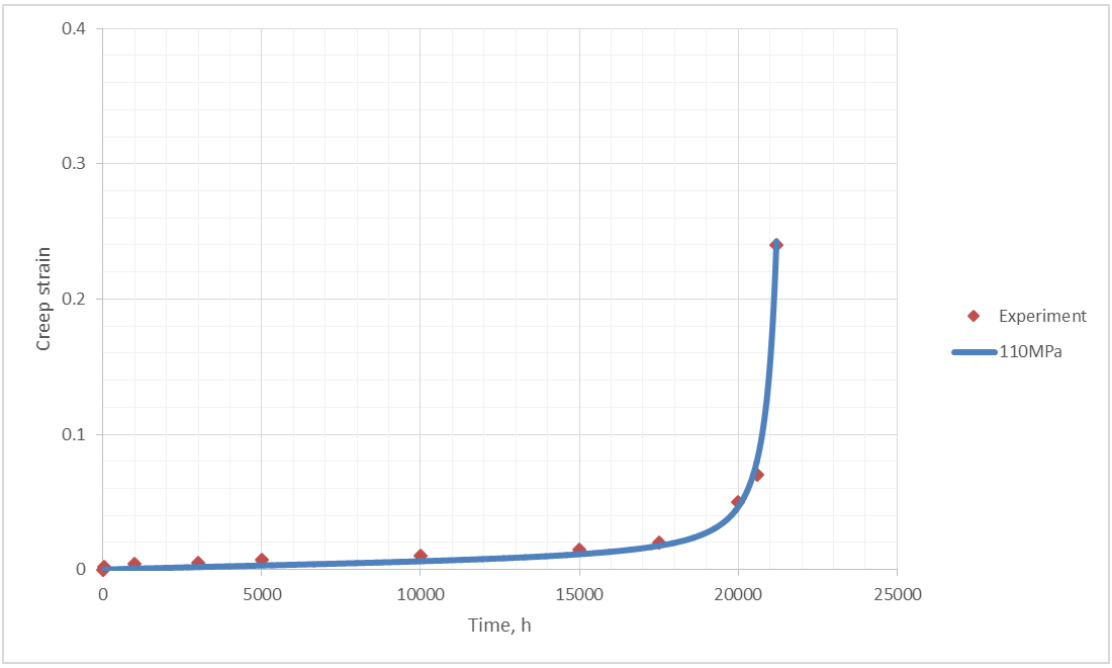

Figure 6.4 The modelling result compared with the experiment under 110MPa at 600℃.

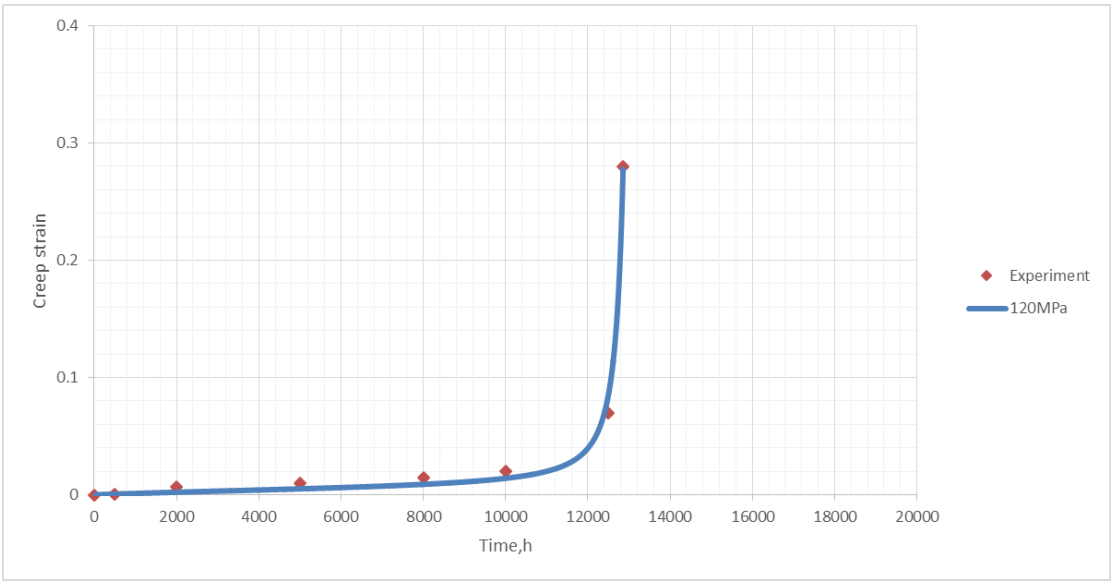

Figure 6.5 The modelling result compared with the experiment under 120MPa at 600℃.

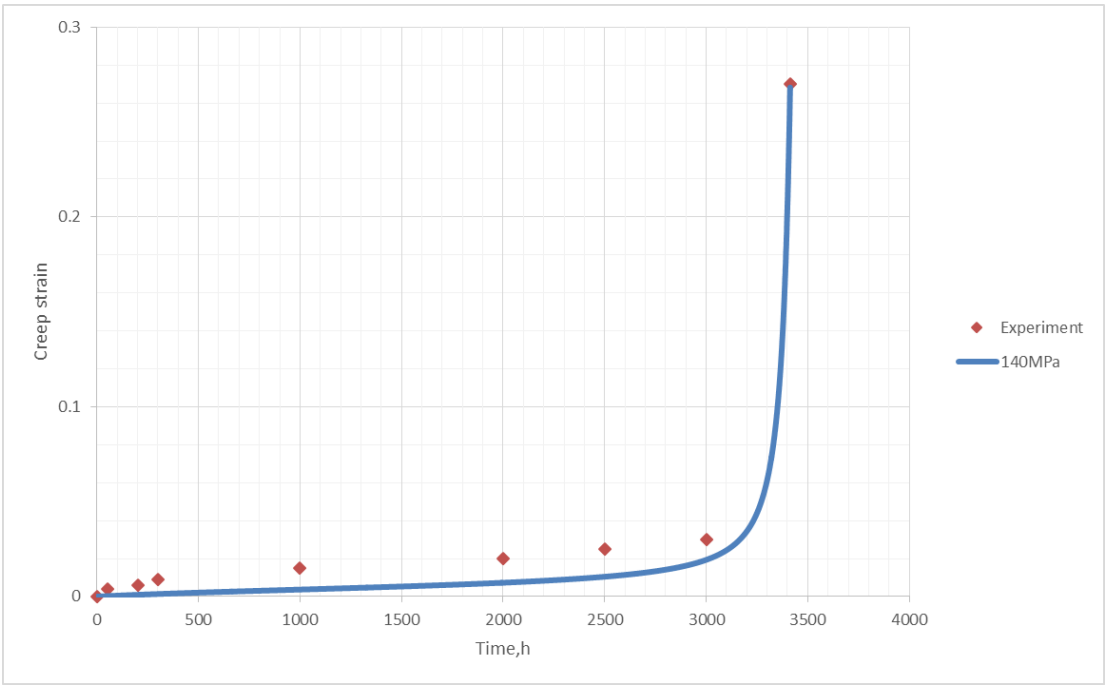

Figure 6.6 The modelling result compared with the experiment under 140MPa at 600℃.

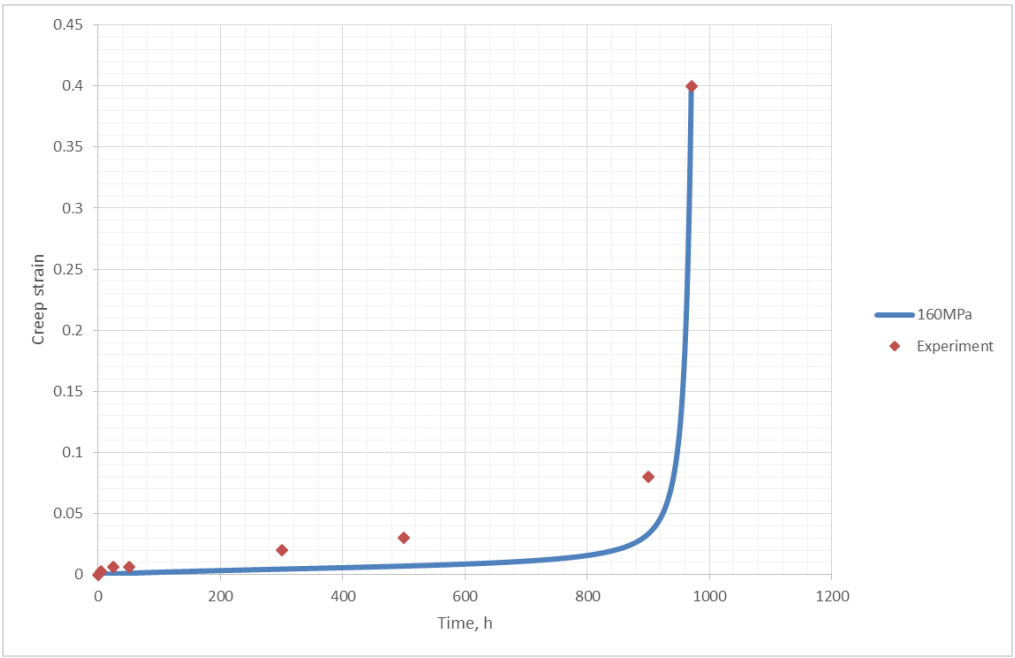

Figure 6.7 The modelling result compared with the experiment under 160MPa at 600℃.

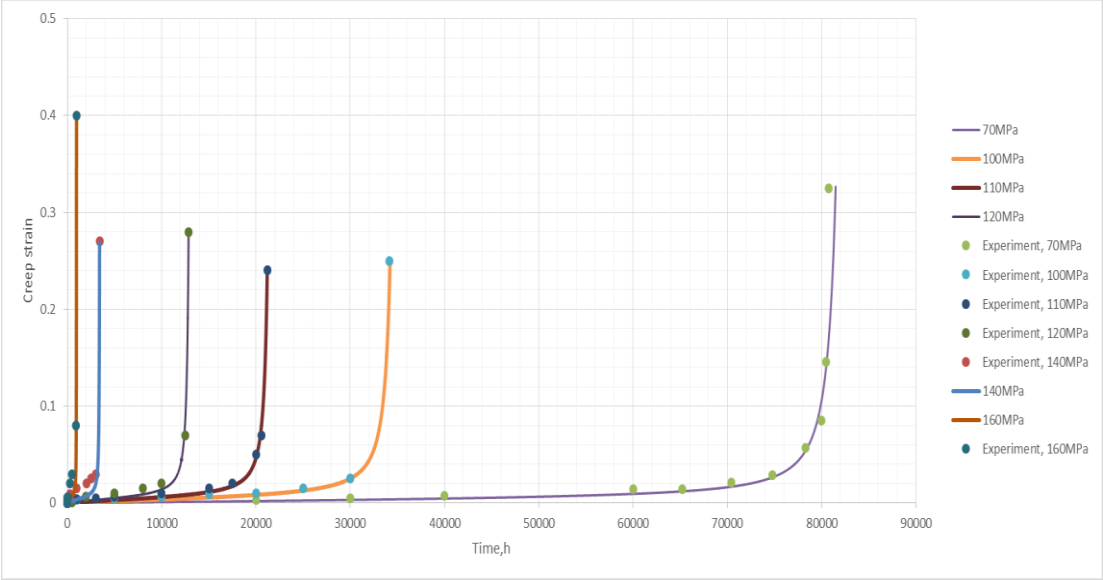

Figure 6.8 The modelling results compared with the experiment of P91 at 600℃ under a stress range.

The modelling results fit closely with the experiments during the stress range of 70-120MPa, having a deviation of just 15.6% in creep strain. It is noted that the deviation in the secondary stage of creep test increases with higher stress (140-160MPa). The secondary stage is related to steady strain rate (minimum creep strain rate), the errors of the calibrated parameter for modified hyperbolic sine law in higher stress cause the deviation in the secondary stage, thus optimisation of the material parameters in the function of minimum creep strain rate and applied stress is required in order to reduce the deviation in higher stress conditions.

6.4 Comparing the modelling results with classic uniaxial KRH constitutive equations and experimental data for P91 steel at 600℃

The modelling results of novel constitutive equations would be further validated by comparing them with both the classic uni-axial KRH constitutive equations and experimental data for P91 at 600℃ from NIMS (2014).

The classic uni-axial KRH constitutive equations is written as (Perrin & Hayhurst, 1996) (Hyde et al, 2006):

$$\dot{\varepsilon} = Asinh\left(\frac{B\sigma(1-H)}{(1-\emptyset)(1-\omega)}\right) \quad (2.25)$$

$$\dot{H} = \frac{h}{\sigma}(1-\frac{H}{H^*})\dot{\varepsilon}$$

$$\dot{\emptyset} = \frac{K_c}{3}(1-\emptyset)^4$$

$$\dot{\omega} = D\dot{\varepsilon}$$

The critical value of ω, is approximately 1/3 and denotes the cavitated area fraction for all of the grain boundaries all of the grain boundaries normal to the applied stress.

Table 6.3 Material parameters for P91 steel at 600℃ for KRH equation (Rouse et al., 2013)

Material parameter	A(MPa/h)	B(MPa^{-1})	H^*	$h'(MPa)$	$K_c(h^{-1})$	D
Value	3.44×10^{-9}	0.100561	0.34	13669.67	5.46×10^{-8}	2.6

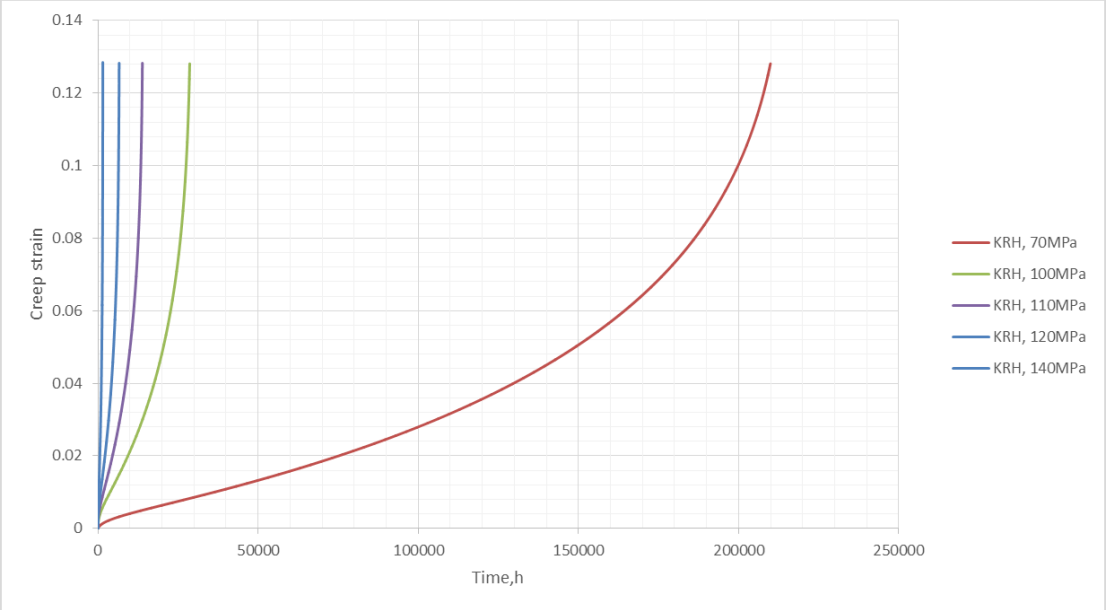

Figure 6.9 The modelling results of classical classic KRH constitutive equations for P91 steel at 600℃

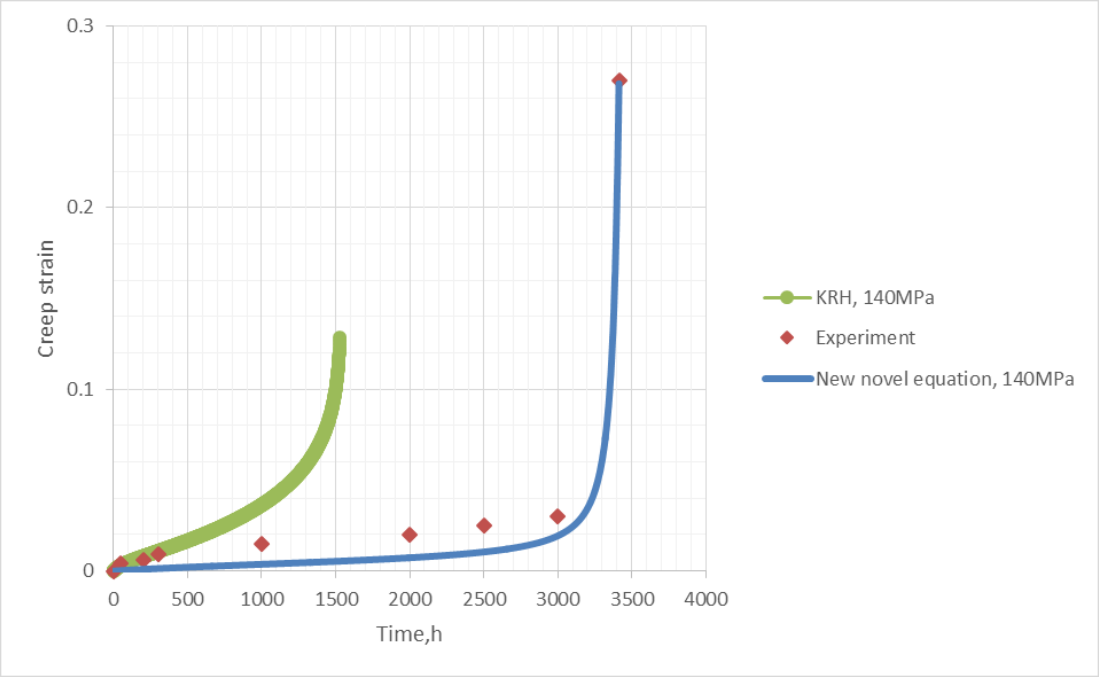

Figure 6.10 The modelling results compared with both KRH equations and the experimental data for P91 steel at 600℃ under 140MPa.

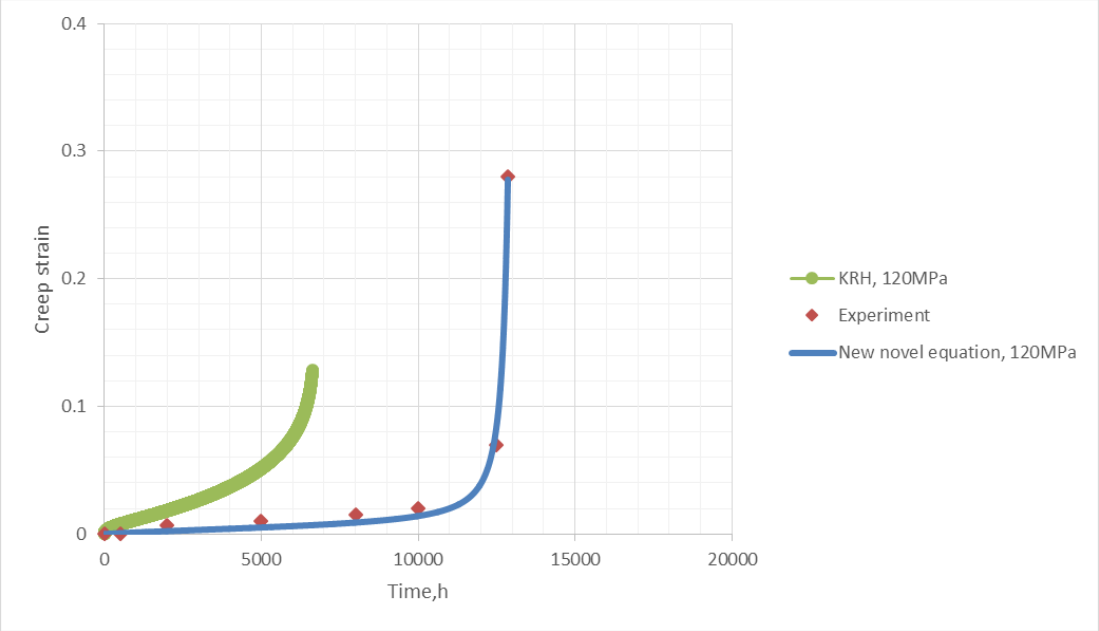

Figure 6.11 The modelling results compared with both KRH equations and the experimental data for P91 steel at 600℃ under 120MPa.

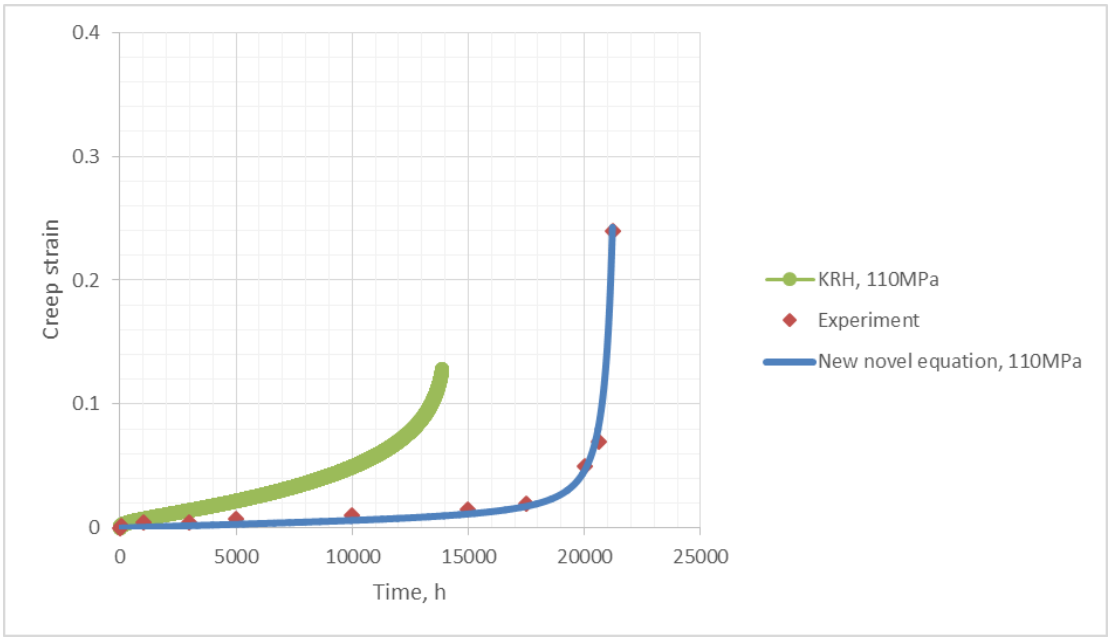

Figure 6.12 The modelling results compared with both KRH equations and the experimental data for P91 steel at 600℃ under 110MPa.

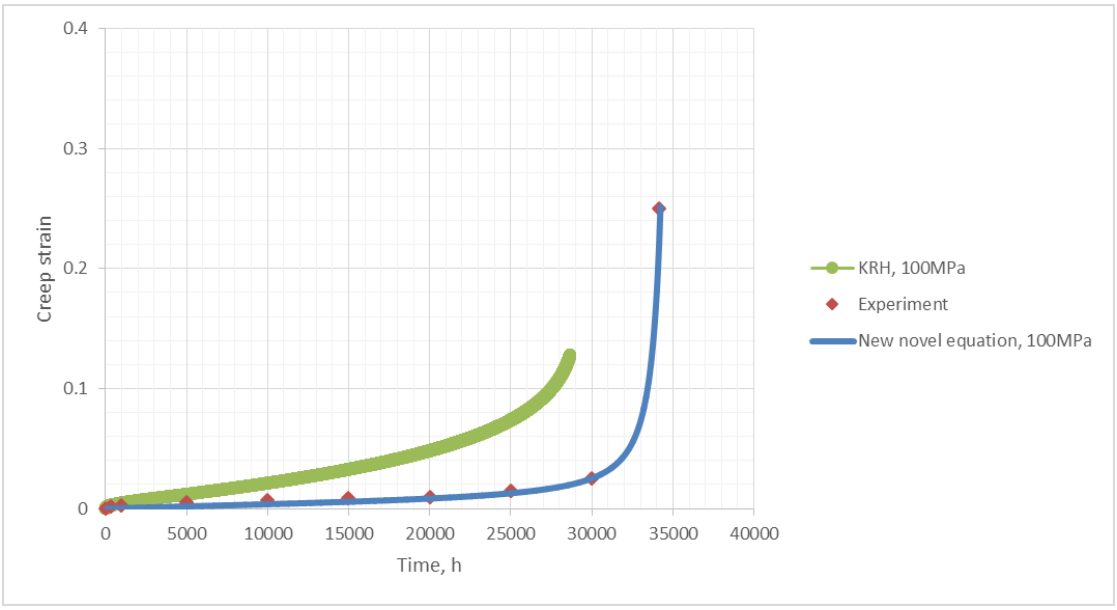

Figure 6.13 The modelling results compared with both KRH equations and the experimental data for P91 steel at 600℃ under 100MPa.

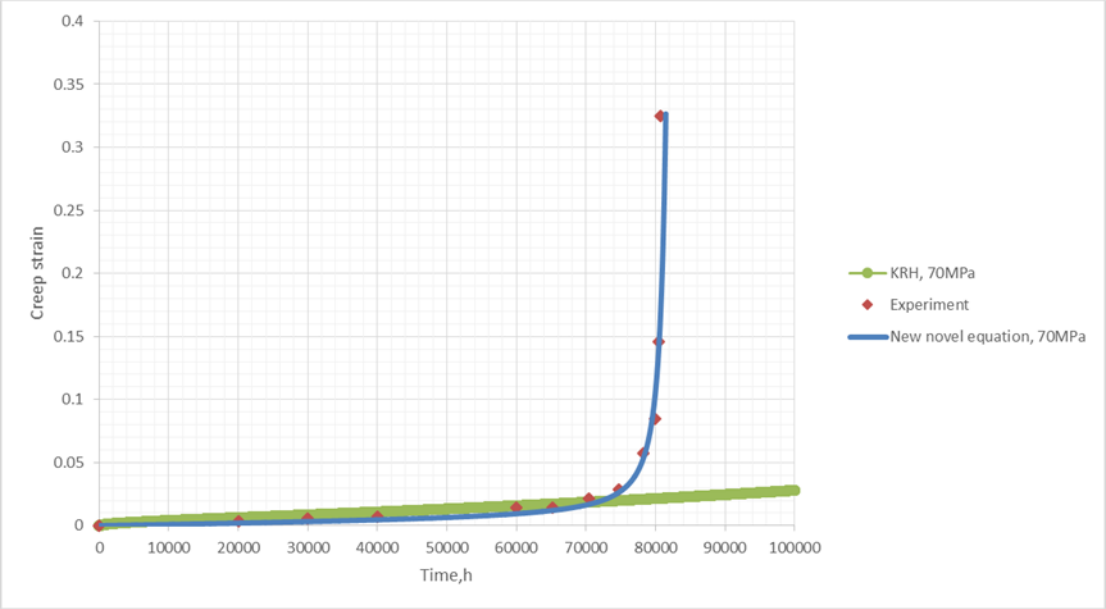

Figure 6.14 The modelling results compared with both KRH equations and the experimental data for P91 steel at 600℃ under 70MPa.

The modelling results of the new equations compares with the uni-axial KRH equations with material constants for P91 at 600℃ (Rouse et al., 2013), it displays the big lifetime error is between the experimental data and the modelling results of KRH equations. The percentage errors in lifetime between the experimental data and the modelling results of KRH equations are 0.55, 0.48, 0.345, 0.16 under 140MPa, 120MPa, 110MPa, 100MPa respectively. The modelling lifetime of KRH equations is 1.6 times that of experiment under 70MPa. The KRH equations, which include different mechanisms of microstructure degradation evolutions and cavitation damage, was successively applied to the description of the creep behaviour of low chromium steel. However, the microstructural deformation and cavitation damage of KRH equations, which was developed based on superalloy and low chromium steel, is not suitable for high chromium steel.

6.5 Applying the model to P91 steel at 625℃

The new equations for P91 steel were also applied at 625℃. The trending of creep curves and creep strain at failure under different stress (90-140Mpa) in Figure 6.15 agrees with the effects of stress for creep behavior in general in Figure 2.2. However, this set of creep tests for P91 steel at 625℃ is still in process under 90MPa and the creep curves are not yet published by NIMS.

Thus, the modelling results of novel constitutive equations for P91 steel at 625℃ will be further compared and analysed by the full experimental data when published.

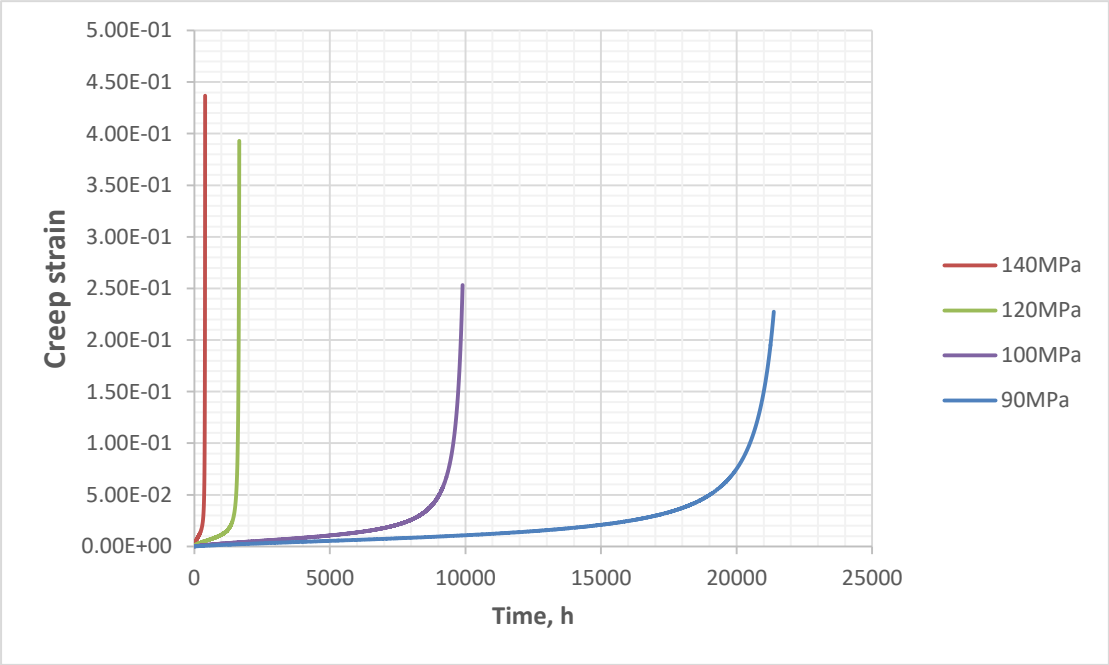

Figure 6.15 The modelling results of novel constitutive equations for P91 steel at 625℃ under 90-140MPa.

Chapter 7 Conclusion and Future work

7.1 Conclusion

This dissertation has successfully developed creep damage constitutive equations for high chromium steel based on the mechanism of cavitation damage. The key significant contributions of this research are summarized below according to previous chapters.

Firstly, a modified hyperbolic sine law was applied to describe the relationship between minimum creep strain rate and stress for high chromium steel, of which the modelling results fitted better with published experimental data of P91 steel at 600℃ by NIMS in comparison with conventional functions, power law, hyperbolic sine law and linear power law. The modified hyperbolic sine law was also successfully applied to P91 steel at 625℃.

Secondly, based on the theory of Riedel's cavity size function for cavity nucleation and growth on grain boundary area, material parameters for the cavitation damage equation and constrained diffusion growth and continuous nucleation mechanisms for high chromium were confirmed, by the quantitatively analysed results of the cavity size distribution along grain boundary using the superior 3D technology of X-ray micro-tomography for high chromium steel (P91, E911). A novel creep cavitation damage equation has successfully been developed for high chromium steel under a range of stress levels.

Thirdly, novel creep damage constitutive equations, coupled with appropriate creep deformation including strain hardening, particle coarsening and mobile dislocation with the new cavitation damage equation, have been successfully developed and applied to high chromium steel. The modelling results matched closely to within 84.4% with experimental data of P91 steel at 600℃ during the stress range of 70-120MPa in creep strain. The deviation of the modelling results in the secondary stage of creep with a higher stress (140-160MPa) could be improved by optimizing parameters for the function of minimum creep rate and applied stress. The validity of these novel creep damage equations was accomplished by comparing it with the KRH models and experimental data of P91 steel at 600℃. There are big lifetime errors between the experimental data

and the modelling results using KRH equations. The developed constitutive equations had also been applied to P91 steel at 625℃, the trending of creep curves and creep strain at failure under 90-140MPa is logical and physical, it will be further validated, when the experimental data of P91 steel at 625℃ is published.

7.2 Future work

Based on the current research work this PhD project has conducted, the author suggests below several aspects that could be undertaken and improved in the future:

1) An optimization software could be developed for the material parameters or constants for the modified sine law, the deviation of the modelling of creep damage constitutive equations under higher stress (140-160MPa) for P91 steel at 600℃. The modelling results will be validated for P91 steel at 625℃, when the experimental data of creep curves and creep ruptures under 90MPa is published.

2) The novel development of creep damage constitutive equations could be extended from uni-axial version stress state to multi-axial stress state, or even applied to finite element analysis software.

3) More experimental data regarding high chromium steel on cavitation damage evolution and cavitated area fraction at fracture with creep exposure time and a given stress and stress state should be obtained by using advanced 3D technology of X-ray micro tomography and subsequently analysed. A detailed experiment for high chromium was designed by me with the help of the supervisor Xu's grant applications, reference Spring-8, 2017A Application No. 37778.

Reference

Abe, F. (2008). Introduction. In F. Abe, T. Kern, & R. Viswanathan (Eds.) Creep-resistant steels (pp. 3-14). Cambridge England: Woodhead Publishing Limited and CRC Press LLC.

Abson, D.J., Rothwell, J.S., & Cane, B.J. (2007). Advances in welded creep resistant 9-12%Cr steels. In 5th International Conference on Advances in Materials Technology for Fossil Power Plants, Retrieved from http://www.twi-global.com/technical-knowledge/published-papers/advances-in-welded-creep-resistant-9-12cr-steels-october-2007/.

Aghajani, A., Somsen, C.h., & Eggeler, G. (2009). On the effect of long-term creep on the microstructure of a 12% chromium tempered martensite ferritic steel. Acta Materialia, 57 (17), 5093-5106. doi: https://doi.org/10.1016/j.actamat.2009.07.010.

Altenbach, H. (1999). Classical and non-classical creep models. In H. Altenbach & J. Skrzypek (Eds.) Creep and damage in materials and structures (pp. 45-95). New York: Springer-Verlag Wien.

Altenbach, H., Gorash, Y., & Naumenko, K. (2008). Steady-state creep of a pressurized thick cylinder in both the linear and the power law ranges. Acta Mechanica, 195, 263-274. doi: 10.1007/s00707-007-0546-5.

An, L.L. (2015). The development of advanced creep constitutive equations for high chromium alloy steel (P91) at transition stress range (Doctor Thesis). University of Huddersfield. Retrieved from http://eprints.hud.ac.uk/26237/.

Ashby, M.F., & Jones, D.R.H. (1996). *Engineering Materials: v. 1: An Introduction to Their Properties and Application* (2nd Ed.). Oxford, UK: Butterworth-Heinemann.

Bailey, R.W. (1930). Creep of steel under simple and compound stress. Engineering. 121,129-265.

Basirat, M., Shrestha, T., Potirniche, G.P., Charit, I., & Rink, K. (2012). A study of the creep behavior of modified 9Cr–1Mo steel using continuum-

damage modeling. *International Journal of Plasticity, 37*, 95-107. doi: http://dx.doi.org/10.1016/j.ijplas.2012.04.004.

Cane, B.J. (1979). Interrelationship between creep deformation and creep rupture in 2.25Cr 1Mo steel. Metal Science, 13 (5), 287-294. doi: http://dx.doi.org/10.1179/03063453.1979.11674139.

Cane, B.J. (1981). Creep fracture of dispersion strengthened low alloy ferritic steels. *Acta Metallurgica, 29* (9), 1581-1591. doi: https://doi.org/10.1016/0001-6160(81)90040-7.

Cane, B.J., & Greenwood, G.W. (1975). The Nucleation and Growth of Cavities in Iron during Deformation at Elevated Temperatures. Metal Science, 9 (1), 55-60. doi: http://dx.doi.org/10.1179/030634575790444405.

Chen, Y.X., Yan, W., Hu, P., Shan, Y.Y., & Yang, K. (2011). CDM modeling of creep behavior of T/P91 steel under high stresses. Acta Metallurgica Sinica, 47 (11), 1372-1377. doi: 10.3724/SP.J.1037.2011.00309.

Chiantoni, G., Comi, C., Mariani, S., & Bonora, N. (2014). Experimental assessment of ductile damage in P91 steel at high temperature. International Journal of Damage Mechanics, 23 (4), 567-587. doi: https://doi.org/10.1177/1056789513503972.

Choudhary, B.K. (2013). Tertiary creep behaviour of 9Cr–1Mo ferritic steel. Materials Science and Engineering: A, 585, 1-9. doi: https://doi.org/10.1016/j.msea.2013.07.026.

Choudhary, B.K., & Samuel, E.I. (2011). Creep behaviour of modified 9Cr–1Mo ferritic steel. Journal of Nuclear Materials, 412 (1), 82-89. doi: https://doi.org/10.1016/j.jnucmat.2011.02.024.

Choudhary, B.K., Saroja, S., Rao, K.B.S., & Mannan, S.L. (1999). Creep-rupture behavior of forged, thick section 9Cr-1Mo ferritic steel. Metallurgical and Materials Transactions A, 30 (11), 2825-2834.

Christopher, J., Sainath, G., Srinivasan, V.S., Samuek, E.I., Choudhary, B.K., Mathew, M.D., & Jayakumar, T. (2013). Continuum Damage Mechanics Approach to Predict Creep Behaviour of Modified 9Cr-1Mo Ferritic Steel at

873 K. Procedia Engineering, 55, 798-804. doi: https://doi.org/10.1016/j.proeng.2013.03.334.

Czyrska-Filemonowicz, A., Zielińska-Lipiec, A., & Ennis, P.J. (2006). Modified 9% Cr steels for advanced power generation: microstructure and properties. *Journal of Achievements in Materials and Manufacturing Engineering. 19* (2), 43-48.Doi: http://jamme.acmsse.h2.pl/papers_vol19_2/1309.pdf

Dobrzański, J., Sroka, M., & Zieliński, A. (2006). Methodology of classification of internal damage the steels during creep service. *Journal of Achievements in Materials and Manufacturing Engineering, 18* (1-2), 263-266. Retrieved from http://jamme.acmsse.h2.pl/papers_amme06/1317.pdf

DTI (2005). Advanced PF Power Plant - Improved Materials for Boilers and Steam Turbines: Project Summary 292. DTI Cleaner Coal Technology Programme, URN 05/1687, DTI, UK. Retrieved from http://ukerc.rl.ac.uk/pdf/DTICC132_file30692.pdf

Dyson, B. & Mclean, M. (1998). Microstructural evolution and its effects on the creep performance of high temperature alloys. In: Straing A, Cawley J, Greenwood GW (eds). Microstructural stability of creep resistant alloys for high temperature plant applications. Cambridge University Press, Cambridge, 371-393.

Dyson, B. (2000). Use of CDM in materials modelling and component creep life prediction. Journal of Pressure Vessel Technology. 122, 281-296. doi:10.1115/1.556185.

Dyson, B.F. & Gibbons, T.B. (1987). Tertiary creep in nickel-base superalloys: analysis of experimental data and theoretical synthesis. Acta Metallurgica, 35 (9), 2355-2369. doi: https://doi.org/10.1016/0001-6160(87)90083-6.

Dyson, B.F. & Mclean, M. (2001). Micromechanism-quantification for creep constitutive equations. In S. Murakami & N. Ohno (Eds.) IUTAM Symposium on Creep in Structures (1st Ed.) (pp. 3-16)

Dyson, B.F. (1983). Continuous cavity nucleation and creep rupture. Scripta Metallurgica. 17, 31-37. Doi: https://doi.org/10.1016/0036-9748(83)90065-0.

Dzięcioł K.P. (2010). Four dimensional characterisation of creep cavity growth in copper (Doctoral thesis). Retrieved from http://www-brs.ub.ruhr-uni-bochum.de/netahtml/HSS/Diss/DzieciolKrzysztofPiotr/diss.pdf

ECCC (2005). Recommendations for Creep Data Validation AND Assessment Procedures, 1(6). In S. R. Holdsworth eds. Retrieved from http://www.ommi.co.uk/etd/eccc/advancedcreep/V1i6x.pdf

Eggeler, G. (1989). The effect of long-term creep on particle coarsening in tempered martensite ferritic steels. *Acta Metallurgica, 37* (12), 3225-3234. doi: https://doi.org/10.1016/0001-6160(89)90194-6.

Eggeler, G., Earthman, J.C., Nilsvang, N., & Ilschner, B. (1989). Microstructural study of creep rupture in a 12% chromium ferritic steel. Acta Metallurgica, 37 (1), 49-60. doi: https://doi.org/10.1016/0001-6160(89)90265-4.

Ennis, P. J., Czyrska-Filemonowicz, A. (2003). Recent advances in creep-resistant steels for power plant applications, Sadhana, 28 (3-4), 709-730. doi: https://doi-org.libaccess.hud.ac.uk/10.1007/BF02706455.

Ennis, P.J., Zielinska-Lipiec, A., Wachter, O., & Czyrska-Filemonowicz, A. (1997). Microstructural stability and creep rupture strength of the martensitic steel P92 for advanced power plant. *Acta Materialia, 45* (12), 4901-4907. doi: https://doi.org/10.1016/S1359-6454(97)00176-6.

European Commission. (Last update: 17/07/2017). Causes of climate change. Retrieved from https://ec.europa.eu/clima/change/causes_en.

Feuillette, C., Schmidt, K., Maile, K., Klenk, A., & Roos, E. (2010). New Concepts for Integrity and Lifetime Assessment of Boiler and Turbine Components for Advanced Ultra-Supercritical Fossil Plants. In D. Gandy, J. Shingledecker, & R. Viswanathan (Eds.) *Advances in Materials Technology for Fossil Power Plants* Proceedings from the Sixth International Conference

August 31–September 3, 2010. Santa Fe, New Mexico, USA (pp. 603-619). The United States of America: ASM International.

French, D.N. (1993). *Metallurgical Failures in Fossil Fired Boilers* (2nd Ed.). Chapter 3: Metallugical principles: ferritic steels. New York, United States: John Wiley and Sons Ltd.

Gaffard, V., Gourgues-Lorenzon, A.F., & Besson, J. (2005). High temperature creep flow and damage properties of 9Cr1MoNbV steels: Base metal and weldment. Nuclear Engineering and Design, 24, 2547-2562. doi: https://doi.org/10.1016/j.nucengdes.2005.07.001.

Ghosh, R.N. (2013). Creep Life Predictions of Engineering Components: Problems & Prospects. *Procedia Engineering, 55*, 599-606. doi: https://doi.org/10.1016/j.proeng.2013.03.301.

Gooch, D.J. (1982). Creep fracture of 12Cr–Mo–V steel. *Metal Science, 16* (2), 79-89. doi: http://dx.doi.org/10.1179/030634582790427190.

Gorash, Y. (2008). Development of a creep-damage model for non-isothermal long-term strength analysis of high-temperature components operating in a wide stress range(Doctor thesis). Zentrum für Ingenieurwissenschaften, Martin-Luther-University Halle-Wittenberg, Halle (Saale), Germany. Retrieved from https://sundoc.bibliothek.uni-halle.de/diss-online/08/08H154/prom.pdf.

Goyal, S., & Laha, K. (2014). Creep life prediction of 9Cr–1Mo steel under multiaxial state of stress. Materials Science and Engineering: A, 615, 348-360. doi: https://doi.org/10.1016/j.msea.2014.07.096.

Goyal, S., Laha, K., Das, C.R., Panneerselvi, S., & Mathew, M.D. (2014). Effect of Constraint on Creep Behavior of 9Cr-1Mo Steel. Metallurgical and Materials Transactions A, 45 (2), 619-632. doi: 10.1007/s11661-013-2025-z.

Guguloth, K., & Roy, N. (2017). Creep deformation behavior of 9Cr1MoVNb (ASME Grade 91) steel. Materials Science and Engineering: A, 680, 388-404. doi: https://doi.org/10.1016/j.msea.2016.10.112.

Gupta, C., Toda, H., Mayr, P., & Sommitsch, C. (2015). Materials Science and Technology. 3D creep cavitation characteristics and residual life assessment

in high temperature steels: a critical review, 3` (5), 603-626. doi: 10.1179/1743284714Y.0000000693.

Gupta, C., Toda, H., Schlacher, C., Adachi, Y., Mayr, P., Sommitsch , C. ... Kobayashi, M. (2013). Study of creep cavitation behavior in tempered martensitic steel using synchrotron micro-tomography and serial sectioning techniques. Materials Science & Engineering A, 564, 525-538. doi: https://doi.org/10.1016/j.msea.2012.12.002.

Hald, J. (2008). Microstructure and long-term creep properties of 9–12% Cr steels. International Journal of Pressure Vessels and Piping, 85 (1-2), 30-37. doi: https://doi.org/10.1016/j.ijpvp.2007.06.010.

Hayhurst, D.R. (2001). Computational continuum damage mechanics: its use in the predication of creep in structures-past, present and future. In S. Murakami & N. Ohno (Eds.) IUTAM Symposium on Creep in Structures (1st Ed.) (pp. 175-188).

Hayhurst, D.R., Dimmer, P.R., & Morrison, C.J. (1984). Development of continuum damage in the creep rupture of notched bars. Philosophical Transactions of the Royal Society A, 311 (1516), 103-129. doi: 10.1098/rsta.1984.0021.

Hayhurst, D.R., Hayhurst, R.J., & Vakili-tahami, F. (2005). Continuum damage mechanics predictions of creep damage initiation and growth in ferritic steel weldments in a medium bore branched pipe under constant pressure at 590 8C using a five-material weld model. Proceedings of THE ROYAL SOCIETY A, 461, 2303-2326. doi:10.1098/rspa.2005.1488.

Hayhurst, D.R., Lin, J., & Hayhurst, R.J. (2008). Failure in notched tension bars due to high-temperature creep: Interaction between nucleation controlled cavity growth and continuum cavity growth. International Journal of Solids and Structures, 45, 2233-2250. doi: https://doi.org/10.1016/j.ijsolstr.2007.11.026.

Holdsworth, S.R. (2008). Constitutive equations for creep curves and predicting service life. In F. Abe, T. Kern, & R. Viswanathan (Eds.) Creep-resistant steels (pp. 403-420). Cambridge England: Wood Publishing Limited.

Holdsworth, S.R., & Merckling, G. (2003). ECCC Developments in the Assessment of Creep-Rupture Properties. Retrieved from http://www.ommi.co.uk/etd/eccc/advancedcreep/srhgmpap1.pdf.

Hyde, T., Sun, W., & Hyde, C. (2013). Applied Creep Mechanics (1st Ed.). New York et al.: McGraw-Hill Education.

Hyde, T.H., Becker, A.A., Sun, W., & Williams, J.A. (2006). Finite-element creep damage analyses of P91 pipes. International Journal of Pressure Vessels and Piping, 83 (11-12), 853-863. doi: https://doi.org/10.1016/j.ijpvp.2006.08.013.

International Energy Agency. (2015). Energy Climate and Change, World Energy Outlook Special Report. Retrieved from https://www.iea.org/publications/freepublications/publication/WEO2015SpecialReportonEnergyandClimateChange.pdf.

Isik, M.I., Kostka, A., & Eggeler, G. (2014). On the nucleation of Laves phase particles during high-temperature exposure and creep of tempered martensite ferritic steels. Acta Materialia. 81, 230-240. doi: https://doi.org/10.1016/j.actamat.2014.08.008.

Jones, D.R.H. (2004). Creep failures of overheated boiler, superheater and reformer tubes. Engineering Failure Analysis, 11 (6), 873-893. doi: https://doi.org/10.1016/j.engfailanal.2004.03.001.

Kassner, M. E. (Ed.) (2008). Fundamentals of Creep in Metals and Alloys (2nd Ed.). Oxford, United Kingdom: Elsevier Science & Technology.

Kassner, M.E. & Hayes, T.A. (2003). Creep cavitation in metals. International Journal of Plasticity, 19 (10), 1715-1748. doi: https://doi.org/10.1016/S0749-6419(02)00111-0.

Kim, W.G., Kim, S.H., & L, C.B. (2011). Long-Term Creep Characterization of Gr. 91 Steel by Modified Creep Constitutive Equations. Metals and Materials International, 17 (3), 497-504. doi: 10.1007/s12540-011-0630-1.

Kimura, K., Kushima, H., & Sawada, K. (2009). Long-term creep deformation property of modified 9Cr–1Mo steel. Materials Science and Engineering: A, 510-511 , 58-63. doi: https://doi.org/10.1016/j.msea.2008.04.095.

Kimura, K., Sawada, K., & Kushima, H. (2010). Long-term creep strength property of advanced ferritic creep resistant steels. In D. Gandy, J. Shingledecker, & R. Viswanathan (Eds.) Advances in Materials Technology for Fossil Power Plants Proceedings from the Sixth International Conference August 31–September 3, 2010. Santa Fe, New Mexico, USA (pp. 732-751). The United States of America: ASM International.

Kimura, K., Sawada, K., Kushima, H., & Kubo, K. (2008). Effect of stress on the creep deformation of ASME Grade P92/T92 steels Read More: http://www.hanser-elibrary.com/doi/abs/10.3139/146.101651. International Journal of Materials Research, 99 (4), 395-401. doi: https://doi.org/10.3139/146.101651.

Kipelova, A., Belyakov, A., & Kaibyshev, R. (2012). Laves phase evolution in a modified P911 heat resistant steel during creep at 923 K. *Materials Science and Engineering: A, 532*, 71-77. Doi: https://doi.org/10.1016/j.msea.2011.10.064.

Kloc, L., & Sklenička, V. (2004). Confirmation of low stress creep regime in 9% chromium steel by stress change creep experiments. *Materials Science and Engineering: A, 387–389* (15), 633-638. doi: https://doi.org/10.1016/j.msea.2003.12.078.

Kloc, L., Skienička, V., & Ventruba, J. (2001). Comparison of low stress creep properties of ferritic and austenitic creep resistant steels. *Materials Science and Engineering: A, 319-321*, 774-778. doi: https://doi.org/10.1016/S0921-5093(01)00943-1.

Klueh, R.L. & Harries, D.R. (2001). *High-Chromium Ferritic and Martensitic Steels for Nuclear Applications*. New York, USA. American Society for Testing and Materials, 5-27.

Kowalewski, Z.L., Hayhurst, D.R., & Dyson, B.F. (1994). Mechanisms-based creep constitutive equations for an aluminium alloy. The Journal of Strain

Analysis for Engineering Design, 29 (4), 309-316. doi: https://doi-org.libaccess.hud.ac.uk/10.1243/03093247V294309.

Landron, C., Maire, E., Bouaziz, O., Adrien, J., Lecarme, L., & Bareggi , A. (2011). Validation of void growth models using X-ray microtomography characterization of damage in dual phase steels. Acta Materialia, 59 (20), 7564-7573. doi: https://doi.org/10.1016/j.actamat.2011.08.046.

Lee, J.S., Armaki, H.G., Maruyama, K., Muraki, T., & Asahi, H. (2006). Causes of breakdown of creep strength in 9Cr–1.8W–0.5Mo–VNb steel. Materials Science and Engineering: A, 428 (1-2), 270-275. doi: https://doi.org/10.1016/j.msea.2006.05.010.

Lin, J., Liu, Y., & Dean, T.A. (2005). A Review on Damage Mechanisms, Models and Calibration Methods under Various Deformation Conditions. International Journal of Damage Mechanics, 14 (4), 299-319. doi: https://doi.org/10.1177/1056789505050357.

Maruyama, K., Sawada, K., Koike, J. (2001). Strengthening Mechanisms of Creep Resistant Tempered Martensitic Steel, ISIJ International, 41(6), 641-653. doi: 10.2355/isijinternational.41.641.

Maruyama, K. (2008). Fracture mechanism map and fundamental aspects of creep fracture. In F. Abe, T. Kern, & R. Viswanathan (Eds.) Creep-resistant steels (pp. 350-364). Cambridge England: Woodhead Publishing Linited and CRC Press LLC.

Maruyama, K., Armaki, H.G., Chen, R.P., Yoshimi, K., Yoshizawa, M., & Igarashi, M. (2010). Creep strength of high chromium steel with ferrite matrix. International Journal of Pressure Vessels and Piping, 87 (6), 276-281. doi: https://doi.org/10.1016/j.ijpvp.2010.03.012.

Massé, T. & Lejeail, Y. (2012). Creep behaviour and failure modelling of modified 9Cr1Mo steel. Nuclear Engineering and Design, 246, 220-232. doi: https://doi.org/10.1016/j.nucengdes.2012.02.006.

Massé, T. & Lejeail, Y. (2013). Creep mechanical behaviour of modified 9Cr1Mo steel weldments: Experimental analysis and modelling. Nuclear

Engineering and Design, 254, 97-110. doi: https://doi.org/10.1016/j.nucengdes.2012.09.007.

Masuyama, F. (2006). Advance power plant developments and materials experience in Japan. In Proc 8th Liege Conference September 2006, Liege, Belgium, Research Centre Julich, 2006, Eds. J Lecompte-Beckers et al, Vol. 53 Part I 175-187.

Masuyama, F. (2016). *Introduction to New CSEF 'Miracle' Steel P93.* Poster presented at International conference on experience with the manufacture, welding, quality control and use of T/P91-92, T/P23-24 steels, 20-22 April 2016, Wuhan, China.

Miannay, D.P. (2001). *Time-Dependent Fracture Mechanics*. New York: Springer-Verlag.

Mustata, R. & Hayhurst, D.R. (2005). Creep constitutive equations for a 0.5Cr 0.5 Mo 0.25V ferritic steel in the temperature range 565 °C–675 °C. International Journal of Pressure Vessels and Piping, 82 (5), 363-372. doi: https://doi.org/10.1016/j.ijpvp.2004.11.002.

Nakajima, T., Spigarelli, S., Evangelista, E., & Endo, T. (2003). Strain Enhanced Growth of Precipitates during Creep of T91. *Materials Transactions. 44* (9), 1802-1808. Doi: https://www.jim.or.jp/journal/e/pdf3/44/09/1802.pdf.

Nandi, S., Vikrant, K., Ahv, P., Singh, K., & Ghosh, R.N. (2013). Creep Modelling of P91 Steel for High Temperature Power Plant Applications. Procedia Engineering, 55, 751-755. doi: https://doi.org/10.1016/j.proeng.2013.03.326.

National Institute for Materials Science (NIMS), Japan. (2014). Data Sheets on the Elevated-temperature Properties of 9Cr-1Mo-V-Nb Steel Tubes for Boilers and Heat Exchangers (ASME SA-213/SA-213M Grade T91), 9Cr-1Mo-V-Nb Steel Plates for Boilers and Pressure Vessels (ASME SA-387/SA-387M Grade 91) and 9Cr-1Mo-V-Nb Steel Seamless Pipe for High Temperature Service (ASME SA-385/SA-385M Grade P91). No.43A. Retrieved from http://smds.nims.go.jp/openTest/en/content/creeplist.html.

Naumenko, K. & Kostenko, Y. (2009). Structural analysis of a power plant component using a stress-range-dependent creep-damage constitutive model. Materials Science and Engineering: A, 510-511, 169-174. doi: https://doi.org/10.1016/j.msea.2008.04.096.

Needham, N.G. & Gladman, T. (1980). Nucleation and growth of creep cavities in a Type 347 steel. Metal Science, 14 (2), 64-72. doi: http://dx.doi.org/10.1179/030634580790426300.

Needham, N.G. (Ed.) (1983). Technical steel research, Properties and service performance, Cavitation and fracture in creep resisting steels, Report: EUR 8121 EN. LUXEMBOURG: Commission of the European Communities.

Ni, Y.Z., Lan, X., Xu, H., & Mao, X.P. (2015). Study on creep mechanical behaviour of P92 steel under multiaxial stress state. Materials at High Temperatures, 32 (6), 551-556. doi: http://dx.doi.org/10.1179/1878641315Y.0000000001.

Nie, N., Zhang, J., Huang, F., Liu, J.W., Zhu, X.K., Chen, Z.L., & Ouyang, L.Z. (2014). Microstructure evolution and life assessment of T92 steel during long-term creep. Journal of Alloys and Compounds, 588 (5), 348-356. doi: https://doi.org/10.1016/j.jallcom.2013.11.080.

Norton, F.H. (1929). The creep of steel at high temperatures. New York: McGraw-Hill book company, Inc. Retrieved from https://archive.org/details/creepofsteelathi00nort.

Nuclear Energy University Programs (NEUP). (2013). Prediction and Monitoring Systems of Creep-Fracture Behavior of 9Cr- 1Mo Steels for Reactor Pressure Vessels. Retrieved from http://www.iaea.org/inis/collection/NCLCollectionStore/_Public/47/066/47066543.pdf.

Office for Nuclear Regulation, Health and Safety Executive (2012). Nuclear Research Index 2012/13. An agency of HSE. Section D. Retrieved from http://www.onr.org.uk/research/2011/section-i.pdf.

Oruganti, R., Karadge, M., & Swaminathan, S. (2011). Damage mechanics-based creep model for 9–10%Cr ferritic steels. *Acta Materialia, 59*, 2145-2155. doi: https://doi.org/10.1016/j.actamat.2010.12.015.

Palaparti, D.P.R., Samuel, E.I., Choudhary, B.K., & Mathew, M.D. (2013). Creep Properties of Grade 91 Steel Steam Generator Tube at 923K. Procedia Engineering, 55, 70-77. doi: https://doi.org/10.1016/j.proeng.2013.03.221.

Panait, C.G., Bendick, W., Fuchsmann, A., Gourgues-Lorenzon, A.-.F., & Besson, J. (2010). Study of the microstructure of the Grade 91 steel after more than 100,000 h of creep exposure at 600 °C. International Journal of Pressure Vessels and Piping, 87 (6), 326-335. doi: https://doi.org/10.1016/j.ijpvp.2010.03.017.

Parker, J. (2013). In-service behavior of creep strength enhanced ferritic steels Grade 91 and Grade 92 – Part 1 parent metal. International Journal of Pressure Vessels and Piping, 101, 30-36. doi: https://doi.org/10.1016/j.ijpvp.2012.10.001.

Perrin, I.J. & Hayhurst, D.R. (1996). Creep constitutive equations for a 0.5Cr–0.5Mo–0.25V ferritic steel in the temperature range 600–675°C. *The Journal of Strain Analysis for Engineering Design, 31* (4), 299-314. doi: https://doi.org/10.1243/03093247V314299.

Pétry, C. & Lindet, G. (2009). Modelling creep behaviour and failure of 9Cr–0.5Mo–1.8W–VNb steel. International Journal of Pressure Vessels and Piping, 86 (8), 486-494. doi: https://doi.org/10.1016/j.ijpvp.2009.03.006.

Raj, R. & Ashby, M.F. (1975). Intergranular fracture at elevated temperature. Acta Metallurgica, 23 (6), 653-666. doi: https://doi.org/10.1016/0001-6160(75)90047-4.

Renversade, L., Ruoff, H., Maile, K., Sket, F., & Borbely, A. (2014). Microtomographic assessment of damage in P91 and E911 steels after long-term creep. International Journal of Materials Research, 105 (7), 621-627. doi: DOI: 10.3139/146.111056.

Riedel, H. (1987). 12 Constrained Diffusive Cavitation of Grain Boundaries. Fracture at High Temperature (pp. 172-197). Berlin, Heidelberg: Springer-Verlag.

Riedel, H. (1987). 6 Nucleation of Creep Cavities/Basic Theories. Fracture at High Temperature (pp. 67-84). Berlin, Heidelberg: Springer-Verlag.

Riedel, H. (1987). Fracture at High Temperatures (1st Ed.). Berlin Heidelberg GmbH: Springer-Verlag.

Rouse, J.P., Sun, W., Hyde, T.H., & Morris, A. (2013). Comparative assessment of several creep damage models for use in life prediction. International Journal of Pressure Vessels and Piping, 108-109, 81-87. doi: https://doi.org/10.1016/j.ijpvp.2013.04.012.

Saeidi, N., Ashrafizadeh , F., Niroumand, B., Forouzan, M.R., & Barlat, F. (2014). Damage mechanism and modeling of void nucleation process in a ferrite–martensite dual phase steel. Engineering Fracture Mechanics, 127 , 97-103. doi: https://doi.org/10.1016/j.engfracmech.2014.05.017.

Samuel, E.I., Choudhary, B.K., Palaparti, D.P.R., & Mathew, M.D. (2013). Creep Deformation and Rupture Behaviour of P92 Steel at 923 K. Procedia Engineering, 55, 64-69. doi: https://doi.org/10.1016/j.proeng.2013.03.220.

Sawada, K., Kushima, H., Tabuchi, M., & Kimura, K. (2011). Microstructural degradation of Gr.91 steel during creep under low stress. *Materials Science and Engineering A, 528*, 5511-5518. doi: https://doi.org/10.1016/j.msea.2011.03.073.

Sawada, K., Kubo, K., & Abe, F. (2001). Creep behavior and stability of MX precipitates at high temperature in 9Cr–0.5Mo–1.8W–VNb steel. Materials Science and Engineering: A, 319-321 , 784-787. doi: https://doi.org/10.1016/S0921-5093(01)00973-X.

Sawada, K., Kushima, H., Hara, T., Tabuchi, M., & Kimura, K. (2014). Heat-to-heat variation of creep strength and long-term stability of microstructure in Grade 91 steels. Materials Science and Engineering: A, 597 (12), 164-170.

Semba, H., Dyson, B., & Mclean, M. (2008). Microstructure-based creep modelling of a 9%Cr matensitic steel. Materials at high temperatures, 25 (3), 131-137. doi: http://dx.doi.org/10.3184/096034008X354873.

Seo, D., Toda, H., Kobayashi, M., Uesugi, K., Takeuchi, A., & Suzuki, Y. (2015). The Iron and Steel Institute of Japan(ISIJ) International . In Situ Observation of Void Nucleation and Growth in a Steel using X-ray Tomography, 55 (7), 1474-1482. doi: http://doi.org/10.2355/isijinternational.55.1474.

Shigeyama, H., Sugiura, R., Matsuzaki, T., & Yokobori, A.T. (2014). Micro- and macro-creep damage formation for P92 under multiaxial stress related to circular notched specimen. Materials Science and Technology, 30 (1), 43-49. doi: http://dx.doi.org/10.1179/1743284713Y.0000000310.

Shinya, N., Kyono, J., & Kushima, H. (2006). Creep Fracture Mechanism Map and Creep Damage of Cr–Mo–V Turbine Rotor Steel. ISIJ International, 46 (10), 1516-1522. doi: 10.2355/isijinternational.46.1516. Retrieved from http://www.readcube.com/articles/10.2355/isijinternational.46.1516.

Shrestha, T., Basirat, M., Charit, I., Potirniche, G.P., & Rink, K.K. (2013). Creep rupture behavior of Grade 91 steel. Materials Science and Engineering: A, 565, 382-391. doi: https://doi.org/10.1016/j.msea.2012.12.031.

Sket, F., Dzieciol, K., Borbély, A., Kaysser-Pyzalla, A.R., Maile, K., & Scheck, R. (2010). Microtomographic investigation of damage in E911 steel after long term creep. Materials Science and Engineering: A, 528 (1), 103-111. doi: https://doi.org/10.1016/j.msea.2010.07.029.

Sklenička, V., Kuchařová, K., Svoboda, M., Kloc, L., Buršı, J., & Kroupa, A. (2003). Long-term creep behavior of 9–12%Cr power plant steels. *Materials Characterization, 51* (1), 35-48. doi: https://doi.org/10.1016/j.matchar.2003.09.012.

Strang, A. (Ed.) (2000). Materials for High Temperature Power Generation and Process Plant Applications. London: Institute of Materials (IOM) Communications Ltd.

Tada, N., Kitamura, T., & Ohtani, R. (1996). Relationship Between Creep Damage Parameters And Distribution Of Creep Cavities On Grain Boundaries. Wessex Institute of Technology (WIT) Transactions on Engineering Sciences, 13, 535-542. doi: 10.2495/LD960531. Retrieved from https://www.witpress.com/Secure/elibrary/papers/LD96/LD96053FU.pdf.

U.S. Energy Information Administration (2016). International Energy Outlook 2016. Retrieved from https://www.eia.gov/outlooks/ieo/pdf/electricity.pdf.

VANAJA, J. & Laha, K. (2015). Assessment of Tungsten Content on Tertiary Creep Deformation Behavior of Reduced Activation Ferritic–Martensitic Steel. Metallurgical and Materials Transactions A, 46A, 4669-4679. doi: 10.1007/s11661-015-3075-1.

Vanaja, J., Laha, K., Mythili, R., Chandravathi, K.S., Saroja, S., & Mathew, M.D. (2012). Creep deformation and rupture behaviour of 9Cr–1W–0.2V–0.06Ta Reduced Activation Ferritic–Martensitic steel. Materials Science and Engineering: A, 533 (30), 17-25. doi: https://doi.org/10.1016/j.msea.2011.10.112.

Westwood, C., Pan, J., & Crocombe, A.D. (2004). Nucleation, growth and coalescence of multiple cavities at a grain-boundary. European Journal of Mechanics - A/Solids, 23 (4), 579-597. doi: https://doi.org/10.1016/j.euromechsol.2004.02.001.

World Nuclear Organization. (Updated June 2017). World Energy Needs and Nuclear Power. Retrieved from http://www.world-nuclear.org/information-library/current-and-future-generation/world-energy-needs-and-nuclear-power.aspx.

Worswick, M.J., Chen, Z.T., Pilkey, A.K., Llody, D., & Court, S. (2001). Damage characterization and damage percolation modelling in aluminum alloy sheet. Acta Materialia, 49 (14), 2719-2803. doi: https://doi.org/10.1016/S1359-6454(01)00163-X.

Wu, R., & Sandström, R. (1995). Creep cavity nucleation and growth in 12Cr–Mo–V steel. Materials Science and Technology, 11 (6), 579-588. doi: http://dx.doi.org/10.1179/mst.1995.11.6.579.

Xu Q, Yang X, &Lu, Z. (2017a). On the development of creep damage constitutive equations, keynote presentation, In HIDA-7: Life/Defect Assessment & Failures in High Temperature Industrial Structures, 15-17 May 2015, Portsmouth University, England.

Xu, Q. & Barrans, S. (2003). The Development of Multi-axial Creep Damage Constitutive Equations for 0.5Cr0.5Mo0.25V Ferritic Steel at 590°C. International Journal Series A Solid Mechanics and Material Engineering, 46 (1), 51-59. doi: http://doi.org/10.1299/jsmea.46.51.

Xu, Q. & Simon, B. (2003). The Development of Multi-axial Creep Damage Constitutive Equations for 0.5Cr0.5Mo0.25V Ferritic Steel at 590℃. *JSME International Journal Series A Solid Mechanics and Material Engineering, 46* (1), 51-59. doi: http://doi.org/10.1299/jsmea.46.51.

Xu, Q. (2001). Creep damage constitutive equations for multi-axial states of stress for 0.5Cr0.5Mo0.25V ferritic steel at 590°C. Theoretical and Applied Fracture Mechanics, 36 (2), 99-107. doi: https://doi.org/10.1016/S0167-8442(01)00060-X.

Xu, Q. (2004). The development of validation methodology of multi-axial creep damage constitutive equations and its application to 0.5Cr0.5Mo0.25V ferritic steel at 590 °C. *Nuclear Engineering and Design, 228* (1-3), 97-106. doi: https://doi.org/10.1016/j.nucengdes.2003.06.021.

Xu, Q., Lu, Z.Y., & Wang, X. (2013). Damage Modelling: the current state and the latest progress on the development of creep damage constitutive equations for high Cr steels. In In 6th International 'HIDA' Conference: Life/Defect Assessment & Failures in High Temperature Plant, 2nd – 4th December 2013, Nagasaki, Japan.

Xu, Q., Lu, Z.Y., & Wang, X. (2017b). Damage modelling: the current state and the latest progress on the development of creep damage constitutive equations for high Cr steels. *Materials at High Temperatures, 34* (3), 229-237. doi: http://dx.doi.org/10.1080/09603409.2017.1289613.

Xu, Q., Group Resesrch Meeting, May 2017, Huddersfield University.

Xu, Q., Lu, Z., & Wang, X. (2017). Damage modelling: the current state and the latest progress on the development of creep damage constitutive equations for high Cr steels. Materials at High Temperatures, 34 (3), 229-237.

Xu, Q.H. (2016) Development of Advanced Creep Damage Constitutive Equations for Low CR Alloy under Long Term Service (Doctor Thesis). University of Huddersfield. Retrieved from http://eprints.hud.ac.uk/27858/.

Yadav, S.D., Rosc, J., Sartory, B., Brunner, R., Sondergger, B., Sommitsch, C., & Poletti, C. (2014). INVESTIGATION OF PRE-EXISTING PORES IN CREEP LOADED 9Cr STEEL. In Proceedings of the 2nd International Congress on 3D Materials Science.pp 85-90. June 29 – July 2, 2014. Annecy, France, TMS (The Minerals, Metals & Materials Society) Retrieved from DOI: 10.1007/978-3-319-48123-4_14.

Yadav, S.D., Sonderegger, B., Sartory, B., Sommitsch, C., & Poletti, C. (2015). Characterisation and quantification of cavities in 9Cr martensitic steel for power plants. Materials Science and Technology, 31 (5), 554-564. doi: DOI 10.1179/1743284714Y.0000000635.

Yang, X., Lu, Z. and Xu, Q. (2015). The Interpretation of Experimental Observation Data for the Development of Mechanisms based Creep Damage Constitutive Equations for High Chromium Steel. In: IEEE International Conference on Automation and Computing (ICAC 2015), 11th - 12th September 2015, Glasgow, Scotland.

Yang, X., Xu, Q. and Lu, Z. (2013). The Development and Validation of the Creep Damage Constitutive Equations for P91 Alloy. In: Proceedings of the 2013 World Congress in Computer Science and Computer Engineering and Application. CSREA Press. 121-127. ISBN 1-60132-238-0.

Yang, X., Xu, Q., & Lu, Z.Y. (2013). The relative significance of internal damage mechanisms on the overall creep damage and ultimate failure of P91 steel. In 6th International 'HIDA' Conference: Life/Defect Assessment & Failures in High Temperature Plant, 2nd – 4th December 2013, Nagasaki, Japan.

Yao, H.T., Xuan, F.Z., Wang, Z.D., & Tu, S.T. (2007). A review of creep analysis and design under multi-axial stress states. Nuclear Engineering and Design, 237 (18), 1969-1986. doi: https://doi.org/10.1016/j.nucengdes.2007.02.003.

Yin, Y.F. & Faulkner, R.G. (2006). Continuum damage mechanics modelling based on simulations of microstructural evolution kinetics. *Materials Science and Technology, 22* (8), 929-936. doi: 10.1179/174328406X102426.

Zhu, S., Yang, M., Song, X.L., Tong, S., & Xiang, Z.D. (2014). Characterisation of Laves phase precipitation and its correlation to creep rupture strength of ferritic steels. Materials Characterization, 98, 60-65. doi: https://doi.org/10.1016/j.matchar.2014.10.004.

Appendix A-Details of high chromium steels, chemical compositions in wt.%

Table Chemical compositions of 9-12wt% chromium steel (Strang, 2000)

	X20	P91	E911	NF616	HCM12A	TB12M	NF12
C %	0.17–0.23	0.08–0.12	0.10–0.13	0.07–0.13	0.07–0.14	0.10–0.15	0.08
Si %	0.5 max.	0.20–0.50	0.10–0.30	0.5 max.	0.5 max.	0.5 max.	0.05
Mn %	1.00 max.	0.30–0.60	0.30–0.60	0.30–0.60	–	0.40–0.60	0.5
P %	0.030 max.	0.020 max.	0.020 max.	0.020 max.	0.020 max.	0.020 max.	–
S %	0.030 max.	0.010 max.	0.010 max.	0.010 max.	0.010 max.	0.010 max.	–
Cr %	10.00–12.50	8.00–9.50	8.50–9.50	8.50–9.50	10.00–12.50	11.0–11.3	11.0
Mo %	0.80–1.20	0.85–1.05	0.90–1.10	0.30–0.60	0.25–0.60	0.40–0.60	0.15
Ni %	0.30–0.80	0.40 max.	0.40 max.	0.40 max.	0.50 max.	0.70–1.00	0.5
Nb %	–	0.06–0.10	0.06–0.10	0.04–0.10	0.04–0.10	0.04–0.09	0.07
V %	0.25–0.35	0.18–0.25	0.15–0.25	0.15–0.25	0.15–0.30	0.15–0.25	0.2
W %	–	–	0.90–1.10	1.50–2.00	1.50–2.50	1.60–1.90	2.6
Al %	–	0.04 max.	–	0.04 max.	0.04 max.	0.010 max.	–
N %	–	0.030–0.070	0.05–0.08	0.030–0.070	0.040–0.100	0.04–0.09	0.05
B %	–	–	–	0.001–0.006	0.005 max.	–	0.004
Co %	–	–	–	–	–	–	2.5

Table Chemical compositions of 9wt% chromium steel (Ennis, P. J., Czyrska-Filemonowicz, A., 2003)

Element	P9	P91	P92	E911
C	max. 0·15	0·10	0·124	0·105
Si	0·20–0·65	0·38	0·02	0·20
Mn	0·80–1·30	0·46	0·47	0·35
P	max. 0·030	0·020	0·011	0·007
S	max. 0·030	0·002	0·006	0·003
Cr	8·5–10·5	8·10	9·07	9·16
Mo	1·70–2·30	0·92	0·46	1·01
W	–	–	1·78	1·00
V	0·20–0·40	0·18	0·19	0·23
Nb	0·30–0·45	0·073	0·063	0·068
B	–	–	0·003	-
N	–	0·049	0·043	0·072
Ni	max. 0·30	0·33	0·06	0·07
Al	–	0·034	0·002	–
Form and dimensions, mm		pipe, Ø159, 20 wall thickness	pipe, Ø300, 40 wall thickness	flat bar, 100 × 16
Heat treatment		1 h/1050°C+ 1 h/750°C,	2 h/1070°C+ 2 h/775°C,	1 h/1050°C+ 1 h/750°C,
1,00,000 h stress rupture strength at 600°C, MPa*	35	94	115	110

Appendix B-Experimental observation of fracture surface for high chromium steel

In 1989, microstructural study of creep rupture in a 12% chromium ferritic steel (type X22 12Mo-1Mo-V steel) was reported by Eggeler et al., a SEM image of the rupture surface on the specimen under 175MPa at 923K (650℃) is shown in Figure 2.15 . The strain at fracture is 40% and the specimen has a ductile fracture characterized by large and sharp dimples (marked in blue arrows) containing second phase particles (Eggeler et al., 1989).

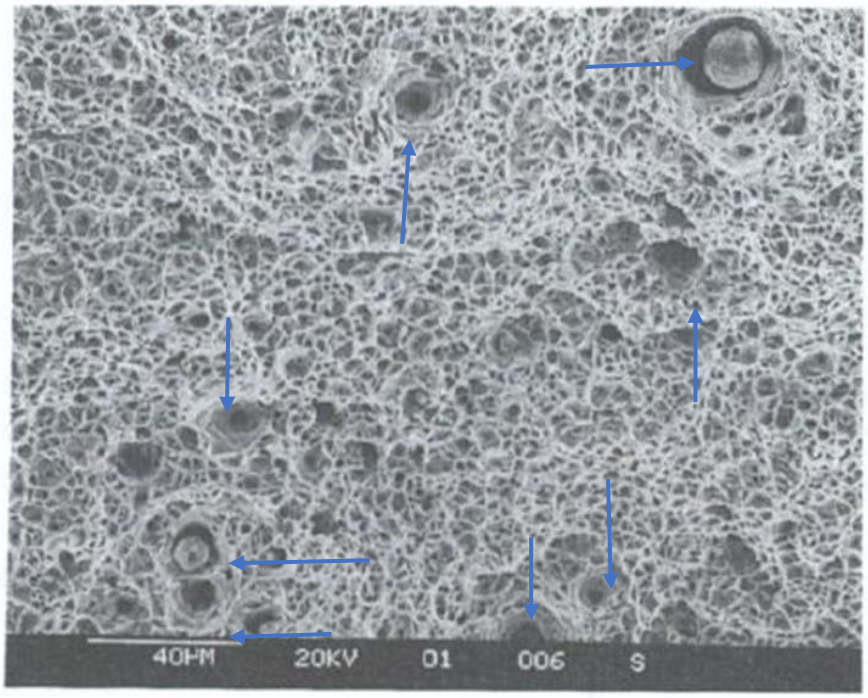

Figure 2.41 SEM image of the rupture surface of a 12% chromium ferritic steel (type X22 12Mo-1Mo-V steel) under 175MPa at 650℃ (Eggeler et al., 1989).

An optical micrograph of the surface of the specimen at strain 5% under 80MPa at 923K (650℃), as shown in Figure 2.16, indicates that cavities are not only found on former austenite grain boundaries (cavities on grain boundaries marked in yellow arrows) but also in former austenite grains (cavities in grains marked in blue arrows).

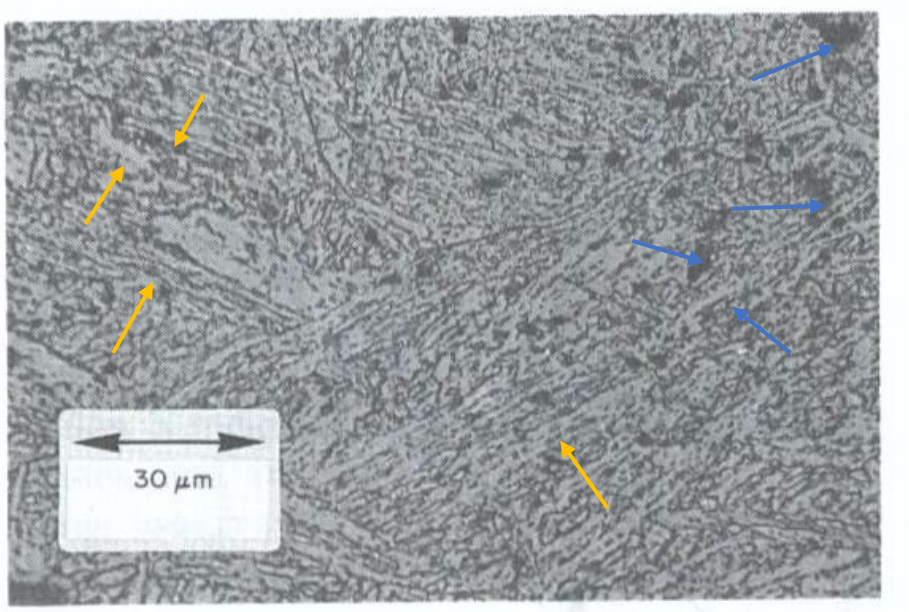

Figure 2.42 Optical micrograph of a specimen at strain 5% under 80MPa at 923K (650℃) shows cavities are found on grain boundaries and within grains (Eggeler et al., 1989).

In 1999, Creep rupture behavior of forged, thick section 9Cr-1Mo Ferritic Steel was studied by Choudhary et al. The specimen's fracture on the surface was characteristic of a transgranular fracture and cavities on any grain boundary facets through SEM images as shown in Figure 2.17(Choudhary et al., 1999).

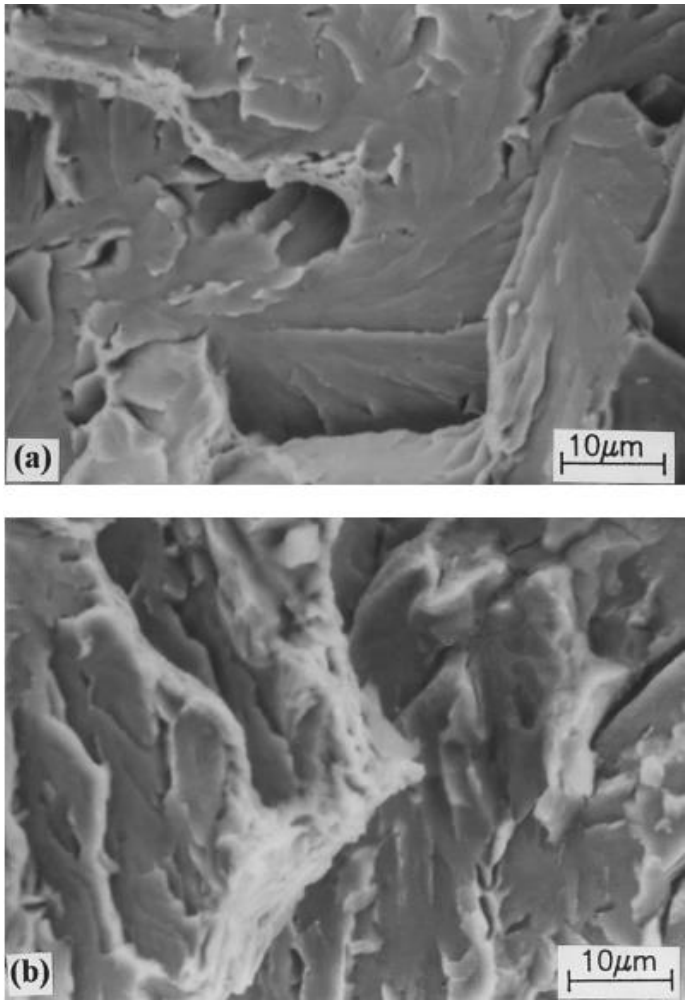

Figure 2.43 SEM images showing transgranular fracture in the specimen's creep tested at (a) 793 K, 150 MPa, and rupture time 10,850h and (b) 873 K, 90 MPa, and 2194 h (Choudhary et al., 1999).

In 2005, Gaffard et al. studied creep flow and the damage properties of base and metal weldment of 9Cr-1MoNbV steels at 625℃. The SEM observation of fracture surfaces of base metal specimen under 120MPa in Figure 2.18 show that cavities nucleate at grain boundaries, preferentially in stress concentration areas (near second phase particles or at triple junctions), leading to ductile fractures with relatively low (10%) volume fractions of cavities (Gaffard et al., 2005).

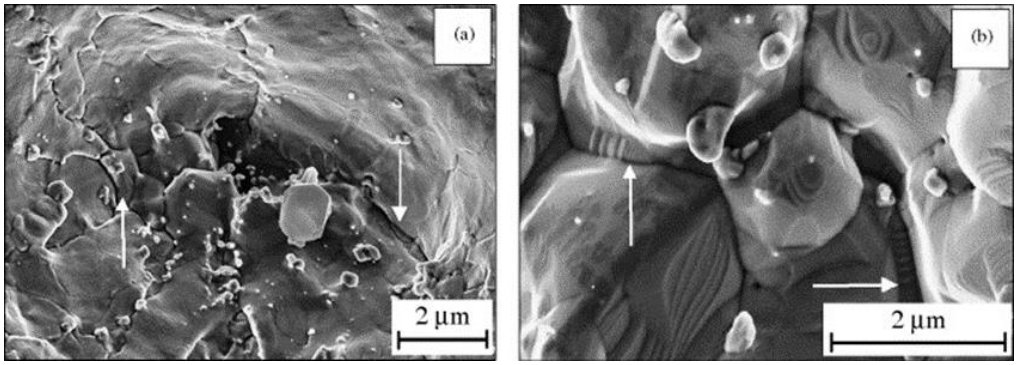

Figure 2.44 Fracture surfaces of creep specimens tested under vacuum, SEM observations (a) base metal (BM) (120 MPa, 1800 h) and (b) weldment (WM) (90 MPa, 950 h), arrows indicate secondary intergranular cracking between the grain boundaries facets. (Gaffard et al., 2005).

In 2006, Lee, et al. studied creep strength in 9Cr-1.8W-0.5Mo-VNb steel (ASTM Grade 92) at 550-650℃ up to 63 151h (Lee, et al., 2006). The experimental observation of fracture surface in Figure 2.19 indicates: (a) a typical ductile transgranular fracture with dimple pattern at high stress level (270MPa) and (b) the absence of a dimple pattern suggests that there exists a brittle intergranular fracture for low stress level (80MPa). Creep cavities are nucleated at coarse precipitates of Laves phase along grain boundaries, the cavity formation and the following brittle intergranular fracture were triggered while the coarsening of Laves phases over a critical size (Lee et al., 2006).

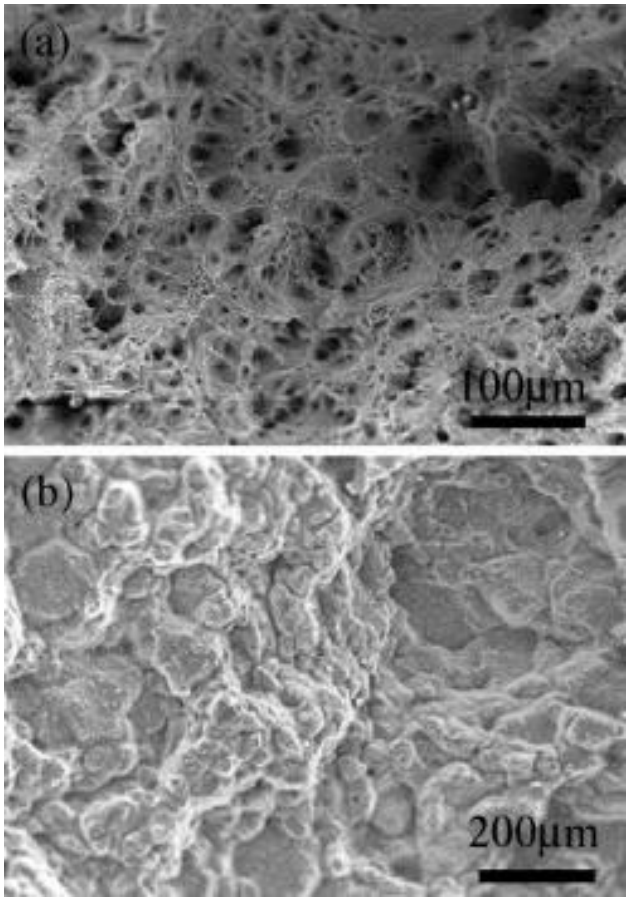

Figure 2.45 Fracture surfaces after (a) 150.2h creep under 270MPa at 550℃ (Ductile fracture), and (b) 26,783h creep under 80MPa at 650℃ (brittle fracture) (Lee, et al., 2006).

In 2009, the study into the effect of long-term creep on the microstructure of a 12% chromium (German Grade X20) tempered martensite ferritic steel under 120MPa at 550℃ was reported by Aghajani et al. SEM images of the rupture surface on the specimen show that creep cavities on a prior austenite grain boundary are perpendicular to the direction of the applied stress in Figure 2.20 (Aghajani et al., 2009).

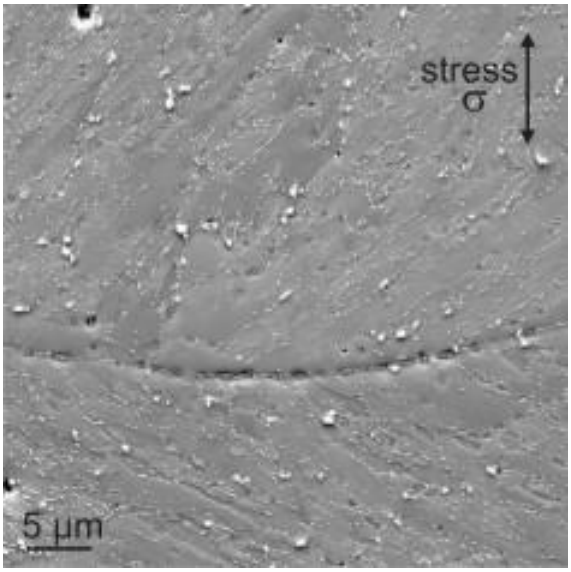

Figure 2.46 SEM micrograph of the ruptured specimen of 12% Cr steel showing creep cavities on a prior austenite grain boundary perpendicular to the direction of the applied stress (Aghajani et al., 2009).

In 2010, Panait et al conducted a study into the microstructure of the Grade 91 steel after more than 100,000h of creep exposure under 80MPa at 600℃. The creep specimen had a rupture time of 113, 431h and a strain (elongation) of 7.3%. The backscatter electron (BSE) or secondary electron (SE) image of the fracture surface in Figure 2.21, displays a high density of cavities of which the cavities seem to nucleate at the grain boundary next to large particles such as Laves phase. Coalescence of cavities was observed at a distance lower than 0.5mm from the fracture surface (Panait et al., 2010).

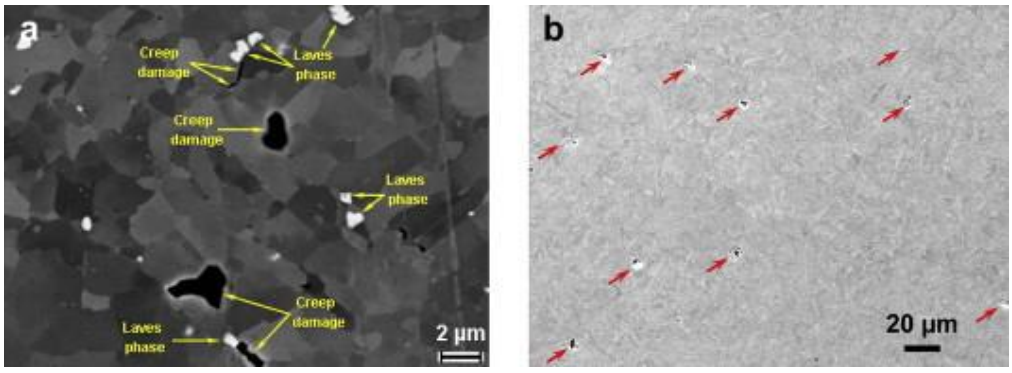

Figure 2.47 SEM images of fracture surface of P91 steel after creep at 600℃ for 113, 431h (Panait et al., 2010).

In 2011, creep behaviour of modified 9Cr-1Mo ferritic steel for steam generator (SG) tube application was study by Choudhary and Samuel. Creep tests were

performed on specimensmat 823, 848 and 873K (550-600℃) under a stress range of 125 to 275MPa. The fracture surface of modified 9Cr-1Mo steel creep tested under 200MPa at 550℃ for 8098h in Figure 2.22 indicates a ductile transgranular fracture resulting from coalescence of micro voids (Choudhary & Samuel, 2011).

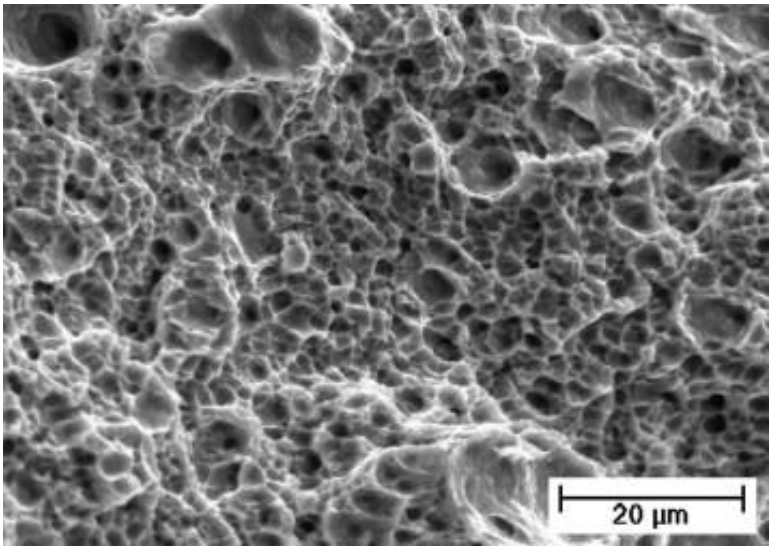

Figure 2.48 SEM image of modified 9Cr-1Mo steel creep tested under 200MPa at 550℃ for 8098h showing ductile transgranular fracture (Choudhary & Samuel, 2011).

In 2012, Vanaja et al. studied creep deformation and rupture behaviour of 9Cr–1W–0.2V–0.06Ta Reduced Activation Ferritic–Martensitic (RAFM) steel. Creep specimens' tests were performed at 773, 823 and 873K (500-600℃) under a stress range of 100 to 300MPa. The SEM image (Figure 2.23) of the fracture surface of creep specimen under 200MPa at 600 ℃ showed a ductile transgranular fracture resulting from coalescence of micro voids (Vanaja et al., 2012).

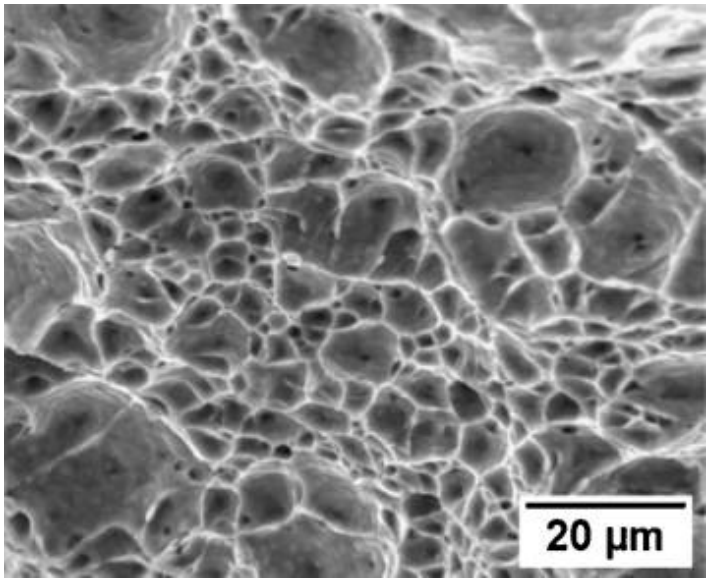

Figure 2.49 SEM image of 9Cr-1Mo steel under 200MPa at 600℃ (Vanaja et al., 2012).

In 2013, Choudhary conducted research into the tertiary creep behaviour of 9Cr–1Mo ferritic steel when quenched and tempered (Q+T). A typical ductile transgranular fracture was observed on the fracture surface of specimens at 873K (600℃) under 100MPa for 412h as shown in Figure 2.24 (Choudhary, 2013).

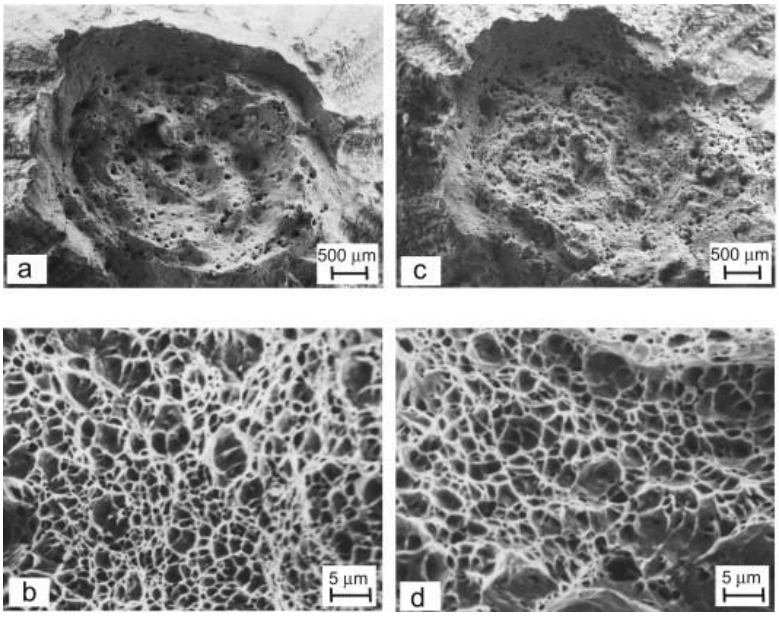

Figure 2.50 SEM images of facture surface of 9Cr-1Mo steel in quenched and tempered (Q+T) showing ductile transgranuar fracture in 100MPa (Choudhary, 2013).

In 2013, creep rupture behaviour of Grade 91 steel in a temperature range of 600-700℃ and a stress range of 35-350MPa was reported by Shrestha et al. The SEM images of fracture surface of specimens (a) under 100MPa at 650℃, c) under 200MPa at 600℃ and (d) under 200MPa at 650℃ are characteristic of a ductile transgranular fracture in Figure 2.25 (Shrestha et al., 2013).

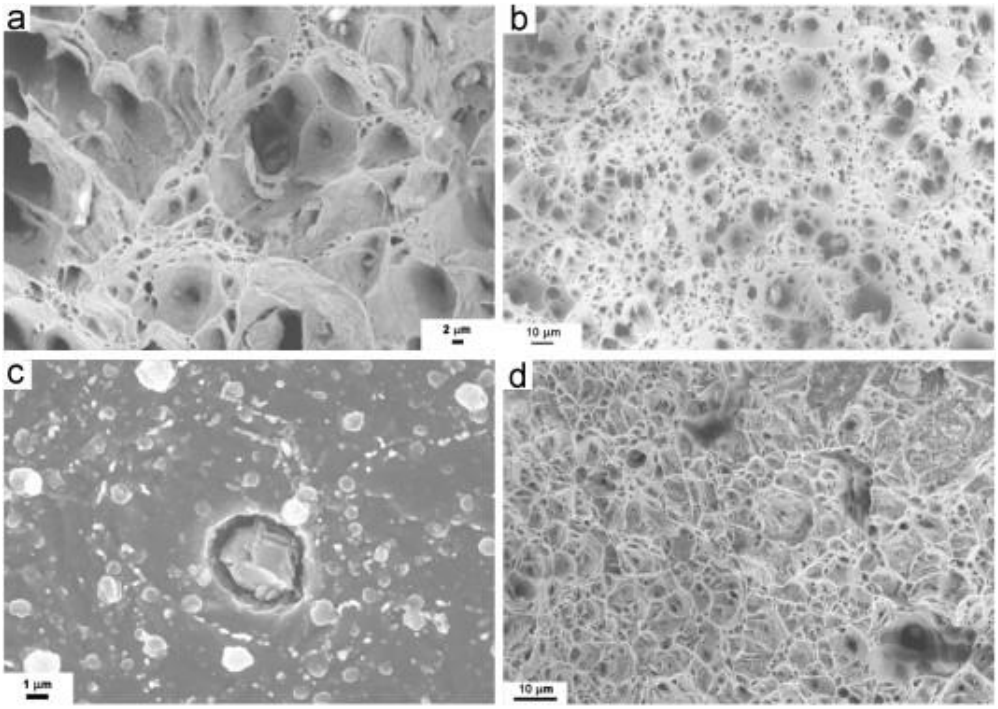

Figure 2.51 SEM images of fracture surface in Grade 91 steel (a) under 100MPa at 650℃, (b) under 80MPa at 700℃, (c) under 200MPa at 600℃, (d) under 200MPa at 650℃ (Shrestha et al., 2013).

In 2013, Parker studied in-service behaviour of creep strength enhanced ferritic steels Grade 91 and Grade 92, the optical micrographs of fracture surface of parent Grade 92 steel with low ductility appear to have suffered from a brittle intergranular fracture, this brittle behaviour is a consequence of high density within creep cavities in Figure 2.25 (Parker, 2013).

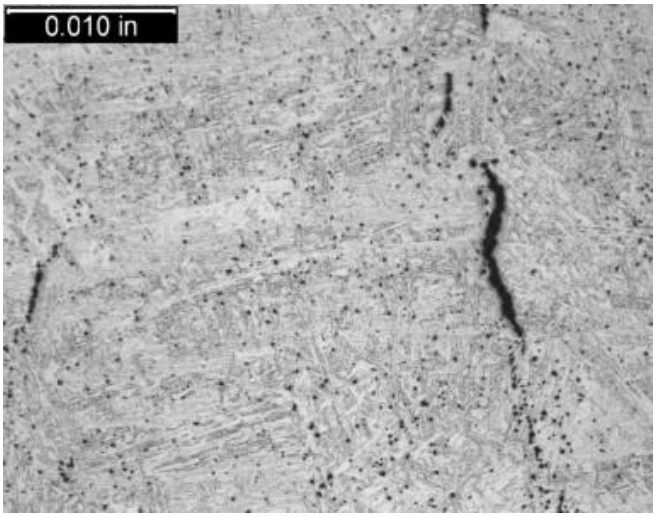

Figure 2.52 Typical optical micrographs from Grade 92 steel which failed with low ductility showing high densities of creep cavities (Parker, 2013).

In 2013, creep properties of Grade 91 steel steam generator tube at 923K (650℃) was studied by Palaparti et al. The SEM fractograph displays a transgranular fracture in a creep tested specimen for Grade 91 (T91) at 923 K at 112 MPa for 332 h as can be seen in Figure 2.27 (Palaparti et al., 2013).

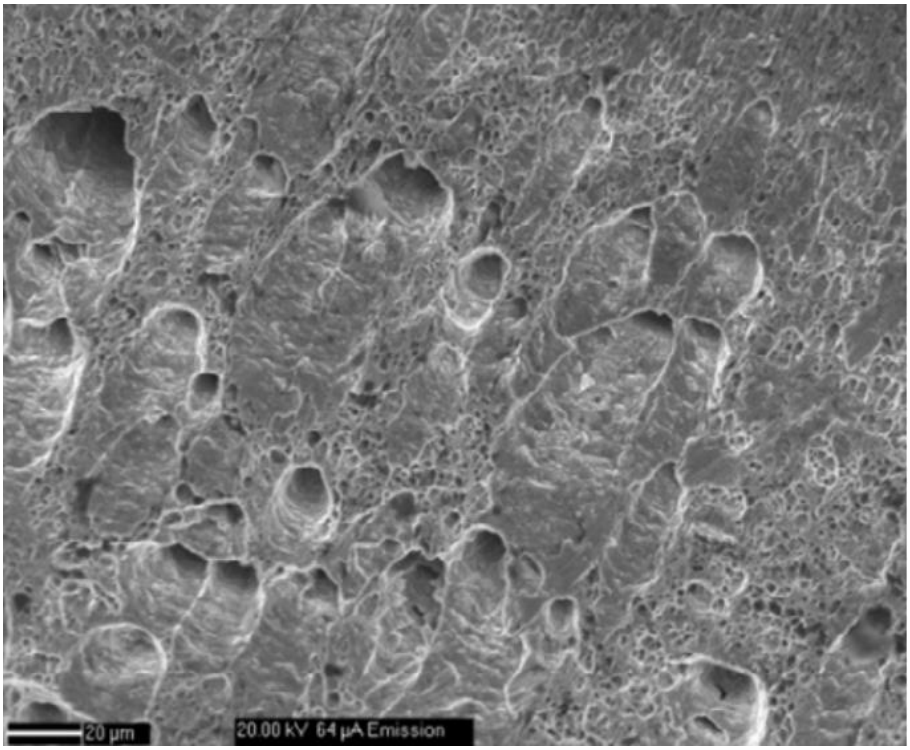

Figure 2.53 SEM image of transgranular fracture in creep tested specimen for Grade 91 (T91) at 923 K at 112 MPa for 332 h (Palaparti et al., 2013).

In 2014, Goyal et al. investigated the effect of constraint on creep rupture behaviour of 9Cr-1Mo steel under 150MPa at 873K (600℃). The SEM image of the fracture surface of the specimen under 150MPa at 873K (600℃) revealed a ductile transgranular fracture in Figure 2.28 (Goyal et al., 2014) (Goyal & Laha, 2014).

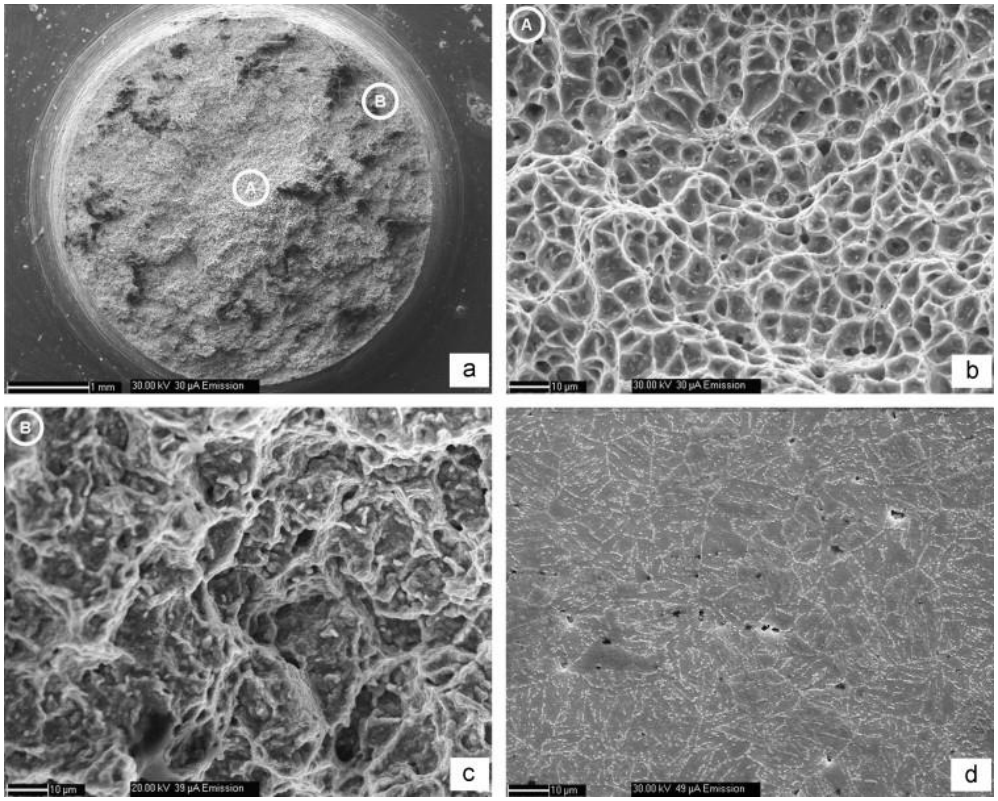

Figure 2.54 Fracture surface of plain specimen at 873K (600℃) under 150MPa (Goyal et al., 2014) (Goyal & Laha, 2014).

In 2014, Nie et al. researched the microstructure evolution and life assessment of T92 steel during long-term creep. Based on the observation of the fracture surface of specimen after creep under 46MPa at 700℃ for 8232h in Figure 2.29, it indicates cavities were formed at proper austenite grain boundaries and intergranular fracture (Nie et al., 2014). Figure 2.29 (b) shows cavities nucleated at the interface of large Laves-phases particles and Laves phase have the potential to provide sites for cavities nucleation. The researcher thought cavities nucleated at the coursing of Laves phase particles on grain boundaries, which triggered a final fracture in the steel (Nie et al., 2014).

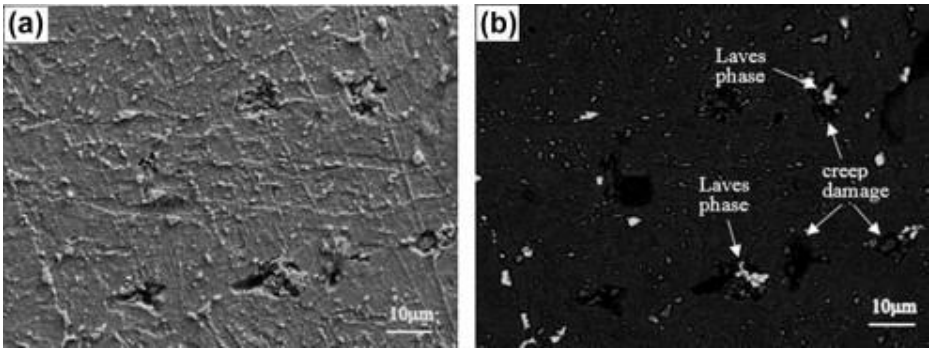

Figure 2.55 Cavity formation in specimens after creep under 46MPa at 700℃ for 8232h: (a) Second electron (SE) image (b) back-scattering electron (BSE) image (Nie et al., 2014).

In 2014, characterisation of Laves phase precipitation and its correlation to creep rupture strength of ferritic steels (an alloy Fe-9Cr-3Co-W without C and N) was reported by Zhu et al., SEM images of fracture surfaces of specimens indicated a ductile transgranular fracture in a high stress range 100MPa and brittle intergranular fracture in a low stress range of 50MPa (Figure 2.30) (Zhu et al., 2014). The researchers suggested that the creep rupture strength started to decrease before the precipitation of Laves phase completed, which may be due to the coarsening of Laves phase particles thus triggering the cavity nucleation (Zhu et al., 2014).

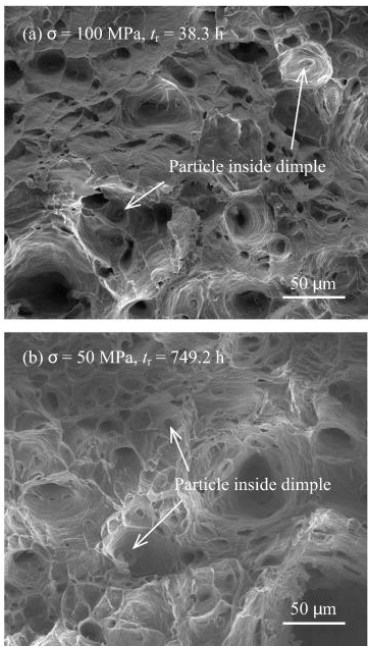

Figure 2.56 SEM images of rupture surfaces of specimens under different stress at 650℃ (Zhu et al., 2014).

In 2015, Vanaja & Laha assessed of creep deformation behaviour in reduced activation ferritic-martensitic (RAFM) steel (9Cr-W-0.06Ta-0.22V) under a high stress level range of 180 to 260MPa at 823K(550℃). The SEM images show the transgranular fracture in the 9Cr steel specimens under 220MPa at 823K (550℃) in Figure 2.31 (Vanaja & Laha, 2015).

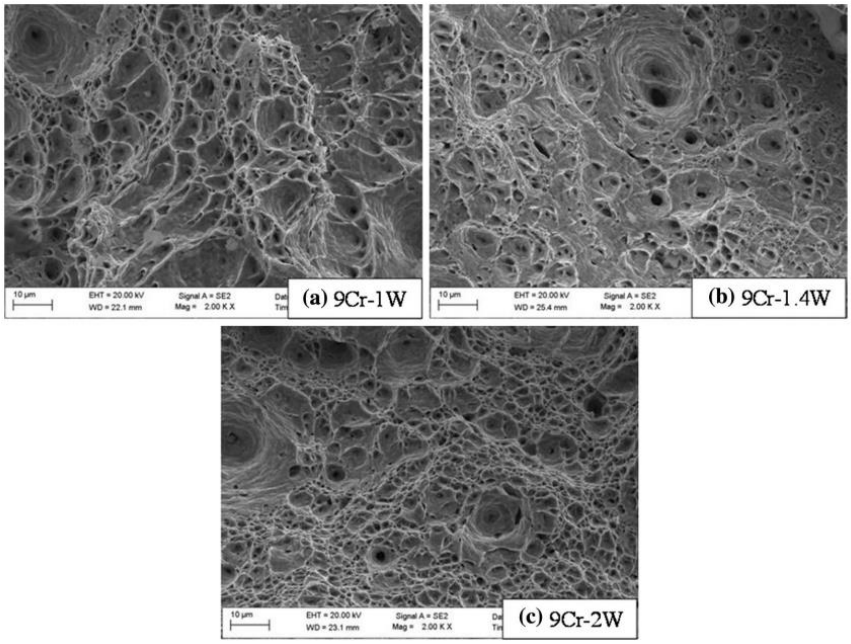

Figure 2.57 SEM images show transgranular fracture in the creep-tested samples at 220 MPa and 823 K (550 C) for (a) 9Cr-1W, (b) 9Cr-1.4W, and (c) 9Cr-2W steels (Vanaja & Laha, 2015).

In 2015, Ni et al. carried out a study on creep mechanical behaviour in P92 steel under multiaxial stress state at 650 ℃, and the creep mechanical behaviour of P92 steel under different stress at 650℃. The microscopic fracture morphologies (Figure 2.32) indicate ductile transgranular factures at high stress level (Ni et al., 2015).

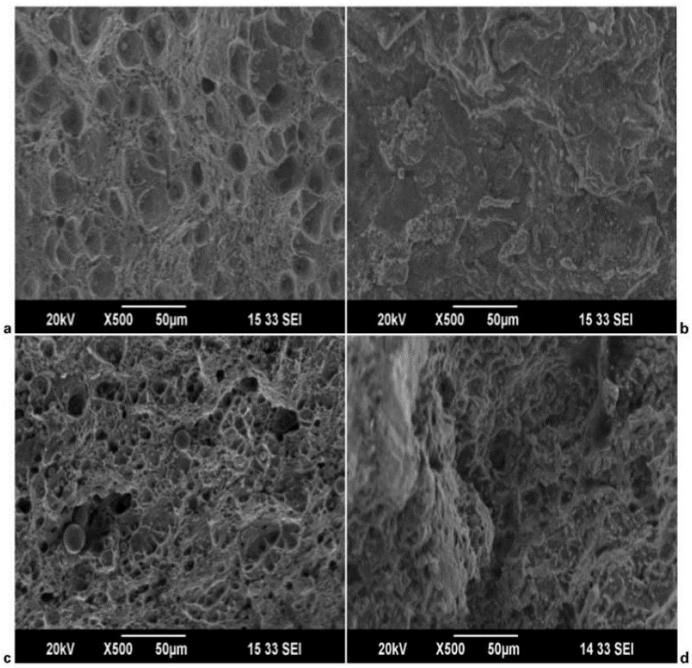

Figure 2.58 Morphologies of different parts of fracture surfaces for P92 specimens under 145MPa (a) centre (b) notch root and 185MPa (c) centre (d) notch root (Ni et al., 2015).

In 2017, Creep deformation behavior of 9Cr1MoVNb (ASME Grade 91) steel was studied by Guguloth & Roy, the SEM images indicate a ductile fracture is resulting in the nucleation and growth of micro voids in Figure 2.33 (b) under 180MPa at 550℃ (c) under 100MPa at 600℃ (Guguloth & Roy, 2017).

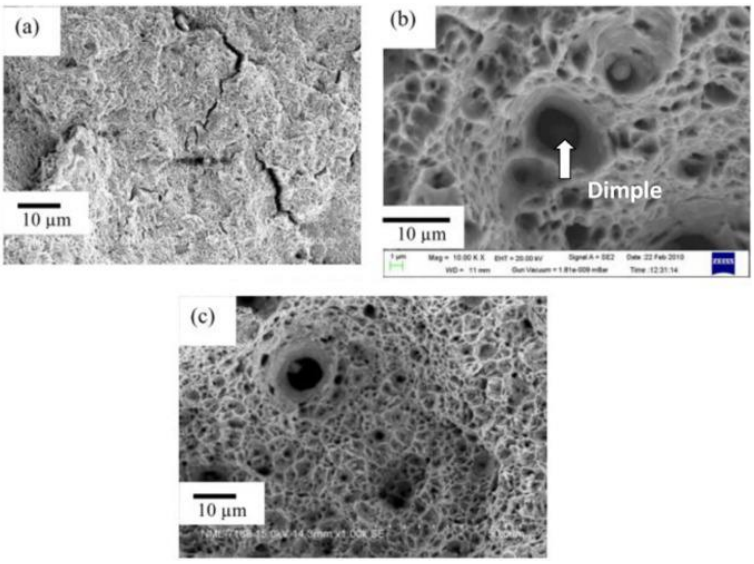

Figure 2.59 The fracture mode changed to classical ductile fracture characterized by the nucleation and growth of micro voids (b) under 180MPa at 550℃ (c) under 100MPa 600℃ (Guguloth & Roy, 2017).

Appendix C-Details of high chromium steels, chemical compositions in wt.%

Material parameters of 9%Cr steel describe creep deformation (microstructural degradation) over a range of stress and temperature from literature.

$Materials$	$Temperature$	H^*	$h'(MPa)$	$K_p(h^{-1})$	C
9CrMoVNb steel [Ghosh, 2013] [Nandi, 2013]	540℃	0.3	10300	2.55×10^{-5}	27
9–10%Cr ferritic steels [Oruganti, 2011]	649℃	0.45			
T/P91 [Chen et al., 2011]	600℃	0.269	10000	5.4×10^{-5}	
9%Cr martensitic steel [Semba, 2008]	600℃	0.35	10000	8×10^{-5}	
9%Cr steel (P92)[Yin and Faulkner, 2006]	600℃	0.57	6000		50

P91 pipes(Bar 257) [Hyde et al., 2006]	650℃	0.35	10000	4.998×10^{-4}	
P91 pipes (A-369 FP91) [Hyde et al., 2006]	625℃	0.203	9000	2.7×10^{-4}	